# Electroforming in titanium dioxide microdevices

## Inaugural-Dissertation

# Abstract

This thesis deals with the effects of electroforming on gas sensing microdevices and its applications. Electroforming can be defined as structural changes in solids in response to applied electric fields. It comprises the drift of ions and charged defects, electric field induced changes in the crystal structure as well as field-induced chemical reactions like oxidation. Electroforming effects typically require electric fields above a material-specific threshold. It is therefore expected that the occurrence of related effects increases as the samples are miniaturized. The objective of the present dissertation is a systematic study of electroforming effects in functional solid-state microstructures and their possible utilization for the preparation or improvement of solid-state based devices.

Titanium oxide has been selected as a paradigmatic material, since it is predestined for pertinent studies: the drift mobility of charged oxygen vacancies is unusually large, the material can be anodized easily, and there are many known oxidation states, with the Magnéli phases being the most prominent example. Also, titanium oxide is used in a wide variety of applications as diverse as, for example, solid state catalysts, memristive devices, gas sensors or inorganic hybrid solar cells.

In the first part of this thesis, studies are presented where electroforming effects occur in a disruptive way, namely as drift effects in gas sensors based on $TiO_2$. It is shown that hydrogen sensing and memristive behavior interdepend in a nontrivial manner in $TiO_x$-based microsensors. This interdependence turned out to be of universal nature and is independent of the fabrication technique and sample geometry. In the second part, we look at active implementations of electroforming for the modification, improvement and even complete preparation of microdevices, with emphasis on microchip-based sensors.

# Eidesstattliche Versicherung

Ich versichere an Eides Statt, dass die Dissertation von mir selbständig und ohne unzulässige fremde Hilfe unter Beachtung der „Grundsätze zur Sicherung guter wissenschaftlicher Praxis an der Heinrich-Heine-Universität Düsseldorf" erstellt worden ist.

_____

Düsseldorf, den 17. Dezember 2018

# Preface

This thesis is the result of my work at the *Institut für Experimentelle Physik der kondensierten Materie* of the *Heinrich-Heine-Universität Düsseldorf* since March 2014. During this time I was supervised by Prof. Dr. Thomas Heinzel and contributed to four scientific papers that have been published in various peer-reviewed journals. The papers related to chapter 2 are Papers I and II. The papers related to chapter 3 are Papers III and IV. Bibliographic details are given below.

I   M. Strungaru, M. Cerchez, S. Herbertz, T. Heinzel, M. El Achhab and K. Schierbaum, *Interdependence of electroforming and hydrogen incorporation in nanoporous titanium dioxide*, Applied Physics Letters **106**, 143109 (2015)

II  S. Herbertz, M. Cerchez and T. Heinzel, *On-Chip planar hydrogen sensor with sub-micrometer spatial resolution*, Sensors and Actuators B **221**, 401-405 (2015)

III S. Herbertz, P. Aleksa, M. Zielinski, D. Welk and T. Heinzel, *Bias voltage-induced oxidation of titanium microelectrodes in planar $Ti/TiO_x$ heterojunctions*, Superlattices and Microstructures **124**, 231-239 (2018)

IV  S. Herbertz, D. Welk and T. Heinzel, *Lateral hydrogen microsensors prepared on-chip by local oxidation of platinum-decorated titanium films*, AIP Advances **8**, 055301 (2018)

# Contents

# Introduction

TiO$_2$ is one of the most studied metal oxides in present research [1, 2]. Its uses range from applications as UV blocker and white pigment in paints to medical applications [3], photocatalysis [4–6], in particular electrolytic water splitting [7], electromotive force (emf) cells [8, 9], chemiresistors [10] and doping-induced ferromagnetism [11, 12]. Its interesting and useful behavior in response to gases has also been widely studied [2, 10, 13, 14]. A lot of effort was put in the development of fabrication techniques, which lead to a variety of structures like nanotubes [15–18], nanowires [19, 20] and nanoporous TiO$_2$ [21–23] with great suitability for gas detection. Especially hydrogen sensing has become increasingly relevant. H$_2$ detection with high spatial resolution [24] is desirable for the analysis of storage and permeation of hydrogen in metals [25–27], in particular hydrogen embrittlement of steels [28–35]. There are huge numbers of studies on the properties of the TiO$_2$ surface [1, 36, 37] and its interaction with gases like H$_2$ [23, 38, 39], O$_2$ [40–42], CO [14, 22, 40, 43] and H$_2$O [22, 40, 44–47]. On the other hand, TiO$_2$ attracted a lot of attention during the last two decades as resistive switching device due to its memristive behavior [48–52]. In this context, the term *electroforming* is defined as structural modifications in the material under high electric fields that are caused by motion of charge carriers. These modifications become manifest in variable, time- and voltage-dependent conductivity. Reports about permanent or volatile motion and rearrangement of ions, defects or impurities exist, as well as forming of conductive filaments [50] with field-induced phase transitions within [53]. However, the consideration of a combination of both specialist fields, electroforming and H$_2$ detection, has been neglected so far.

This issue is addressed in Paper I [54], which is the starting point of this work. In this study, electrochemically prepared nanoporous TiO$_2$ microstructures [39] are used as H$_2$ detectors. Additionally, these structures also exhibit electroforming behavior when exposed to high electric fields. These effects have so far been studied only independently. The main finding of this study is that electroforming can not only be observed as undesired drift in the gas sensors but incorporation of H$_2$ and memristive behavior also interdepend in a nontrivial way. For example, an unexpected resistance increase caused by H$_2$ has been observed when the material is kept in the electroforming mode by applying high voltages. This effect has not been demonstrated hitherto. As an explanation, we suggested the possibility of structural changes like phase transitions inside the oxide, as well as a theoretically proposed mechanism [55], by which atomic H$_2$ substitutes oxygen vacancy sites. Unfortunately, both suggestions for the underlying mechanism of these new phenomena are difficult to verify experimentally.

Furthermore, it was unclear whether the observed effects would be present in TiO$_2$ structures of completely different fabrication and geometry. In particular, one might ask the question whether this nontrivial behavior would be revealed or even become stronger, when the TiO$_2$ is downscaled. This question is adressed in Paper II [56], where

samples were investigated which were developed in the frame of an applied research project[1]. This project was a main part of this work and had the aim to develop a multifunctional gas sensor, smaller than state-of-the-art sensors and capable of being integrated in Si technology. Here, the focus lied on the development of $TiO_2$ nanowires in lateral geometry where the oxide thickness was downscaled by a factor of 20. Despite the differing fabrication technique and $TiO_2$ texture, both, functionality as a gas sensor and electroforming could be demonstrated. Surprisingly, the described interdependence could indeed be observed with amazing resemblance to the effects described in Paper I. We concluded from this, that the discovered interdependence of $H_2$ incorporation and electroforming has a universal character. Of course, this also raises the question, why these phenomena have not been observed in earlier studies. One reason for this might be the lack of studies that combine the field of interactions of $TiO_2$ and $H_2$ with electroforming behavior.

Until now, electroforming has been considered in structures of fixed outward geometry, with more or less reversible changes in the internal structure. The novel design in lateral geometry with an increased surface-to-volume ratio also allows for investigations of morphological changes by simple means like optical microscopy, atomic force microscopy (AFM) and scanning electron microscopy (SEM). This way, it was found that high electric fields can cause structural changes in the oxide under atmospheric conditions. These changes concern, on the one hand, the geometry, i.e. the height and width of the nanowire but also the oxide morphology. A comprehensive characterization is given in Paper III [57]. Here it was shown, that the reported phenomena cannot always be strictly separated. Ionic motion in high fields causes not only phase transitions and filament formation but additional effects, that we attributed to strain changes in the oxide through growth, distortion and even swelling, as well as post-growth crytal reordering [58]. To avoid any misunderstanding – processes like field-induced oxidation or anodization of metals like Ti are very well known [59–62]. Here the attention is called to structural modifications that can easily happen unintentionally in ambient conditions and which are generally not kept in mind when it comes to gas sensing applications or investigation of memristive effects.

In the last study, these recently obtained findings were successfully utilized to define a novel sensor element on-chip under electroforming conditions. The gas sensor is optimized for the operation in the low-voltage mode to avoid further unintended structural modifications. On top of this, the number of production steps could be considerably reduced using this new technique. The fabrication procedure and characterization as sensor is subject of Paper IV [63]. Admittedly, electroforming is not implemented in terms of directed phase transitions. In fact, the exact phase composition in our devices remains unclear since it is difficult to characterize on an atomic level in layers of such small dimensions. Nevertheless, such applications would be imaginable, given the fact that the phase composition in $TiO_2$ can have significant influence on the gas sensing performance [64]. However, the focus in this work lies rather on the development of an implementation for easier fabrication of scalable and tunable gas sensing devices. Instead of a prefabricated oxide, only a Ti film in the proper layout is needed for on-chip preparation of gas-sensitive $TiO_2$ via anodization. Moreover, surprising effects on

---

2

anodization became evident, when Pt serving as catalyzing agent in $H_2$ detection, was deposited beforehand. The microsensors are comparable in height to those of Papers II and III, but are producible with a much larger lateral dimension. Therefore a structural analysis was possible, not only with a view on the morphology and surface roughness by means of AFM, but also regarding an investigation of the elemental composition via energy dispersive x-ray spectroscopy (EDX).

This thesis is organized as follows. The first chapter deals with the fundamental concepts. An overview of the history and terminology in the field of memristive devices, as well as an introduction to state-of-the-art resistive switches is given. The term electroforming, as it was investigated in this work, is defined. The structures that are subject in all publications comprise similar materials, these are mainly Ti, $TiO_2$ and Pt. For this reason, the relevant material properties are shortly described. Afterwards, a description of the experimental techniques for the preparation, characterization and measurements is given. Chapter 2 is focused on electroforming as a disruptive phenomenon in $TiO_2$-based gas sensors. Therefore, the two different fields are first discussed separately. Different techniques for gas sensing based on $TiO_2$ are introduced with emphasis on the detection of $H_2$ and $O_2$, followed by a description of electroforming behavior in $TiO_2$. Afterwards Paper I and II are introduced and merged under the aspect that in two $TiO_2$ structures of very different geometry, fabrication and structural properties, very similar effects arise under high electric fields and gas exposure. Chapter 3 deals with an active implementation of electroforming in the modification of microsensors on-chip. In both studies, Paper III and Paper IV, possible oxidation mechanisms are discussed. Some of the results of the EDX analysis are included in the second part of chapter 3 as additional support of our line of arguing concerning the underlying processes. The thesis ends with a conclusion of the main findings and an outlook towards potential future research.

# 1 Fundamental Concepts

## 1.1 Resistive switching and Electroforming

Hysteretic current-voltage charactersitics and measurments of a negative differential resistance were already reported in 1962 by Hickmott [65] for metal/insulator/metal (MIM) structures of alumina. However, these findings were not assigned to memristive devices but to current-limiting space charges in the oxides. Resistive switches are two-terminal devices or elements that can reversibly change their resistance between two or more levels upon electrical stimuli which affect an internal state variable [66]. This happens in a *nonvolatile* manner, which is why the devices are called *memristive*. Memorized resistance changes are closely linked to the *memristor*, which was postulated in 1971 by Chua [67] based on fundamental symmetry arguments. Memristive systems as special case of nonlinear dynamical systems are described by the equations [66]

$$V = R\left(\boldsymbol{x}, I, t\right) \cdot I \tag{1.1}$$

$$\dot{\boldsymbol{x}} = f\left(\boldsymbol{x}, I, t\right) \tag{1.2}$$

where the variable $\boldsymbol{x}$ denotes the state of the system, the current $I$ is an external input variable and the voltage $V$ is the observed output variable. These equations apply for a current-controlled memristive system. For the voltage-controlled system the equations are

$$I = G\left(\boldsymbol{x}, V, t\right) \cdot V \tag{1.3}$$

$$\dot{\boldsymbol{x}} = f\left(\boldsymbol{x}, V, t\right) \tag{1.4}$$

The ideal memristor as proposed by Chua as the fourth passive circuit element is yet another special case of memristive systems and has only one state variable, which is the charge $q$ in current-controlled systems or the magnetic flux $\phi$ in the voltage-controlled system:

$$V = R\left(q\right) \cdot I \qquad\qquad I = G\left(\phi\right) \cdot V$$
$$\dot{q} = I \qquad\qquad \dot{\phi} = V.$$

A typical property of memristive elemets is a pinched hysteresis loop that is more pronounced when the frequency of the external input is comparable to the frequency of internal processes that cause the memory effects [66]. In the 1990s titania, perovskite-type manganites and other rather complex transition metal oxides became of popular interest as electrically or thermally activated resistance change devices [53]. In 2008 the theory of the ideal memristor was linked to resistive switches for the first time by Strukov et al. [48] (*'The missing memristor found'*), who claimed that memristance

arises naturally in nanoscale systems, in which electronic and ionic transport are coupled under an external bias voltage. This led to further increase in research activities and was controversially discussed, e.g. by Vongehr and Meng [68] (*'The missing memristor has not been found'*).

In the query for alternatives to flash memory devices in data storage, resistive switches with two or multilevel resistance states have attracted great attention. The devices can be roughly classified depending on the internal state variable. In the so called 'redox-based resistive switching random access memory', short ReRAM, the resistance changes due to ionic motion on the nanoscale. Typically a ReRAM cell consists of a metal oxide like $NiO$, $TiO_2$, $SrZrO_3$ or $SiO_2$ (semiconducting or insulating) sandwiched between two metal electrodes [53]. Others are, for example, phase-change RAMs (PRAM), where the resistance changes, typically in chalcogenides, due to transformations between the crystalline and the amorphous state, magnetoresistive RAMs (MRAM) based on magnetic tunnel junctions, or ferroelectric RAMs (FeRAM) where the polarization of a ferroelectric material is reversed [69].

Compared to CMOS technology and capacitance based RAMs with an inherent scaling problem [52], an important feature of the simple two-terminal structure of ReRAMs is their potentially good scalability. This allows not only for low-voltage operation but also implies the potential for high-density arrays of memory cells. Cross-point structures and multilevel stacking have already been realized [49, 51, 70, 71] in cells with small device areas of $4F^2$ with a minimum feature size $F$ that is lithographically defined [66]. High connectivity and high density are facilitated by small feature sizes and are promising for neuromorphic systems. An example are hybrid systems of CMOS based 'neurons' and memristive synapses in crossbar architecture [72], which is shown in Fig. 1.1. Current challenges in this field are for example the emulation of biological neuronal functions in *'neuristors'* like action potential generation or spike-time-dependent plasticity [73]. Apart from stackability and multilevel storage, other important parameters of ReRAMs
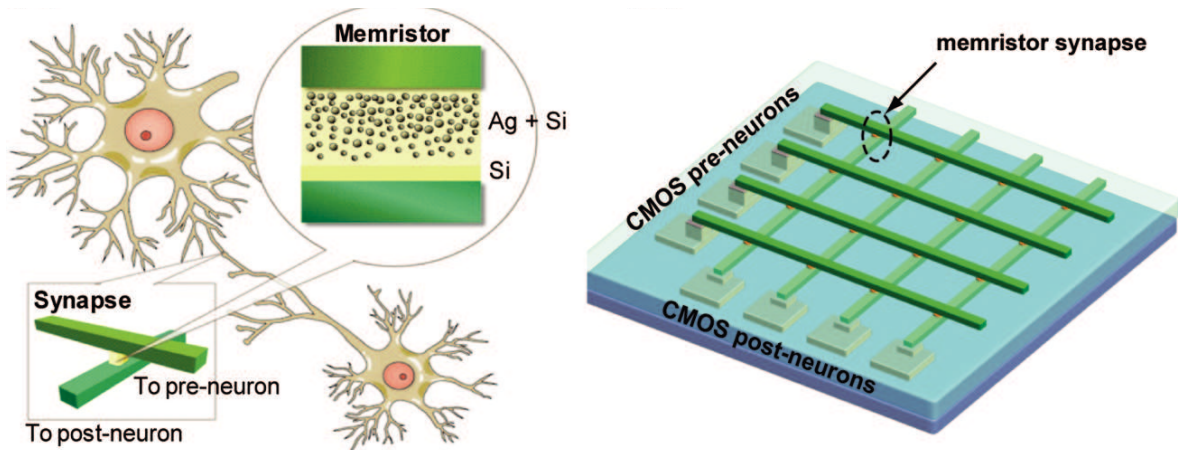


**Figure 1.1:** ReRAM based artificial synapse with a scheme of the two-terminal device geometry in the inset (left) and crossbar configuration of CMOS neurons and synapses (right). Reprinted with permission from Ref. [72]. © (2010) American Chemical Society.

concern the reliability like long data retention time, i.e. the time a device remains in a state without an external input, and memory endurance, i.e. the possible number of switching cycles. Also a low cell-to-cell signal variation is desired. Extrapolated retention characteristics measured at high temperatures yield retention times of over ten years [53], and endurance values of over $10^6 - 10^{12}$ cycles have been reported. Naturally, the absolute values of the resistance in the low-resistive 'on-state' (LRS) and the high-resistive 'off-state' (HRS) in devices of two resistance levels are important parameters that characterize a ReRAM's type and performance. The same applies to the voltages or currents that are required for the 'set' and 'reset' operations and the times these voltages or currents have to be applied. Switching times of a few nanoseconds or less have been reported [53,73]. Also a low energy consumption per switching event is desirable. Pickett et al. [73] report transition energies in their neuristor of $\lesssim 100\,\mathrm{fJ}$.

The driving mechanisms for resistive switching behavior are not fully elucidated. Various models have been proposed, depending on the material, the switching behavior (polarity) and conducting path [53]. The three most common operation modes of resistive switching in ReRAM elements are bipolar, unipolar or complementary resistive switching, which are depicted in Fig. 1.2. Bipolar resitive switching is the most common operation and can also be found in $Pt/TiO_2/Ti$ devices. It depends on the polarity of the applied voltage. Although the pulse mode is typically used for switching, the periodic current-voltage sweep mode allows for an investigation of the general character and to obtain the threshold voltages [66]. The transformation from the initial HRS to the LRS (set process) is triggered by a voltage $V_{SET} > V_{th1}$. Reading can be done at considerably smaller voltages $V_{rd}$ to not change the state of the device. The reset is performed with a voltage of opposite polarity $V_{RES} < V_{th2}$. In the unipolar operation the switching depends only on the voltage amplitude, not the polarity. By applying a high voltage, the memory cell is in the 'forming' process transferred from the as-prepared HRS to a LRS. The reset process (LRS to HRS) is achieved by applying a certain threshold voltage that is typically smaller than $V_{SET}$ [52,66]. The complementary operation can be seen as two bipolar resistive switches that are connected in an antiserial manner; for details the reader is referred to [66].

For both, unipolar and bipolar switching behavior, models exists that are based on the formation and rupture of conductive filaments in a less conductive matrix (*filament model*) [53]. In 2010 Kwon et al. [50] were able to visualize such conductive filaments by means of high-resolution TEM during resistive switching and gained important insight into their phase composition, structure and dimensions. It is widedly agreed that in bipolar switches filament forming and rupture is closely related to electrochemical migration of oxygen ions and vacancies [53]. Often the driving mechanism is distinguished between an interface-type and a filament-type switching which differ in their area dependence of the resistance. Especially in titania based resistive switches often characteristics of both mechanisms are observed. For example, in $SrTiO_3$ thin film devices a coexistence of filamentary and homogeneous resistive switching has been reported [74]. Lately, models were formulated which include both, formation of filamentary conductive paths and the importance of the interfaces with field-dependent contact resistance [49,70,71,75]. This subject is discussed in detail in section 2.2.

In the description of such state changes in a device during resistive switching, the term

*electroforming* has been established. We define electroforming based on its phenomenology as changes in the resistance that result from electric fields, e.g. when a voltage is applied.
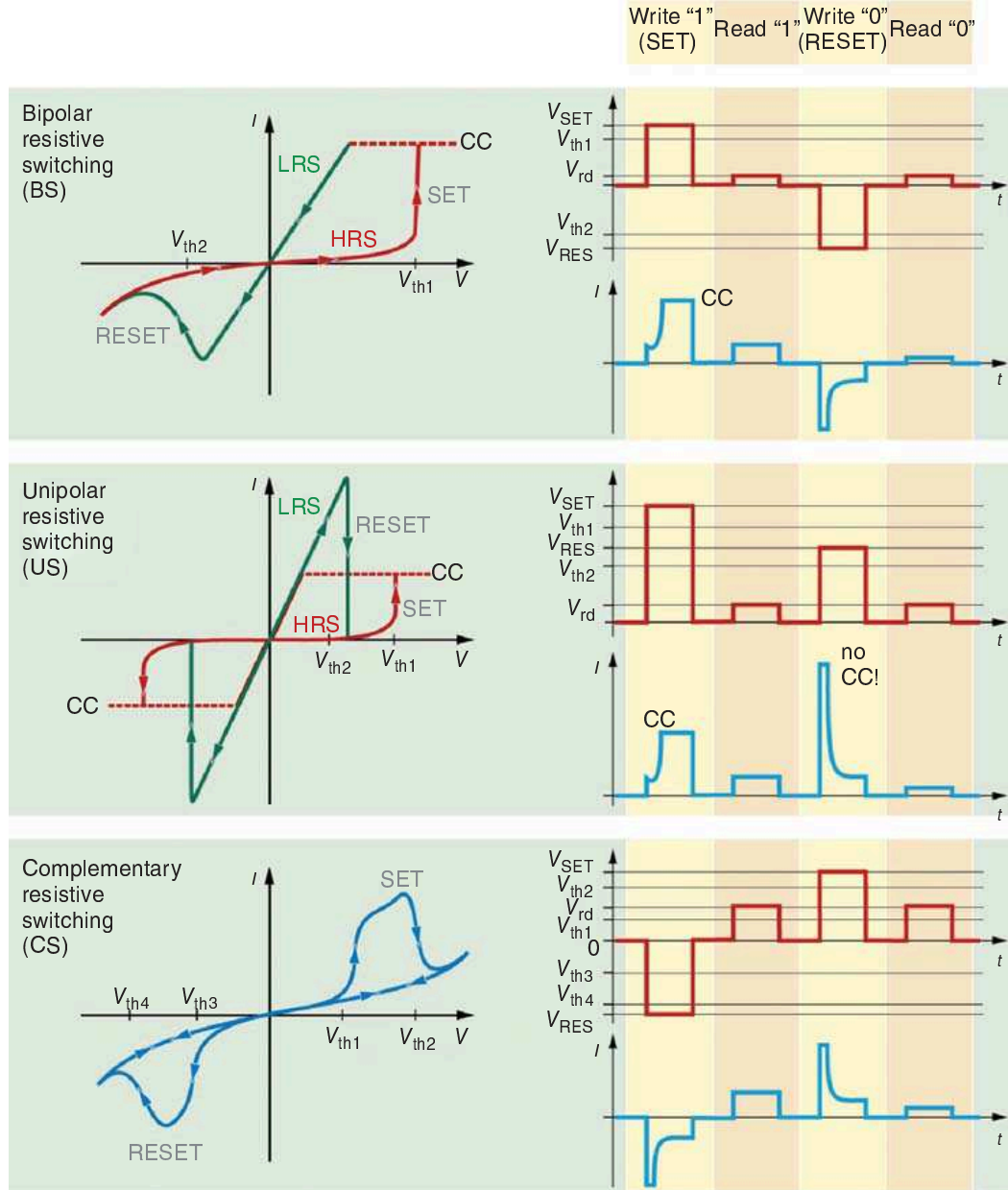


**Figure 1.2:** Three operation modes of ReRAM cells: bipolar (top), unipolar (middle) and complementary resistive switching (bottom). The I-V sweep operation is shown on the left and the pulse operation on the right. Figure reprinted with permission from Ref. [76]. © (2016) Wiley-VCH.

The reasons for these changes can be manifold, comprising effects such as drift of ions and defects (mainly oxygen vacancies), expansion and contraction of defect-rich regions of different conductivity, as far as modifications in the microstructure, like formation and rupture of highly conductive filaments, phase transitions and chemical reactions like oxidations. In chapter 3, electroforming appears as field-induced structural changes that

are visible on the macroscopic scale and result, among other things, in modified resistance. Our definition of the term is more general and its meaning is different in some aspects to electroforming as it is used by some authors. In many publications [51, 52, 66, 71, 77] electroforming means a transfer from an initially highly insulating state of a device, often a metal oxide, into a highly conducting state via strong reduction, whereby the resistivity decreases up to six orders of magnitude. From this state, the device can be switched between the on-state and the off-state, which again differ by a factor of $\approx 1000$ in conductivity. Other authors [78] use the term *electroforming voltage* as the voltage that has to be applied in order to transfer a device from the HRS to the LRS. To avoid any confusion, the process of initial reduction in the following will be referred to as initialization or electroreduction.

## 1.2  Materials

In this section, the materials that were used in this work and their relevant properties are discussed. In the focus of interest are titanium (Ti), platinum (Pt) and, of course, titanium dioxide ($TiO_2$). Ti served as electrode and also as precursor for the functional oxide, in the form of Ti foils and as evaporated or sputtered thin films. Due to its versatile features, Pt served four different purposes: as sensitizer deposited on top of $TiO_2$ for hydrogen sensing, as component in Schottky contacts of $Pt/TiO_2$ structures, and as on-chip integrated meander for both temperature sensing and local heating. An overview over the properties of the used materials is given in tables 1.1 and 1.2.

   Since all studies presented in this thesis are based on titanium oxide structures, its electronic properties, most important defects and phase diagram are discussed in detail, with emphasis on the known polymorphs of $TiO_2$. Also the mechanism of the adsorption of molecules and atoms on the surface of $TiO_2$ and Pt will be discussed. It should be noted that the term adsorption is differentiated between physisorption and chemisorption. A physisorbed molecule or atom is bound to a surface by van-der Waals forces only, with binding energies of $80\,kJ/mol$ ($\sim 0.8\,eV/atom$), whereupon the electronic structure of the adsorbant is barely perturbed. In contrast to that, chemisorption involves chemical modification of the adsorbant, generally with adsorption energies in the order of chemical bond energies $800\,kJ/mol$ ($\sim 8\,eV/atom$).

   In the last part, the interplay of Pt and $TiO_2$ and the relevance for this work is adressed.

**Titanium**

Titanium is a transition metal (4th group) with atomic number 22. At room temperature it crystallizes in the hcp structure ($\alpha$-*phase*) with two atoms per unit cell. It exists in the hcp ($\alpha$-*phase*) and the bcc ($\beta$-*phase*) form [59]. The electrical resistivity of Ti at room temperature is $420\,n\Omega m$ [83]. Ti is known for its rather good resistance to corrosion in oxidizing media. This is due to the formation of a natural oxide layer (5-70 Å) on Ti, that practically instantly forms in the presence of oxygen [59, 84]. A description of the growth of this native oxide layer was first presented by Mott and Cabrera [60, 85, 86] and is shortly described in section 3.2.

| | Ti | Pt | Au | Cr |
|---|---|---|---|---|
| Atomic number [79] | 22 | 78 | 79 | 24 |
| Group | 4 | 10 | 11 | 6 |
| Period | 4 | 6 | 6 | 4 |
| Block [79] | d | d | d | d |
| Electron config. [80] | [Ar] $3d^24s^2$ | [Xe] $4f^{14}5d^96s^1$ | [Xe] $4f^{14}5d^{10}6s^1$ | [Ar] $3d^54s^1$ |
| Electrons per shell [80] | 2 8 10 2 | 2 8 18 32 17 1 | 2 8 18 32 18 1 | 2 8 13 1 |
| Density [79] | $4.506\,g/cm^3$ | $21.45\,g/cm^3$ | $19.30\,g/cm^3$ | $7.19\,g/cm^3$ |
| Atomic weight [79] | $47.87\,u$ | $195.08\,u$ | $196.97\,u$ | $51.99\,u$ |
| Crystal structure [81] | hcp ($\alpha$), bcc ($\beta$) | fcc | fcc | bcc |
| El. resistivity [82] | $420\,n\Omega \cdot m$ | $105\,n\Omega \cdot m$ | $22.14\,n\Omega \cdot m$ | $125\,n\Omega \cdot m$ |

**Table 1.1:** Overview over the metals that were used in this work and their relevant properties.

As can be seen in the electron configuration [Ar] $3d^24s^2$, in addition to the 4s valence electrons, there are two electrons in the 3d shell. In titania, depending on the oxidation state (+2 for TiO, +3 for $Ti_2O_3$, and +4 for $TiO_2$ and $SrTiO_3$), the 3d-like states are partially occupied ($Ti^{2+}$ and $Ti^{3+}$) or unoccupied ($Ti^{4+}$). In the following, only the case of $TiO_2$ will be discussed. However, a detailed investigation of systematic changes in the electronic structure by changing both the crystal structure and the filling of the 3d-like states can be found in Ref. [66].

**Titanium dioxide**

Three modifications of crystalline titanium dioxide are known: rutile, anatase and brookite. Table 1.2 shows parameters of the three crystal modifications, their unit cell and space groups. Of these three, rutile is the most common and thermodynamically most stable form. At high temperatures, brookite and anatase can be transformed into the more stable rutile in an irreversible, constructive process, i.e. involving bond breaking and forming of new bonds. Rutile crystallizes in the tetragonal space group $P4_2/mnm$ (no 136) and anatase in $I4_1/amd$. As can be seen in Fig. 1.3 a), one unit cell of rutile contains two units of $TiO_2$ with Ti cations coordinated octahedrally at the corner (0, 0, 0) and center (1/2, 1/2, 1/2) and O anions at ($1\pm u$, $1\pm u$, 0) and ($1/2\pm u$, $1/2\pm u$, 1/2) with $u = 0.305$ [87, 88]. This way, every Ti atom is surrounded by six O atoms and each O atom is coordinated to three Ti atoms in both, anatase and rutile. The strong ionic bonding in the crystal and distorted trigonal planar coordination of oxygen is due to the three lone electron pairs of oxygen anions interacting with the titanium cations. With a Madelung constant of 2.408 for rutile [89] the lattice energy is around -12 MJ/mol.

Brookite has a more complicated structure, with eight formula units in the orthorhombic cell. It has six different Ti-O bonds and accordingly 12 different O-Ti-O bond angles, in contrast to rutile and anatase, with only two kinds of Ti-O bonds and O-Ti-O bond angles [90].

|  | Rutile [91] | Anatase [92] | Brookite [93] |
|---|---|---|---|
| Density | $4.23\,\mathrm{g/cm^3}$ | $3.79\text{-}3.97\,\mathrm{g/cm^3}$ | $4.08\text{-}4.18\,\mathrm{g/cm^3}$ |
| Crystal system | tetragonal | tetragonal | orthorhombic |
| Crystal class | Ditetragonal dipyramidal | Ditetragonal dipyramidal | Dipyramidal |
| Unit cell | a = 4.59 Å<br>c = 2.96 Å<br>Z = 2 | a = 3.7845 Å<br>c = 9.5143 Å<br>Z = 4 | a = 5.4558 Å<br>b = 9.1819 Å<br>c = 5.1429 Å<br>Z = 8 |
| Bandgap [94] | 3.02 eV | 3.23 eV | 3.14 eV |

**Table 1.2:** Structure parameters and electronic properties of the three polymorphs of TiO$_2$: rutile, anatase and brookite.
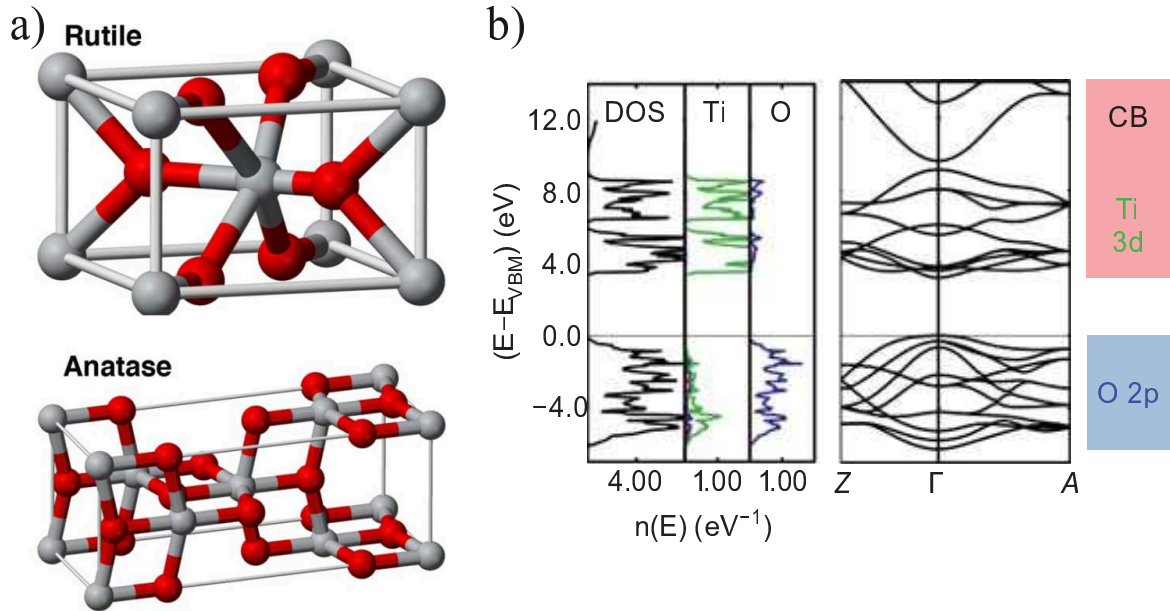


**Figure 1.3:** a) Crystal structure of rutile (top) and anatase (bottom). Figure taken from Ref. [95], © (2008) National Academy of Sciences. b) Electronic structure of rutile: total DOS and partial DOS of Ti and O (left) and corresponding band structure (right). Figure reprinted with permission from Ref. [96]. © (2016) Wiley-VCH.

Stoichiometric TiO$_2$ has a large bandgap in all three polymorphs (3-3.2 eV). The size of the bandgap is also of interest for the photocatalytic activity and photoexcitation of electrons from the valence band to the conduction band, which would be allowed for excitation wavelengths around 400 nm and below. Our observed photocurrents even at illumination with light of a photon energy of 1.8 eV indicate excitation from defect states inside the bandgap, which will be discussed later on. A detailed experimental study on the near-bandgap optical response of TiO$_2$ single crystals using resonant-Raman-scattering was done by Amtout and Leonelli [97].

Fig. 1.3 b) shows the electronic structure of rutile. On the left are pictured the total and partial ion-decomposed density of states (DOS) of Ti and O, subdivided into s (red), p (blue) and d (green) contributions, and the band structure is shown on the right [66]. The 3d-like states of Ti are unoccupied ($TiO_2$ is a $d^0$ compound, oxidation state +4), since all 4 valence electrons of Ti are transferred to O. These unoccupied Ti 3d states are the lowest conduction states, while the valence band is dominated by O 2p electrons. There is, however, some hybridization of Ti 3d states and O 2p states in the valence band, which has also been confirmed experimentally via inelastic electron scattering by Grunes et al. [98]. Moreover, the partial DOS of Ti reveals two separated blocks in the d states. This separation is due to crystal field splitting: the fivefold degeneracy of the d states is lifted when the metal atom is placed into a ligand field of oxygen. The d-orbitals split into $e_g$ (higher in energy: here 7-9 eV) and $t_{2g}$ (3-6 eV) states in an octahedral field. Since the Ti-$O_6$ octahedron is slightly distorted, the bands are split further.

In anatase, the conduction band is also mainly formed by Ti 3d states and the valence band mainly by 2p states. However, there are differences to rutile, concerning the band structure and bandgap. An essential difference is that anatase appears to have a wider optical absorption gap and a smaller electron effective mass, leading to a higher charge carrier mobility [90]. Although a large number of studies exists on mixed anatase-rutile systems, with focus on the electronic structure at the interface [99–101], the fundamental band alignment between the two polymorphs is still not understood. At the same time, these mixed systems are of special interest, since they outperform the individual polymorphs for example in photocatalytic applications. In fact, a synergetic effect has been observed in mixtures of 60 % anatase and 40 % rutile, where the catalytic activity is improved by a factor of two compared to pure anatase [102]. Scanlon et al. [99] reported, that a staggered band alignment of $\sim 0.4$ eV exists between anatase and rutile, with anatase possessing the higher electron affinity, explaining the robust separation of photoexcited charge carriers between the two polymorphs.

The electronic and optical properties are strongly influenced by the defect structure and doping. For example, it has been reported that doping by the transition metal Cr can influence the anatase to rutile ratio [103] and therefore the photocatalytic properties [104] and gas sensing properties [64] of $TiO_2$ nanopowders.

Intrinsic dopants can be interstitial or substitutional, while defects can be produced by removal of lattice atoms. Important intrinsic point defects in the bulk $TiO_2$ are interstitial Ti and oxygen vacancies ($V_O$), which can be produced by reduction, for instance by increasing the temperature. The resulting defect concentration depends mainly on the temperature [105], oxygen partial pressure and on other crystal impurities. Typical values for vacancy concentrations on the $TiO_2$ surface are around 2-8 % ML [106]. Even small oxygen deficiencies $\delta$, introduced either by removal of O [107] or by insertion of interstitial Ti, make $TiO_{2-\delta}$ an n-type semiconductor, with $V_O$ states in the bandgap located 0.75 eV-1.18 eV below the conduction band [108]. From these, trapped charge carriers can get into the conduction band for example via thermal excitation. This way, the resistivity of undoped anatase and rutile is similarly insulator-like ($10^4 - 10^7 \, \Omega$cm), but after doping by thermal reduction they differ ($10^{-1} \, \Omega$cm for anatase and $10^2 \, \Omega$cm for rutile) and are decreased by several orders of magnitude [109]. Bonapasta et al. [110] found remarkable differences in the properties of bulk $V_O$ in rutile and anatase, namely a shallow level

induced by bulk $V_O$ only in anatase, which could serve as explanation for the higher electron mobility ($\mu_{\text{rut}} \sim 1\,\text{cm}^2/(\text{Vs})$, $\mu_{\text{ana}} \sim 10\,\text{cm}^2/(\text{Vs})$) and photocatalytic activity in anatase. According to von Oertzen and Gerson [87], $V_O$ result in the population of the bottom of the conduction band (location of the Ti 3d orbitals in the pure structure), thereby increasing the size of the bandgap, while Ti interstitials introduce a defect state into the bandgap without an overall reduction of the bandgap size.

The Kröger-Vink notation is often used to describe the charge and lattice position of point defects. The electric charge relative to the site that is occupied is marked as neutral $^\times$, positive $^\bullet$, or negative $'$. This way a $Ti^{3+}$ ion in a Ti lattice site is written as $e'$ (quasi-free electron) and an $O^-$ ion in an oxygen site as $h^\bullet$ (quasi-free hole). The lower index can be a lattice site but may also be a lattice interstice (i). The following intrinsic defects of undoped $TiO_2$ are considered [66], which in contrast to extrinsic defects do not change the stoichiometry.

Displacement of Ti cations from a regular lattice site to an interstitial position (*Frenkel defects*) follows the equilibrium equation

$$\text{Ti}_{\text{Ti}}^\times + \text{V}_\text{i}^\times \rightleftharpoons \text{Ti}_\text{i}^{\bullet\bullet\bullet\bullet} + \text{V}_{\text{Ti}}'''' \qquad\qquad K_F = [\text{Ti}_\text{i}^{\bullet\bullet\bullet\bullet}][\text{V}_{\text{Ti}}''''], \qquad (1.5)$$

where $K_F$ denotes the equilibrium constant. *Schottky defects* form, when oppositely charged ions leave their lattice sites, creating vacancies:

$$\text{Ti}_{\text{Ti}}^\times + 2\,\text{O}_\text{O}^\times \rightleftharpoons 2\,\text{V}_\text{O}^{\bullet\bullet} + \text{V}_{\text{Ti}}'''' + \text{TiO}_2 \qquad\qquad K_S = [\text{V}_{\text{Ti}}''''][\text{V}_\text{O}^{\bullet\bullet}]^2. \qquad (1.6)$$

The process is accompanied by an expansion of the volume. Also, the electronic intrinsic disorder needs to be considered, i.e. the formation of electron hole pairs when an electron is transferred to the conduction band, leaving behind an electron hole in the valence band:

$$\text{nil} \rightleftharpoons e' + h \qquad\qquad K_T = np. \qquad (1.7)$$

Surface defects of $TiO_2$ have been extensively studied [1, 37, 111–114], usually on the thermodynamically most stable $TiO_2$ (110) surface of rutile. It has been shown that this surface is characterized by rapid gas-bulk reactions due to small activation barriers for bulk diffusion, compared for example to ZnO ($10\bar{1}0$), where gas-bulk reactions are negligible at low temperatures [37]. The reason for this is a strong electrochemical potential gradient near the surface which leads to fast dissipation of charges and defects and bulk reactions, subsequent to high charge accumulations at the surface.

As can be seen in Fig. 1.5a), the rutile (and also anatase) surface has fivefold coordinated Ti atoms and O exists in threefold (in-plane O) or twofold (bridge-bonded O) coordination. According to DFT studies [111], formation of a vacancy by taking bridge-bonded O is slightly more favorable than by taking an in-plane O out. Oxygen vacancies play an important role for the chemical properties of the surface, for instance they act as chemisorption sites for $H_2$, $O_2$ and CO and influence the electronic charge transfer during exposure. Also they have the ability to migrate, preferably parallel to the bridge-bonded O rows, with activation energies around 1.15 eV and with hopping rates that exponentially increase with the temperature.

Fig. 1.5 shows the representation of defect disorder of pure $TiO_2$ as Brouwer diagram, based on simplified charge neutrality conditions that apply for the different oxygen partial pressures and majority defects. To gather information about the defect concentrations the equilibrium constants of the defect formation equations have to be known (see Ref. [115] for details).
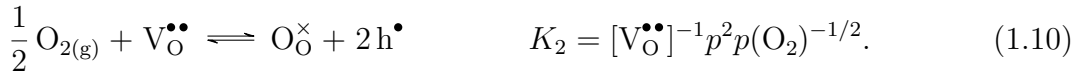
For instance, under strongly reducing conditions, excorporation of oxygen must be taken into account:

$$O_O^\times \rightleftharpoons V_O^{\bullet\bullet} + 2\,e' + \frac{1}{2}\,O_{2(g)}, \qquad\qquad K_1 = [V_O^{\bullet\bullet}]n^2 p(O_2)^{1/2}. \qquad (1.8)$$

The majority defects here are electrons, and the neutrality condition is $2[V_O^{\bullet\bullet}] = n$. With the equilibrium constant $K_1$, the concentration of electrons and holes can be derived, yielding

$$n = 2^{1/3}\,K_1^{1/3}\,p(O_2)^{-1/6} \qquad\text{and}\qquad p = \frac{K_T}{n} \propto p(O_2)^{1/6}. \qquad (1.9)$$

On the other hand, recent studies have shown that strong oxidation of $TiO_2$ can also lead to formation of the metal-deficient oxide $Ti_{1-x}O_2$ [115]. Then the predominating defect type are titanium vacancies, which cause p-type properties. For example, under oxidizing conditions, oxygen may be incorporated, according to the following reaction when oxygen vacancies are still present:

$$\frac{1}{2}\,O_{2(g)} + V_O^{\bullet\bullet} \rightleftharpoons O_O^\times + 2\,h^\bullet \qquad K_2 = [V_O^{\bullet\bullet}]^{-1}p^2 p(O_2)^{-1/2}. \qquad (1.10)$$

Together with titanium vacancy formation according to equation 1.6 it follows

$$O_2(g) + Ti_{Ti}^\times \rightleftharpoons V_{Ti}'''' + 4\,h^\bullet + TiO_2 \qquad K_3 = [V_{Ti}'''']p^4 p(O_2)^{-1} \qquad (1.11)$$

With the neutrality condition $2[V_{Ti}''''] = [V_O^{\bullet\bullet}]$ and equation 1.6 resulting in $p \propto p(O_2)^{1/4}$ and $n \propto p(O2)^{-1/4}$.

The mechanism of $O_2$ adsorption appears to be more complicated than just filling of surface vacancies, as has implicitly been assumed in many studies. $O_2$ does not adsorb at low temperatures (100K) to a stoichiometric (110) surface [1]. For this temperature range, a model was derived, in which $O_2^-$ species are bound in the vicinity of a vacancy [1]. In scanning tunneling microscope (STM) scans, $O_2$ adsorption becomes evident by healing of vacancies and additionally by appearance of O adatoms adsorbed on top of fivefold Ti atoms [106]. Formation of oxygen adatoms can lead to additional dissociation of $H_2O$ [1]. At room temperature and below, diffusion of these on-top O atoms is completely inhibited due to a large diffusion barrier. The exact mechanisms, especially the role of $Ti^{3+}$ at elevated temperatures, is not yet consentaneously clarified. Apart from $V_O$, an important role in the adsorption of $H_2$ and $H_2O$ also play $OH^-$ groups. It was found experimentally [116] that under atmospheric conditions surface OH groups, which are mainly located at bridging oxygen sites, form strong hydrogen bonds with adsorbed water molecules. On the ideal, defect-free surface it is hard for molecular $H_2$ to adsorb, or interact in any other way as has been shown by UHV studies [113], but surface defects like $V_O$ increase the (dissociative) adsorption [37]. For this reason, hydrogen in $TiO_2$
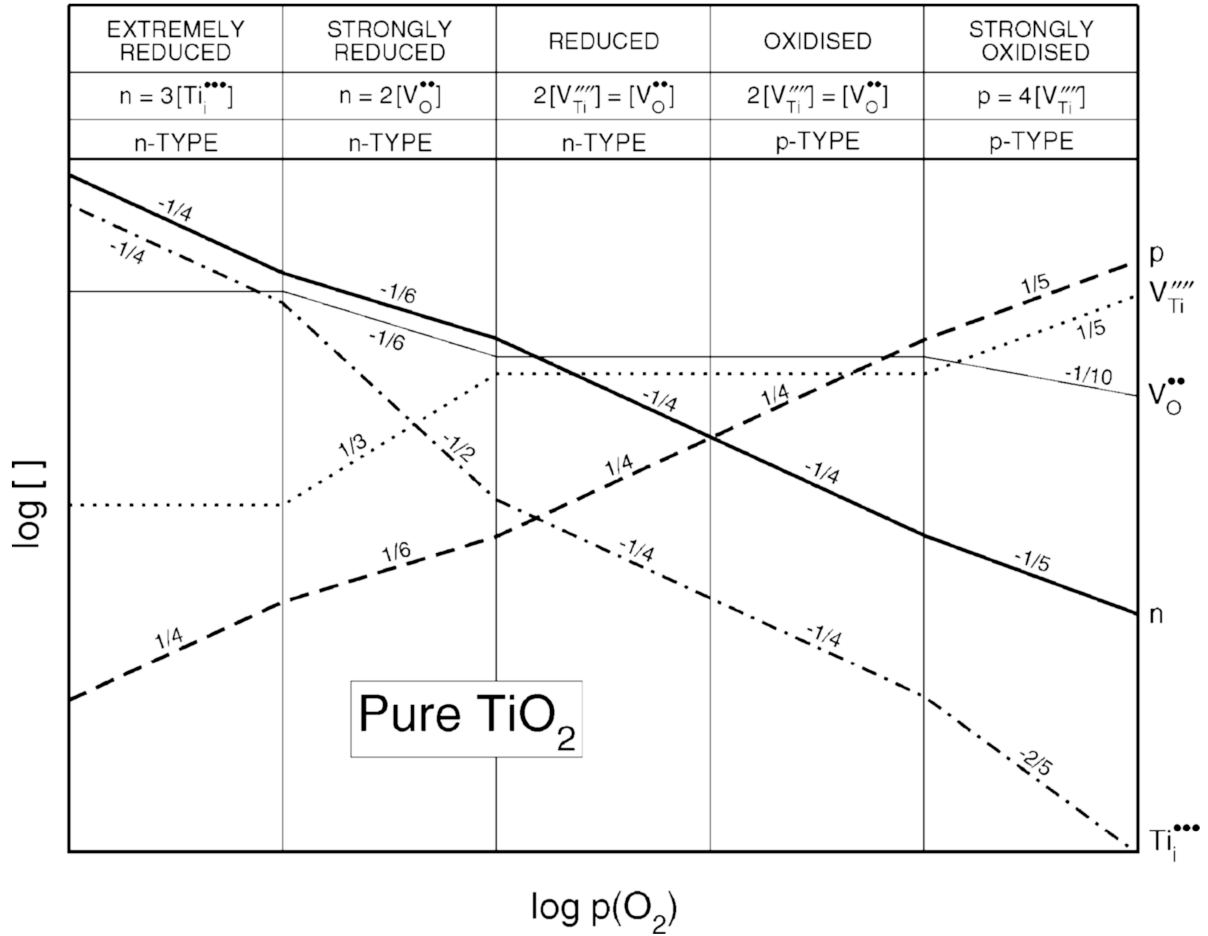
**Figure 1.4:** Brouwer diagram of undoped rutile $TiO_2$: dependence of the defect concentrations on the oxygen partial pressure $p(O_2)$. Reprinted with permission from Ref. [115]. © (2008) American Chemical Society.

exists mainly in the form of $OH^-$ groups. However, even in extremly hydrogen-rich conditions, the surface cannot be fully hydroxylated, a maximum coverage with hydrogen of 0.6-0.7 ML has been calculated [111]. Compared to the rutile (110) surface, the H binding energy on the anatase (101) surface is 0.2-0.3 eV smaller. On this surface, Islam et al. [117] identified three main diffusion mechanisms, i.e. surface migration, diffusion into the bulk, and desorption of $H_2$. By comparison of the calculated activation barriers, they concluded that migration of H into the bulk is the kinetically most favorable process. The mechanisms for hydrogen diffusion in $TiO_2$ rutile have also been studied by Bates et al. [118]. In $OH^-$ groups the oxygen occupies a regular oxygen ion site. It is suggested that H diffuses parallel to the c-axis and bridging oxygen rows easily (activation energy 0.6 eV) by proton jump from one $O^{2-}$ ion to another, and also in perpendicular direction by rotation of the $OH^-$ bond to move one proton to an adjacent channel (activation energy 1.28 eV). A diffusion coefficient of hydrogen in compact $TiO_2$ of $10^{-15}$ cm$^2$/s has been reported [119].

For photocatalytic processes [2, 7, 120, 121], water is one of the most important adsorbates at $TiO_2$ surfaces. In ambient conditions, the surface is found to be fully covered by
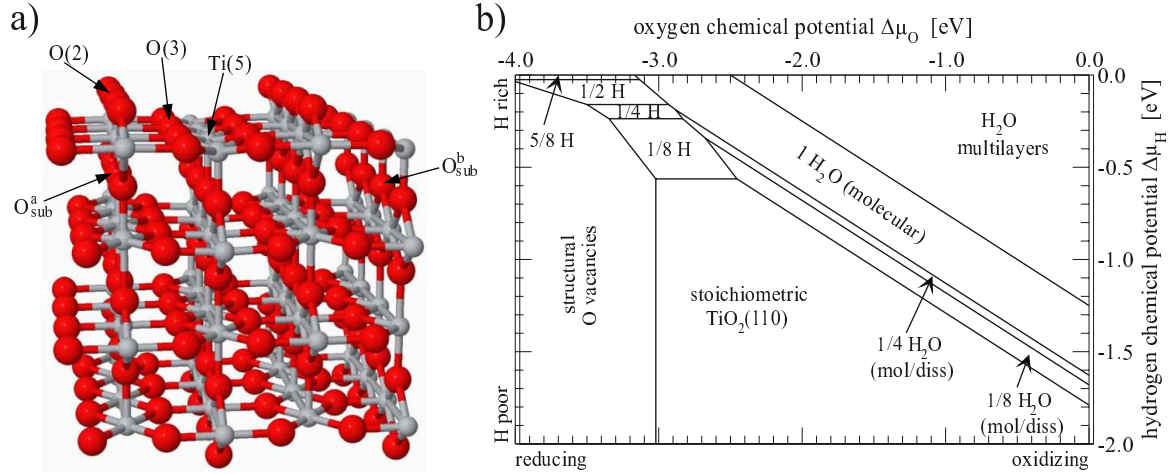
a)

b)



**Figure 1.5:** a) Twofold O(2), threefold O(3) coordinated O sites, and fivefold coordinated Ti sites Ti(5) on the stoichiometric rutile $TiO_2(110)$ surface. b) Surface phase diagram with $H_2$ and $O_2$ reservoirs controlling the chemical potentials $\Delta\mu_H$ and $\Delta\mu_O$. Both figures reprinted with permission from Ref. [111]. © (2009) American Physical Society.

molecularly absorbed $H_2O$ [111]. At higher temperatures and for single isolated water molecules, adsorption also happens partly dissociatively with formation of $OH^-$ groups, simultaneously to desorption of physisorbed water. Dissociative adsorption of $H_2O$ occurs at defects ($V_O$ on bridging sites), but at flat terraces the molecule stays intact during adsorption and is located at fivefold coordinated Ti sites with H atoms pointing away from the surface. STM studies [106,122] have shown that water dissociation at vacancies also leads to formation of very stable paired bridging hydroxyls.

Fig. 1.5 b) shows a phase diagram of the $TiO_2$ (110) surface obtained as a function of the two chemical potentials of oxygen ($\Delta\mu_O$) and hydrogen ($\Delta\mu_H$) that sums up a detailed theoretical study on the defects on this surface, done by Kowalski et al. [111]. It is dominated by the ideal stoichiometric surface, the oxidized surface that is saturated with water, and the surface structures reduced by oxygen depletion and hydrogen adsorption.

Many stable phases of other stoichiometry than $TiO_2$ exist, e.g. $Ti_2O$, $TiO$ and $Ti_2O_3$, as is depicted in the phase diagram for Ti-O systems in Fig. 1.6. The region Ti-$Ti_2O$ contains metallic phases of $\alpha$ (hexagonal) and $\beta$ (cubic) structure. At larger O/Ti ratios, phases of variable composition mixed with high temperature (ht) and low temperature (lt) TiO emerge.

The region O/Ti = [1.75,1.9] contains seven discrete phases of the homologous series $Ti_nO_{2n-1}$ ($4 \leq n \leq 10$), the so-called Magnéli phases. Magnéli phases crystallize in the triclinic crystal system and can be produced by high temperature reduction in a hydrogen atmosphere. Their $Ti - O_6$ octahedra are connected in a more complex way than in the structures previously discussed. The structures can also be described as compositions of rutile like slabs of infinite extension separated by crystallographic shear planes [66]. Smith et al. [123] give an overview about Magnéli phase titanium oxide materials, their properties, electrochemical behavior and applications. A comparative study of the

temperature dependent AC electrical properties of $TiO_2$ and $Ti_nO_{2n-1}$ was done by Regonini et al. [124]. Fig. 1.7 shows that these reduced phases can have conductivities larger by three orders of magnitude [125], with a local maximum of conductivity for $Ti_4O_7$, compared to stoichiometric $TiO_2$. For these reasons, Magnéli phases of titanium oxide can play an important role for resistive switching and electroforming in these structures, apart from and together with oxygen vacancy migration. This issue will be discussed in detail in section 2.2.
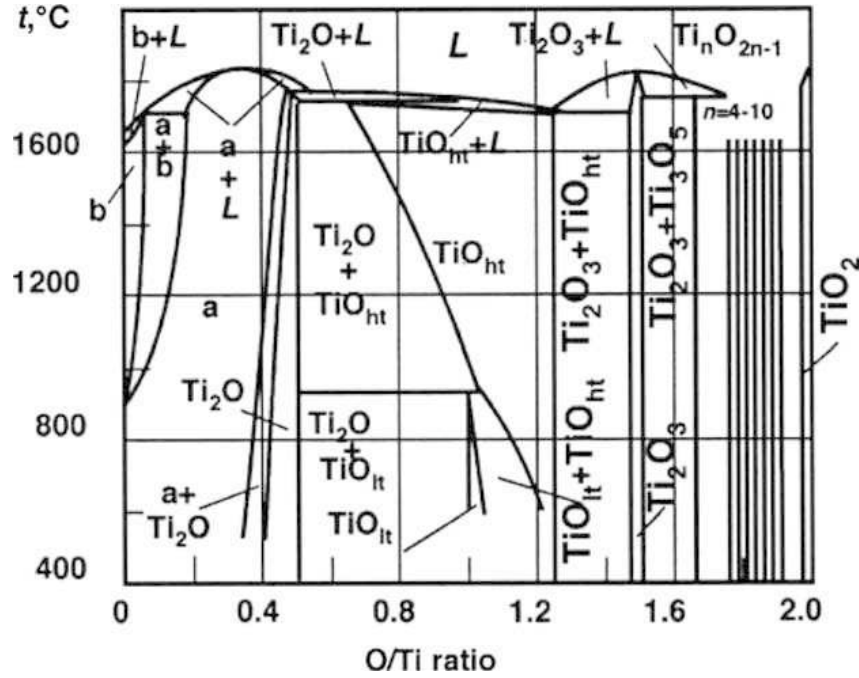


**Figure 1.6:** Phase diagram of Ti-O systems. Reprinted with permission from Ref. [1] © (2003) Elsevier, adapted from Ref. [126] © (2006) Wiley.

There is a wide range of possible fabrication techniques for $TiO_2$ devices and the way of fabrication can influence the phase composition, defects and electronic structure of the resulting material. Chen and Mao [2] provide a review over commonly used synthesis methods like the sol-gel method, chemical or physical vapor deposition and others, with a description of their properties, modifications and applications, e.g. in catalytics, photovoltaics or hydrogen storage. Other examples are thermal oxidation, plasma enhanced atomic layer deposition (PEALD) of $TiO_2$ [127] and reactive ion-beam sputter deposition [128].

Subject of this work are titanium oxide structures produced by local anodic oxidation (LAO) of Ti thin films, plasma-induced electrochemical oxidation of Ti foils [23, 39], and RF sputtering of $TiO_2$. The procedures are described in the experimental section 1.3.1. On-chip anodic oxidation of Ti and Ti-Pt thin films is discussed separately in chapter 3.
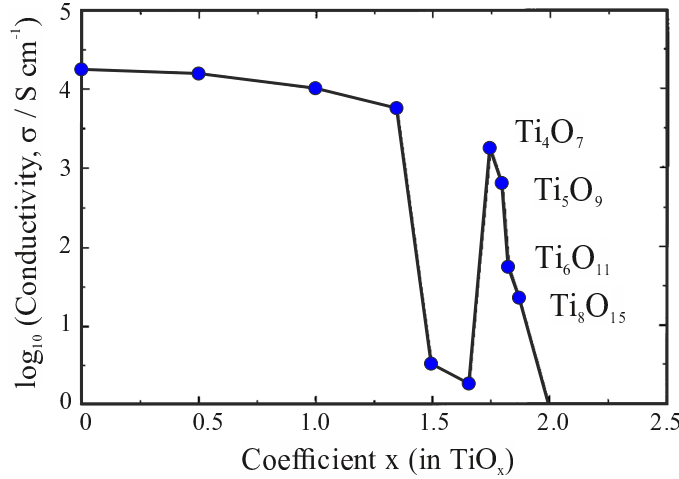
**Figure 1.7:** The conductivity of $Ti_nO_{2n-1}$ at $300\,K$ with denoted Magnéli phases of $n = 4 - 8$. Figure adapted from Ref. [129].

### Platinum

As mentioned above, Pt is a greatly versatile material with many applications and not only known for its properties as catalyzing agent. First of all, Pt was used in this work as sensitizer for hydrogen detection on top of $TiO_2$ (Papers II-IV). Apart from that, structures based on a $Pt/TiO_2$ interface were studied (Paper I). In the context of the project for the development of on-chip sensors, Pt based elements were implemented as temperature sensors and heating units, with a distance of $\approx 200\,\mu m$ to the gas sensing units. For this purpose, Cr/Pt films in the shape of meander structures were deposited on the $SiO_2$ substrates (image on the top right in Fig. 1.17).

Platin (Pt) has the atomic number 78 and belongs to the group of transition metals. It crystallizes in the fcc structure and has the electron configuration $[Xe]4f^{14}5d^96s^1$. On the one hand, it behaves chemically inert, as typical for noble metals and is stable even at high temperatures. On the other hand, it is highly reactive and has catalytic selectivity towards certain reaction environments and substances. A well known example for the heterogenous catalysis is the explosive reaction of hydrogen and oxygen to form water, when Pt is present: $2H_2 + O_2 \rightarrow 2H_2O$ ($2.5\,eV$ reaction heat per water molecule) [89]. The underlying mechanisms of hydrogen oxidation are more complex than this reaction equation suggests, e.g. the reaction rate differs a lot below and above $170\,K$, which is the desorption temperature of water on Pt [130], i.e. the temperature at which adsorbates leave the surface because the thermal energy is high enough to break the surface bonds. The reason for this lies in the autocatalytic properties of adsorbed $H_2O$ on Pt, meaning that water is a reaction product and is also a catalyst for the reaction. This way the activation energy below $T_{des}$ is much smaller ($0.13\,eV$ [131]) than above this value ($0.5$-$0.7\,eV$ [132]). By means of scanning tunneling microscopy and high resolution electron energy loss spectroscopy, the processes could be observed on an atomic scale [133, 134], Gorodeskii et al. [135] provide a review about recent findings concerning the hydrogen oxidation reaction on a Pt surface. It has been found that the formation of hydroxyl

groups from adsorbed hydrogen and oxygen is an intermediate stage during hydrogen oxidation [130, 133, 136]. With more hydrogen available, these OH-groups, which are also existent as adsorbates, form adsorbed water that can pass into the gas phase above $T_{des}$.

$$O_{(ad)} + H_{(ad)} \rightarrow OH_{(ad)}$$

$$H_{(ad)} + OH_{(ad)} \rightarrow H_2O_{(ad)} \rightarrow H_2O_{(gas)}$$
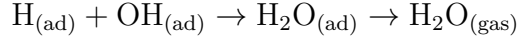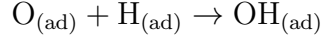
Furthermore, the autocatalytic process could be explained by adsorbed oxygen and water that form new hydroxyle groups according to the reaction

$$H_2O_{(ad)} + O_{(ad)} \rightarrow 2OH_{(ad)}$$

or

$$2H_2O_{(ad)} + O_{(ad)} \rightarrow 3OH_{(ad)} + H_{(ad)}.$$
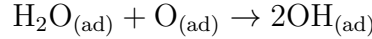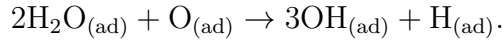
Interaction of oxygen with the Pt surface has also been extensively studied [137–139]. As mentioned above, the ability of Pt in its active state to bind the involved molecules like $H_2$, $O_2$ and other gases by chemisorption [112] is a basic requirement for the remarkable catalytic activity of Pt. It has been found that chemisorption and surface catalysis is strongly structure-sensitive, i.e. catalytic activity is increased for rough, kinked and stepped surfaces, at sites with high coordination numbers and open surfaces, where the second layer is also accessible. In 1984, Falicov and Somorjai [140] presented a theory of metal catalysis that proposes correlations between catalytic activity and low-energy local electronic fluctuations in transition metals. The theory starts off with the traditional view of the intermediate-compound theory of catalysis: a transition metal atom with given electronic configuration can either form a stable compound with a molecule, or no compound is formed. To describe an effective catalyst however, there has to be a weakly-bound intermediate compound with availability to release the molecule again to form the final product. From a different point of view, the transition metal atom should be susceptible to stable low-energy electronic fluctuations. They suggest electronic fluctuations of importance may be charge fluctuations, configuration fluctuations, spin fluctuations, and term and multiplet fluctuations [140]. The unfilled d shells of transition metal atoms are of particular importance and directly related to the catalytic activity, since they are relatively narrow and provide metallic character with a high density of states but are not dominated by Coulomb repulsion and other effects that lead to suppression of local electronic fluctuations. Calculations of the DOS with 5d-contribution to the DOS and the band structure of a Pt(111) face, can be found in Refs. [141] and [142], showing a large 5d-DOS and d band located close to the Fermi edge.

A key step for hydrogen sensing with Pt-TiO$_2$ structures is the dissociative adsorption [143] of H$_2$ molecules on the Pt surface, which leads to H-H bond breaking of the adsorbate and two singly-bonded hydrogen atoms. Recent studies [144, 145] have shown by means of thermal desorption spectroscopy that this process can be actuated and accelerated by atomic defects. The simplified reaction equation for dissociative chemisorption reads

$$H_2 + 2\,Pt \rightarrow 2(Pt - H_{(ad)}). \tag{1.12}$$

This process is followed by surface diffusion of the adsorbed hydrogen and transfer to the $TiO_2$ surface or into the bulk. The structure-sensitive character of chemisorption comes into play here, as H atoms adsorbed at kink sites desorb at higher temperatures than those at steps, and those adsorbed at flat terraces are bound even less strongly [112]. When Pt is present not as a continuous layer but as cluster or islands on top of $TiO_2$, the particle size and morphology can be decisive for its catalytic activity [146]. In this work, small amounts of Pt were deposited on top of $Ti/TiO_2/Ti$ structures as catalyst for gas sensing. The nominal layer thickness ranged from monolayers to 3 nm. Although it could not be verified experimentally, formation of cluster-like structures for the smallest amounts of Pt after a heat treatment is assumed, as has been reported elsewhere for similar fabrication conditions [147, 148]. Also surface activation by such Pt nanoclusters for gas sensing applications have been reported [149].

Pt was also deposited in much lager amounts, namely as top electrode on nanoporous $TiO_2$, where it also serves as catalyst for hydrogen detection. The $Pt/TiO_2$ Schottky transition that is biased in this case and other peculiarities of the combination will be discussed in the following.

**The platinum - titanium dioxide system**

The metal-semiconductor (M-S) junction of Pt and (n-type) $TiO_2$ exhibits rectifying properties, which makes the junction a Schottky diode. In Schottky transitions minority charge carriers do not contribute to the charge transport. Faster switching times compared to diodes based on p-n junctions can be achieved, due to fast electrons (majority charge carriers), that quickly react to electric fields. Apart from the versatile operations in semiconductor devices like Schottky diodes and Schottky transistors these properties of M-S junctions have been used for various applications for example in the research for chemical sensors [9, 13, 43, 150–153] and electromotive force cells [8, 9].

Fig. 1.8 a) shows the energetic schemes of an n-type semiconductor (left) and a metal (right) with different distances $\Phi_M$ and $\Phi_{sc}$ between their chemical potentials $\mu$ and the vacuum level $E_{vac}$. The chemical potentials are shifted against each other by $\Phi_M - \Phi_{sc}$. For metals, $e\Phi_M$ is the work function, i.e. the minimum energy needed to remove an electron from the solid ($e\Phi_{Pt} = 5.12 - 5.93$ eV, $e\Phi_{Ti} = 4.33$ eV). It depends on the configuration of surface atoms. For the semiconductor $e\Phi_{sc} = e\chi + eV_n$ holds, where $e\chi$ is the distance from the conduction band edge to vacuum level, the electron affinity ($\chi_{TiO_2} = 3.9$ eV). With $\Phi_{Pt} > \Phi_{TiO_2}$ a potential barrier of height $\Phi_{SB}$ is formed at the interface when metal and semiconductor are contacted, see Fig. 1.8 b). Electrons diffuse from $TiO_2$ thereby leaving positively ionized donors behind and accumulate at the Pt surface. This way a positively charged depletion layer forms in $TiO_2$ near the metal, with almost no free charge carriers. Due to the high concentration of free charge carriers in Pt, the width of the negative space charge layer is negligible (usually $< 1$ nm) [154]. The electron flow comes to a hold when thermodynamic equilibrium is reached, i.e. the chemical potential of Pt and $TiO_2$ are adjusted. The charge imbalance leads to a band bending $e\Delta V$ and creates a barrier $e\Phi_{SB} = e\Delta V + E_C^n - E_F$. Solving Poisson's equation

for a charge density $en_D$ in the semiconductor gives

$$\phi(x) = (\Phi_{Pt} - \Phi_{TiO_2}) - \frac{en_D}{2\epsilon\epsilon_0}(x + d_n)^2, \tag{1.13}$$

and for the width of the depletion region follows

$$d_n = \sqrt{\frac{2\epsilon\epsilon_0}{en_D}(\Phi_{Pt} - \Phi_{TiO_2})}. \tag{1.14}$$

With a voltage in forward direction (n-type $TiO_2$ negatively biased), electrons from the semiconductor are pushed into the depletion region and the height of the barrier from semiconductor to metal decreases. This allows electrons to flow from $TiO_2$ to Pt.

If a reverse-bias is applied (Pt negatively with respect to n-type $TiO_2$) there is almost no current flow as long, as the voltage is kept below the break down voltage, because electrons are pushed towards the metal and the width of the depletion region increases. However, a few electrons from the metal can overcome the barrier by thermal excitation or cross it via tunneling. Hence, for an applied voltage $V$, $d_n$ is given by

$$d_n = \sqrt{\frac{2\epsilon\epsilon_0}{en_D}(\Phi_M - \Phi_{sc} \pm eV)}. \tag{1.15}$$

From the voltage dependence in $d_n$ follows a voltage dependent capacitance ($C \sim d_n^{-1}$). From a plot of $C^{-2}(V)$ (*Mott-Schottky plot*), system properties like the doping density and flatband potential can be deduced [155]. This so called *Schottky-Mott rule* applies for the ideal Schottky contact; in reality the SB height and electronic properties of the transition layer are modified by the M-S bond and by adsorbed molecules on the surface. The chemical termination of the semiconductor against the metal leads to electron states in the bandgap (*metal-induced gap states, MIGS*) and to an effect called *Fermi level pinning*: the gap states tend to pin the center of the bandgap to the Fermi level. Therefore the SB height is almost independent from the metal work function, but dominated by the energy and distribution of the transition layer states. As shown by theoretical studies [156], MIGS appear as bridging O p-Pt d hybridization in the layer-decomposed local DOS. They also decrease the formation energy for $V_O$ in the interface layers, since excess electrons introduced by the removal of an O atom are accommodated in the MIGS (for $V_O$ away from the interface they localize on the three surrounding Ti atoms and a $V_O$ state appears in the bandgap). Thus the interfacial $TiO_2$ layer is expected to be easily reducible and upon reduction changes from Schottky-type (= fully oxidized) to ohmic (=strongly reduced). This behavior is often referred to as *switching effect*.

Chargeable states in the bandgap can be already present at the semiconductor-vacuum surface (surface states), effectively leading to an alignment of the bands relative to these. In this case, a potential barrier exists already before contact as a consequence of electron transfer from the metal into the surface states. Hence, the charge transfer at the gas/metal/bulk oxide three-phase boundary is of particular relevance.

It is known that noble metals like Pt (and Au) on $TiO_2$ can act as reactive catalyst in photocatalytic reactions, e.g. in the generation of $H_2$ or $CO_2$ [157–159]. In 1978 De
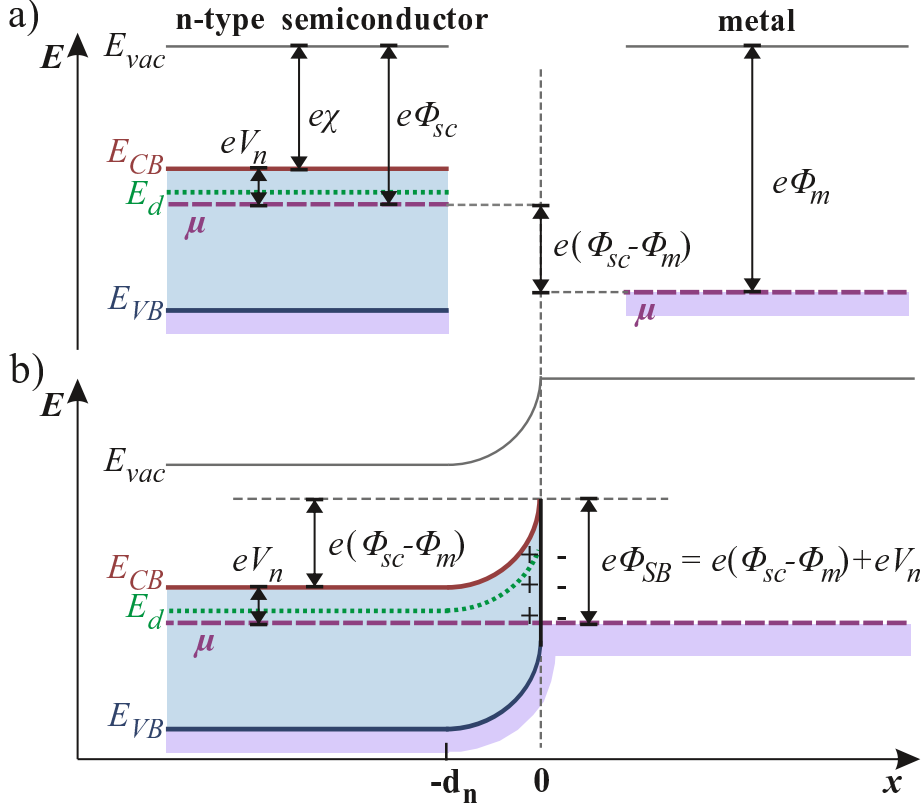
**Figure 1.8:** Scheme of the Schottky transition for $\Phi_M > \Phi_{sc}$ a) before contact of the n-type semiconductor (left) and the metal (right), b) in thermal equilibrium after contact. Figure adapted from Ref. [154].

Bruin [160] reported that chemical reactions occur at metal-ceramic interfaces, for example Pt and Au react with oxygen and form thin layers of $PtO_2$ and $Au_2O$, respectively. $Pt^{2+}$ and $Pt^{4+}$ ion species that occur due to oxidation of Pt atoms on the surface of $Pt/TiO_2$ systems [153] were found experimentally, as well as $Ti^{3+}$ that arises in the lattice from Pt deposition [159]. Moreover, a strong adsorption of visible light hints at energetic defect levels in the bandgap of the Pt modified $TiO_2$. Electronic charge transfer, however, was only observed in defective, pre-reduced $TiO_2$ (110) surfaces with $Ti^{3+}$, between Ti 3d states and Pt atoms [36, 161] but hardly on the stoichiometric surface. Angular resolved photoemission studies of the valence band stucture showed that sub-monolayer Pt evaporation resulted in two Pt-derived 5 d states in the bandgap region of $TiO_2$ (110). One was attributed to a high amount of very small atomic-like Pt species, the other to metallic-like clusters at higher coverages [162]. High concentrations of $Ti^{3+}$ ($TiO_{2-x}$) surface states are achieved e.g. by Ar bombardment and lead to localized charge transfer from $Ti^{3+}$ to Pt. Adjusting this so called SMSI (*strong metal/support interaction*) state can change for instance the CO and $H_2$ chemisorption and drastically enhance the catalytic activities.

However, it has been reported that proceeding oxidation of Pt (and Au) eventually leads to a degradation of the photocatalytic activity [115].

Kirner et al. [152] utilized the influence of extrinsic interface states on the SB height in Pt/TiO$_2$ low temperature ($\sim 400$ K) oxygen sensors. Upon exposure to small oxygen partial pressures ($10^{-5} - 1$ Pa) significant shifts of the forward voltage in the I-V characteristics were found. The reversible increase of the SB height is explained by trapping of electrons in chemisorbed oxygen species such as O$_2^-$ or O$^-$ and an additional band bending at the TiO$_2$ surface. Yamamoto et al. [13] measured an increased work function of Pd in the similar system of Pd/TiO$_2$ Schottky diodes when exposed to oxygen. They observed the opposite effect in response to the reducing gas hydrogen in H$_2$/air mixtures: the device loses its rectifying property and the onset voltage for positive current decreases, for large H$_2$ concentrations the device becomes ohmic. This behavior was attributed to a decrease of the Pd work function upon H$_2$ adsorption, involving interaction with and removal of oxygen from the Pd surface leading to a diminished barrier height at the interface. Similar effects were reported for the threshold voltage of H$_2$ sensitive Pd/SiO$_2$ based MOSFETS [150, 151].
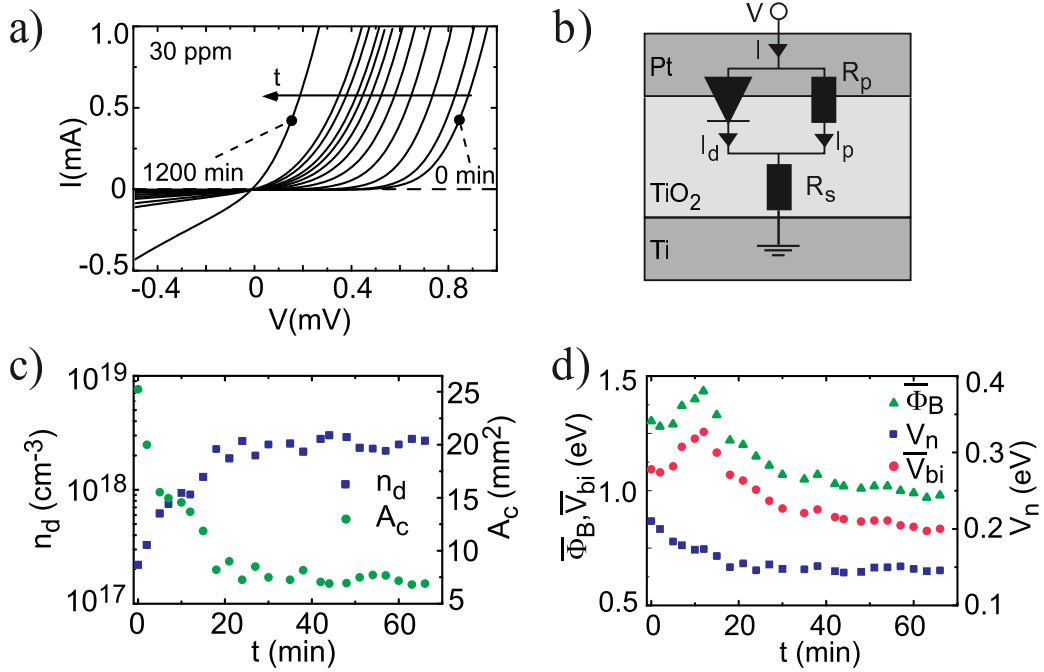


**Figure 1.9:** I-V characteristics of TiO$_2$/Pt as a function of H$_2$ exposure time (a). Scheme of the equivalent circuit model (b). Doping density $n_d$ and capacitive area $A_C$ (c), and average SB height $\bar{\Phi}_B$, average built-in potential $\bar{V}_{bi}$ and $V_n$ (d) , as a function of H$_2$ exposure time. All figures reprinted from Ref. [39], with the permission of AIP Publishing.

Fig. 1.9 shows corresponding results of a study on the time dependence of H$_2$ exposure with Pt/TiO$_2$ Schottky diodes [39]. The data were obtained from a Mott-Schottky analysis [155] of the I-V and C-V characteristics. With increasing H$_2$ exposure time $t$ the I-Vs [Fig. 1.9 a)] evolve from an exponential towards an ohmic behavior. Water formation or other interaction of H with O$_2$ were avoided by carrying out the experiments in the dark in N$_2$ flux. The sample was modeled with an equivalent circuit [Fig. 1.9b)],

where a Schottky diode is in series with the bulk resistance $R_S$ and in parallel to a resistance $R_p$, which decreases with $H_2$ concentration and exposure time. The following mechanisms causing the I-V transformation were considered: firstly, a reduced average barrier width due to H doping increases the tunneling probability; secondly, a decrease of the SB height due to formation of interface states upon $H_2$ exposure; and thirdly, chemisorption of hydrogen leading to a formation of electron accumulation layers in the porous $TiO_2$ [16]. Due to the continuous interface transformation with $H_2$, a gaussian barrier height distribution was assumed, as had been suggested in earlier studies [163]. The capacitive area decreases with time, while the doping density and resistive area of the device increase [Fig. 1.9 c)]. A rapid saturation of $n_d$ is observable, while the evolution of the SB height shows a non-monotonically decreasing behavior [Fig. 1.9 d)]. This was attributed to atomic H getting trapped at the $Pt/TiO_2$ interface and is suspected to be the limiting factor for the response time of the sensor, rather than doping of the bulk.

Interaction of CO with $TiO_2$ was reported to lead to donor-type chemisorption and hence to a decrease of the interface resistance [43, 153]. This reverses at large enough $O_2$ partial pressure [$p(CO) < \frac{1}{2}p(O_2)$], when interaction of the two compounds leads to catalytic oxidation of CO to form $CO_2$ molecules, which desorb afterwards.

The influence by acceptor- and donor-type molecules also concerns oxide/oxide interfaces at grain boundaries. It was noted that the charge transfer model for chemisorption at nanocrystalline metal oxides has to be modified when the grain size is below the Debye length of electrons [153]. Then band-bending effects can be neglected (e.g. space charge layer width for $SnO_2 \approx 100\,nm$, smaller than average crystallite size) and rather a homogeneous charging is assumed upon chemisorption.

In many applications, like in $TiO_2$ grains decorated with Pt islets [115], Pt is used as catalyst on top of $TiO_2$. Also here, the difference between the work functions of Pt and $TiO_2$ is the driving force for the transfer of (photoinduced) electrons from $TiO_2$ to the reacting molecules at the Pt surface [164].

Catalytic Pt clusters on the surface of $TiO_2$ can be prepared by thermal evaporation [36, 161, 162, 164, 165] or sputter deposition [147] with controllable size distribution, which has practical advantages in the fabrication procedure compared to the established chemical deposition. At elevated temperatures, growth of Pt clusters from layers starts due to surface diffusion of mobile Pt atoms [153]. As nucleation sites for the three dimensional growth, five-fold coordinated Ti surface atoms were experimentally identified. The growth mode of Pt on $TiO_2$ is Volmer-Weber like [1], i.e. interactions between adatoms are stronger than those of the adatom with the surface, leading to the formation of three-dimensional clusters or islands. The majority have hexagonal shape ($40\,\text{Å}$ high and $200\,\text{Å}$ wide), and resemble 'icebergs' that reach tens of Å deep into the substrate [1]. The substrate itself and its termination has an influence on the surface chemistry of Pt clusters. Additionaly, with high temperature treatment these clusters can get encapsulated. A recent study on the size effect of photocatalytic Pt particles on anatase by DFT calculations investigated the coupling of both, the photoelectron transfer and the surface catalytic reaction to the Pt particle size [146]. It was found that with decreasing number of Pt layers, the clusters become less metallic and a gap in the metallic states of $0.5$-$1.3\,eV$ opens, depending on the cluster size. Moreover, electron transfer and surface catalysis show opposing trends concerning the particle size. An optimal size for quasi

two-Pt-layer clusters of $\approx 1\,nm$ and roof-like ridge shape for photocatalytic $H_2$ evolution was found.

## 1.3 Experimental techniques

In the following section, the sample preparation, the experimental set-up and techniques for the characterization of the produced samples are described. There are many possibilities to fabricate titanium dioxide films. In this work, Ti films were oxidized anodically to produce $TiO_2$. Moreover, $TiO_2$ films were depositied directly by various sputtering techniques. The nanoporous $TiO_2$ structures investigated in Paper I are an exception: these were kindly provided by Mhamed el Achhab and coworkers[1] and were produced electrochemically. The process is shortly described at the end of section 1.3.1.

The description of the sample preparation here is focused on the lateral micro structures corresponding to Papers II-IV. This includes patterning by optical lithography, followed by material deposition and electrical contacting. Depending on the application, the prepared films were structured further by AFM nano-lithography techniques. The special method of fabrication of on-chip oxides that are discussed in chapter 3 is separately given in section 3.1.

Afterwards the measurement set-up is described. This set-up was particularly designed and assembled within the framework of the project for the development of the multifunctional gas sensor array. Furthermore, techniques are presented that were used for structural characterization of the produced $TiO_2$, including AFM, SEM combined with EDX analysis and a study of the optical properties.

### 1.3.1 Sample preparation

As substrate $SiO_2$ is chosen for its insulating properties, high thermal stability and good adhesion to the materials used, in particular Ti, Cr and $TiO_2$. For these and other reasons $SiO_2$ is an important material in the semiconductor industry and micro systems technology. Wafers with a 300 nm thick layer of $SiO_2$ on Si were used that were produced by thermal oxidation. Samples with substrates of pure quartz with better dielectric strength but more difficult handling were also prepared for experiments involving oxidation by high voltages up to 0.5 kV. Layers of Cr were deposited as adhesive agent for films of Au and Pt on $SiO_2$.

The order of the layer deposition was, unless noted otherwise, the following. At first Ti films were deposited on the substrate using evaporation or sputtering techniques, then meanders of Cr/Pt for heating and temperature sensing were sputtered, followed by deposition of Cr/Au bond pads via evaporation. The production of each layer involves a lithographic step, followed by material deposition and a lift-off step. When the $TiO_2$ in a device was produced directly by sputter deposition, this was done in the last step to prevent undesired contamination with photoresist in subsequent lithography steps.

---

[1]Department of Materials Science, headed by Prof. Dr. K. D. Schierbaum, Institute of Experimental Condensed Matter Physics, HHU

**Optical Lithography**

Optical lithography, also termed photolithography, is a method to pattern thin films by transfer of a geometrical pattern from a photomask to a light-sensitive photoresist on the substrate. A scheme of the sample processing with optical lithography is shown in Fig. 1.10. The first step is consecutive cleaning the $SiO_2$ substrate in acetone, isopropanol and deionized water. Afterwards, the sample is dried in nitrogen gas flux and heated out for 1 min at 110 °C to remove residues of water. An image reversal resist for high resolution (AZ 5214 E) can be used for both, positive and negative lithography. The resist is applied to the sample, and uniformly distributed using a spin coater (3500 rpm), resulting in 1-2 µm thick coating. Afterwards, the sample is heated on a hotplate (*soft bake*), which removes solvents from the resist layer. Before illumination can be done, rehydration is necessary, since water is needed in the photoreaction. This is done by pausing the process and leaving the sample in air of ideally $\approx 45\%$ relative humidity. In the positive process, only those parts of the structure are illuminated, which are desired to be resist free after development. The polymer chains in the resist break when exposed to UV light in such a way that these regions are dissoluble in the developer (AZ 726 MIF). For better adhesion of the deposited layers, the developed sample is cleaned in oxygen plasma for 20 s, and shortly dipped into HCl to remove burned residues of photo resist. After deposition of the material (see next section), the lift-off follows. Lift-off is done in acetone (optionally using a heated ultrasonic bath) followed by cleaning in isopropanol and deionized water again, whereupon all residues of resist and material thereon are removed.

In the negative process those regions are illuminated, which are not supposed to be developed. For this, two more steps are necessary compared to the positive process: During the *reversal bake* the illuminated regions lose the ability to be developed because the polymers become cross-linked and immune to the solvent. The subsequent *flood exposure* makes regions susceptible for the developer that were not exposed during the first illumination step. The main advantage of the negative process is that it generates an undercut resist profile and facilitates the lift-off step.

**Material deposition**

A common method to deposit thin films of Ti, Au and Cr is evaporation. In the evaporation system used in this work, the source material is heated by an electron beam (5 keV) in a vacuum chamber ($10^{-6}$ mbar). This way, evaporated particles can travel directly to the target substrate without collision with gases or vapors other than the source material. An oscillating quartz next to the sample holder measures the evaporated film thickness (QCM = quartz crystal microbalance). By controlling the electron beam current, the deposition rate can be tuned. Sufficiently smooth films can usually be achieved at deposition rates of 1-2 Å/s.

Another method for deposition of metals and metal oxides is sputtering, whereby particles are ejected from a solid target by energetic gas ions, here argon. Sputtering is done in a vacuum chamber using either a DC voltage (DC sputtering) or an AC voltage (RF sputtering). In DC sputtering a constant voltage is applied between target (negative bias) and the substrate (positive bias). Ar atoms get ionized by collision and
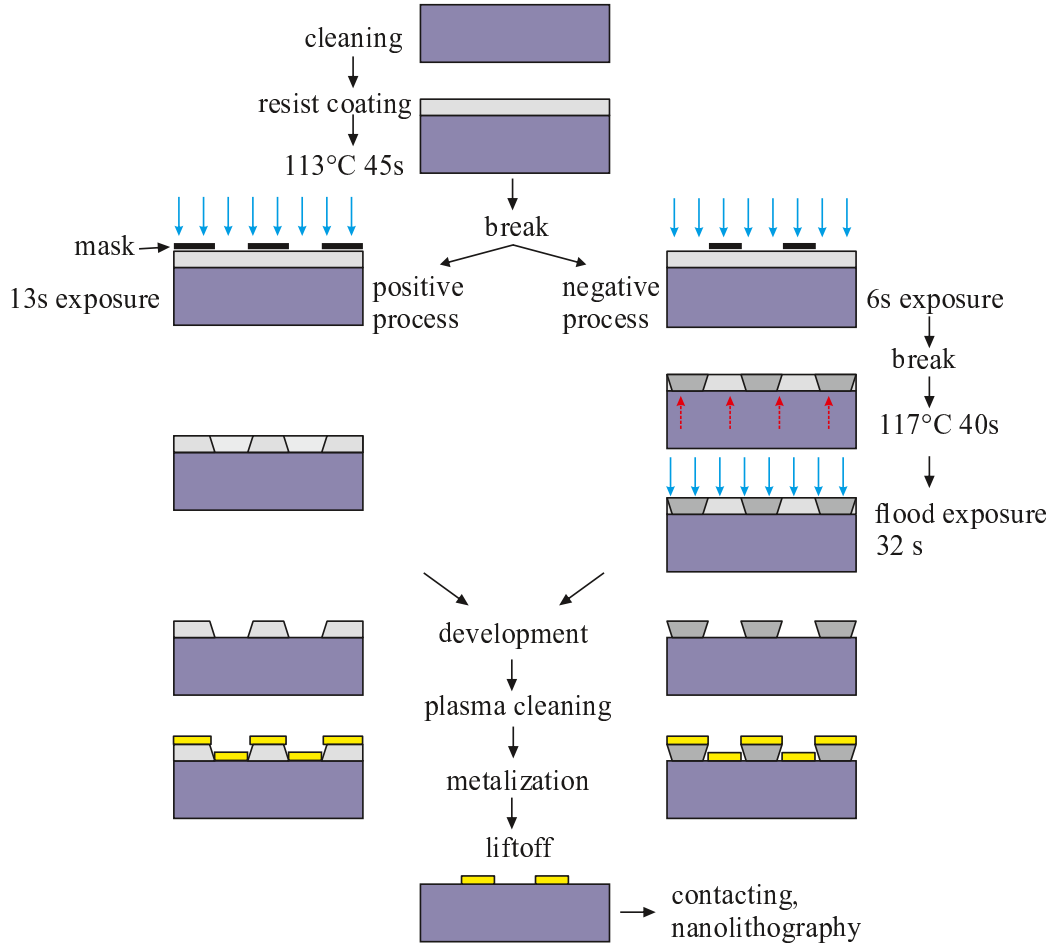
**Figure 1.10:** Schematic illustration of the sample processing steps. The structures on the samples are defined via positive or negative optical lithography followed by metalization and a lift-off step. Afterwards the samples are electronically contacted for measurements and/or nanolithography.

a low-pressure plasma state forms with electrons and Ar$^+$ ions, that are seperated by the DC voltage. A sufficiently energetic incident Ar ion will set off a collision cascade in the target. A target atom will be ejected (sputtered), when the cascade recoils and reaches the surface with a larger energy than the binding energy and an impact pointing away from the target. Only conductive materials can be sputtered in DC mode. With an insulating material, both target and substrate would be charged and compensate the electric field. The achieved sputtering rates and deposition rates are below those of e-beam evaporation. Ten times larger sputtering rates and also deposition of insulators can be achieved with RF (*radio frequency*) sputtering. Because of their larger mass, Ar$^+$ ions cannot follow the alternating field (13.56 MHz) as electrons can, resulting in more collisions and thus larger sputtering rates. The AC field is superimposed with an offset field that pulls Ar$^+$ towards the target, where target atoms are ejected in the same way as in the DC mode. Despite the larger sputtering rates, the effective deposition rates in RF mode are not larger compared to the DC method. Especially for metal oxides it is

advisable to avoid sudden variations in the power, to prevent cracks in the target. Since $TiO_2$ is rather prone to sudden variations of temperature, a $TiO_2$ target attached to a 3 mm thick copper substrate was used.

The number of collisions between electrons and Ar atoms can be further increased by applying an additional magnetic field behind the cathode (*magnetron sputtering*). Charge carriers then follow a helical curve due to the Lorentz force and cover a larger distance before they reach the target. The choice of sputtering parameters can influence the resulting film properties, structure and morphology. For instance, the roughness of magnetron sputtered Ti films increases with increasing pressure, temperature and sputtering power and the crystal orientation changes under parameter variation [166]. Also, added reactive gases like $O_2$ or $N_2$ can react with the target material during DC or RF sputtering (*reactive sputtering*), to deposit for instance metal oxides or nitrides. Using an optical control system that measures the relative intensity of the Ti emission line the sputtering rate of $TiO_2$ can be controlled through its influence on the target oxidation state [167]. During the deposition of $TiO_2$ the grain orientation and stoichiometry of anatase thin films can be tuned by variaton of the $O_2$ partial pressure [168]. Löbl et al. [169] studied the dependence of nucleation and growth in amorphous, anatase or anatase/rutile films during reactive DC sputtering on the deposition and annealing parameters.

In IBSD (*ion beam sputter deposition*) an ion beam is used as $Ar^+$ source, with the opportunity of tunable particle energies. $TiO_2$ films grown by reactive IBSD display low surface roughness ($< 0.22$ nm) and properties that are not significantly affected by the ion species and energy [128].

Sputtering methods are typically used to deposit smooth films of low roughness by choice of low deposition rates, compared for example to thermal evaporation. For some applications, however, rough or even porous films are desirable, particularly in the field of gas detection [170]. In a recent study, a sputtering technique was presented, from which $TiO_2$ films of nanoporosity (1-5 nm) and mesoporosity (10-50 nm) emerge [170, 171]. In this so called *gig-lox* process, Ti is sputtered in $O_2$ atmosphere in a pointed inclination angle, which leads to a shadowing effect and forming of porous $TiO_2$ structures.

**Electrical contacting**

Electrical access to the Ti or $Ti/TiO_2$ thin films is made via gold wire interconnections between the ohmic contacts on the thin film and the chip carrier using a ball bonder (*F&K Delvotec*). The technique is also known as thermosonic bonding because heat, ultrasound and pressure are used to connect the contacting pad to the wire material. For this, the chip carrier together with the sample is heated to $140\,°C$. As contact pads, usually a layer of $\approx 150$ nm Au on top of 10 nm Cr was evaporated on the thin films. Gold wires were successfully bonded on Pt pads as well, for this it appeared that $120\,°C$ was the best temperature of choice. Fig. 1.11 shows a series of photographs taken of a fabricated sample mounted in a chip carrier (left), the wiring between ohmic contacts (middle) and wire connections to Au bond pads on top of Ti thin films with three $TiO_2$ structures (right). If the sample is further processed by AFM-LAO, the contacting must be done beforehand since a connection from the Ti film to the ground is necessary for

this step.

Ti-TiO$_2$ structures prepared by electrochemical preparation were contacted in a different way due to their different geometry (see Fig. 2.1). These as-prepared samples consist of Ti foil encapsulated in a TiO$_2$ layer with a 50-200 nm Pt layer sputtered on top. Parts of the TiO$_2$ on the opposite side were scratched off and the laid bare Ti was glued to the chip carrier using conductive silver epoxy (*Epotek H20E, Epoxy Technology*) to form the ohmic back contact. Using the same glue, the Pt contact was connected to bond pads via gold wires.
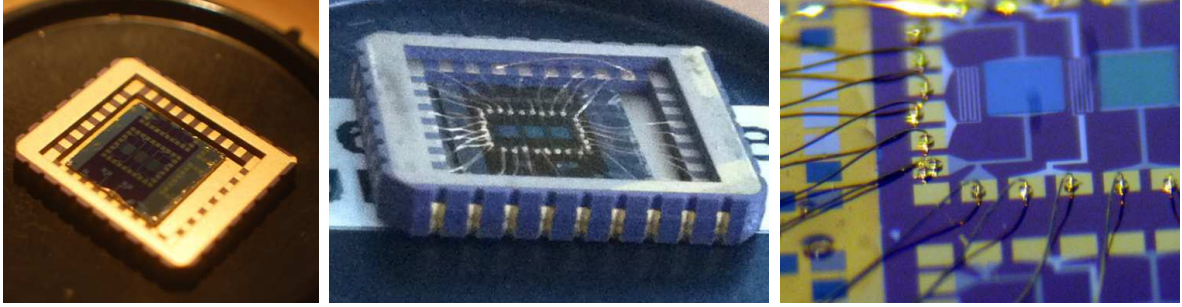


**Figure 1.11:** Photographs of a sample glued into a chip carrier after optical lithography and metalization (left) and with contact pads wire-bonded to the chip carrier (middle and right).

### Nanolithography

After preparation of the Ti films, structuring via nanolithography was done using an atomic force microscope (AFM). For the general set-up of the AFM that was used in this work, its functionality and operational modes, the reader is referred to section 1.3.3. Two types of sample structuring methods were performed, these are local anodic oxidation and nanoplowing. Both allow to structure thin films on the nanometer scale with a precision (down to 1 nm [172]) that can hardly be achieved by optical lithography. Due to their great relevance for this work, the two techniques are described in detail in the following. Both nano-lithographic techniques were done using the software *NanoMan* by Veeco.

*Local anodic oxidation* (LAO)
Tip induced oxidation using an STM was first demonstrated on wet-chemically passivated n-Si surfaces by Dagata et al. [173] and in UHV conditions by Lyding et al. [172]. Complex structures like semiconductor quantum point contacts [174] and antidot lattices [175, 176] were made using AFM based LAO.

Fabrication of TiO$_2$ structures on Ti by AFM oxidation is widely known and used [177–182]. The procedure is sketched in Fig. 1.14 a) for LAO on Ti thin films. TiO$_2$ lines prepared this way, separating the Ti stripe into two Ti electrodes are primary subject of Papers II and III. While anodizing is done in contact mode using a conductive diamond coated Si probe (DCP 20), imaging is done in tapping mode. By adjusting the $z$-distance depending on the amplitude setpoint the tip is moved close to the surface ($\approx 5$-$10$ nm).

The AFM was placed in a closed box with controllable humidity supply, which was set to 40-60 % r.h. during LAO. At this relative humidity a thin layer of water is adsorbed on the Ti film forming a meniscus between tip and sample surface [183, 184], which serves as electrolyte and oxygen source. A negative voltage is applied to the probe (hence the term *anodization*) with respect to the grounded Ti stripe and the tip is moved across the film. Due to the small curvature of the tip and distance between tip and sample, the maximum electric field is directly beneath the tip, hence the term *local* oxidation. This way a 10 μm long and ≈ 200 nm wide oxide line (nanowire) forms, depending on the writing velocity. For the exact parameters used in this work, the reader is referred to Paper II [56] and Paper III [57].
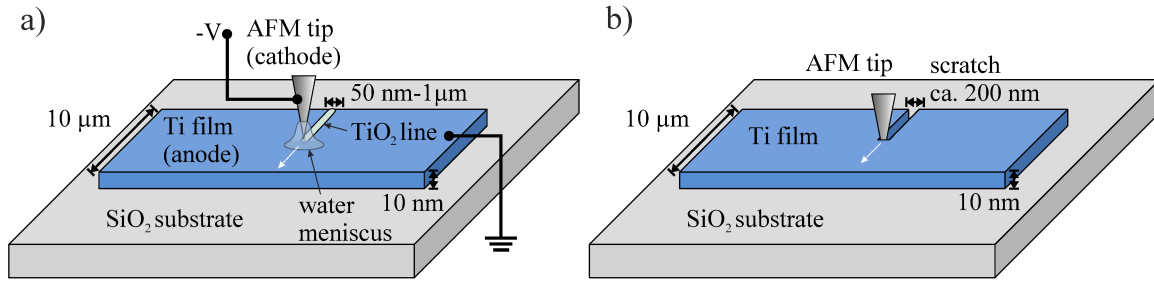


**Figure 1.12:** Illustration of AFM nanolithography done on Ti thin films: a) Local anodic oxidation (LAO) and b) nanoplowing.

Many studies on the LAO kinetics can be found in the literature, most of which investigate the dependence of the growth on parameters like the sample [185] and tip type [181, 186], the ambient relative humidity [174, 181, 185, 187], the applied voltage [179, 185, 187, 188], the duration of oxidation [174, 179, 181, 185], the writing velocity [179], AFM mode [188], and the tip-sample distance [179, 188]. In Paper III [57] we describe the effect of the tip speed, that is in accordance with observations reported elsewhere [179]. A faster tip motion leading to thinner oxide lines can be understood in terms of a shorter effective anodization time for a moving tip compared to a stationary tip. When looking at the various studies about tip-induced oxidation, it becomes clear that the kinetics depend on a variety of parameters in a complex way. For this reason, some of the approaches that can be found in the literature are discussed in more detail in the following.

It is widely agreed that the first step in the model for anodic oxidation involves the native oxide layer on Ti and an adsorbed layer containing oxygen [59]. Inside the native oxide, oxygen-related anions (mainly $OH^-$) and / or Ti cations can migrate along the electric field in opposite directions, towards the $Ti/TiO_2$ interface and the $TiO_2/H_2O$ interface, respectively [181]. Leaving out intermediate steps of water adsorption and formation of hydroxyl groups, the probable net reaction for oxidation of Ti is [179, 185]:

$$Ti + 2\,H_2O \longrightarrow TiO_2 + 4\,H^+ + 4\,e^-. \tag{1.16}$$
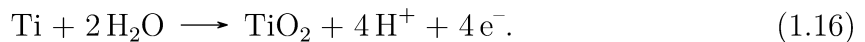
Beyond that, various approaches were made to explain the underlying mechanisms, partly based on contradictory observations. For example, both oxide height and width were

reported to increase with both, anodization time and voltage, but the exact relations vary.

Cabrera and Mott [60, 85] developed the first model for field-induced oxidation of thin films (see section 3.2). They assumed that the field lowers the activation barrier for ion diffusion through the oxide. In this picture, the initially fast growth rate decreases because the grown oxide decreases the field inside, slowing down drift of hydroxyl ions towards Ti [179, 187]. It became clear that this model alone could not explain the observed kinetics, especially the dependence of the growth rate not only on the electric field strength, but also on the applied volage [187]. Moreover, the initially fast growth rate also decreases because of a space charge build-up [189]. Therefore, the observed relation between growth rate and thickness [187] differed from the model:

$$\text{Mott \& Cabrera: } \frac{\mathrm{d}h}{\mathrm{d}t} \propto \exp\left(\frac{1}{h}\right) \qquad \text{v.s. observation [187]: } \frac{\mathrm{d}h}{\mathrm{d}t} \propto \exp\left(\frac{-h}{L_c}\right)$$

with $L_c$ being the characteristic length for a given anodization voltage. Deviations from the Cabrera-Mott model of field-induced oxidation were also interpreted in terms of a volume mismatch of oxidized and unoxidized Ti leading to local stress in the oxidized layer [179, 187]. Strains are assumed to be relieved by formation of a defect-rich oxide with a rather open structure.

Stievenard et al. [190] applied the model developed by Cabrera and Mott with the voltage $V$ seen as superposition of the applied voltage between tip and a Si surface and the contact potential. With this, they obtain a relation between the height of the oxide line and the tip velocity $v$ of $h \propto 1/\log(v[m/s])$, and a linear relation between $h$ and the applied bias, which is in good agreement with some experimental findings [179, 181]. Their deduced value for $W$, i.e. activation energy that an interstitial ion has to overcome for diffusion added to the initial potential barrier, of 0.1-0.4 eV indicates that LAO is rather an electrochemical process than high temperature thermal oxidation (for Si $\approx 2$ eV) [190]. The necessity of humidity for tip-induced oxidation was also interpreted as a hint towards this, expressed for example by Sugimura et al. [181]. This assumption, however, could not be proven, until Avouris et al. [187] were able to measure electrochemical currents during the oxidation process of Si, that agreed with Faraday currents calculated from the assumed electrochemical reaction. A similar approach was presented by Lemeshko et al. [185]. They derived a model that confirms the assumed electrochemical anodization, using Faraday's law to get an expression for the height of the growing oxide:

$$h_i(t) = \frac{Q\,M_{TiO_2}}{A\,\rho_{TiO_2}\,z\,F} = \frac{M_{TiO_2}}{A\,\rho_{TiO_2}\,z\,F}\int_0^t I_i(\tilde{t})\mathrm{d}\tilde{t}$$

where $Q$ is the consumed charge, $M_{TiO_2}$ and $\rho_{TiO_2}$ are the molar mass and densitiy of TiO$_2$, respectively, $I$ is the anodic current passing through the elemental area $A$ of the oxidized surface, $z$ is the number of electrons taking part in the oxidation (=4) and $F$ is Faraday's constant. A voltage distribution over the native oxide $V_{ox,0} = Eh_0$, over the growing oxide $V_{ox,i} = Eh_i(t)$, the electrochemical circuit $V_{c,i} = I_i(t)R_{c,i}$, and the space charge build-up $V_{pol}$ was assumed. With the reaction equation 1.16 the not purely linear relation in $h(V)$ and $h(t)$ [179] for ultra thin Ti films could be reproduced.

These considerations apply for DC conditions. The usage of voltage pulses can influence the space charge build-up and can also effect whether growth happens predominantly in vertical or lateral direction depending on the pulse durations [179, 188].

Calleja et al. [188] discussed the dimensions of the water meniscus between the AFM tip and a Si surface and its dependence on the electric field and the voltage mode. They found a rupture of the water bridge at a tip-sample distance of about 10 nm. Up to this value oxide width and height increase with increasing distance [179] because of a larger area covered by water. For the same reason, the resolution becomes worse with increasing humidity (and with it, the amount of adsorbed water) [181] and is determined by the defocusing of the electrical field [187].

The crystalline form of the written nanowire is not clear. Due to the small dimensions, a structural investigation is difficult and was not done in this work. All three modifications (rutile, anatase and brookite) as well as amorphous constituents have been found in anodic titanium oxide, although the latter transforms into anatase at 150 °C [59].

For the usage in gas sensing applications, the sample is afterwards sensitized with Pt. Deposition of 3 nm Pt on the Ti film beforehand was also tested but did not lead to successful oxidation of the Ti film. This can be understood, considering the necessity of ion migration through the oxide in vertical direction, which might be not possible in the Pt film. Similar fabrication techniques based on $TiO_2$ or $SiO_2$ for gas sensing applications were reported [20, 178].

Since the discovery of tip-induced oxidation, the technique was also used to remove oxidized structures via etching, e.g. in dilute hydroflouric acid, to produce grooves. Also, AFM tips were used to pattern photoresist layers for example on $SiO_2$ films by dynamic plowing, followed by wet-chemical etching to transfer the patterns into the films [191].

*Nanoplowing*

Grooves in thin films can also be achieved directly without an extra oxidation step [192]. Nanoplowing, i.e. scratching of Ti films to form nanosized gaps is done similarly to LAO. Such gaps served as separation of the Ti electrodes used for the on-chip oxidation that is subject of Paper IV [63] and discussed in chapter 3. Since no oxidation is desired, the tip is grounded. Also, no water film is needed, therefore the process is independent of the ambient humidity. Using contact mode the $z$-distance is adjusted in a way that the tip penetrates the Ti film and reaches down to the substrate. Scanning across the Ti film leaves a $\approx 200$ nm wide gap behind, as is depicted in Fig. 1.12 b). Minimum trench widths of 50 nm in Al were reported by Irmer et al. [193], who fabricated Josephson junctions in Al using tips especially fabricated for this purpose.

**Electrochemical preparation of TiO$_2$**

The samples based on electrochemical oxididation of Ti foil were prepared by Mhamed el Achhab and coworkers. Details of the preparation procedure and parameters are described in Refs. [23, 39, 194]. A kinetic model for the $TiO_2$ growth process is presented in Ref. [195]. Here, a short description of the technique and the film parameters is given. The process is also known as plasma-electrolytic oxidation or micro-discharge electrolysis, because it is coupled with a plasma-induced partial phase transition of

thermally and anodically oxidized $TiO_2$ from anatase to rutile. Commercially available Ti foil is etched in aqua regia and afterwards anodized in a 14 molar solution of $H_2SO_4$ at voltage sequences between 90 V and 180 V. Because of the high voltages involved, the process has also been described as continuously occurring partial breakdown [59]. The 200 nm-4 μm thick oxide layer grows into and out of the Ti foil and exhibits a complex pore structure, visible in SEM scans. The pores evolve from micro-discharges along conducting channels, where a plasma state is developed with high local temperatures and pressures. By tuning of the anodization voltage, anodization time and concentration of the electrolyte the layer thickness and the pore structure complexity can be controlled. For gas sensing applications, this large inner surface is advantageous and allows $H_2$ and other gases to diffuse quickly into the pore system of the structure. It was revealed by XRD and Raman spectroscopy that the $TiO_2$ layers are composed of rutile and anatase with variable proportion, as a result of thermally-induced phase transitions from anatase to rutile in the surface of pores along the discharging channels.

## 1.3.2 Measurement set-up

The measurement set-up is shown in Fig. 1.13. All measurements were carried out in a temperature and gas atmosphere controlled measurement chamber (*Linkam*). Gas line, chamber and set-up components making contact with the ambient air are made from special steel or aluminum, to prevent permeability or storage of humidity and other gases. Nitrogen, oxygen and hydrogen (4 %) flow are each regulated by a mass flow controller (El-FLOW Select, *Bronkhorst*) and are carried via steel tubes ($\varnothing_{int} = 4$ mm, *Swagelok*).

When required, the gas mixture is afterwards humidified via a bypass leading through a water bath, which instantly saturates the gas mixture (100 % r.h.) at flow rates around 1 l/min, as used in the experiments. The exact relative humidity of the gas can be tuned using the regulating valves that control the flow through the bypass and blocking valves to prevent backflow. The concentration of the gas components are read out by reference sensors for hydrogen (Neo904b, *neohysens*) and oxygen (GOX100, *Greisinger*).

The arrangement for controlling the gas temperature consists of a cooling unit and a heating unit. For measurements below room temperature, the gas flow is conducted through a bypass and a coil in a liquid nitrogen bath container, yielding gas temperatures below $-50$ °C. Measurements in this temperature range were carried out only with dry gases and the humidification bypass was kept shut to avoid freezing of condensed water. This can be done, since it reflects realistic conditions, i.e. water vapor pressure is near zero at such low temperatures. Gas heating is done with a porous aluminum alloy block (AlSi7 *Exxentis*, pore size 0.35-1.00 mm) with external heat supply. The required geometry of the heating block was estimated using Darcy's law, which describes the flow of a fluid through a porous medium:

$$Q = \frac{\kappa \cdot \Delta P \cdot S}{\mu \cdot H}$$

where $Q$ is the total discharge (volumetric flow rate), $\kappa$ is the intrinsic permeability of the medium, $\Delta P$ is the pressure drop across the filter (Pa), $S$ is the cross-sectional area to flow, $\mu$ is the dynamic viscosity (Pa · s) and $H$ is the length over which the pressure

drop is taking place and corresponds to the filter thickness. The gas line between heating unit and measurement chamber is kept as short as possible to prevent temperature loss. Relative humidity and gas temperature are controlled at multiple locations using a reference sensor with both functionalities (SHT7x, *Sensirion*). One is positioned behind the junction of humidified gas and dry gas line as a reference during humidity tuning. Another is located between gas cooling and heating unit to regulate temperatures between $-50\,°C$ and room temperature using the adjustable external temperature control of the heating unit. One last reference sensor for temperature and humidity is positioned directly behind the measurement chamber. At the end of the gas line an overpressure valve prevents outer gases from diffusing into the measurement chamber. It should be noted that the opening pressure of the valve should be small because in general the performance of $TiO_2$ based hydrogen sensors is downgraded with increasing ambient pressure.

The measurement chamber itself has its own temperature control in form of a Pt based heating element beneath the sample holder and liquid nitrogen cooling controlled by an external pump (*Linkam*). The screw cap can carry a gas-tight slide with screwed-in holders, which allows to build in LEDs without changing the atmosphere in the measurement chamber when illumination of the sample is required. Unless not otherwise described, samples were measured in the dark. Also shown in Fig. 1.13 is the electric measurement scheme for highly resistive ($\mathcal{O}(R) = \text{G}\Omega$) samples using a current preamplifier (*DL instruments*). To lower resistive samples ($\text{k}\Omega - \text{M}\Omega$) generally a voltage was applied and the current was measured directly.
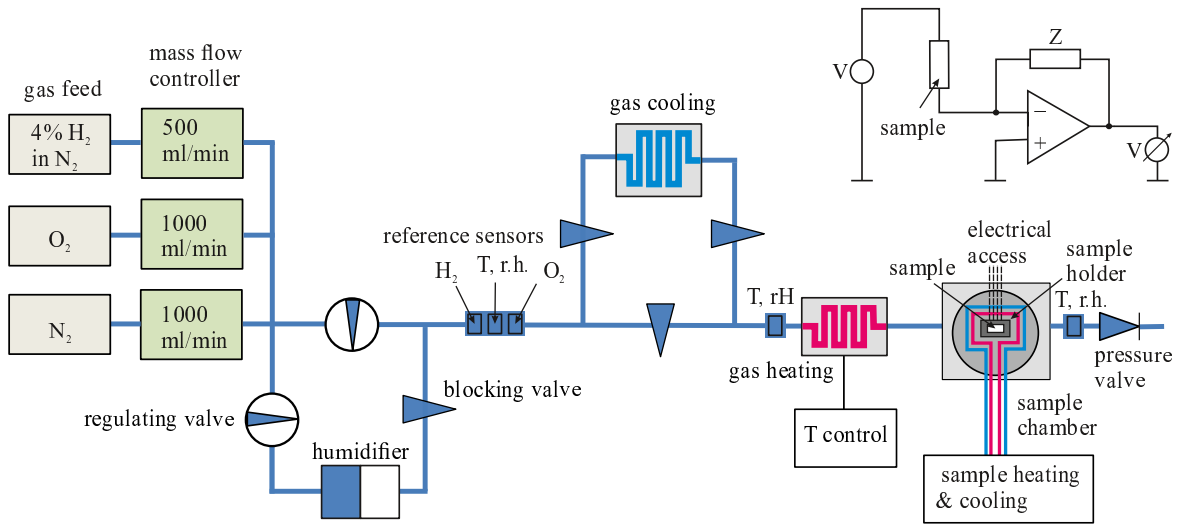


**Figure 1.13:** Measurement set-up with temperature- and atmosphere-controlled measurement chamber. Top right: electronic measurement set-up for small sample signals.

As initial treatment, the as-prepared samples were usually heated to $180\,°C$ in $N_2$ flow for at least one hour to remove residues of $H_2O$ in the $TiO_2$. It turned out that for gas sensing experiments the devices had to be exposed to the gas a few times in order to gain a balanced and stable response. As it is described in section 2.2, for electroforming

experiments, $V_O$ can be produced by reduction of $TiO_2$ to $TiO_{2-x}$. This was done by initialization in $H_2/N_2$ gas mixtures in combination with heating and an applied voltage.

### 1.3.3 Further characterization

**Atomic force microscope (AFM)**

Apart from the two types of nanolithography described in section 1.3.1, an AFM (Nanoscope III, *Digital Instruments*) was used for measurement of film heights, morphology and roughness. The sample surface is scanned line-by-line with a fine tip that is attached to a cantilever. Interaction between tip and sample surface leads to a distortion of the cantilever, which is measured via deflection of a laser beam on a photodiode with a four quadrant detector (see Fig. 1.14) and transferred into a height profile. Detector and feedback electronics visualize the surface information and control the deflection of the piezo element. Both, the scanning and the distance between tip and surface are regulated by the piezo element. In this work two operational AFM modes were used, which are shortly described in the following.

In the dynamic mode (*tapping mode*) the cantilever is driven to oscillate near its
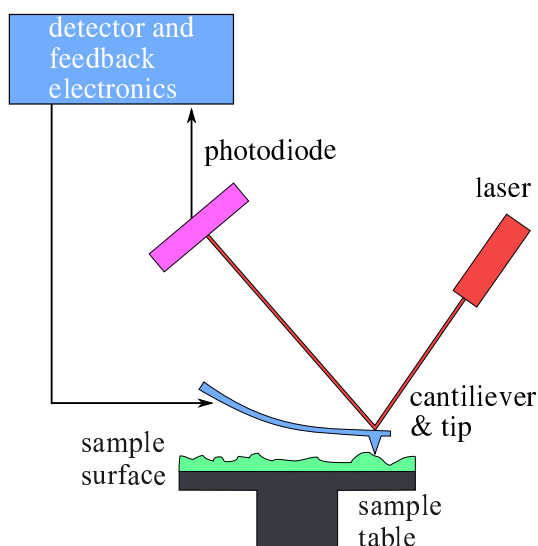
**Figure 1.14:** Scheme of an AFM scanning the sample surface by usage of beam deflection detection.

resonance frequency (typically 50-450 kHz) with an amplitude around several nanometers to 200 nm, which is kept constant. The oscillations are also achieved with a piezo element in the cantilever holder. In tapping mode there is no contact between tip and sample surface. This even allows for the scanning of surfaces that are covered with an absorbed water film [196]. Interactions of the tip and the surface are typically Van der Waals or electrostatic forces, but can also be dipole-dipole interactions. When the tip comes near the surface, these interactions cause changes in the oscillation amplitude, which are fed into the feedback loop that regulates the tip height. Compared to contact mode the forces on tip and surface can be much higher in tapping mode. However, due to the much

shorter times these forces are applied during oscillation, the damage done to surface and tip is negligible. In this work, surface imaging, roughness and height measurements were done in tapping mode, usually using n-type Si probes coated with hard carbon with a typical resonance frequency of 160 kHz and a force constant of 5.7 N/m (NSC14 *Mikromasch*). When tapping mode is used for imaging, normally a *z*-position is chosen, where the overall force between tip and surface is repulsive to prevent damaging of the tip and the surface due to collision. This was deliberately induced and utilized in structuring of Ti films with the nanolithography methods described in section 1.3.1. Nanolithography, i.e. local anodic oxidation and scratching of Ti films (nanoplowing) was done in *contact mode*. In this static mode, the cantilever is kept at a constant position above the surface and the surface profile is measured using the feedback signal required to achieve this. Usually, different cantilevers with a lower spring constant are used in contact mode to keep the forces low and achieve a sufficient deflection. Here conductive diamond coated Si probes were used with a typical resonance frequency of 420 kHz and a force constant of 48 N/m (DCP 20 *TipsNano*).

**Scanning electron microscopy (SEM) and energy-dispersive X-ray spectroscopy (EDX)**

SEM and EDX are often combined, since both methods are based on electron bombardment, but use different secondary effects as signal source. The on-chip oxidized films that are subject in chapter 3 were investigated using an electron microscope with integrated equipment for EDX analysis. In EDX analysis, the used information are characteristic X-rays that are generated during dissipation of kinetic energy of electrons within the specimen. The electrons are generated by an electron gun and accelerated towards the sample with a kinetic energy that is proportional to the acceleration voltage. Typical electron energies are 15-25 keV. At sufficiently large acceleration, the incident electrons can strike electrons from the inner shells of an atom and the produced hole can be filled by an electron from an outer shell. The energetic difference is thereby emitted as characteristic X-rays. This process is sketched in Fig. 1.15 a). For each element, the characteristic X-rays have different energies with the intensity being proportional to the element concentration [197]. From the measured X-ray spectra one can gather information about the elemental composition of the specimen. Depending on the shell from which the higher energetic electron comes and on the energy of the shell where the electron is missing, different transitions with characteristic energies are possible. The EDX spectrum background is a result of continuum X-rays that are emitted when the primary electrons are decelerated by the electric field close to the atomic nuclei, as is shown in Fig. 1.15 c). The X-ray generation area can be calculated using Castaing's equation [198]

$$R_g[\mu m] = 0.033 \frac{A}{\rho Z}(E_0^{1.7} - E_c^{1.7}) \tag{1.17}$$

where $E_0$ is the acceleration voltage in kV, $E_C$ is the minimum emission voltage in kV, $A$ is the atomic mass, $\rho$ is the density and $Z$ is the atomic number. As it is shown in Fig. 1.15 b), different signals are generated in different regions and depths in the
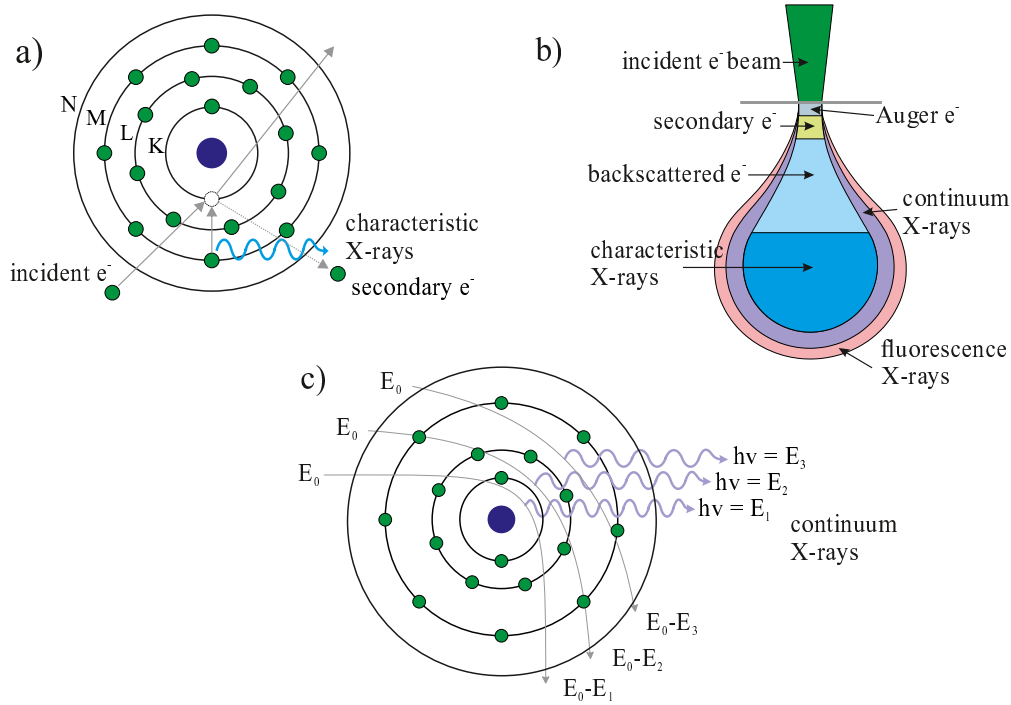
**Figure 1.15:** Schematic scetches of a) the origin of characteristic X-radiation, b) generation depth of electrons and X-rays in the specimen and c) the origin of the continuous X-radiation, adapted from [197].

specimen. For imaging with SEM mainly secondary electrons and backscattered electrons are detected. Secondary electrons are electrons of lower energy that are emitted from the material when it gets ionized by the incident beam. As a result, also Auger electrons can be generated, when a hole in an inner shell is filled by an electron from a higher shell and the energy difference is transferred to yet another electron which than leaves the atom. Backscattered electrons come from elastic scattering of primary electrons with the surface or a few tens of nanometers below. The X-rays used in EDX analysis are emitted isotropically but due to absorption effects which depend on the sample composition, density and other parameters, quantitative corrections are required to make accurate estimations of the sample composition.

**Photoexcitation**

Photoexcitation turned out to be a useful tool to improve the sensing performance of $Ti/TiO_2/Ti$ devices, as is described in section 2.1.2. Furthermore, in addition to the measurement of current-voltage characteristics, measurements of photocurrents were carried out to control whether the LAO by AFM had successfully produced two electrodes separated by $TiO_2$. As an example, Fig. 1.16 shows photoexcitation experiments with a sample of nanoporous $TiO_2$ sandwiched between Pt and Ti. The current was measured with the $Pt/TiO_2$ Schottky transition biased in reverse direction. The sample was illuminated with several diodes emitting in UV (375 nm, spectral bandwidth at 50 % of maximum intensity (BW): 12 nm), bluish-green (505 nm, BW: 40 nm), green (520 nm
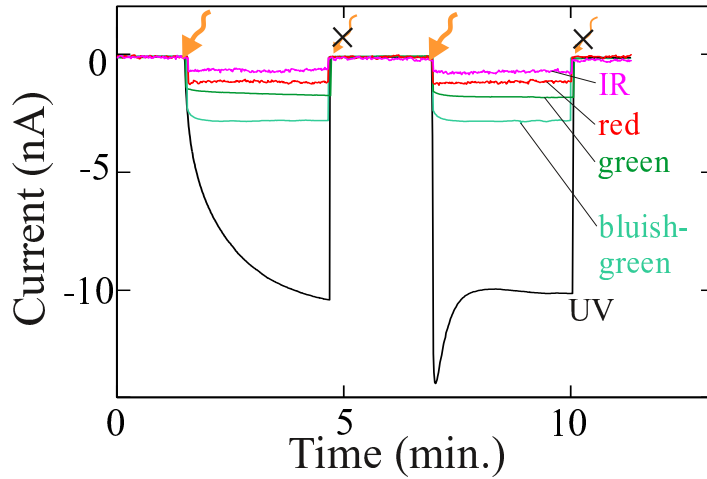
**Figure 1.16:** Current vs. time in a Pt/TiO$_2$/Ti structure that was photoexcited under 0.5 V reverse bias with light of various wavelengths between ultra-violet and infrared.

BW: 40 nm), red (700 nm, BW: 45 nm) and infrared (880 nm, BW: 80 nm). The orange arrows in the figure mark the beginning of a light pulse, crossed out arrows mark the end of the pulses. A photocurrent was detected even at light with energy below the reported bandgap of 3 eV for rutile. Since TiO$_2$ consists of a mixture of anatase and rutile [23] one would expect a distribution of even larger bandgaps (see Tab. 1.2). On the other hand, it has been reported that the energy gap of anatase can be decreased to the visible region by tuning the surface preparation conditions [199].

However, there are significant differences in the form of the photoexcitation pulses for the different colors: while photocurrents caused by green-bluish light and energies below that reach saturation after minutes, the situation looks different for UV light. During the first UV pulse, the (negative) current increases slowly without reaching saturation, during the second pulse however a maximum amplitude is reached within seconds followed by a decrease and a slight increase in the absolute current value afterwards. This might be a sign for formation of electron hole pairs only by UV illumination and not for energies of 2.4 eV or below. The observed phenomenology can then be explained by the filling of a defect state that lies roughly in the middle of the bandgap. Also, electronic excitation from shallow traps that were introduced by atomic hydrogen have been measured in the IR-band [200]. The shape of the first UV peak would then result from formation of electron hole pairs increasing the absolute value of the current, superimposed by filling of a defect state which opposes this trend. When the illumination is paused, the defect states remain filled. Subsequently, during the second pulse charge carriers may be released from the trap and are excited into the conduction band, thereby increasing the current abruptly together with formation of new electron hole pairs. After exhaustion of the defect states the current transient evens out and resumes the prior trend. A detailed analysis of the defect structure in the different TiO$_2$ systems in this work is, however, beyond the scope of this thesis.

**Optical properties**

Due to its strong interference colors, $TiO_2$ finds use in colored coatings. The perceived color of $TiO_2$ depends strongly on the layer thickness, the substrate and fabrication parameters [201]. This property is used for example in Bragg reflectors based on $TiO_2$ nanoparticles [202]. Sometimes the real thickness of a layer produced by sputtering or evaporation deviates from the nominal thickness, due to missing or wrong calibration or parameter variations during the process. Also, measurements of the absolute height by means of AFM can be difficult, when for example the surface is very rough or is not easily accessible. Therefore, it is practical to have a tool that allows to extrapolate from the color as seen in an optical microscope to the $TiO_2$ layer thickness. The color diagram
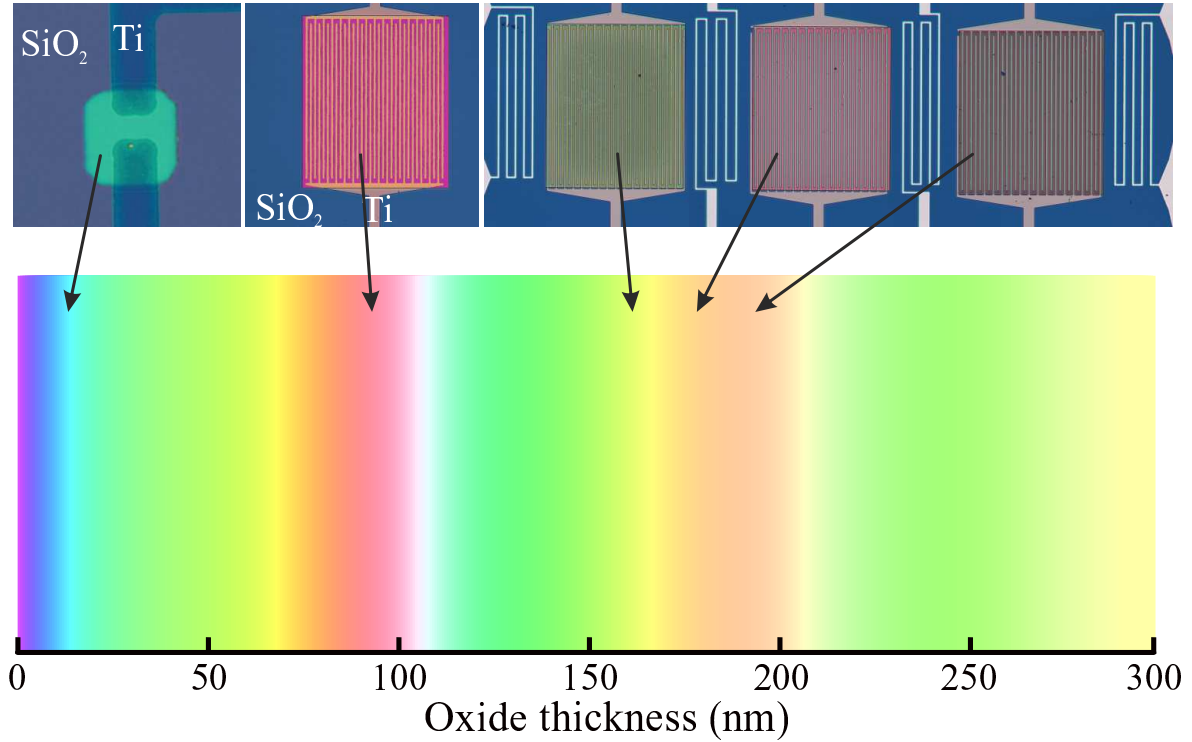


**Figure 1.17:** Color vs. thickness diagram for a layer stack of $Si/SiO_2/TiO_2$ and pictures of five samples of different thickness and colors as seen in an optical microscope.

shown in Fig. 1.17 was obtained considering the light reflection at a stack consisting of three layers of different material. We consider the sample as a film assembly that consists of a substrate layer of Si (layer m), covered with a 300 nm thick layer of $SiO_2$ (layer 2) and a $TiO_2$ layer of variable thickness on top (layer 1). The reflected intensity $R(\lambda, d)$ for this layer stack can be obtained using the characteristic matrix equation (*Abelès method*) for normal incidence [203–205]

$$\begin{pmatrix} B \\ C \end{pmatrix} = \begin{pmatrix} \cos(\delta_1) & i\sin(\delta_1)/n_1 \\ i\,n_1\sin(\delta_1) & \cos(\delta_1) \end{pmatrix} \times \begin{pmatrix} \cos(\delta_2) & i\sin(\delta_2)/n_2 \\ i\,n_2\sin(\delta_2) & \cos(\delta_2) \end{pmatrix} \begin{bmatrix} 1 \\ n_m \end{bmatrix}, \quad (1.18)$$

where the phase $\delta_i = 2\pi\,n_i\,d_i/\lambda$ is related to the wavelength $\lambda$, the refractive index $n_i$ and thickness $d_i$ of the $i$th layer, and $n_m$ is the refractive index of the substrate. With

the admittance $Y = C/B$, the reflection at the surface can be calculated by the following equation:

$$R = \left(\frac{n_0 - Y}{n_0 + Y}\right)\left(\frac{n_0 - Y}{n_0 + Y}\right)^* \tag{1.19}$$

with the refractive index of air $n_0$. To account for the dependency of the refractive indices on the wavelength, fits from empirical data of dispersion formulas [206–208] in the visible range[2] were inserted into equation 1.18. The refractive index of $TiO_2$ also depends on the structure and crystalline modifications, values in the range of 2.2 to 2.5 have been reported [59]. For each thickness $d_1$, the calculated reflectance value was multiplied with the wavelength spectrum that was converted into RGB values[3] by multiplication with the R, G or B sensitivity curves. The result was integrated over all spectral wavelengths of the visible range to obtain the perceived color.

---

[2]Dispersion formulas:

$$n_{TiO_2}(\lambda[\mu m]) = \sqrt{5.913 + \frac{0.2441}{\lambda^2 - 0.0803}}$$

$$n_{SiO_2}(\lambda[\mu m]) = \sqrt{\frac{0.6961663\lambda^2}{\lambda^2 - 0.0684043^2} + \frac{0.4079426\lambda^2}{\lambda^2 - 0.1162414^2} + \frac{0.8974794\lambda^2}{\lambda^2 - 9.896161^2} + 1}$$

$$n_{Si}(\lambda[\mu m]) = 17706.108 \cdot \exp\left(\frac{-\lambda}{0.04125}\right) + 5.69759 \cdot \exp\left(\frac{-\lambda}{0.23792}\right) + 3.48196$$

[3]Matlab Function *Spectrum RGB* from *Spectral and XYZ Color Functions* version 1.1.0.0 (33.3 KB) by Jeff Mather, BSD-like license

# 2 Electroforming as disruptive phenomenon

This chapter broaches the issue of electroforming (EF) as a disruptive phenomenon in $TiO_2$ based gas sensors. The majority of industrially-used gas sensing devices based on $TiO_2$ consist of sandwich structures of oxide and electrodes aligned vertically. Sandwich $Pt/TiO_2/Ti$ structures with micron scale oxide components prepared via electrochemical oxidation as it is described in Ref. [23] and section 1.3.1 were operated as $H_2$ sensors under low electric fields and during EF in Paper I. In Fig. 2.1 a) the sample scheme is shown, together with SEM images of the porous oxide morphology that is achieved under the given anodization voltages during the preparation.

The smaller scale nanowires prepared by AFM-LAO are shown in Fig. 2.1 b). The AFM scan shows an oxide line of about 500 nm broadness that was sensitized with Pt particles for $H_2$ sensing. The $H_2$ sensing performance under low operation voltages and under EF conditions with a view to the potential application as sensor with high spatial resolution due to the nanoscale active region was investigated in Paper II. Additionally, these wires were also sensitized with gold and operated as sensors for $O_2$. As expected, the downscaling of the active region allowed gas sensing at low voltages (0.8 V at room temperature). However, the nanoscale devices are not characterized by faster operation, indicating that the time constants are not dominated by differences in the $H_2$ diffusion path lengths on the regarded scales. The similarly good sensitivity might, to some degree, be attributed to the smaller film thicknesses compared to the depletion region width of the $TiO_2$ surface [18].

Since local oxidation via AFM nanolithography is not practicable in industrial fabrication, other ways of fabrication were sought for the devices in planar geometry. For this, structures were developed that can be fabricated compatible to Si-technology via lithographic patterning and deposition of the functional layers by evaporation or sputtering techniques, as they are described in section 1.3.1. The advantage of the planar geometry, and with it the facilitated miniaturization, was used in a sensor array design with many functions on small scales. The developed design is promising for independent side by side $TiO_2$-based detection of different gases (e.g. $H_2$, $O_2$ and $H_2O$), which can be realized by choice of different catalysts or by different methods of measurement. In addition, Pt meander structures were deposited between the single sensors for both, local heating and local temperature sensing. Especially the latter provided interesting insight into chemical reactions that might happen during $H_2$ sensing (see section 2.1.1). The vertical micron-scale devices do not offer this opportunity.

Surprisingly, the effects caused by EF during $H_2$ exposition arise in a universal manner, in devices of all mentioned scales with similar phenomenology.

This chapter is organized as follows. First a definition of the parameters that charac-

terize the sensor performance is given and the most often used techniques and important mechanisms for H$_2$ and O$_2$ gas detection are described. The (to our knowledge new) modifications to improve the oxygen sensitivity of the nanowires and the results are discussed in detail. Afterwards the common models for the mechanisms underlying electroforming and resistive switching in TiO$_2$ devices are presented. In the last section an introduction to the attached Papers I and II is given, with special emphasis on the central theme, namely a hitherto unreported interdependence of EF and hydrogen incorporation. In both, microscale and nanoscale structures similar effects during gas sensing operations were observed, which were also embraced under the topic of disruptions caused by EF.
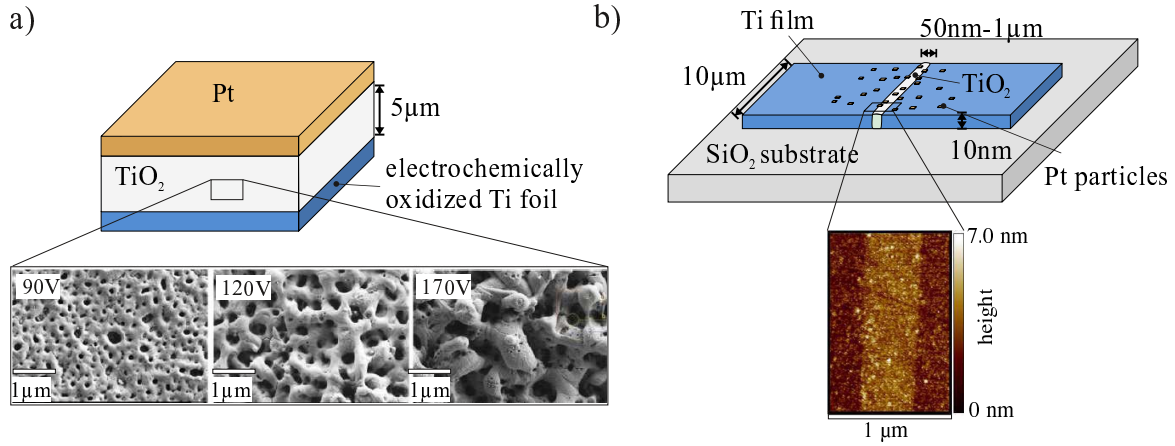


**Figure 2.1:** Comparison of the sample schemes that are subject of Papers I and II, respectively. a) Macro samples in vertical geometry of electrochemically oxidized Ti foil decorated with a Pt electrode are studied in Paper I. The SEM scans show different stages of TiO$_2$ porosity achieved at different anodization voltages (taken from [21]). b) Sample in planar layout consisting of a TiO$_2$ wire fabricated on a Ti thin film via AFM nanolithography. The AFM scan shows the surface of the oxide line after decoration with Pt particles for H$_2$ sensitization.

## 2.1 Gas sensing with TiO$_2$

TiO$_2$ materials are used for the detection of both, reductive gases like hydrogen (H$_2$), carbon monoxide (CO), ammonia (NH$_3$) and hydrogen sulfide (H$_2$S), and for oxidative gases like oxygen (O$_2$) and nitrogen dioxide (NO$_2$) [40]. In general, these gases are detected via measurements of resistance changes in the TiO$_2$, although the microscopic origins of these changes differ for the different gases. An overview over the sensor applications and mechanism in TiO$_2$ nanomaterials is given in a review by Bai and Zhou [40]. They describe the sensing process divided into two functions: The receptor function, where a gas molecule is physisorbed at first and then chemisorbed to the surface atoms, and the transducer function, involving electron transport [153]. For both processes, surface vacancies play an important role. Furthermore a strong dependence on the temperature can often be found, not only due to its effects on the output signal (resistance) itself, but also on the doping density and the involved mechanisms, e.g.

physisorption and chemisorption.

The parameters that characterize the sensor performance include the sensor response $S$ (sensitivity) and the time constants for response $\tau_S$ and recovery $\tau_R$. The definitions of these parameters are not standardized. We used the common definition

$$S = \frac{\Delta R}{R_a} = \frac{|R_a - R_g|}{R_a} \tag{2.1}$$

for the response, with $R_a$ and $R_g$ being the resistance in ambient conditions and in the detected gas, respectively. The time constant $\tau_S$ was defined as the time the signal needs to reach $90\,\%$ of the response signal upon exposition to the gas; $\tau_R$ accordingly, as the time needed to return to $10\,\%$ of the amplitude, after removal of the gas sets in. Also often mentioned are the working temperature and the detection limit, which is the minimum detectable concentration.

In Papers I, II and IV our structures were characterized with regard to their hydrogen sensing performance. In the following, the mechanism of hydrogen detection is shortly addressed, and additional measurements are shown, supplementing the characterization that was done in Paper II. Moreover, interesting findings regarding the oxygen sensing performance and its improvement are presented, that have not been published so far.

## 2.1.1 Hydrogen detection

It is widely agreed that porous structures [22, 39, 171, 209] have advantageous properties for gas sensing, like faster and easier diffusion and a larger inner surface compared to dense and compact structures. For example, a larger active surface enhances the adsorption of $H_2$ molecules and favors electron transfer. This is for instance the case in nanoporous $TiO_2$ structures fabricated by anodization in $H_2SO_4$ (described in section 1.3.1 and Paper I) or in various tubular structures reported in the literature [16, 18, 210]. Other nanostructures for gas sensing are NST (nanostructured titania) sponge-like arrays [41] that are highly sensitive to $H_2$ and $O_2$. In agglomerates of $TiO_2$ nanoparticles, electron transfer occurs at contact points between the particles, which is why their sensitivity is often deteriorated when compared to nanotubes [40]. Summaries of the different state-of-the-art sensor types and their performance parameters can be found in Ref. [38] and [211]. The interaction of gases with the $TiO_2$ surface is in many cases enhanced by deposition of metals like Pt [39, 212], Pd [13, 18, 148, 212, 213] and Au [214, 215]. In Paper II, we studied the effect of an increasing Pt amount deposited on a $TiO_2$ nanowire on the $H_2$ sensitivity.

The mechanism of $H_2$ detection is well established. $H_2$ molecules can, to a small degree, get dissociated at defects on the $TiO_2$ surface [16, 216]. Direct hydrogenation of $TiO_2$ is, however, very limited [217]. Instead, Pt plays the crucial role for $H_2$ splitting, catalyzing the dissociative adsorption [143] (*catalytic boost*). This way, activated hydrogen species can diffuse even through thick Pt layers and spill over into the $TiO_2$ lattice [1, 25, 118, 135, 217, 218]. They adsorb at surface sites and bulk sites, where they act as electron donors [200, 219], though the former, i.e. chemisorption of dissociated hydrogen on the surface oxygen forming OH groups, is the dominant process for fast and reversible $H_2$ sensitivity [16]. This is accompanied by an electron accumulation at the

surface and charge transfer from hydrogen to the conduction band of TiO$_2$, decreasing its resistance [18]. The sensor response is a function of the H$_2$ concentration [16] and the exposure time. When H$_2$ is removed from the atmosphere, electron transfer is directed back to the adsorbed hydrogen, followed by H$_2$ desorption [216].

In air, oxygen may be chemisorbed in the form of O$_2^-$, thereby trapping electrons from the conduction band and increasing the base resistance [18, 40], but can be removed again by H$_2$ [118]. It is assumed that direct chemisorption of H$_2$ in the absence of O$_2$ is dominant for the resistance decrease. At the same time, when present, O$_2$ faciliates the removal of chemisorbed H$_2$ [18], which is then manifested in much shorter $\tau_R$. Concerning this matter, the film thickness should be regarded as well. Paulose et al. [18] made a connection between the wall thickness of nanotubes in relation to the width of the depletion region caused by the adsorption of oxygen, which is usually a few tens of nanometers in metal oxides, and the restistance change in response to H$_2$. They found the best sensitivity for flat band conditions, when the wall thickness (times the factor 1/2, due to adsorption on both sides of the wall) was smaller than the depletion region width. In very thin films the space charge layer modulation (creation or depletion) encompasses the entire bulk [20, 148, 220]. For our films in the range of 10 nm thickness, similar conditions may apply and explain their good sensitivity in air.
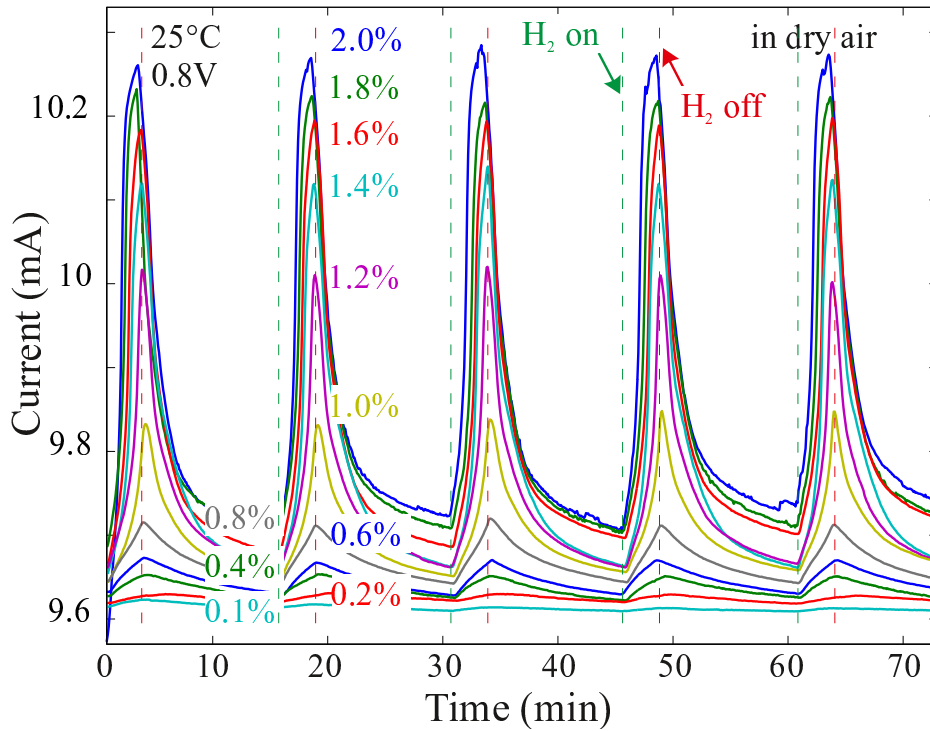


**Figure 2.2:** Hydrogen sensing performance of an AFM-written oxide line sensitized with platinum and biased with 0.8 V, measured at room temperature. Each cycle consists of 3 minutes exposure to H$_2$ in dry air mixture (H$_2$ concentration given in the plot) followed by 12 min of air exposure.

Fig. 2.2 shows the sensing performance of a TiO$_2$ nanowire, as it is described in Paper II, for a larger concentration range of H$_2$ in air. The response is reproducible

and a concentration resolution of at least $0.2\%$ is possible. $\tau_S$ is faster compared to $\tau_R$, indicating different dynamics for incorporation and removal of hydrogen. This is not surprising, since interstitial hydrogen in $TiO_2$ acts as shallow donor [221, 222] but can also be trapped in deeper trapping sites [223]. The larger binding energy to these sites causes the slow release [26].
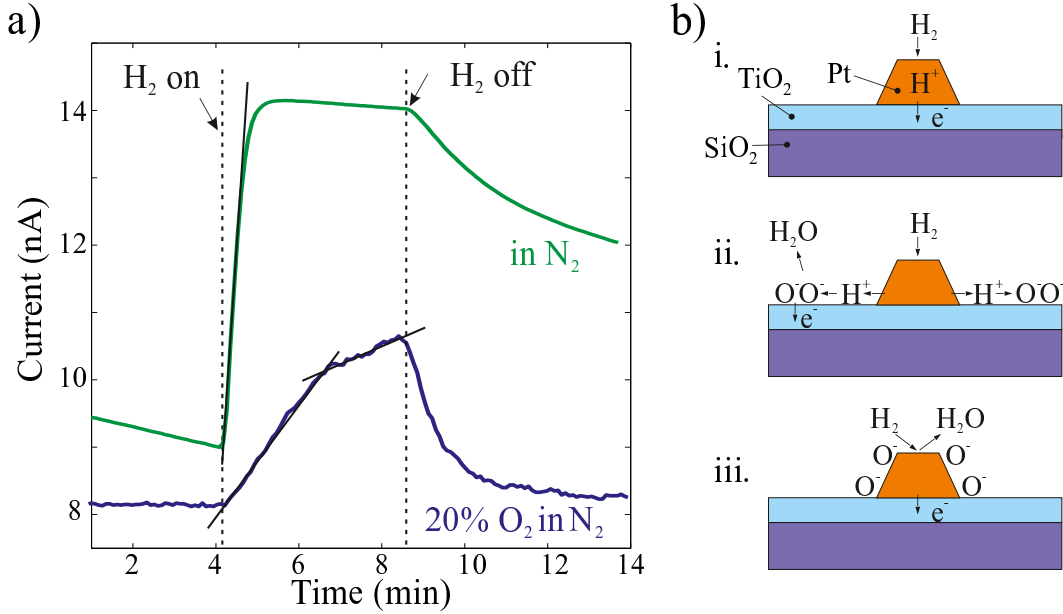


**Figure 2.3:** a) Comparison of the current change during $250\,ppm$ $H_2$ exposure in $N_2$ and dry air. b) Mechanisms that lead to an increase in conduction upon $H_2$ dissociation on Pt, after [148].

Fig. 2.3 a) shows a comparison of one $H_2$ pulse measured in $N_2$ atmosphere and in air. In $N_2$ the curve exhibits single slope response kinetics. This is due to electronic sensitization [148] [mechanism i) in Fig. 2.3 b)], i.e. (1) creation of an accumulation layer by hydrogen acting as electron donors and (2) dissolution of $H_2$ in the Pt particles lowering its work function and the Schottky barrier between Pt particles and $TiO_2$ (see section 1.2). Dual slope response kinetics can be observed in the presence of $O_2$ and is explained by first chemical sensitization followed by electronic sensitization [148]. Chemical sensitization denotes the process in which activated hydrogen reacts with oxygen that is chemisorbed on $TiO_2$ [mechanism ii) in Fig. 2.3 b)] or on Pt [mechanism iii) in Fig. 2.3 b)] to form water [135]. In both cases, trapped electrons are released and the conduction is increased. It has been reported that chemical sensitization is visible only for lower concentration ranges, while for larger concentrations mechanism i) is dominant. Continuing diffusion of hydrogen to interstitial sites in the Pt, i.e. formation of Pt hydride, may at some point oppose the trend of increasing conductivity and also be accompanied by an expansion of the particle volume [148]. Formation of Pt hydride might therefore explain the slight decrease in the current vs. time curve in $N_2$ while $H_2$ is still present.

There are also huge differences concerning the operating temperatures. Most devices operate at relatively high working temperatures above $150\,°C$, where $H_2$ diffusion and

therefore the sensitivity is improved. An example is shown in Fig. 2.5, where an increase in the temperature significantly improves the on/off ratio.

In humid conditions, a layer of chemisorbed OH groups forms on the TiO$_2$ surface, on which more layers of physisorbed water molecules can form, blocking the active sites for hydrogen adsorption [18, 40]. This sensitivity decreasing effect can also be counteracted by increasing the operating temperature, resulting in an increased H$_2$O desorption. Technically however, it would be desirable to avoid heating for reasons like energy efficiency and safety, especially in environments containing high concentrations of H$_2$. A detailed study of the temperature dependent sensing performance of our devices, i.e. Pt sensitized TiO$_2$ in form of nanoporous structures and nanowires can be found in Papers I and II. In both cases significant response signals were achieved at room temperature even for very low (15 ppm) fractions of H$_2$.
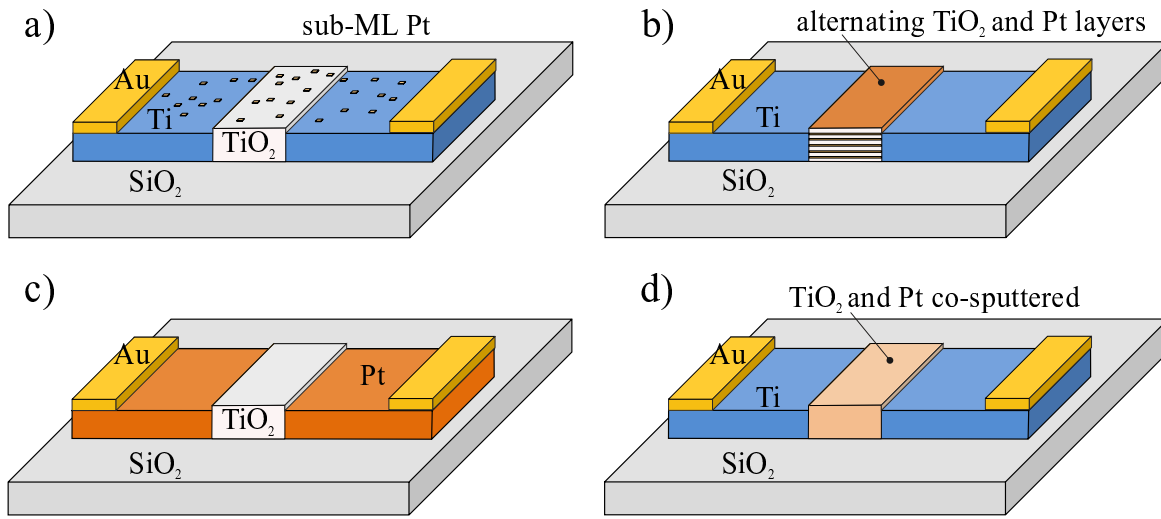


**Figure 2.4:** Sample schemes of sputtered TiO$_2$ structures sensitized for hydrogen sensing via a) Pt deposition in the range of sub-ML to 3 nm layer, supposedly clusters, b) a fivefold alternation of TiO$_2$ (20 nm) and Pt layers (3 nm) with Pt layer on top, c) usage of Pt as electrodes instead of Ti, with no further Pt deposition on top of the TiO$_2$, and d) a layer of co-sputtered TiO$_2$ and Pt.

The gas sensing behavior is influenced by a variety of parameters. In most cases and also in the structures used in this work, exposure to H$_2$ causes a resistance decrease. However, the opposite behavior can occur, i.e. a resistance decrease in response to reducing gases, namely when the TiO$_2$ changes to p-type behavior, for example by doping. Zakrzewska and coworkers studied the grain-size dependence of gas sensing properties in nanomaterials fabricated with TiO$_2$ nanopowders [224] and in TiO$_2$/SnO$_2$ nanocomposites, where charge transfer from SnO$_2$ to TiO$_2$ occurs due to the formation of a contact potential at grain boundaries [225]. Also the composition of anatase and rutile, which can be tuned for instance by doping [64], annealing [40], or by sputtering parameters [226], can have significant influence on the H$_2$ sensing performance [64]. Anatase has been reported to have higher sensitivity towards reducing gases compared to rutile, which may be due to its higher electron mobility and to the larger $c/a$ ratio in

the anatase lattice [see table 1.2 and Fig. 1.3 a)] which allows better accomodation of H at interstitial sites [16, 118].

As mentioned before, other geometries and $TiO_2$ fabrication techniques were tested. The objective was the query for fabrication procedures for larger numbers of sensor elements compared to LAO fabrication, compatible to Si technology. A straightforward method of choice is RF sputter deposition of $TiO_2$ layers on top of $SiO_2$. For this, the sample geometry and layout were adapted, in order to reach a comparable film resistance, since sputtered layers have in general a rather compact and uniform structure. A resistance decrease by five orders of magnitude was achieved by usage of finger electrodes, increasing the effective width by a factor of $5 \cdot 10^3$, and larger film thicknesses (200 nm). An example is given in Fig. 1.17 (top right), where a sensor array of three $TiO_2$ pad/Ti finger electrode structures is shown, equipped with neighboring Pt meanders. The tested approaches for the deposition of Pt are sketched in Fig. 2.4 with a simplified depiction of the electrode geometry.

The deposition scheme in Fig. 2.4 a) is, as ever, a sub-monolayer up to 3 nm thick layer of Pt on top of $TiO_2$. The approach shown in Fig. 2.4 c), namely usage of Pt as electrode instead of Ti with no further Pt deposition on top, allowed no or unsatisfactory $H_2$ detection, probably due to lower permeability and number of active sites available for $H_2$ adsorption. In contrast to this, the performance is significantly improved when additional layers of Pt are available for $H_2$ inside the $TiO_2$ matrix, by alternating sputter deposition of Pt and $TiO_2$ as it is depicted in Fig. 2.4 b).
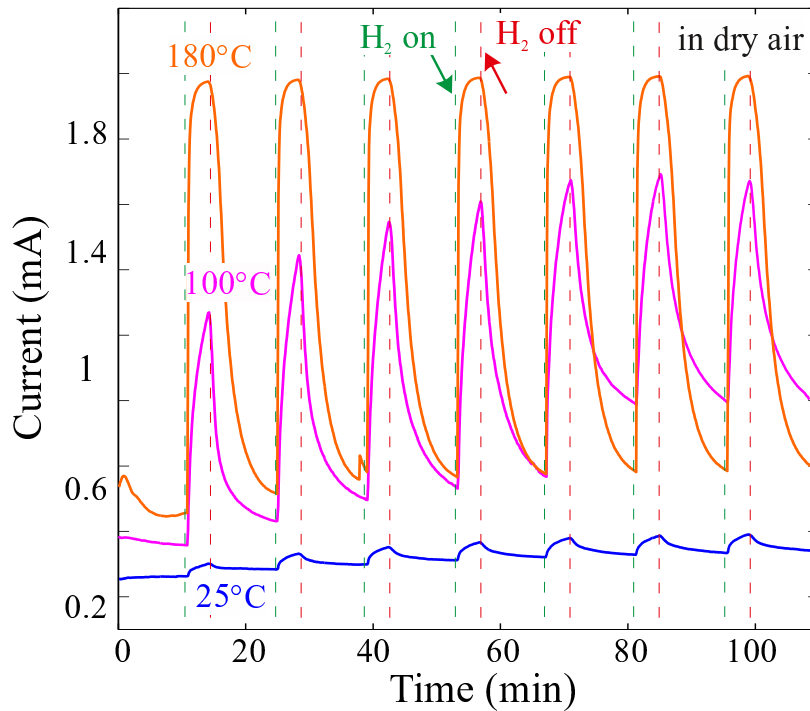


**Figure 2.5:** Signal of a sensor pad consisting of alternating layers of sputtered $TiO_2$ and Pt in response to $4\%$ $H_2$ pulses in dry air at $25\,°C$, $100\,°C$ and $180\,°C$. The sample was biased with $0.8\,V$.

Fig. 2.5 shows the response of a sputtered TiO$_2$/Pt layer series to 4 % H$_2$ in air. Here, despite the compact texture, H$_2$ seems to efficiently reach the additional Pt sites, supposedly also with better coupling to the TiO$_2$ bulk and charge transfer. The peaks in the current in response to H$_2$ exposure have a shape similar to the curves in Fig. 2.2 and also the baseline current is of same order of magnitude. All current transients exhibit an upwards drift with time, which can be attributed to incomplete hydrogen removal. When substituting for oxygen in metal oxides, hydrogen bonds to surrounding metal atoms via strong multicentre bonds [227]. Yet it is obvious by looking at the curve measured at room temperature that the device cannot compete with the sensitivity of the nanowire. Similar results can in principal be achieved by simultaneous co-sputtering of Pt and TiO$_2$ (Fig. 2.4 d). This way of fabrication, however, is less defined and mostly leads to an increased baseline conductance. In order to reach better responses with TiO$_2$ based on sputter deposition further development work is necessary. In this regard, e.g. the *gig-lox* technique has already been mentioned in section 1.3.1 for the improvement of gas permeability by increasing the porosity.
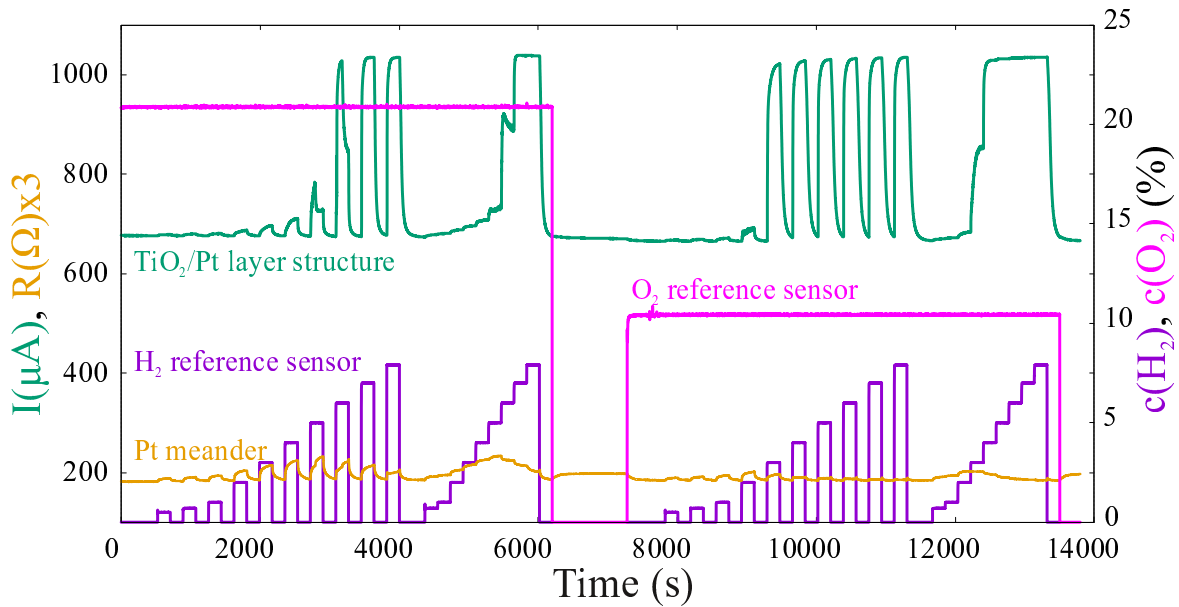


**Figure 2.6:** Measurement sequence on a sensor pad, like it is shown in Fig. 2.4 b), conducted by *neohysens*. In the time interval 0-6200 s, the O$_2$ concentration was set to 20.9 % and the H$_2$ concentration was varied in two sweeps. Afterwards the O$_2$ concentration was set to 10.45 % and the same H$_2$ sweeps were done. Simultaneously, the resistance of a neighboring Pt meander was recorded to measure temperature changes. The sensor pad was biased with 0.8 V. Measurements were done at room temperature.

Nevertheless, this special design allows an insight to other interesting points. Fig. 2.6 shows a measurement sequence on the alternating layer structure, which was done by our cooperation partners at *neohysens* [1]. Two sweeps of H$_2$ exposure were done in 20.9 %

---

[1]D. Ostermann, H. Lüder and O. Hissel, *neo hydrogen sensors GmbH*

and 10.45 % $O_2$ in $N_2$, respectively. To monitor local temperature changes in the sensor pad during gas exposure, the resistance of a neighboring Pt meander was measured simultaneously (orange curve). Also shown are the signals of the reference sensors for $H_2$ (purple curve) and $O_2$ (magenta curve). It can be observed that under such small voltages the saturation current does not show any signs of drift. The response to $H_2$ clearly depends on the $O_2$ concentration and for both $O_2$ concentrations measured, the relation between the $H_2$ concentration and the current signal is non-linear. The meander resistance increases noticeably upon interaction with $H_2$, with a maximum change during the 5 % pulse in the larger $O_2$ concentration. At the same time, the $H_2$ sensing signal tumbles. For the sweeps at 10.45 % $O_2$ the meander resistance increase is not that large with a smaller maximum during the 2-3 % pulses. Most likely, these observations can be interpreted as water forming via exothermic $H_2$ oxidation (see section 1.2) competing with the $H_2$ detection and heating up the $TiO_2$/Pt pad and the neighboring meander. The maximum resistance change $\Delta R = 17.4 \, \Omega \,\hat{=}\, \Delta T \approx 43 \,°C$ is enormous (the amplitude in the figure is tripled for better visibility). Assuming water forming via hydrogen oxidation with a reaction heat of 2.5 eV per product $H_2O$ molecule, the reaction process happens in the order of $10^{10}$ times.[2]

## 2.1.2 Oxygen detection

During the last decades, oxygen sensors for various applications with a variety of different performance characteristics have been developed. Ramamoorthy et al. [228] provided an overview over the different materials and their applications and limitations. For example, the material of choice in state-of-the-art high temperature potentiometric and amperometric $O_2$ sensors is yttria stabilized zirconia (YSZ). Resistive type metal oxides are also used, mainly in the high temperature range. The general relationship between the electronic conductivity $\sigma$ of an oxide sensor and the oxygen partial pressure is [228]

$$\sigma = A \exp\left(\frac{-E_A}{k_B T}\right) p(O_2)^m \tag{2.2}$$

where $A$ is a constant and $E_A$ is the activation energy for conduction. The parameter $m$ is determined by the carrier type and defects. For the n-type $TiO_2$ with oxygen vacancies equations 1.8 and 1.9 apply and $m = -1/6$.

TiO₂ based $O_2$ sensors exist for various operating temperatures [152], among them the already discussed Pt/$TiO_2$ Schottky diodes that work at low temperatures. Most bulk defect sensors, however, require heating far above 200 °C [41, 114]. Like the $H_2$ sensors, the performance for $O_2$ sensing also depends on the micro- and nanostructure of the films [40, 41, 114, 209]. The basic principle of detection is tracing the resistance increase when $TiO_2$ is exposed to $O_2$. Oxygen vacancies and interstitial oxygen ions work as electron donating states and permit adsorption of an oxygen ion layer or the formation of additional donors near the surface [40]. This way, the resistance increases

---

[2]Assuming all the reaction heat goes into heating of the $TiO_2$ volume of $200 \,nm \cdot (700 \,\mu m)^2$, with c = 771.74 J/(kg · K), and the temperature change in the Pt meander and $TiO_2$ are the same.

due to reoxidation of the lattice according to the following equations [1, 40]:

$$O_2(ads) + e^- \longrightarrow O_2^- \tag{2.3}$$
$$O_2^- + e^- \longrightarrow 2\,O^- \tag{2.4}$$

Fig. 2.7 shows the response of a TiO$_2$ line that was biased with 1 V and was exposed to 3 min pulses of 20 % O$_2$ in N$_2$ every 30 minutes. Oxygen in the ambient atmosphere instantaneously increases the resistance. When the chamber is flooded with pure nitrogen, the current slowly recovers. As can be seen in the figure, the long recovery time leads to a drift of the sensor signal during a pulse series of O$_2$ at room temperature, indicating reoxidation of the formerly reduced oxide. For these types of measurement sequences, the leveling of the device towards the balance current takes one whole day. When O$_2$ is absent, the recovery takes much longer to regain the original resistance compared to H$_2$, because reduction happens on much larger timescales [16]. In this picture, the leveled resistance oscillations here starting from around 25 h are mainly due to adsorption and desorption processes at the surface. This way, also the O$_2$ pulse duration determines the leveling time. Drift effects are a known problem and make it hard to detect low concentrations of O$_2$ [40].
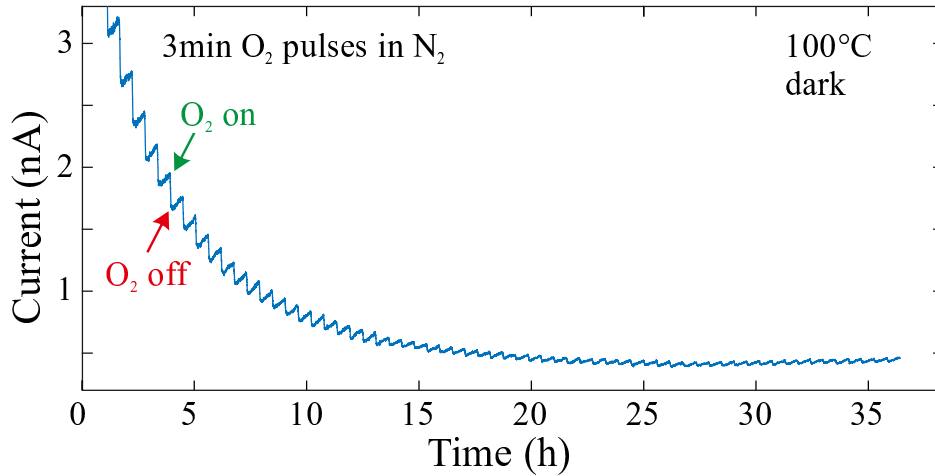


**Figure 2.7:** Current vs. time during a sequence of 3 min exposures of 20 % O$_2$ in N$_2$, measured at 1 V bias and 100 °C. The long recovery time is attributed to re-oxidizing of the oxide and causes a downwards drift that takes several hours to balance out.

Various studies on the enhancement of O$_2$ sensors by usage of noble metals for catalytic activation can be found in the literature. Many focus on the improvement of the sensitivity and a reduction of the response time. It is known that O$_2$ dissociatively and molecularly adsorbs on the Pt (111) surface and even forms (2×2) overlayers of atomic oxygen [137–139]. Surprisingly, we did not find any improvement in the O$_2$ sensing by usage of Pt particles compared to pure TiO$_2$ nanowires, probably due to the large number of already available surface binding sites for O$_2$ on TiO$_2$ in the presented geometry. Nb doping of TiO$_2$ allows 'low' temperature (190 °C) operation of oxygen sensors [229]. The

grain size of rutile, which is generally larger than the space charge layer [40] can also be controlled by doping with Nb. Furthermore, there are reports about the usage of the synergetic effect [102] that arises by combining $TiO_2$ with other oxygen sensitive semiconductor materials like $V_2O_5$ or $CeO_2$ [40] or by variation of the anatase and rutile composition.

Unexpectedly, we found that deposition of very small amounts of gold significantly increases the response $S$ to $O_2$. Also, illumination of the sample with UV light during the measurements not only increased the response, but also leads to much faster recovery, which may be explained by hole-induced photodesorption of chemisorbed oxygen [230]. Wang et al. [42] reported that exposure of photoactive $TiO_2$ thin films to UV light improves the reactions of adsorbed surface oxygen and thus the $O_2$ sensing performance. Fig. 2.8 shows the current signal of a $TiO_2$ nanowire during pulses of 3 minutes duration in which the sample is exposed to $20\%$ $O_2$ in $N_2$. The oxide line was sensitized via sputter deposition of Au for ten seconds at a sputtering rate of $0.05\,\text{Å/s}$. Under illumination using a UV diode ($375\,\text{nm}$, $12\,\text{nm}$ BW), much shorter times are needed for current leveling. Also, high temperatures improve the on/off ratio of the current. In Fig. 2.9
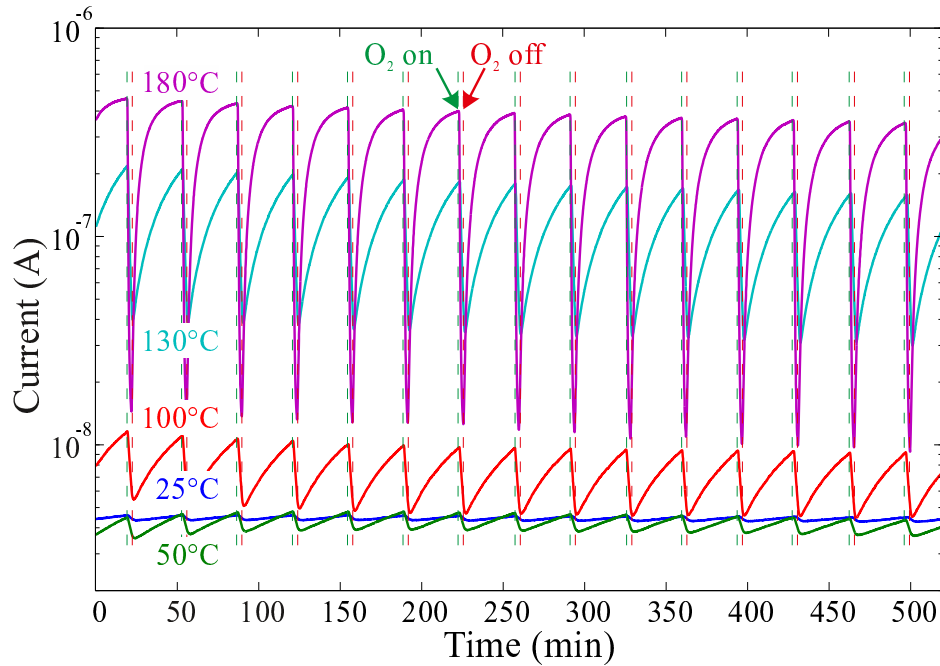


**Figure 2.8:** Oxygen sensing performance of AFM written oxide line sensitized with gold under UV illumination. One cycle consists of three minutes exposure to $20\%$ $O_2$ in $N_2$, followed by a $30\,\text{min}$ exposure to pure $N_2$. Measurement cycles were done at temperatures between $25\,^\circ\text{C}$ and $180\,^\circ\text{C}$ at $1\,\text{V}$.

the effects of UV illumination, Au deposition and temperature increase on the sensor response $S$ are summarized for two concentrations of $O_2$. Interestingly, the response to $100\%$ $O_2$ is on average increased by around one order of magnitude compared to the $20\%$ response. This is on the one hand intuitively expected, but on the other hand it contradicts some of the reports [40]. Also, a non-linearity of the response with increasing

temperature has often been reported. For 100 °C, UV illumination improves the response by a factor of almost ten, the effect of Au deposition is a little smaller but still clearly visible. Surprisingly, upon additional deposition of $\approx 2$ nm Au on the nanowire, this improvement is reversed and no difference in $S$ compared to the unsensitized nanowire was found. Naturally the question rises, why Au deposition has such an influence on the
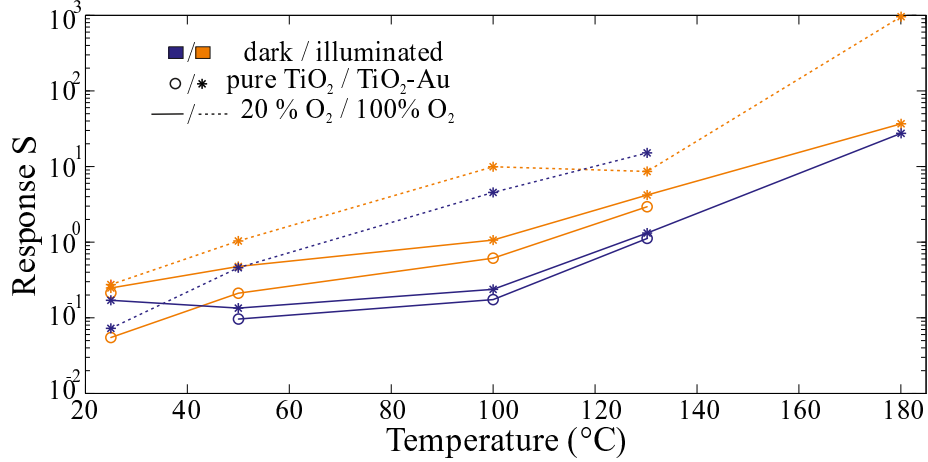


**Figure 2.9:** Response $S$ of a TiO$_2$ line during exposition to O$_2$ gas. Effect of sensitization with gold and illumination with UV light is shown for varied temperatures and two concentrations of oxygen. Measured in dry nitrogen under 1 V bias.

O$_2$ sensing and especially, why the response degrades again for larger amounts of Au. As TiO$_2$ is irradiated with UV light, it undergoes charge separation whereby electrons are lifted into the conduction band and holes are left behind in the valence band.

$$\text{TiO}_2 + h\nu \longrightarrow \text{TiO}_2\,(\text{e}_{\text{CB}}, \text{h}_{\text{VB}}) \tag{2.5}$$

TiO$_2$ particles with accumulated charge upon UV irradiation are reported to exhibit blueish coloration [231]. Although the majority of the charges recombine, a fraction can get trapped, for instance on surface vacancies. It has been reported that holes are scavenged e.g. by ethanol, while electrons also get trapped at Ti$^{4+}$. In air however, dissolved oxygen acts as scavenger for the photogenerated electrons according for example to equations 2.3 and no charge accumulation can be found [158]. It is known that Au catalysts can oxidize molecules such as CO at room temperature and even below, although flat Au or TiO$_2$ alone are not particularly active for CO or O$_2$ adsorption [1]. As mentioned before, O$_2$ shows strong interactions only with defects. A review about catalysis by gold was given by Bond and Thompson [232]. They report, that reactant molecules cannot chemisorb to the massive gold in any useful extent. For catalytic activity, e.g. for the oxidation of CO, forming of gold into very small particles with an adequate number of low-coordination surface atoms is necessary.

Diebold [1] summarized the conditions determining the catalytic activity of Au on TiO$_2$. First, Au must be in the form of small ($<5$ nm) particles, although there seems to be a minimum cluster size necessary for activity. Due to a quantum size effect, the particles do not have metallic character; the smallest clusters exhibit a bandgap of

>1 eV [233]. Secondly, the clusters need the right type of substrate, for which e.g. $SiO_2$ and $TiO_2$ are suited well. Special relevance for the activity was attributed to sites in the area between cluster and support [233, 234], also interaction between them might cause lattice strains in Au. Another important role plays the preparation technique and resulting coupling between the Au particles and $TiO_2$. It is noteworthy that in contrast to Pt / $TiO_2$, see section 1.2, there is no evidence for SMSI in the Au / $TiO_2$ system.

As has been shown by SPM measurements [182], gold films of a nominal thickness of about 0.5 nm result in island-like structures and typically become electrically continuous at a thickness of about 5 nm. A detailed study on the growth and morpholgy of Au clusters on $TiO_2$ can be found in Refs. [233, 235]. Although we have no experimental proof, we assume that Au may form clusters of quasi-2D morphology on the nanowire, with the nominal thickness of deposited Au of around 0.5 ML (1 ML = 0.23 nm) [233]. It is assumed that low-coordinated Au atoms in small particles might be responsible for the activation of $O_2$.

A number of studies [158, 231, 236] have investigated the effect of Au nanoparticles on $TiO_2$ and their unique mediating role of storing and shuttling photogenerated electrons. When Au nanoparticles come into contact with $TiO_2$ that has been charged by UV light, the high electron accumulation and following charge equilibration leads to a shift of the apparent Fermi level towards the bottom of the conduction band. An increase in the charge separation efficiency in the redox activity from 52 % to 89 % was achieved by usage of Au nanoparticles on $TiO_2$ particles [158]. The results depicted in Fig. 2.9
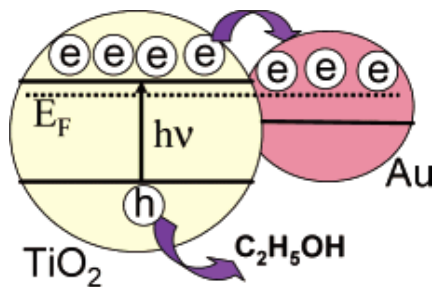


**Figure 2.10:** Scheme of Fermi level equilibration in a $TiO_2$/Au composite. Reprinted with permission from Ref. [231]. © (2003) American Chemical Society.

may be explained on the basis of these findings: The response of pure $TiO_2$ under UV irradiation (orange open dots) is increased compared to $S$ in the dark (blue open dots), because most of the photogenerated electrons that cause an increased baseline current in $N_2$ are scavenged by oxygen adsorbates when $O_2$ exposure starts. Assuming that no OH or redox species are present on the surface to which electrons can be transferred, the Au particles might act as storage for electrons. It has been reported that storage of electrons in Au happens in a quantized fashion [231] and is facilitated by double layer charging around the Au particle. The increased response of $TiO_2$ sensitized with Au (filled blue dots) can be interpreted as an increase of the capacitance and filling of the accumulation layer during $N_2$ exposure. A release from the Au particles and injection into shallow traps is thinkable, as it was reported for electrons from hydrogen spilled

over Au nanoparticles [237]. The effect is even more pronounced under UV illumination (filled orange dots), where a larger number of photogenerated electrons may exploit the extra storage space offered by the Au particles.

The fact that the response increasing effect disappears for additional Au deposition may be attributed to both, the particle size and number, if we assume an unknown size distribution of Au nanoparticles. As mentioned above, it is widely known that the size of Au particles is related to their catalytic activity [234]. Subramanian et al. [158, 236] and Jakob et al. [231] found that the particle size is a determining factor for charge transfer and the overall energetics of the TiO$_2$/Au system. For instance, smaller Au particles (3 nm) cause a larger shift of the Fermi level of 60 meV than larger ones (8 nm, 20 meV) [236]. Also it is postulated that more oxygen adsorbs on smaller Au nanoparticles [233, 234]. Moreover, a maximum of the photocurrent was measured for concentrations of 2.2 % (wt. Au/wt. TiO$_2$) [158].

To some extent, noble metals like gold and Pt react with oxygen and TiO$_2$ [115, 157–159]. Upon these reactions thin layers of Au$_2$O can form [115] which leads to deterioration of the photocatalytic activity [157, 160, 236]. In particular, photocatalytic oxidation of Au was reported to lead to formation of Au$^+$ at the TiO$_2$/Au interface [158]. These are likely to serve as recombination centers and can lead to a net loss of electrons during long term UV illumination. Such long term detoriation can be the reason for the slight downwards drift of the current in Fig. 2.8 as time goes by. Another possible explanation is an increase in the particle size caused by coalescence [233, 235]. When clusters of quasi-2D morphology (0.1-2.5 ML) grow and become 3D-spherical they lose their non metal properties.

Hitherto, the most prominent and widely studied reaction enhanced by Au nanoparticles is the oxidation of CO [157, 234, 238], although Au/TiO$_2$ composites were also used in the detection of other substances like catechol [239]. CuO/TiO$_2$ composites, functionalized with Au nanoparticles, were used for resistive sensing of flammable gases like ethanol, ozone and hydrogen [240].

Macak et al. [241] made use of Au particles on TiO$_2$ nanotubes as catalyst for electrochemical oxygen reduction. They successfully demonstrated a significant improvement of $\tau_S$ and $S$ in the detection of oxygen in aqueous solutions with Au. The results reported here have shown that our Au/TiO$_2$ systems have the potential for room temperature O$_2$ sensors.

## 2.2 Electroforming in TiO$_2$

Although resistive switching and electroforming in TiO$_2$ have lately attracted much attention, but due to the variability and complexity of the system, not all questions concerning the underlying processes have been answered. In Refs. [51, 66] Waser and coworkers relate the status quo of models and collected data on resistive switching in TiO$_2$ systems with experimental findings of the recent years. The following mechanisms that may be of global or local nature, e.g. of filamentary type, and may possibly appear as a combination, are attributed to resistive switching [53, 73, 77]:

1) the *valence change memory (VCM) effect* denotes mechanisms of electrochemical

type, e.g. diffusion of ions and valence changes in the Ti sublattice;

2) the *thermo chemical memory (TCM) effect*, e.g. thermally induced and assisted formation and rupture of filaments;

3) mechanisms of pure electronic nature;

4) phase transitions, e.g. transitions between the oxygen deficient stoichiometric titanium dioxide $TiO_{2-x}$ and Magnéli phases $Ti_nO_{2n-1}$.

In many reported resistive switches based on titania, mechanism 4) is essential, where the switching is related to reversible insulator-metal transitions (IMT). Above a value of $x \approx 0.001$ for the oxygen deficiency, the material undergoes structural transformations during which the concentration of point defects and their ordering can change dramatically, and a new material of other stoichiometry is formed. Szot et al. [51] describe the formation of different shear planes for increasing $x$ via interaction of shear plane defects. These drastic modifications in the crystal structure are accompanied by just as dramatic changes in the electronic structure, when the band insulator $TiO_2$ ($x \approx 0$) is transformed into the metallic type $Ti_4O_7$. The direct transition from $TiO_2$ to $Ti_4O_7$ is, however, improbable. Instead a stepwise phase change via the homologous series of Magnéli phases (see Fig. 1.6) is thermodynamically more favorable [51]. The transformation towards larger $x$ requires reducing conditions and the ability of oxygen atoms and $V_O$ to migrate [242]. With decreasing O/Ti ratio the diffusion of oxygen increases and likewise does the conductivity of the material in the range of Magnéli phases, as is shown in Fig. 1.7. In the figure it can also be seen, that the conductivity of $Ti_2O_3$, which strictly speaking is not a Magnéli phase ($4 \le n \le 10$), is at least three orders of magnitude lower than that of $Ti_4O_7$. This is the crux for the switching mechanism with large signal margins. From the starting point of maximum conductivity as the ON state, which is $Ti_4O_7$, the material can be switched to the OFF state with orders of magnitude lower conductivity via both further reduction or oxidation.

To transfer the sample from nearly insulating $TiO_2$ into a higher conductive state, e.g. with Magnéli phases, an initialization step is necessary (in contrast to the definition of the term in this work, see section 1.1, this step is often referred to as *electroforming* or *soft-breakdown* [49, 51, 52, 70, 71, 75]), meaning a one-time exposure to highly reducing conditions to produce $V_O$. This can be done with a chemical gradient, i.e. low oxygen partial pressure, and electrical stimuli, i.e. polarization by applying a voltage or a current. It has been shown by means of X-ray analysis that exposure of a $TiO_2$ single crystal surface to very low $p(O_2)$ ($10^{-20}$ mbar) at high temperatures (1200 °C) causes a 'hierarchical transformation' from $TiO_2$ to Magnéli phases with $n$=6-9, where the average $n$ increases with the depth [51]. The transformation can be reversed when the sample is exposed to oxidizing conditions. It is furthermore noted that the surface layer and extended defects that serve as reaction sites play an important role in the oxygen exchange processes. A large surface to volume ratio, like it is given, for example, in our nanowires and on-chip oxidized thin films, facilitates the reduction. Release of large oxygen amounts during additional exposure to an electric field ($10^6$ V/m) was observed as 'bubbles' and blueish coloration [242], suggesting valence changes from $Ti^{4+}$ to $Ti^{3+}$ [51] and thus electrochemical reduction of the material. It was experimentally excluded via

studies in vacuum [75] that interaction with ambient oxygen plays a role for bubble formation. O$^{2-}$ ions in the film drift towards the anode, where they are discharged, thereby evolving O$_2$ gas leading to physical deformation and cracking of the films [75], which is generally a problem. When the oxygen gas is trapped under the film layers and cannot leave the structure because the gas pressure is too small to crack the film, it can also be reincorporated via electrochemical reactions [75] when the polarity is reversed. The important mechanism during electroreduction is that the created V$_O$ accumulate, align to extended defects and form conductive paths inside the bulk. It was found that, due to the smaller bulk part in very small structures (e.g. 4 nm thick layers [75]), the electroreduction step can be eliminated. Another way to avoid the neccessity of this step is to implement conductance channels during fabrication, e.g. by introduction of highly reduced TiO$_{2-x}$ [75]. The local character of electroreduction can differ along the surface regions and an asymmetry is introduced during the process: especially after 'soft' reduction, which means that not all parts of the crystal are transferred into a resistance state of a few Ohms yet, the interface close to the anode dominates the resistance [51]. After 'heavy' electroreduction, during which the resistance can decrease by 13 (!) orders of magnitude, this asymmetry can be observed, for example, as hysteresis, but not before the sample is exposed to oxygen again. This implies that depending on the polarization one electrode/oxide interface, which is less reduced due to remaining oxygen anions, can be dominant in the resistive switching and the other regions are not involved.

The majority of models describe the aggregation of point defects to extended defects, implying effects of type 2) and 4). It was found that resistive switching in TiO$_2$ is often closely related to reversible formation and rupture of conductive Ti$_4$O$_7$ nanofilaments during voltage or current application [50–53]. These filaments can appear as conducting spots in conductive AFM measurements during resistive switching. Choi et al. [52] stated the possibility of formation of very thin filaments by alignment of point defects, which gather together and form even stronger filaments when the material is transferred into the LRS. This is also referred to as *filament multiplication* model. It is assumed that filament forming might be triggered at local defects or protrusions at one TiO$_2$/electrode interface and occurs stepwise: an applied current will be concentrated in a conducting path, formed from gathered point defects. The generated heat enhances motion of more point defects in the vicinity, which form new tiny filaments, in turn creating more heat and more point defects that can fill up the space between the network of tiny filaments. As a result, filaments of larger diameter emerge and can grow fast, connecting cathode and anode (LRS). Finally, when the current reaches a threshold limit and too much heat is generated, the conducting path is ruptured and the device state turns into HRS. In this case the transition from LRS to HRS is marked by an abrupt increase in the resistance at $V_{off}$ while the transition from HRS to LRS can be smoother. Kwon et al. [50] experimentally confirmed forming of Ti$_4$O$_7$ Magnéli phase filaments via HR-TEM combined with in situ I-V measurements during resistive switching.

It was noted however, that resistive switching can also be based on the 'non-conducting' area, meaning the area between the conducting spots, that also has a few times higher conductivity in the HRS. This can be due to non-completed filaments contributing to the leakage current or just by variation of the point defect density in different areas [52]. Choi et al. [52] also stated, that the low area-density of filaments (few tens per µm$^2$)

must mean that in devices of $<100\,\mathrm{nm}$ size the resistive switching necessarily depends on the non-conducting area, yielding smaller signal margins ($\approx 5$) compared to filamentary resistive switching ($\approx 10^3$), which is still sufficient for operation in memory cells. On the other hand, multiple filaments may detoriate the reproducibility of resistive switching [50].
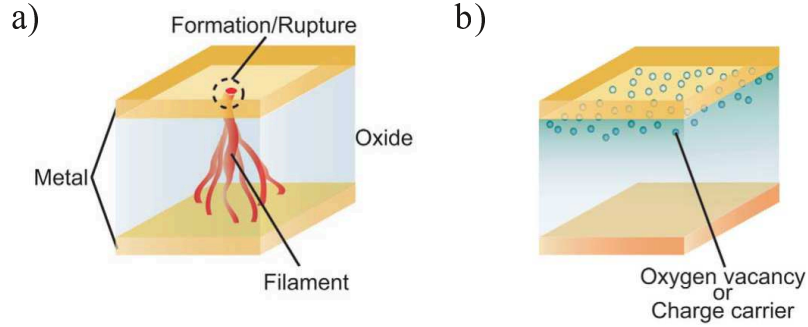


**Figure 2.11:** Scheme of proposed models for resistive switching via a) formation and rupture of highly conducting filaments; and b) changes in an interface-type conducting path. Both figures reprinted from Ref. [53], © (2008) with permission from Elsevier.

Concerning mechanism 3) it was pointed out that a defect density of $10^{19}/\mathrm{cm}^3$, which is $<1\,\%$ of the total ion concentration, is enough to significantly change the resistance of $TiO_2$ [52,70]. Therefore the distribution of vacancies leading to regions of $TiO_2$ and oxygen deficient $TiO_{2-x}$ must play an important role [49]. Now, heavily doped $TiO_2$ with a lot of vacancies [107] typically makes ohmic type contacts with metals, while Schottky-like interfaces form in the case of low doping [75, 156]. (This is, however, not always the case. Recently Lee et al. [243] found seemingly anomalous behavior in $Pt/Nb:SrTiO_3$ cells, where larger $V_O$ concentration underneath the electrode resulted in a higher interface resistance, contrary to this principle.) Two of such metal/oxide interfaces influence the transport and so the current-voltage characteristics of the device. Yang et al. [49,70,75] were able to identify the effects of single interfaces by clever sample design and $V_O$ profile engineering. They found that mainly the location, the distribution and the concentration of $V_O$ control the conductance, the rectification behavior and the switching polarity [49]. More precisely, the blocking interface is dominant for electrical transport. In addition, the switching is heterogeneously localized in conductance channels that form when $V_O$ drift in the electric field along favorable diffusion paths such as grain boundaries [49]. This way, the device is switched ON when a voltage is applied causing the filaments to penetrate the interface barrier and is switched OFF with opposite voltage polarity (*bipolar switch*). Their model can therefore be seen as an expansion of the filament model [see Fig. 2.11 a)] taking changes in the interfaces into account [see Fig. 2.11 b)] and is also referred to as *parallel conduction* model.

Fig. 2.12 shows a diagram of device states describing the possible operations with devices consisting of two metal/oxide junctions in series. The four possible quasi-static 'field configured' [49] states are the forward or reverse rectifier, the shunted rectifier and the head-to-head rectifier. The latter two are characterized by symmetric I-V plots, but

the shunted rectifier typically has a lower resistance. Drift towards or away from an interface depends not only on the voltage polarity, but also on the as-prepared V$_O$ profile, i.e. the distribution of TiO$_2$ (orange) and TiO$_{2-x}$ (yellow) [70]. For example, the forward rectifier can be shunted when a negative voltage (red) is applied to the top electrode. During the transition, the bottom interface remains ohmic, while positively charged V$_O$ are pulled towards the top electrode, changing the top interface from Schottky-type to ohmic. In contrast to shunting and opening, the inverting process needs changes at both interfaces. A direct transition from shunted rectifier to head-to-head rectifier has not been observed so far, for the simple reason that this would mean that V$_O$ drift in two opposite directions simultaneously [49]. Jiang et al. [71] in the same model describe that the voltage amplitudes of both polarities can dictate the initial ON or OFF state and lead to varied switching behavior. For example, a large enough negative voltage on the top electrode can also lead to a depletion of the bottom electrode after the conductive channel has been formed, when the high electric field pulls away V$_O$ from the bottom electrode. This would result in an OFF state after forming and the switching occurring at the bottom electrode.
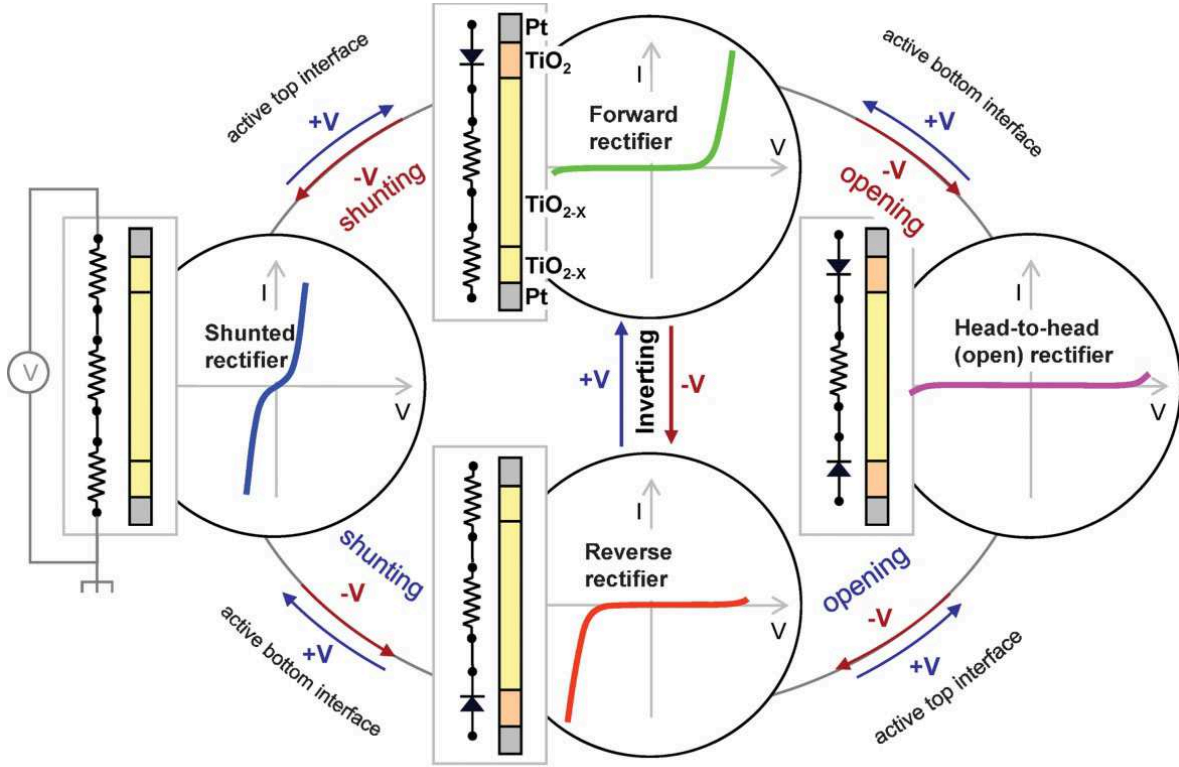


**Figure 2.12:** Device states of two dynamic metal/semiconductor junctions operated in series. V$_O$ drift towards or away from an electrode, depending on the as-fabricated V$_O$ profile in the oxide and on the voltage polarity. Reprinted with permission from Ref. [70], © (2009) Wiley-VCH.

For the interpretation of EF behavior in our micron-scale structures, as they are shown in Fig. 2.1 a), a model was applied in which regions of differing conductivity are redistributed inside TiO$_2$ in response to electric fields. The scheme is sketched in the

insets of Fig. 2.14 and can be understood in terms of both, a single filament or the whole oxide volume. In the supplement to Paper I, additional simulations are presented, confirming that the approach can be extended to a set-up of multiple filaments circuited in parallel and the results are in good agreement with the measurements. Before the EF experiments in Papers I and II were carried out, the samples were initialized by heating to $180\,°C$ in $N_2$ or $N_2/H_2$ to create oxygen vacancies. This process can be understood in terms of 'soft' electroreduction. To create comparable initial conditions a large negative voltage of -30 V was applied to one electrode (Pt in Fig. 2.14 and Paper I) in order to accumulate the generated vacancies at one interface. The sweeping and DC voltage were chosen in such a way that EF would be well observable on the measurement timescales. The main phenomenology of EF in the experiments is that during application of a voltage, smaller than the accumulation voltage but of opposite sign, the conductivity (measured current) increases with time until a maximum is reached, which is interpreted as LRS. In simulations the behavior was replicated by an expansion of the oxygen vacancy rich region of higher conductivity $\sigma_2$ at the expense of the initially larger oxygen vacancy poor region $\sigma_1$. This state can be kept with relatively long retention time. At some point the resistance starts to slightly increase again but at much larger timescales than the initial decrease requires. The reason for this is not yet clear; In our model a finite reservoir of vacancies was assumed to be present after initialization. When this reservoir is gradually being depleted a third phase of lower conductivity $\sigma_3$ than the other phases is assumed to slowly expand into the volume, as is depicted in the inset of Fig. 2.14 b). For details on the measurements, the applied model and simulation parameters the reader is referred to Paper I.

Some of our observations gathered in EF experiments with the micron-scale structures [Fig. 2.1a)] and nanowires [Fig. 2.1b)] indicate that the processes underlying the resistance changes differ in the two types of samples. These differences argue against resistive switching in the nanowires being dominated by highly conducting filaments of large diameter. First of all, the LRS of the nanowires ($10^8 - 10^9\,\Omega$) as it is described above is not as low-resistive as it was observed in the micron-scale samples ($10^5 - 10^6\,\Omega$) and as it was reported for other $TiO_2$ resistive switches (e.g. after heavy electroreduction) [51]. It may be possible that the reduction state is not sufficient to form Magnéli phases on large scales. The initial resistance might be decreased further via reduction in even more reducing conditions, e.g. in UHV, higher temperatures and for longer durations combined with larger electric fields. An increase of the temperature, however, is limited, since the Ti thin films run the risk of being easily thermally oxidized. Consequently, although the same qualitative phenomenology was observed in micron samples and nanowires, they differ significantly in their on/off ratio and also in the timescales needed for EF. While in the micron samples signal margins $R_{HRS}/R_{LRS}$ of $10^2 - 10^3$ are reached after $t_{EF} \approx 1 - 2\,h$ at $3 \times 10^6\,V/m$, a margin of only 10-30 during far more than $10\,h$ at $4 \times 10^7\,V/m$ was reached in the nanowires. It should be noted that the micron samples reach comparable [49, 51, 75] or even larger margins than some reported values for very similar structures [78]. We ascribe this difference to the structural properties resulting from highly different fabrication procedures, e.g. the nanowires have most likely a much higher density and may possibly have a completely different crystal composition than the porous $TiO_2$ fabricated by electrochemical anodization. Yang et al. [70] similarly

observed that larger voltages for EF are required when the sample is downsized to a few tens of nanometers of more resistive oxide, which they attributed to the enhancement of EF by Joule heating due to higher currents in the thicker and more conductive structures.
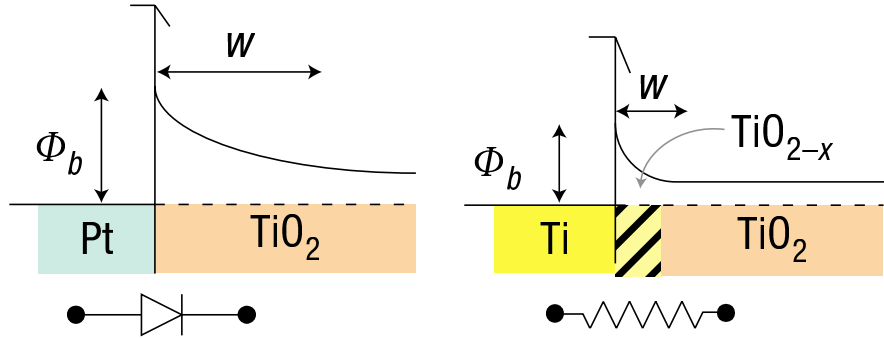


**Figure 2.13:** Energy diagram of the metal electrode / oxide interface. A low V$_O$ concentration maintains the rectifying Schottky barrier between Pt and TiO$_2$ (left), whereas Ti produces a high concentration of V$_O$ at the interface and the Schottky barrier collapses producing ohmic contacts (right). Reprinted by permission from Nature Springer Ref. [49] © (2008) Macmillan Publishers Ltd.

Furthermore, we assume that both metal/oxide interfaces in the Ti/TiO$_2$/Ti nanostructures are less sensitive for changes in the vacancy density. It has been reported that the chemically active Ti reduces TiO$_2$ and produces vacancies that accumulate at the interfaces to TiO$_2$ [49]. As a result of this V$_O$ accumulation, and in addition the lower work function of Ti, the Schottky barrier at both interfaces decreases and so does the electric field when a voltage is applied, causing a much lower V$_O$ drift velocity in the interface region. This is schematically shown in Fig. 2.13. Therefore, the resistance change in the nanowires is presumably bulk-dominated resulting in larger timescales.

Finally, no abrupt changes are observed marking a transition from the LRS towards increasing resistance (without polarization reversion) as it would be expected from rupture of large diameter filaments at metal/TiO$_2$ interfaces [52]: the curves in Fig. 2.14 show how the current first gradually increases upon positive voltage sweeps between 0 and 10 V [Fig. 2.14 a)]. This can be accelerated by sweeping the voltage around higher values without going back to 0 V [Fig. 2.14 b)]. The resistance decreases until a minimum is reached (meeting point of orange and violet curve) from which a much slower resistance increase is registered. Such a smooth inversion of resistance change indicates that the underlying process is rather homogeneous. It should be noted that the 'real' LRS to HRS transition is achieved by applying a negative voltage to Pt in the macro samples, and this transition happens at much shorter timescales. On the basis of these observations the assumption seems probable that in both systems the resistance change is caused by vacancy migration. In the macro samples these may possibly even involve a distribution of a large number of very thin filaments. The microscale processes that determine the observed phenomena during EF are not clear and were not further experimentally pursued in this work. The structures in planar geometry could be suitable for LC-AFM

or STM, as it has been reported for structures of comparable geometries in measurement set-ups of tunable pressure and gas atmosphere [51]. For investigations of this type on the macro samples, the Pt top electrode has to be removed, e.g. by etching [52], or delamination [75] without damaging the interface of interest.
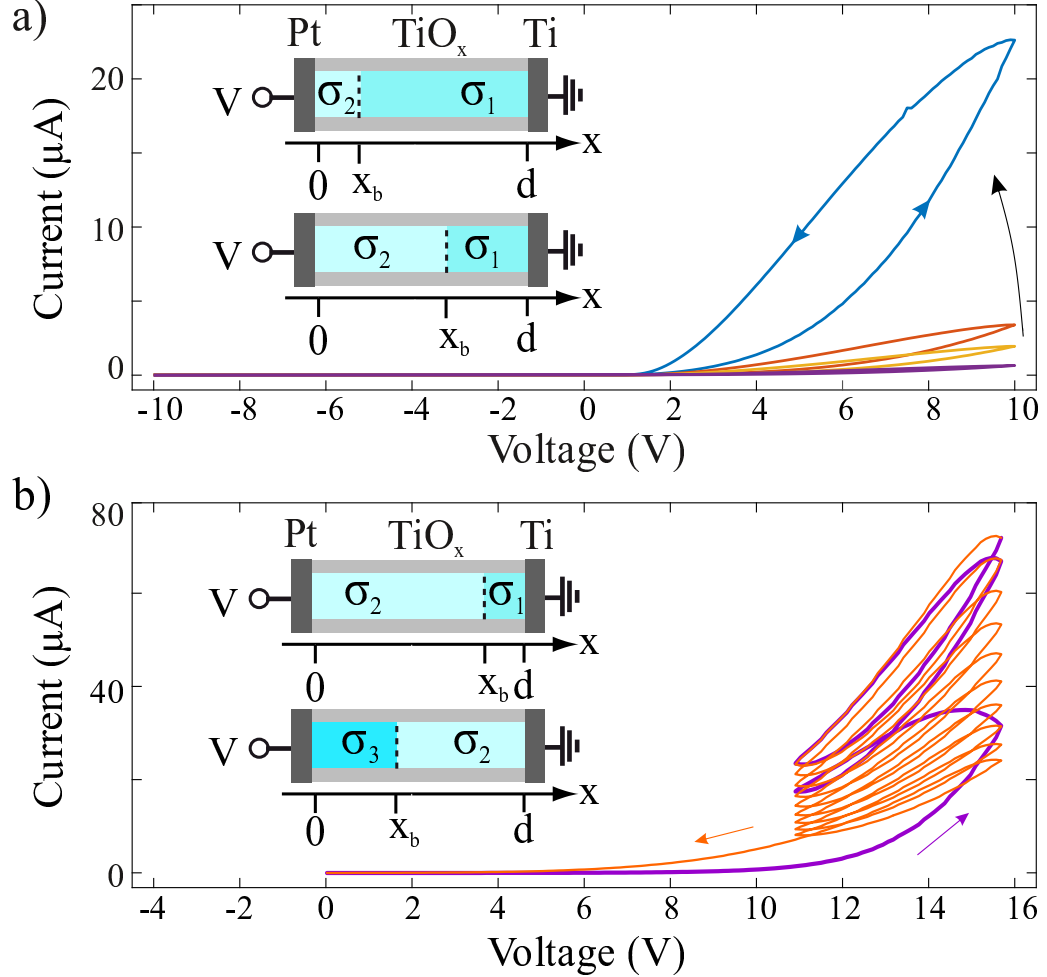


**Figure 2.14:** Electroforming in $Pt/TiO_2/Ti$ structures and interpretation in the picture of moving vacancies (insets, reprinted from Ref. [54], with the permission of AIP Publishing). a) After initialization (generation and accumulation of vacancies at Pt), application of positive voltage sweeps to the Pt leads to an expansion of the vacancy rich, more conductive ($\sigma_2$) region, decreasing the resistance. b) Sweeps around even more positive voltages first lead to a minimum resistance (LRS at full expansion of $\sigma_2$ region), followed by a slower resistance increase as a less conductive $\sigma_3$ area expands.

## 2.3 Electroforming during gas detection

One of the main findings in Paper I is that progression of EF occurs faster when the device is exposed to $H_2$ compared to EF in $N_2$. This acceleration of EF concerns both, the time that is needed to reach the point of current saturation and the smaller current decrease afterwards (blue curve in Fig. 2.15).
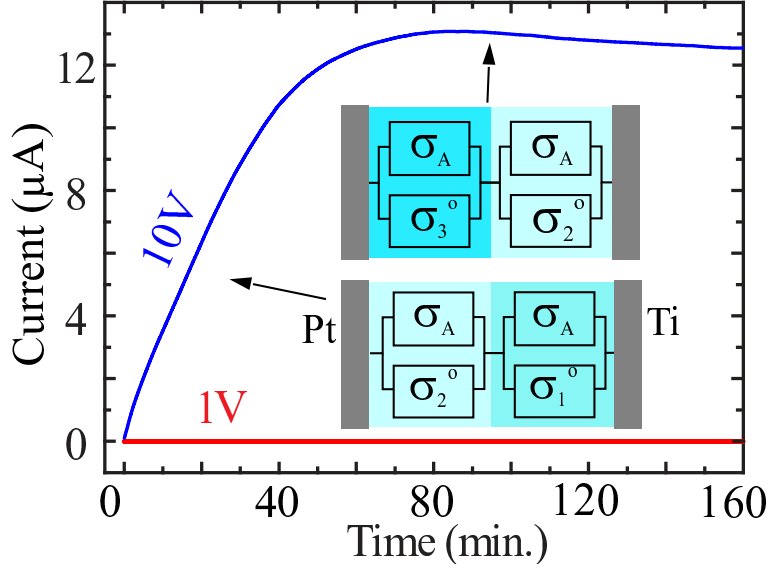


**Figure 2.15:** Applying a high voltage (10 V) to a Pt/TiO$_2$/Ti sandwich structure causes the current to increase with time due to electroforming (blue curve), while with a low voltage applied no changes arise in the current transient at the observed timescale (red curve). In the inset, our model of a single fiber is depicted with a vacancy profile that results in regions of different conductivity. Also shown are the contributions of oxygen vacancies $\sigma_i^O$ and hydrogen doping $\sigma_A$. Figure adapted from Ref. [54].

In addition, an unexpected increase in the resistance is observed when $H_2$ is offered, manifesting itself in two different ways: First, when EF starts and the sample is in a state of increasing conductance and $H_2$ is offered for the first time, which would normally also cause a conductance increase due to OH-doping, surprisingly the combination of EF and $H_2$ causes a reaction with opposing effect on the conductance. With more $H_2$ exposure this effect is at some point compensated and disappears. The second way this effect is constituted is during the regime of EF with slightly increasing resistance, where $H_2$ exposure causes a gradual and irreversible current decrease. The applied model of a single fiber undergoing EF, that was already mentioned in the last section and depicted in the insets of Fig. 2.14 is based on the assumption that the conductivity is affected differently by regions of differing $V_O$ doping level. Now the phenomenology of accelerated EF was reconstructed in simulations assuming that in each phase $i$ the conductivity is the sum of a $V_O$ generated component $\sigma_i^O$ and a phase independent component due to hydrogen doping $\sigma_A$, as it is depicted in the scheme of the fiber in Fig. 2.15. The additional resistance increase during the two different stages of EF was integrated assuming that

$H_2$ decreases the doping density and conductivity of the reduced phase $\sigma_2^O$ while the other phases with less $V_O$ are unaffected. While this model qualitatively reproduced all observations from the experiments, it is not clear by which mechanism hydrogen decreases the doping density. This issue is further discussed in Paper I.

The nanowires investigated in Paper II exhibit striking analogies to the behavior reported in Paper I, although the contacting, geometry and structure of the $TiO_2$ differs significantly from the micron-scale devices. We conclude from this, that incorporation of atomic hydrogen and EF in $TiO_2$ are interdependent in a universal way. For instance, the device size and fabrication are not critical, and the effects are not incidentally limited to devices with a large Schottky barrier at one or at both metal/oxide interfaces.
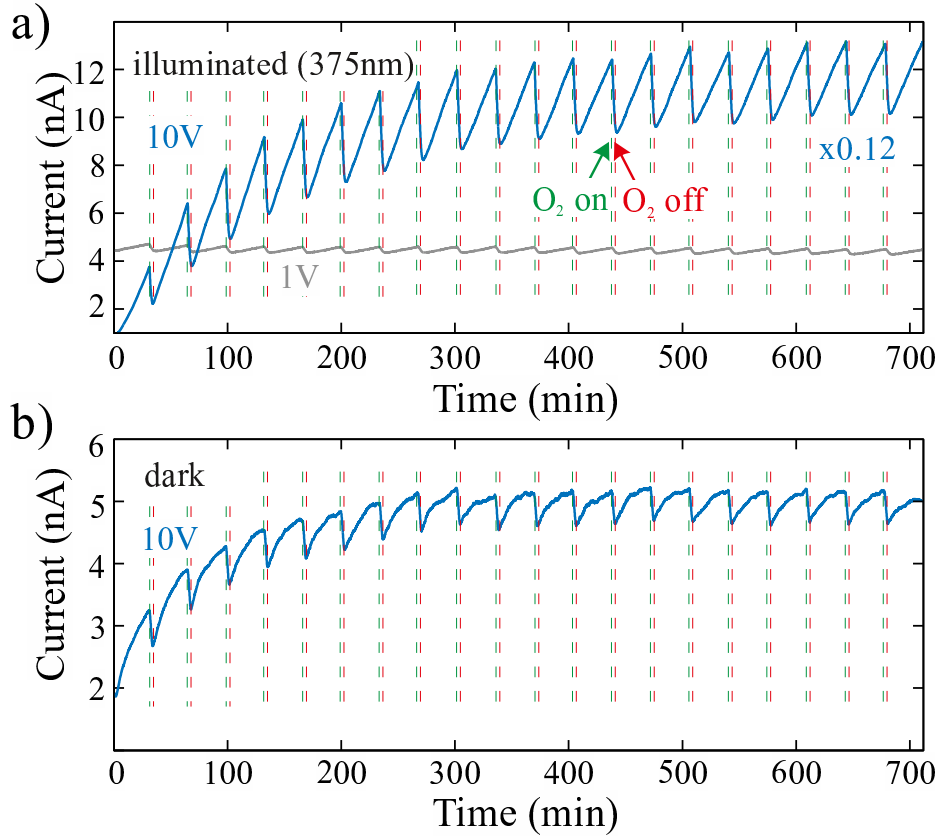


**Figure 2.16:** Current transients of a $TiO_2$ nanowire exposed to pulses of $20\,\%$ $O_2$ in $N_2$ during EF, with the sample a) illuminated with UV light for $1\,V$ and $10\,V$ bias (multiplied with the factor $0.12$ for better visibility) and b) in the dark for $10\,V$ bias. All measurements were carried out at room temperature.

Furthermore, we learn from this that when the devices are operated as sensors for $H_2$ gas, it is advisable to chose operating voltages below the EF threshold. On the one hand, upwards or downwards drifts of the baseline signal are avoided this way, and on the other hand the sensor response is not superimposed and thus degraded with the conductance decreasing effect described above.

Although exposing the samples to high fields and $O_2$ simultaneously turns out as superposition of EF and the usual $O_2$ sensing response without unexpected effects, this

advise of low operation voltage applies also for our $O_2$ sensor element. As discussed in section 2.1.2, irradiation with UV light improves the $O_2$ sensor response significantly. Balancing of the baseline is fast or not even necessary under illumination during pulsed $O_2$ exposure at low voltages. This can be seen in the grey curve in Fig. 2.16 a), especially when compared to Fig. 2.7. In the EF regime the increase in the baseline takes longer to reach saturation during UV illumination than in the dark, as can be seen by comparison of the blue sensing curves in Fig. 2.16 a) and Fig. 2.16 b). This is not surprising, since UV light is known to produce vacancies by increasing the oxygen excorporation rate. For the same reason, the recovery is much faster under illumination when the sample is exposed to $N_2$. This may prolong the EF duration compared to $O_2$ exposure in the dark, where $V_O$ are healed and ion migration eventually ceases.

# Paper I    Interdependence of electroforming and hydrogen incorporation in nanoporous titanium dioxide

## Interdependence of electroforming and hydrogen incorporation in nanoporous titanium dioxide

M. Strungaru,[1,a)] M. Cerchez,[1] S. Herbertz,[1] T. Heinzel,[1,b)] M. El Achhab,[2] and K. Schierbaum[2]

[1]*Solid State Physics Laboratory, Heinrich-Heine-Universität Düsseldorf, 40204 Düsseldorf, Germany*
[2]*Materials Science Laboratory, Heinrich-Heine-Universität Düsseldorf, 40204 Düsseldorf, Germany*

It is shown that in nanoporous titanium dioxide films, sensitivity to atmospheric hydrogen exposure and electroforming can coexist and are interdependent. The devices work as conventional hydrogen sensors below a threshold electric field while above it, the well-known electroforming is observed. Offering hydrogen in this regime accelerates the electroforming process, and in addition to the usual reversible increase of the conductance in response to the hydrogen gas, an irreversible conductance decrease is superimposed. The behavior is interpreted in terms of a phenomenological model where current carrying, oxygen-deficient filaments with hydrogen-dependent conductivities form inside the $TiO_2$ matrix. © *2015 AIP Publishing LLC.* [http://dx.doi.org/10.1063/1.4917034]

## Reference

M. Strungaru, M. Cerchez, S. Herbertz, T. Heinzel, M. El Achhab and K. Schierbaum
Applied Physics Letters **106**, 143109 (2015), ©2015 AIP Publishing LLC
https://doi.org/10.1063/1.4917034

## Copyright statement

## Contributions

I participated in the conductance of the experiments and analysis of the experimental data. I contributed to manuscript writing.

# Interdependence of electroforming and hydrogen incorporation in nanoporous titanium dioxide

M. Strungaru,[1,a)] M. Cerchez,[1] S. Herbertz,[1] T. Heinzel,[1,b)] M. El Achhab,[2] and K. Schierbaum[2]

[1]*Solid State Physics Laboratory, Heinrich-Heine-Universität Düsseldorf, 40204 Düsseldorf, Germany*
[2]*Materials Science Laboratory, Heinrich-Heine-Universität Düsseldorf, 40204 Düsseldorf, Germany*

It is shown that in nanoporous titanium dioxide films, sensitivity to atmospheric hydrogen exposure and electroforming can coexist and are interdependent. The devices work as conventional hydrogen sensors below a threshold electric field while above it, the well-known electroforming is observed. Offering hydrogen in this regime accelerates the electroforming process, and in addition to the usual reversible increase of the conductance in response to the hydrogen gas, an irreversible conductance decrease is superimposed. The behavior is interpreted in terms of a phenomenological model where current carrying, oxygen-deficient filaments with hydrogen-dependent conductivities form inside the $TiO_2$ matrix. © 2015 AIP Publishing LLC. [http://dx.doi.org/10.1063/1.4917034]

Titanium dioxide is one of the most intensely studied metal oxides in present research.[1,2] Two important properties of $TiO_2$ are memristive behavior, also known as electroforming,[3–6] and strong response to exposure of various atmospheric gases.[2,7–9] These effects have so far been studied only independently of each other. An interdependence would not only be of fundamental interest but may also become relevant for applications. For example, electroforming may be one reason for drift effects in gas sensors or the coupling strength of an artificial synapse[10] may be controllable by atmospheric additives. Here, we show that nanoporous titanium dioxide films[11–13] show such an interdependence of hydrogen incorporation and memristive effects.

A commercially available Ti foil (purity 99.6%) is anodically oxidized at room temperature in a solution of 75% $H_2SO_4$ in DI water kept below 30 °C. The oxidation voltage was increased in steps up to 150 V.[14] This produces a nanoporous oxide layer of 5 $\mu$m thickness, composed of a mixture of mostly rutile with a small admixture of anatase.[13] The oxide surface is coated with Pt paste yielding a contact area of 12.5 mm$^2$ area. The surface morphology before and after Pt coating is shown in the inset of Fig. 1(a). The sample is inserted in a measurement chamber with controlled atmosphere and initialized before each measurement sequence by exposing it to dry air for one hour at $T = 180$ °C.[14] Microscopic studies on single crystalline $TiO_2(110)$ surfaces indicate a complicated interplay between surface defects and adsorbed $O_2$.[15] In our system, exposure to $O_2$ heals the point defects partially and leaves the sample in a weakly reduced state, $TiO_{2-\delta}$. Afterwards, a voltage of $V = -30$ V is applied to the Pt electrode with respect to the grounded Ti substrate for 12 h, again in dry air, which causes the drift of oxygen ions ($O^{2-}$) towards the Ti substrate[16] and of the donor-type oxygen vacancies[17] towards the Pt electrode. All subsequent experiments are carried out at room temperature, in the dark and in a nitrogen atmosphere (purity 99.999%), to which

molecular hydrogen gas ($H_2$) is added via a gas flow controller after purging the lines to exclude contamination effects.

The sample initialized this way shows the typical response to atmospheric $H_2$[7,11,12,18] as well as electroforming, as illustrated in Fig. 1. Current-voltage ($IV$)-loops from $V = -10$ V to 10 V and back are hysteretic, see Fig. 1(a), indicating electroforming.[19,20] The absence of a hysteresis for negative voltages is due to the $Pt/TiO_{2-\delta}$ Schottky barrier under reverse bias, which decreases the electric field in the bulk. According to the widely used model for electroforming in comparable systems,[5,6] filaments which predominantly carry the current form inside a $TiO_2$ matrix. They are composed of a phase 1 of low conductivity $\sigma_1$ (smaller $\delta$), in series with a phase 2 with $\sigma_2 > \sigma_1$ (larger $\delta$),[3] see the inset in
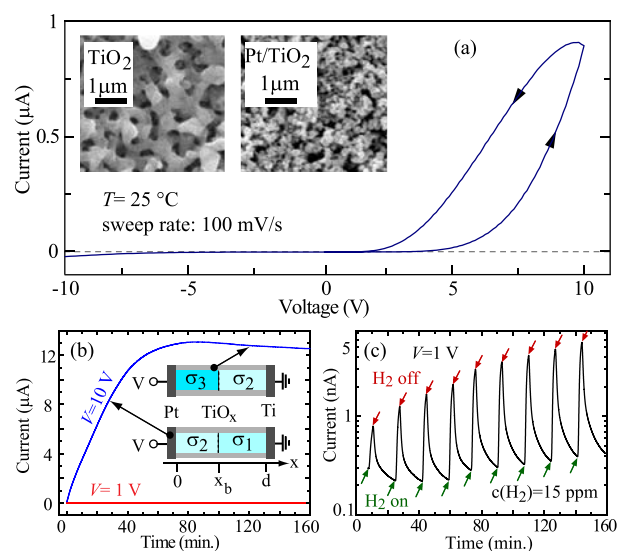


FIG. 1. (a) $IV$-measurement for a voltage loop in $N_2$ atmosphere. The sweep direction is indicated by the arrows. Inset: scanning electron microscope images of the sample surface before (left) and after (right) coating with Pt. (b) Time dependence of $I$ at different voltages. Inset: sample geometry within the single filament model. Phases 1 to 3 are sketched before and after $I_{max}$ has been reached. (c) Current transients in response to $H_2$-pulses in $N_2$ atmosphere for $V = 1$ V.

a)Present address: Faculty of Physics and CARPATH, Alexandru Ioan Cuza University, Blvd. Carol I, 11, 700506 Iasi, Romania.
b)thomas.heinzel@hhu.de

Fig. 1(b). After the *IV* loop, the phase boundary, located at $x_b$, thus resides close to the Pt electrode, and the sample has a low conductance. Afterwards, we apply positive voltages, such that the Schottky barrier is open and electroforming causes a current *I* that increases with time *t*, see Fig. 1(b). *I* is approximately constant for $V < 2$ V, corresponding to electric fields $\varepsilon < 4 \times 10^5$ V/m, for which electroforming is negligible. For $V = 10$ V, $I(t)$ increases by two orders of magnitude as time proceeds. A maximum ($I_{max}$) is reached after 20–90 min, depending on the sweep, followed by a slight decrease. Pulsed measurements have been used to exclude Joule heating as a possible origin.[14] While the shape of $I(t)$ is reproducible, its amplitude varies up to a factor of 100. This indicates that a few filaments with distributed properties like their cross sectional area or $x_b$ are formed under identical external conditions. Within our model system composed of just one filament, the increase of $I(t)$ is caused by the expansion of phase 2 at the expense of phase 1. Saturation is reached for $x_b = d$. As the $O^{2-}$ ions keep drifting towards the Pt electrode, phase 3 (small $\delta$) with a low conductivity $\sigma_3 < \sigma_2$ is formed close to $x = 0$. This phase grows in *x*-direction with time and causes the current to decrease.[14]

Below the threshold voltage, the current also responds to $H_2$ as reported previously for similar structures,[11,12,21] with a detection threshold of hydrogen volume fractions $c(H_2)$ $< 15$ ppm, see Fig. 1(c). Regarding the sensing mechanism, it has been established that $H_2$ splits catalytically at the Pt film, the H atoms diffuse into the $TiO_{2-\delta}$,[12,22,23] form O-H groups with the oxygen of the host crystal[24,25] (interstitial hydrogen) in the bulk or at the surface, and act as donors.[26–28] Adsorption at the surfaces of the $TiO_2$ pores may play a role as well,[29] where atomic hydrogen tends to rest preferentially at the top of bridging oxygen atoms.[30] However, the diffusion of hydrogen atoms into the subsurface is significant,[23] and hydrogen diffuses extremely well into the bulk along the c-axis in rutile.[31] The time constant of the approximately exponential response of $I(t)$ is 2 min for $c(H_2) = 15$ ppm and decreases rapidly as $c(H_2)$ is increased. The sensing is mostly reversible, except a slowly increasing current background, which we attribute to incomplete hydrogen removal.

In Figs. 2(a) and 2(b), the response of $I(t)$ to $H_2$ pulses of 3 min duration is shown for $V = 10$ V in the interval where electroforming increases the conductance. In response to the first hydrogen pulse, offered at $t = 1$ min, $I(t)$ first *decreases* and then begins to increase. The decrease, which is absent for voltages below the electroforming threshold, can be larger than one order of magnitude. For $c(H_2) < 100$ ppm, it dominates the overall behavior and the conventional sensing response is not observed. Only for $c(H_2) \geq 100$ ppm, a current peak starts to develop shortly after the decrease. The negative response gets faster as $c(H_2)$ is increased, while its amplitude shows no clear correlation with $c(H_2)$ and fluctuates among $I(t)$ traces under nominally identical conditions (not shown). Afterwards, the sample responds to hydrogen in the usual way[11,12,21] in this time interval. Furthermore, for $c(H_2) \leq 30$ ppm, hydrogen sensing and electroforming appear approximately as a superposition, while for larger hydrogen volume fractions, no further increase of $I(t)$ due to electroforming can be observed after the
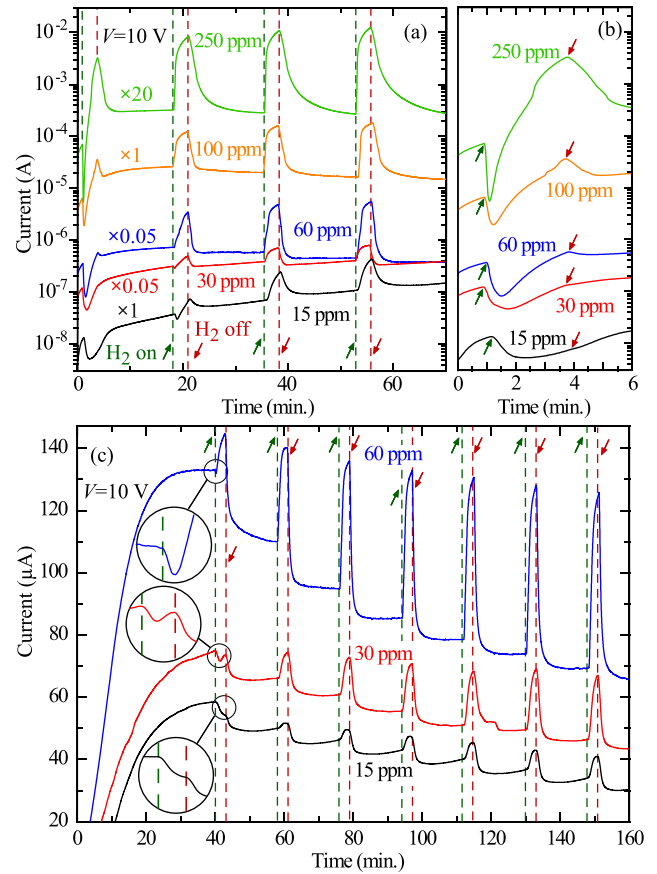


FIG. 2. (a) $I(t)$ for $H_2$ pulses of different volume fractions. Some traces have been scaled by factors as indicated to avoid overlaps. The times where hydrogen was turned on (off) is marked by the dashed lines and the upwards (downwards) pointing arrows. (b) Zoom-in of $I(t)$ shown in (a) for the first six minutes. (c) Response to $H_2$ pulses close to and after current saturation. The traces for 15 ppm and 30 ppm have been offset by $-20\,\mu A$ and $-10\,\mu A$, respectively.

first two hydrogen pulses. This suggests that exposure to hydrogen accelerates the electroforming.

We proceed by studying the response of $I(t)$ to $H_2$ after $I_{max}$ has been reached, i.e., when phase 1 has disappeared. Again, an initial decrease of $I(t)$ in response to the first $H_2$ pulse is observed, which can be very strong[14] and vanishes rapidly under subsequent $H_2$ pulses. In addition to the increase of $I(t)$ in response to the $H_2$ pulse, a simultaneous process is active that decreases $I(t)$ continuously in the presence of hydrogen.[14] This manifests itself in plateaus of $I(t)$ in between the $H_2$ pulses that form steps towards a smaller current as time proceeds. While the positive response of $I(t)$ is essentially reversible, its accelerated decrease is irreversible but can be reset by our initialization procedure.

This interdependence of hydrogen sensing and electroforming is interpreted in terms of an *ad hoc*-extension of the single filament model.[3] In each phase j, the conductivity $\sigma_j(t)$ is assumed to be the sum of an oxygen vacancy—generated component $\sigma_j^o$ and a phase-independent component $\sigma_A(t) = \sigma_A$ $(c(H_2)) \times [1 - e^{-t/\tau_A}]$ due to hydrogen doping (mechanism A), see the insets in Figs. 3(a) and 3(d). The doping therefore tends to homogenize $\varepsilon(x)$ along the filament, leading to an increase of $\varepsilon_2$, the electric field in phase 2. Since the velocity $v_b(t)$ of $x_b(t)$ is determined by $\varepsilon_2$, hydrogen doping accelerates
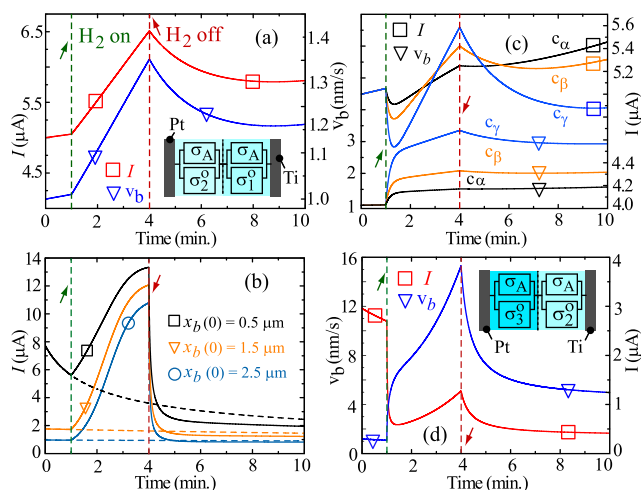
FIG. 3. (a) Simulation of $I(t)$ and $v_b(t)$ in a filament before $I(t)$ has reached $I_{max}$ (see the inset for the equivalent circuit), in response to $H_2$ exposure of volume fraction $c_\gamma$. (b) Simulation of $I(t)$ and $x_b(t)$ as in (a) after $I_{max}$ has been reached, shown with (full lines) and without (dashed lines) hydrogen exposure. (c) Simulation as in (a) for hydrogen concentrations $c_\alpha < c_\beta < c_\gamma$, with mechanism B included. (d) Simulation of $I(t)$ and $v_b(t)$ as in (b) with mechanism B included. The inset shows the equivalent circuit used in (b) and (d). The remaining simulation parameters are given in Ref. 32.

$x_b(t)$. Before $I_{max}$ is reached, the hydrogen doping accelerates the expansion of phase 2 and with it the increase of $I(t)$. After $I_{max}$ has been reached, the doping accelerates the diminution of phase 2, which gets replaced by the less conductive phase 3. This process is readily incorporated in the single filament model.[3,14] In the simulations, a filament of $5\,\mu m$ length and an oxygen vacancy drift mobility of $\mu(V_O) = 10^{-15}\,m^2/(Vs)$ are used. In Fig. 3(a), the result of such a calculation is shown for a $H_2$-induced exponential increase of $\sigma_1(t)$ and $\sigma_2(t)$, with $\tau_A$ set to $200\,s$. Both $I(t)$ and $v_b(t)$ increase during the hydrogen pulse, and $I(t)$ shows good qualitative agreement with the measured phenomenology. Likewise, $I(t)$ can be modeled after $I_{max}$ has been reached, see Fig. 3(b). Here, after a $H_2$ pulse has finished, $I(t)$ has dropped below the value it would have reached without hydrogen exposure, and this difference decreases as phase 3 spreads out and $x_b$ approaches the Ti substrate.

In order to integrate the additional, initial decrease of $I(t)$ in response to $H_2$ exposure, we postulate a co-existing mechanism by which atomic hydrogen decreases the conductivity (mechanism B). A decrease of $\sigma_1$ and $\sigma_3$, i.e., of phases composed of weakly reduced $TiO_2$, in response $H_2$ exposure has not been observed up to now and is not to be expected, considering that interstitial hydrogen acts as donor.[25–28] We therefore assign mechanism B to the strongly reduced phase 2. A microstructural explanation of mechanism B could be related to the work of Filippone *et al.*,[24] who suggested that a H atom may form a complex with an oxygen vacancy, with the effect of localizing one of its two delocalized electrons. The effect would be a decrease of the electron density in the conduction band. Furthermore, since the binding energy of such a hydrogen-oxygen vacancy complex has been calculated to be $0.49\,eV$ larger than that one of the oxygen vacancy,[24] this configuration is expected to be stable, in agreement with the observed irreversibility. Figs. 3(c) and 3(d) show that the effects of mechanism B on $I(t)$ can be reproduced as well within the single filament model. Here, it is assumed that due

to mechanism B, only $\sigma_2^o$ develops a dependence on $c(H_2)$ and experiences a nonrecurring exponential decrease according to $\sigma_2^o(t) = \sigma_{2,B}^o(c(H_2)) + [\sigma_2^o - \sigma_{2,B}^o]e^{-t/\tau_B}$ with time constant $\tau_B = 10\,s$, while $\sigma_1$ and $\sigma_3$ remain unaffected. Different hydrogen concentrations are modeled by different final conductivities for all phases.[32]

As hydrogen is offered, an initial decrease of $I$ is obtained which correlates with an acceleration of $x_b$ due to the additional increase of $\varepsilon_2$. A subsequent increase of $I$ shows that mechanism A starts to dominate again. Here, $v_b$ is larger than before the hydrogen pulse because of the increase of $\varepsilon_2$. After hydrogen is turned off before $I(t)$ has reached $I_{max}$, the current increases more slowly due to the growth of phase 2 or, depending on the hydrogen volume fraction, decreases, in qualitative agreement with the experimental studies, see Fig. 2(c). After $I(t)$ has passed $I_{max}$, the accelerated expansion of phase 3 during $H_2$ exposure causes $I(t)$ to decrease below the value it would have reached if hydrogen were absent, see Fig. 2(d).

It has been recently established that electroforming leads to a transformation of $TiO_2$ into the $Ti_4O_7$ Magnéli phase inside filaments,[5] which can be thought of as a local recrystallization of reduced $TiO_{2-\delta}$. We therefore conclude by stressing that the observed behavior is also consistent with the formation of Magnéli phases $Ti_nO_{2n-1}$ with integer n. Let us assume that phase 2 is composed of $Ti_4O_7$. Since it is well established that $\sigma(Ti_4O_7) \approx 10^3\sigma(TiO_2)$,[6,33] it will have a larger conductivity than phase 1. Offering hydrogen may reduce $Ti_4O_7$ further, i.e., to n = 2 or 3, with smaller conductivities than $Ti_4O_7$,[6,33] which would be an alternative explanation for mechanism B.

To summarize, the coexistence and interdependence of electroforming and hydrogen incorporation in titanium dioxide films have been demonstrated. Atmospheric hydrogen accelerates the electroforming via doping and a corresponding redistribution of the electric fields among the phases characterized by different oxygen deficiencies. In addition, a rapidly decreasing, nonrecurring and irreversible current component in response to hydrogen is observed. It is tentatively attributed to hydrogen-oxygen vacancy complexes, but can also be understood within a picture based on Magnéli phases. The measurements can be reproduced qualitatively by simulations based on the filament model. It is a task for the future to study the microscopic origin of these effects, their interplay with other atmospheric gases like, e.g., oxygen, which is known to be nontrivial even below the electroforming threshold,[34] as well as the role of the pore surfaces vs. that one of the bulk material.

[1]U. Diebold, Surf. Sci. Rep. **48**, 53 (2003).

[2]X. Chen and S. S. Mao, Chem. Rev. **107**, 2891 (2007).

[3]D. B. Strukov, G. S. Snider, D. R. Stewart, and R. S. Williams, Nature **453**, 80 (2008).

[4]J. J. Yang, M. D. Pickett, X. Li, D. A. A. Ohlberg, D. R. Stewart, and R. S. Williams, Nat. Nanotechnol. **3**, 429 (2008).

[5]D.-H. Kwon, K. M. Kim, J. H. Jang, M. M. Jeon, M. H. Lee, G. H. Kim, X.-S. Li, G.-S. Park, B. Lee, S. Han, M. Kim, and C. S. Hwang, Nat. Nanotechnol. **5**, 148 (2010).

[6]K. Szot, M. Rogala, W. Speier, Z. Klusek, A. Beshehm, and R. Waser, Nanotechnology **22**, 254001 (2011).

[7]N. Yamamoto, S. Tonomura, T. Matsuoka, and H. Tsubomura, Surf. Sci. **92**, 400 (1980).

[8]S. A. Akbar and L. B. Younkman, J. Electrochem. Soc. **144**, 1750 (1997).

[9]D. H. Kim, Y.-S. Shim, H. G. Moon, H. J. Chang, D. Su, S. Y. Kim, J.-S. Kim, B. K. Ju, S.-J. Yoon, and H. W. Jang, J. Phys. Chem. C **117**, 17824 (2013).

[10]M. D. Pickett, G. Medeiros-Ribeiro, and R. S. Williams, Nat. Mater. **12**, 114 (2013).

[11]O. K. Varghese, D. Gong, M. Paulose, K. G. Ong, and C. A. Grimes, Sens. Actuators, B **93**, 338 (2003).

[12]M. Paulose, O. K. Varghese, G. K. Mor, C. A. Grimes, and K. G. Ong, Nanotechnology **17**, 398 (2006).

[13]M. El-Achhab, A. Erbe, G. Koschek, R. Hamouich, and K. Schierbaum, Appl. Phys. A **116**, 2039 (2014).

[14]See supplemental material at http://dx.doi.org/10.1063/1.4917034 for details.

[15]S. Wendt, R. Schaub, J. Matthiesen, E. Vestergaard, E. Wahlström, M. Rasmussen, P. Thostrup, L. Molina, E. Laegsgaard, I. Stensgaard, B. Hammer, and F. Besenbacher, Surf. Sci. **598**, 226 (2005).

[16]J. J. Yang, F. Miao, M. D. Pickett, D. A. A. Ohlberg, D. R. Stewart, C. N. Lau, and R. S. Williams, Nanotechnology **20**, 215201 (2009).

[17]P. Knauth and H. L. Tuller, J. Appl. Phys. **85**, 897 (1999).

[18]L. A. Harris, J. Electrochem. Soc. **127**, 2657 (1980).

[19]S. Lee, J. S. Lee, J.-B. Park, Y. K. Kyoung, M.-J. Lee, and T. W. Noh, APL Mater. **2**, 066103 (2014).

[20]R. Münstermann, T. Menke, R. Dittmann, and R. Waser, Adv. Mater. **22**, 4819 (2010).

[21]M. Cerchez, H. Langer, M. E. Achhab, T. Heinzel, D. Ostermann, H. Lüder, and D. Ostermann, Appl. Phys. Lett. **103**, 033522 (2013).

[22]U. Roland, T. Braunschweig, and F. Roessner, J. Mol. Catal. A: Chem. **127**, 61 (1997).

[23]U. Aschauer and A. Selloni, Phys. Chem. Chem. Phys. **14**, 16595 (2012).

[24]F. Filippone, G. Mattioli, P. Alippi, and A. A. Bonapasta, Phys. Rev. B **80**, 245203 (2009).

[25]T. Bjørheim, S. Stølen, and T. Norby, Phys. Chem. Chem. Phys. **12**, 6817 (2010).

[26]D. A. Panayotov and J. T. Yates, Chem. Phys. Lett. **436**, 204 (2007).

[27]P. W. Peacock and J. Robertson, Appl. Phys. Lett. **83**, 2025 (2003).

[28]F. Herklotz, E. V. Lavrov, and J. Weber, Phys. Rev. B **83**, 235202 (2011).

[29]P. Kowalski, B. Meyer, and D. Marx, Phys. Rev. B **79**, 115410 (2009).

[30]M. Islam, M. Calatayud, and G. Pachioni, J. Phys. Chem. C **115**, 6809 (2011).

[31]J. B. Bates, J. C. Wang, and R. A. Robertson, Phys. Rev. B **19**, 4130 (1979).

[32]For (a), $\tau_A$ is also the recovery time after $H_2$ is turned off. In Figs. 3(b) and 3(d), $\tau_A = 50$ s was used. We chose $\sigma_1^o = 3.5 \times 10^{-12}$ Sm, $\sigma_2^o = 6 \times 10^{-12}$ Sm, $\sigma_3^o = 10^{-13}$ Sm, $\sigma_A(c_\alpha) = 2.0 \times 10^{-12}$ Sm, $\sigma_A(c_\beta) = 2.2 \times 10^{-12}$ Sm, $\sigma_A(c_\gamma) = 2.6 \times 10^{-12}$ Sm, $\sigma_{2,B}^o(c_\alpha) = 4.7 \times 10^{-12}$ Sm, $\sigma_{2,B}^o(c_\beta) = 4.2 \times 10^{-12}$ Sm, and $\sigma_{2,B}^o(c_\gamma) = 4.1 \times 10^{-12}$ Sm.

[33]R. F. Bartholomew and D. R. Frankl, Phys. Rev. **187**, 828 (1969).

[34]Ö. Cakabay, M. ElAchhab, and K. Schierbaum, Appl. Phys. A **118**, 1127 (2015).

# Interdependence of electroforming and hydrogen incorporation in nanoporous titanium dioxide

M. Strungaru[a], M. Cerchez, S. Herbertz, and T. Heinzel[†]

*Solid State Physics Laboratory, Heinrich-Heine-Universität*

*Düsseldorf, 40204 Düsseldorf, Germany*

M. El Achhab and K. Schierbaum

*Materials Science Laboratory, Heinrich-Heine-Universität*

*Düsseldorf, 40204 Düsseldorf, Germany*

(Dated: March 2, 2015)

## Abstract

This supplement provides further measurements and additional simulations for long hydrogen exposure times and for a multi-filament system. Also, the preparation and initialization procedures of the samples are motivated.

PACS numbers: 07.07.Df, 73.50.-h, 81.05.Rm

---

[a] Present address: Alexandru Ioan Cuza University, CARPATH, Faculty of Physics, Blvd. Carol I, 11, 700506, Iasi, Romania

[†] thomas.heinzel@hhu.de

1. Choice of the oxidation voltage and of the initialization procedure

The oxidation voltage determines both the thickness of the film and the anatase/rutile composition ratio. The combination of sensing and electroforming experiments require sufficiently thin films in order to be able to measure a current and apply electric fields above the electroforming threshold, which sets an upper limit of the oxidation voltage of $\approx 170V$. On the other hand, the films grown at voltages of 120 V or below break down before the threshold electric field is reached. Thus, we have chosen fabrication parameters that result in samples that present both strong hydrogen detection signals and electroforming.

The initial treatment of the material in $180°\,$C in dry air has the purpose to remove hydrogen and heal the oxygen vacancies produced by the hydrogen. The temperature is chosen sufficiently low such that it does not influence the crystal structure, but sufficiently high to accelerate the reoxidation process. After heating in dry air, the sample is cooled to $25°\,$C, and the negative voltage of -30V is applied. This value was chosen in order to drive the bulk material above the electroforming threshold. The absolute value of this voltage is larger than that one used in forward direction (+10 V), since a fraction of the reverse voltage drops across the reversely biased Schottky barrier.

2. Irrelevance of Joule heating for the increase of the current with time

Joule heating can be an important ingredient of the formation of conductive channels by increasing the mobility of oxygen vacancies. However, the current increase shown in Figs. 1(b) and 2 is primarily due to the migration of vacancies. If the increase in the current were due to Joule heating, it should evolve in a reproducible way under subsequent voltage pulses with a sufficiently long waiting time in between. In Fig. S 1(a) we show the current as a function of time during an alternating sequence of 10V/0V applied to the sample (after being initialized as presented in the paper), on a time scale of 6 hours. A persistent change of the conductance is observed, even for waiting times of 40 min. in between the voltage pulses. This is also reflected in the IV traces taken before and after the electroforming (Fig. S 1 (b)), indicating also that

the conductivity of the sample is permanently increased, thus excluding Joule heating as possible reason.
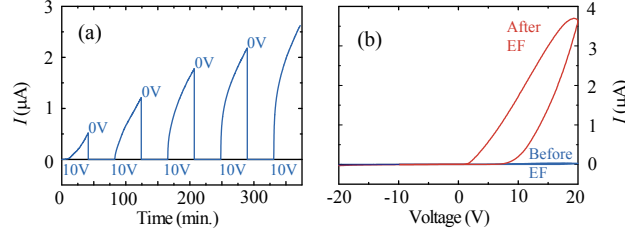


FIG. S 1. (Color online). (a) Response of the current to a sequence of voltage pulses, indicating the persistent changes in conductance with an applied voltage. (b) Current-voltage characteristics before and after electroforming (EF).

3. Additional measurements and simulations

In Fig. S2 (a), an example of a strong negative response of the current to atmospheric hydrogen is observed. Such dramatic collapses of $I(t)$ are only observed close to $I_{max}$. Within the single filament model, this reflects the dominance of phase 2 for the conductance, which fills the whole filament close to $I(t) = I_{max}$.
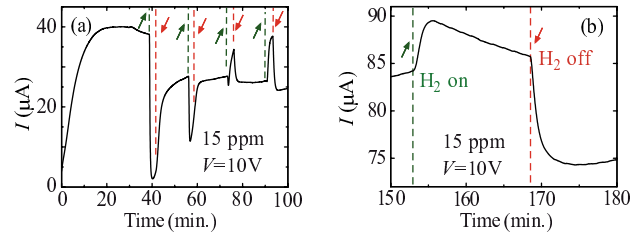


FIG. S 2. (Color online). (a) Example of a strong negative response to $H_2$ close to the maximum of $I(t)$. (b) Time dependence of the current during a hydrogen pulse of 15 min. duration, applied well after $I(t)$ has reached its maximum.

Fig. S 2 (b) shows the evolution of the current after $I_{max}$ has passed during a hydrogen pulse of 15 min. duration. After the initial increase of the current, it decreases continuously as long as hydrogen is offered. Within the single filament model, this corresponds to the accelerated motion of the boundary between phases 2 and 3, and is qualitatively well reproduced by a corresponding simulation, see Fig. S 3 (a), carried

3

out with the same parameters as the ones used in the paper.
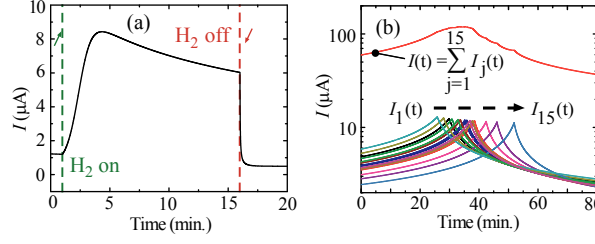


FIG. S 3. (Color online). (a) Simulation of $I(t)$ in the decreasing interval with hydrogen left on for 15 min., corresponding to the measurement shown in Fig. 2 (b). (b) Simulated evolution of $I(t)$ over the full measurement for an ensemble of 15 filaments with a Gaussian distribution of their cross sections. The contributions of the individual filaments labelled by $j$ to the total current are shown as well.

In Fig. S 3 (b), we show the current as a function of the applied voltage for a number of 15 filaments with gaussian distributed conductivities, in a simplified simulation of the effect of the presence of more than one conductive channel, of different cross-sections. The mean values of the distributions for the three phases are $\sigma_1^0$, $\sigma_2^0$ and $\sigma_3^0$ as given in the paper. The width of the distribution was taken 0.3 times the mean value of the distribution, for each phase. The picture indicates that even a few filaments can considerably smear out the sharp variation of the current simulated for the case of a single filament. Better agreement of such simulations with the experimental traces can be achieved by introducing further parameters like a stronger representation of thinner filaments, or a waiting time between the vanishing of phase 1 and the formation of phase 3, which has been set to zero here.

4

# Paper II    On-chip planar hydrogen sensor with sub-micrometer spatial resolution

On-chip planar hydrogen sensor with sub-micrometer spatial resolution

S. Herbertz, M. Cerchez, T. Heinzel*

*Solid State Physics Laboratory, Heinrich-Heine-Universität Düsseldorf, 40204 Düsseldorf, Germany*

**A B S T R A C T**

We present an on-chip thin film device with a planar geometry suited for electronic detection of atmospheric hydrogen with a spatial resolution well below $1\,\mu m$. A titanium stripe of a few nanometers thickness is defined on an insulating substrate and separated into two metallically disconnected electrodes by oxidizing it locally to titanium dioxide with the tip of an atomic force microscope. The titanium dioxide line forms the active area. It is sensitized by a platinum sputtering step such that the two Ti electrodes remain disconnected. It is shown that electroformation processes can interfere with the sensing response above a threshold bias voltage, and the influences of oxygen gas as well as water vapor on the sensing are discussed.

© 2015 Elsevier B.V. All rights reserved.

## Reference

S. Herbertz, M. Cerchez and T. Heinzel
Sensors and Actuators B **221**, 401-405 (2015) ©2015 Elsevier
`https://doi.org/10.1016/j.snb.2015.06.113`

## Copyright statement

## Contributions

I designed and prepared the samples, conducted the experiments and analyzed the experimental data. I wrote the main body of the manuscript.

Contents lists available at ScienceDirect

# Sensors and Actuators B: Chemical

# On-chip planar hydrogen sensor with sub-micrometer spatial resolution

S. Herbertz, M. Cerchez, T. Heinzel *

*Solid State Physics Laboratory, Heinrich-Heine-Universität Düsseldorf, 40204 Düsseldorf, Germany*

A B S T R A C T

We present an on-chip thin film device with a planar geometry suited for electronic detection of atmospheric hydrogen with a spatial resolution well below $1\,\mu m$. A titanium stripe of a few nanometers thickness is defined on an insulating substrate and separated into two metallically disconnected electrodes by oxidizing it locally to titanium dioxide with the tip of an atomic force microscope. The titanium dioxide line forms the active area. It is sensitized by a platinum sputtering step such that the two Ti electrodes remain disconnected. It is shown that electroformation processes can interfere with the sensing response above a threshold bias voltage, and the influences of oxygen gas as well as water vapor on the sensing are discussed.

© 2015 Elsevier B.V. All rights reserved.

## 1. Introduction

Sensing of hydrogen gas [1] has become increasingly relevant over the past two decades due to rapidly evolving hydrogen-related technologies like fuel cells [2], energy storage [3], automotive mobility [4], or anaerobic digestion in biotechnology [5]. Hydrogen detection with high spatial resolution is desirable for analyzing hydrogen-induced embrittlement of materials [6], in particular steels [7], as well as for hydrogen-based leak detection [1]. A spatial resolution of 10 nm in one direction is possible by proton recoil detection [8]. High lateral resolution in two dimensions in the range of 100 nm has been demonstrated with $\gamma$-radiography based on tritium [9] and by hydrogen – microcontact printing [10], both of which require coating of the sample with a suitable resist. Local Kelvin-probe techniques have been used to detect hydrogen with a spatial resolution of $1\,\mu m$ [11]. Also a concept based on percolation transport through Pd cluster arrays with a resolution of $100\,\mu m$ has been demonstrated [12,13].

Here, we present a hydrogen detector that combines sub-micrometer spatial resolution with the high sensitivity of the Pt/TiO$_2$-system [14–16], and with the possibility of on-chip implementation by established lithographic techniques.

## 2. Material and methods

### 2.1. Sensor design and preparation

The sample layout is sketched in the insets of Fig. 1. A Ti stripe of $8\,\mu m$ width and 10 nm thickness is deposited on a Si/SiO$_2$ substrate by optical lithography, followed by metallization and a lift-off step. The SiO$_2$ layer has a thickness of 100 nm and is highly insulating. The Ti stripe shows a surface roughness of $\approx 2$ nm. The sample is mounted into a chip carrier and the Ti stripe is electrically accessed by gold wires attached to its ends. A linear current–voltage (IV) characteristics that appears as almost vertical line in Fig. 1 is measured. The stripe has a conductance of $1.5 \times 10^6\,\Omega^{-1}$ in good agreement with the literature value of the conductivity for Ti, $\sigma_{Ti} = 2.38 \times 10^6\,(\Omega m)^{-1}$, see [17]. Afterwards, the stripe is locally oxidized by scanning probe lithography [18]. During this step, the conductive tip of an atomic force microscope is biased by a voltage of $-15$ V with respect to the grounded Ti stripe, while being scanned in the transverse direction with a velocity of $10\,\mu m/s$ across the stripe. In our setup, the electrolyte is formed by the ambient water film on top of the sample, the thickness of which ($\approx 10$ nm) is controlled by the relative humidity, adjusted to 40%. The oxide line is $\approx 2$ nm higher than the Ti film and has a comparable roughness. Its width is 450 nm under these conditions, see the upper inset of Fig. 1, while we have prepared oxide lines of widths down to 200 nm by decreasing the tip voltage, or by increasing the scanning velocity of the tip. We note that partial oxidation of metals for on-chip sensing applications has been reported already by Archanjo et al. [19]. After the oxidation is completed, the IV characteristics between the two electrodes is nonlinear and for an applied voltage of $V = 1$ V, the

* Corresponding author.
  *E-mail address:* thomas.heinzel@hhu.de (T. Heinzel).
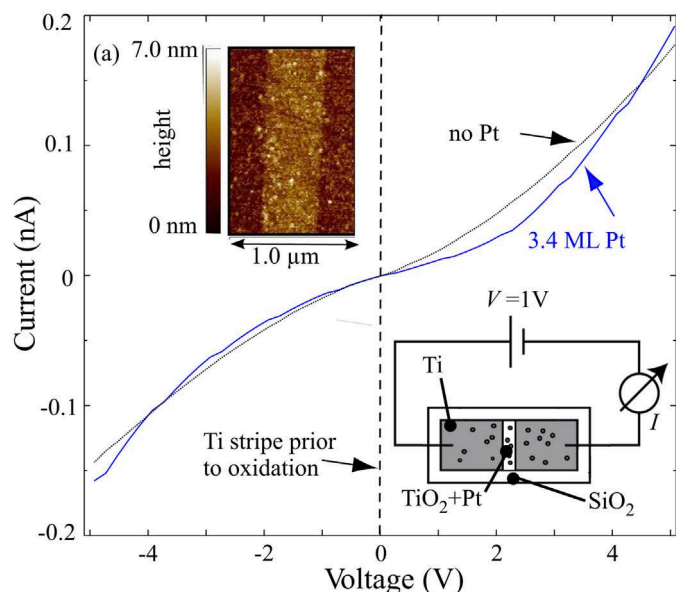
**Fig. 1.** Lower inset: top view scheme of the sensor layout. A Ti film on top of SiO$_2$ is separated by the oxide line into two electrodes, which are connected to leads. Pt islands on top are indicated by black circles. Upper inset: Atomic force microscope image of the TiO$_2$ line (bright) in between the two Ti electrodes. This picture has been taken after the deposition of nominally 3.4 Pt monolayers which cannot be identified here. Main figure: Current–voltage characteristics of the pristine Ti stripe (dashed line) and, after the oxidation step, across the TiO$_2$ line before (dotted line) and after (full line) the deposition of Pt. The measurements have been taken at room temperature ($T$ = 295 K).

**Fig. 2.** Sensor response to atmospheric hydrogen of $c(H_2)$ = 1000 ppm as a function of the nominal thickness of the Pt layer, as observed at room temperature. The hydrogen volume fraction was decreased to $c(H_2)$ = 150 ppm in the measurement of the sample with a coverage of 4.2 nominal monolayers of Pt (uppermost trace).

conductance has decreased by a factor of 10$^5$. This indicates that the Ti stripe has been oxidized all the way down to the substrate, and the resistance is dominated by the oxide line. Furthermore, the large change of the conductance allows to monitor the electronic separation of the Ti stripe into two isolated electrodes by *in-situ* conductance measurements. In a final step, Pt is deposited on top by magnetron sputtering. The amount of which is characterized by the nominal number of Pt monolayers according to control depositions on unpatterned substrates. In our deposition setup, the Pt film remains disconnected up to a nominal thickness of five monolayers. This is indicated by the fact that after the Pt deposition, the current–voltage characteristics is somewhat modified but remains highly resistive and nonlinear.

### 2.2. Measurement setup

For the sensing experiments, the sample is mounted into the measurement chamber of a liquid nitrogen cryostat (Linkam HFSX 350) with an adjustable temperature in the range between −196 °C and +350 °C, with an accuracy of ±2 °C. The atmosphere is provided via gas flow controllers (Bronkhorst EL-Flow series). Prior to each measurement sequence, the sample is heated to 180 °C for 1 h and kept for 10 h in dry synthetic air (N$_2$+20%O$_2$). This procedure ensures that water is absent and that the sample gets re-oxidized after a possible reduction during the measurements (see below). The measurements described in the following were carried out in a gas flow of 200 ml/min N$_2$ of 99.999% purity, to which further gases (hydrogen and oxygen) of the same purity were added. All experiments have been conducted in the dark.

## 3. Results

### 3.1. Elementary sensor characterization

It has been established that the Pt/TiO$_2$ combination is a very efficient hydrogen sensor where molecular hydrogen gets split and
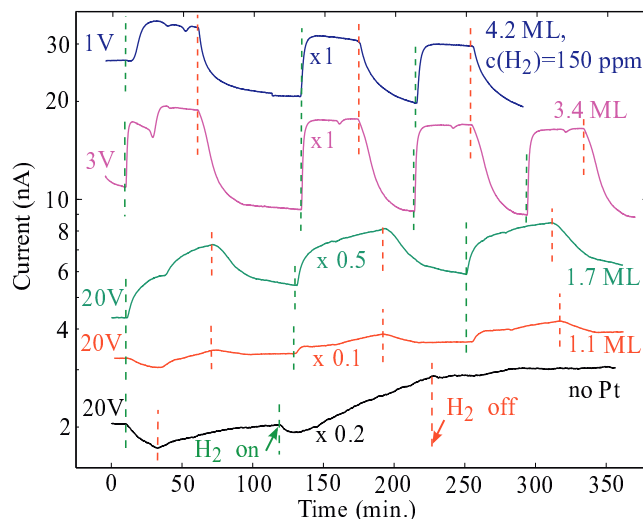
adsorbed at the Pt surface, from where hydrogen atoms diffuse through the Pt into the TiO$_2$ [20,15,21]. Atomic hydrogen in TiO$_2$ can form O—H groups with the oxygen in the bulk or at the surface of the host crystal [22,23], which is referred to as *interstitial hydrogen*. The hydrogen atoms bound this way act as shallow donors and increase the conductivity of the TiO$_2$ [24–26].

The relevance of the Pt deposition in our implementation is shown in Fig. 2, where the sensor response to atmospheric hydrogen of $c(H_2)$ = 1000 ppm volume fraction for various nominal Pt film thicknesses is reproduced. Prior to the Pt deposition, the sample reacts only weakly to atmospheric hydrogen and only under large source-drain bias voltages (bottom trace in Fig. 2). Under $V$ = 20 V, the current first deceases as hydrogen is offered for the first time and starts to increase 30 min later, when hydrogen is removed from the atmosphere. During the second hydrogen pulse, the initial current is smaller, and an increase is observed afterwards while hydrogen is still present in the atmosphere. This observation implies that our device is almost, but not completely, insensitive to hydrogen molecules. It has been reported that Ti can, to a small degree, work as catalyst that splits H$_2$ into atomic hydrogen [27] which may then act as interstitial dopant in the way described above. This mechanism may cause the weak sensitivity to molecular hydrogen in the absence of Pt.

The conductance starts to respond with a current increase to the hydrogen gas after a Pt deposition of ≈ 1.1 nominal monolayers, and the response improves continuously up to a deposition of 4.2 nominal monolayers, the largest coverage we have studied. We use the common definition $S = \frac{\Delta R}{R_N}$ for the sensor response where $\Delta R = |R_N - R_H|$ with $R_N$ denotes the resistance in dry nitrogen atmosphere, and $R_H$ is the resistance in the presence of additional atmospheric hydrogen. A response of $S$ = 0.9 is observed for $c(H_2)$ = 150 ppm and for a bias voltage of 1 V.

### 3.2. Electroformation and sensing

This response shows some further remarkable properties which reflect the small dimensions of the sensing unit. First, note that the conductance of the device varies strongly and non-monotonously after the Pt deposition steps but prior to hydrogen exposure. This indicates that the resistivity of the oxide line is not homogeneous and changes during the Pt deposition and/or the initialization
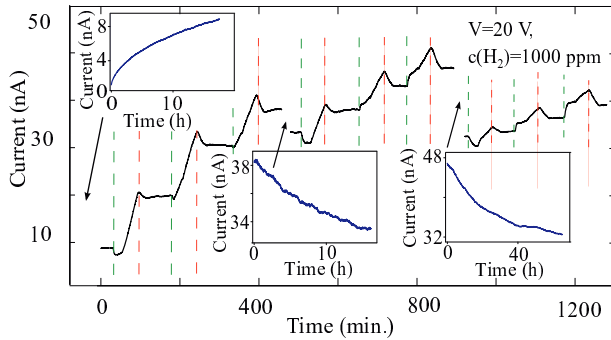
**Fig. 3.** Transients and time evolution of the current for a device with a Pt coverage of 1.1 nominal monolayers at a bias voltage of $V = 20$ V. All measurements have been carried out at room temperature.



**Fig. 4.** (a) Current transients as a function of the hydrogen volume fraction for pulse durations of 3 min (left) and 30 min (right), measured at room temperature. (b) Dependence of the response ($\tau_s$) and recovery ($\tau_r$) time, as well as of the sensor response S, on the hydrogen volume fraction.

procedure described above. Also, a decrease of the conductance in response to hydrogen incorporation in TiO$_2$, as observed in the two lowermost traces shown in Fig. 2, is unusual. We note that the electric field in these measurements is quite strong, namely of the order of $4 \times 10^7$ V/m which is in the regime where electroformation (also known as memristive effects) is known to take place in TiO$_2$ [28,29], and therefore an influence of electroformation processes on the sensing response cannot be excluded. We have therefore carried out further sensing experiments in the regime of large electric fields with the objective to find signatures for electroformation. The results of these studies, which have been carried out on a sample with a Pt coverage of nominally 1.1 monolayers, are summarized in Fig. 3. Prior to the measurement sequence, the sample was biased with $V = -20$ V for 10 h, a procedure which accumulates oxygen vacancies at the cathode [28], i.e., the negatively biased Ti electrode. It has been reported recently that in Pt nanoporous TiO$_2$ Schottky diode structures, the incorporation of atomic hydrogen and electroformation are interdependent [30]. In the following, we argue that our sensor shows a qualitatively similar behavior. Application of $V = 20$ V across the oxide line in dry nitrogen atmosphere causes the current to increase by more than one order of magnitude in the absence of hydrogen (left inset). The substantial electric field may cause the formation of conductive filaments of reduced titanium dioxide TiO$_{2-\delta}$ (with $0 < \delta < 1$) of higher resistivity [31], and we therefore interpret this increase of the current as an indication of an electroformation process, which would contribute to the increase of the base line observed in the two lowermost traces of Fig. 2. Offering hydrogen pulses under these conditions causes a response of the sensor current that shows striking analogies to the behavior reported by Strungaru et al. [30], namely an initial decrease of the current in response to the first and to the second hydrogen pulse, followed by an increase of the current. The increase of the base line current during hydrogen exposure is faster, while exposing the sample to the bias voltage in dry nitrogen atmosphere causes only a moderate reduction of the current. This indicates that both slow and incomplete hydrogen removal and electroformation contribute to the baseline current (see the insets in the center and to the right of Fig. 3). Also, the sensor response degrades over time under these conditions.

We thus conclude that the bias voltage should be kept sufficiently small in order to avoid disturbances of the sensing by electroformation processes. Furthermore, the observation of the coexistence of electroformation effects and hydrogen sensing in our device also shows that the effects reported in Ref. [30] are not a particular property of nanoporous thick films or of the Pt/TiO$_2$ interface, but have a more universal character.
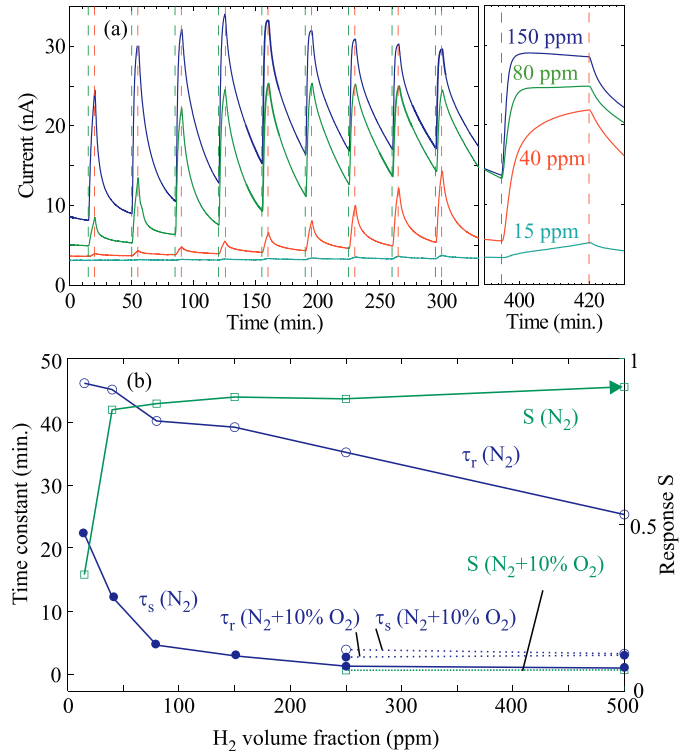
### 3.3. Sensor performance under varying external conditions

We proceed with the characterization of the sensor response as a function of temperature and additional atmospheric components. To avoid the voltage induced drift effects discussed above, we use the sample with a nominal Pt coverage of 4.2 monolayers and choose a working point of $V = 1$ V in all experiments discussed below. In Fig. 4 it is shown that the current is increasing monotonously as $c(H_2)$ is increased and that detection of a volume fraction of $c(H_2) = 15$ ppm, the lowest volume fraction we can provide with our setup, is possible.

The recovery after hydrogen has been turned off is much slower than the response when hydrogen is offered. This is illustrated by the response and recovery times $\tau_s$ and $\tau_r$, see Fig. 4(b), with $\tau_s$ defined as the time required for the current to reach 90% of the saturated response signal after the hydrogen pulse has started (*response time*), and $\tau_r$ being defined as the time after which the current has decayed from its maximum to 90% of the saturated value on the absence of hydrogen (*recovery time*). This indicates that hydrogen atoms enter into the TiO$_2$ relatively quickly but can be removed only on much longer time scales. Both time constants decrease rapidly and the ratio $\tau_r/\tau_s$ increases as $c(H_2)$ is increased. Furthermore, $\tau_s$ depends approximately exponentially on $c(H_2)$, while $\tau_r$ shows an approximately linear dependence. This behavior confirms earlier observations in various implementations that the dynamics for incorporation and removal of hydrogen are quite different [32,33], and that the long recovery time contributes to the background current that increases over time. By Kelvin probe measurements, Evers and Rohwerder concluded that besides interstitial hydrogen which is embedded and released rather quickly, also deep traps exist which get filled rapidly, but the release of hydrogen is significantly slower due to the larger binding energies
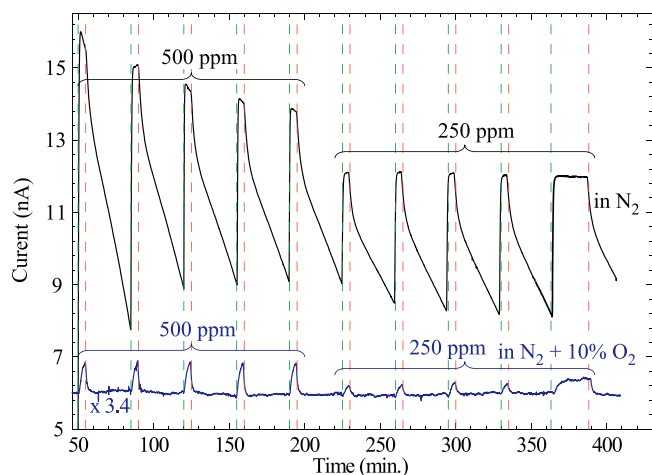
**Fig. 5.** Effect of oxygen gas at room temperature in ambient atmosphere on the sensor response to hydrogen pulses of 3 min duration. The waiting time between successive pulses was 30 min.

[34]. It appears plausible that a similar mechanism is taking effect in our oxide lines.

In Fig. 5, we show the effects of adding 10% oxygen gas to the nitrogen atmosphere. The strong decrease of the current transient amplitude increases the detection threshold to $c(H_2) \approx 100$ ppm.

Oxygen furthermore tends to equalize the two time constants to $\tau_s \approx \tau_r \approx 3$ s for $c(H_2)$ in the range between 250 ppm and 500 ppm. While $\tau_s$ increases, $\tau_r$ decreases strongly as compared to their values in dry nitrogen. We attribute this behavior to water formation, which inhibits the incorporation of hydrogen into the $TiO_2$ and at the same time facilitates its removal. In future work, a more detailed analysis of the reaction kinetics of the system may be helpful in gaining a better understanding of the mechanisms that dominate the time constants.

Additional measurements (not shown) reveal that the sensor characteristics do not change qualitatively, as compared to its performance in dry air, when the humidity is increased. However, the formation of a water film should be avoided because it may short the two Ti electrodes. Interestingly, for $c(H_2) \approx 100$ ppm, S increases somewhat in comparison to that one in dry air. We attribute this to a possible inhibition of water formation if water is already present.

In Fig. 6(a), the temperature dependence of the current transients is shown. For $T < -40\,^\circ$C, the sensor responds only weakly to a hydrogen volume fraction of $c(H_2) = 80$ ppm, and saturation is not reached even after 30 min. Above a threshold temperature of $\approx -10\,^\circ$C, the device starts to respond both more strongly and faster. As the temperature or $c(H_2)$ is further increased, the response S increases, see Fig. 6(b) while the response times decrease. Also here, $\tau_s$ decreases rapidly as T is increased, and $\tau_r$ shows a weaker temperature dependence.

## 4. Discussion

The device is thus capable to detect atmospheric hydrogen with a spatial resolution in two dimensions which is given by the $TiO_2$ surface area. The width of the oxide line can be adjusted via the parameters of the scanning probe lithography, and we have operated devices with oxide line widths down to 200 nm. The size of the sensitive area in the transverse direction is determined by the width of the Ti stripe, which we patterned by optical lithography. This size can be easily decreased into the 100 nm regime. It should be noted that due to the large diffusion constant of molecular hydrogen in air of $0.67\,cm^2/s$ at 300 K [35], the detection of hydrogen with submicron resolution desirable for some of the questions mentioned
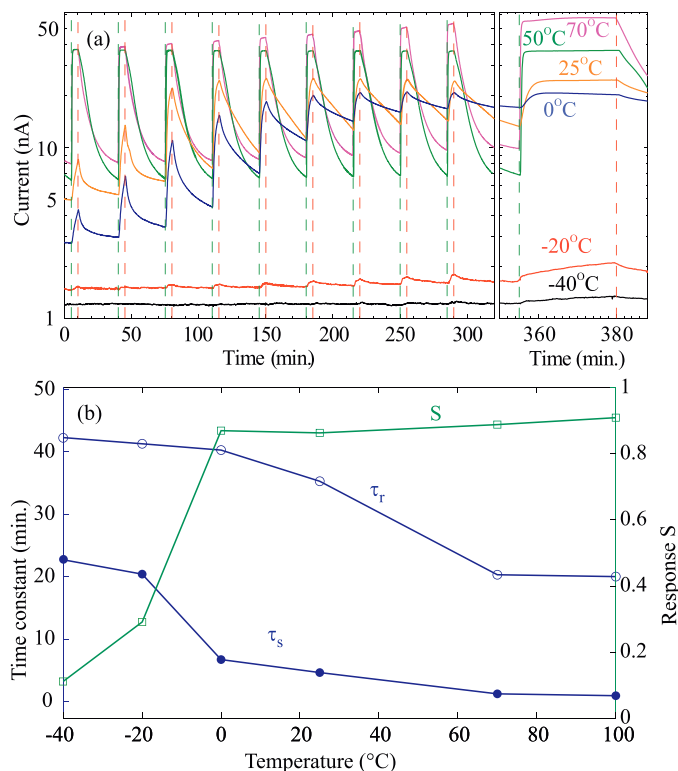


**Fig. 6.** (a) Temperature dependence of the transients in response to hydrogen pulses of volume fraction $c(H_2) = 80$ ppm, measured in dry nitrogen atmosphere and for pulse durations and waiting times as in Fig. 5. In (b), the response and the time constants are shown as a function of the temperature for the selected hydrogen volume fraction of $c(H_2) = 80$ ppm.

above requires, besides a small active area, also to place the detector sufficiently closely to the hydrogen source, or to fill the space in between the source and the sensor with a medium with a smaller hydrogen diffusion constant. The first approach has been demonstrated by Senoz et al. [11], who use the tip of a scanning probe microscope as detector, while the latter concept has played a role in the experiments reported by Katano et al. [9] as well as by Ovejero et al. [10]. A possible concept for our sensor could by to integrate it into the tip of an atomic force microscope, or to prepare suitable tips on the sensing chip to use them for controlling the distance to the hydrogen source, which could be a metal sheet, for example.

Deposition of a Pt layer with a connectivity below the percolation threshold in the area of the oxide line is essential for good sensing operation. Unfortunately, we were unable to identify the Pt unambiguously by atomic force or electron beam microscopy, and the morphology of the Pt layer is presently not known. However, our measurements indicate that a deposition of approximately four nominal monolayers of Pt gave the best performance in terms of sensitivity and response time, while Pt layers of larger thickness run the risk to form a metallic path across the oxide line. It is a task for the future to characterize the Pt layer in more detail, as well as to study the performance of other catalytic metals like Pd.

In relation to earlier sensor layouts, our structure can be seen as a symbiosis of the approach presented by Archanjo et al. [19], who reported on-chip sensors prepared by partial oxidation of suitable but undecorated metal films, and the work of Kolmakov et al. [36], where tin oxide nanowires were decorated by Pd, deposited on a substrate and contacted electrically. In our approach, the oxide line written by scanning probe lithography takes the role of a nanowire in the experiments of Kolmakov et al. [36], with the difference that our oxide lines are prepared under full control of its parameters like its dimensions and its position on-chip. It allows the production of

two-dimensional sensor arrays with the possibility to address their elements individually in a straightforward way.

A new physical aspect of the measurements is the observation that lowering the detection threshold by increasing the bias voltage is not just limited by the breakdown electric field, but rather by a threshold field above which electroformation sets in. The effects that occur in our device above this threshold are worth being studied further, considering the generally very limited knowledge regarding sensing under electroforming conditions.

The behavior of the time constants is remarkable regarding several aspects. The large difference between the response time when hydrogen is offered and the recovery time and their dependence on atmospheric oxygen indicates that water formation may play an important role. Also, even though the sensor has a thickness of 10 nm and a lateral extension of a few 100 nm only, the time constants are not very different from those observed in Pt/TiO$_2$ – based hydrogen detectors with much larger detection volume. This suggests that the diffusion of the hydrogen atoms in TiO$_2$ is not the limiting factor for the response time. Finally, we note that in contrast to many other sensor implementations based on Pt/TiO$_2$ or closely related systems [37,38,14–16], there is no voltage applied across this Schottky barrier in our device, and we can conclude that the properties of the biased Schottky barrier does not play a major role in the sensing.

## 5. Conclusions

To summarize, we have presented a lateral geometry for a TiO$_2$-based hydrogen sensor with high spatial resolution (200 nm), and concentrations of H$_2$ in the ppm range. The sensor can be operated under ambient conditions and does not require heating. Arrays of such sensors are straightforward to implement. In an application where the spatial resolution requires a small distance from a sample, distance control on a length scale comparable to the lateral resolution via an integrated tip of a scanning probe microscope appears feasible. It has been shown that due to the small lateral dimensions, large electric fields above the electroformation threshold are readily obtained, and that above this threshold, electroformation processes interfere with the sensing. Further work is required to study these interdependencies as well as to elucidate the mechanisms that determine the response times of the sensor.

## Acknowledgement

## References

[1] T. Hübert, L. Boon-Brett, G. Black, U. Banach, Sens. Actuators B 157 (2011) 329.
[2] P.P. Edwards, V.L. Kuznetsov, W.I.F. David, N.P. Brandon, Energy Policy 36 (2008) 4356.
[3] S. Satyapal, J. Petrovic, C. Read, G. Thomas, G. Ordaz, Catalysis Today 120 (2007) 246.
[4] K. Schlapbach, A. Züttel, Nature 414 (2001) 353.
[5] B. Demirel, P. Scherer, O. Yenigun, T.T. Onay, Crit. Rev. Environ. Sci. Technol. 40 (2010) 116.
[6] M.S. Daw, M.I. Baskes, Phys. Rev. Lett. 50 (1983) 1285.
[7] Q. Liu, A. Atrens, Corros. Rev. 31 (2013) 85.
[8] W.A. Lanford, Nucl. Instrum. Methods Phys. Res. B 66 (1992) 65.
[9] G. Katano, K. Ueyama, M. Mori, J. Mater. Sci. 36 (2001) 2277.
[10] J. Ovejero-Garcia, J. Mater. Sci. 20 (1985) 2623.
[11] C. Senöz, S. Evers, M. Stratmann, M. Rohwerder, Electrochem. Commun. 13 (2011) 1542.
[12] J. van Lith, A. Lassesson, S.A. Brown, M. Schulze, J.G. Partridge, A. Ayesh, Appl. Phys. Lett. 91 (2007) 181910.
[13] T. Kiefer, L.G. Villanueva, F. Fargier, F. Favier, J. Brugger, Appl. Phys. Lett. 97 (2010) 121911.
[14] O.K. Varghese, D. Gong, M. Paulose, K.G. Ong, C.A. Grimes, Sens. Actuators B 93 (2003) 338.
[15] M. Paulose, O.K. Varghese, G.K. Mor, C.A. Grimes, K.G. Ong, Nanotechnology 17 (2006) 398.
[16] M. Cerchez, H. Langer, M.E. Achhab, T. Heinzel, H. Lüder, D. Ostermann, Appl. Phys. Lett. 103 (2013) 033522.
[17] D.R. Lyde (Ed.), CRC Handbook of Chemistry and Physics, Section 12: Properties of Solids, CRC Press, Boca Raton, USA, 2003.
[18] R. Held, T. Heinzel, P. Studerus, K. Ensslin, M. Holland, Appl. Phys. Lett. 71 (1997) 2689.
[19] B.S. Archanjo, P.S. Siles, C.K.B.Q.M. Oliveira, D.L. Baptista, B.R.A. Rives, Adv. Mater. Sci. Eng. 2013 (2013) 898565.
[20] U. Roland, T. Braunschweig, F. Roessner, J. Mol. Catal. A: Chem. 127 (1997) 61.
[21] U. Aschauer, A. Selloni, Phys. Chem. Chem. Phys. 14 (2012) 16595.
[22] F. Filippone, G. Mattioli, P. Alippi, A.A. Bonapasta, Phys. Rev. B 80 (2009) 245203.
[23] T. Bjørheim, S. Stølen, T. Norby, Phys. Chem. Chem. Phys. 12 (2010) 6817.
[24] D.A. Panayotov, J.T. Yates, Chem. Phys. Lett. 436 (2007) 204.
[25] P.W. Peacock, J. Robertson, Appl. Phys. Lett. 83 (2003) 2025.
[26] F. Herklotz, E.V. Lavrov, J. Weber, Phys. Rev. B 83 (2011) 235202.
[27] W. Göpel, G. Rocker, R. Feierabend, Phys. Rev. B 28 (1983) 3427.
[28] D.B. Strukov, G.S. Snider, D.R. Stewart, R.S. Williams, Nature 453 (2008) 80.
[29] K. Szot, M. Rogala, W. Speier, Z. Klusek, A. Beshehm, R. Waser, Nanotechnology 22 (2011) 254001.
[30] M. Strungaru, M. Cerchez, S. Herbertz, T. Heinzel, M. El Achhab, K. Schierbaum, Appl. Phys. Lett. 106 (2015) 143109.
[31] D.-H. Kwon, K.M. Kim, J.H. Jang, M.M. Jeon, M.H. Lee, G.H. Kim, X.-S. Li, G.-S. Park, B. Lee, S. Han, M. Kim, C.S. Hwang, Nat. Nanotechnol. 5 (2010) 148.
[32] G.K. Mor, M.A. Carvalho, O.K. Varghese, M.V. Pishko, C.A. Grimes, J. Mater. Res. 19 (2004) 628.
[33] K.D. Benkstein, S. Semancik, Sens. Actuators B 113 (2006) 445.
[34] S. Evers, M. Rohwerder, Electrochem. Commun. 24 (2012) 85.
[35] T.R. Marrero, E.A. Mason, J. Phys. Chem. Ref. Data 1 (1972) 3.
[36] A. Kolmakov, D.O. Klenov, Y. Linach, S. Stemmer, M. Moskovits, Nano Lett. 73 (1998) 1206.
[37] N. Yamamoto, S. Tonomura, T. Matsuoka, H. Tsubomura, Surf. Sci. 92 (1980) 400.
[38] R. Könenkamp, Phys. Rev. B 61 (2000) 11057.

## Biographies

**Svenja Herbertz** received her M.Sc. in Medical Physics from the Heinrich-Heine University Düsseldorf (Germany) in 2013. Her current research activities as a member of the Solid State Physics Laboratory at the HHUD include the development of hydrogen gas sensors based on titania and memristive behavior in these materials.

**Mihai Cerchez** received his D.Sc. title in Physics at the Alexandru Ioan Cuza University in Iasi, Romania, in 2001. He was an Alexander von Humboldt research fellow in 2003–2004, at the University of Duisburg-Essen. He habilitated and is currently a Privatdozent at the Heinrich-Heine University Düsseldorf. His current research and teaching activities are in the experimental physics of semiconductor devices.

**Thomas Heinzel** received his Ph.D. in Physics at the Ludwig-Maximilians-University in Munich (Germany) in 1994. He is a professor at the Heinrich-Heine University Düsseldorf where he is in charge of the Solid State Physics Laboratory. His research group is conducting experiments in the field of mesoscopic transport phenomena in semiconductors and has recently added titanium dioxide to the portfolio of studied materials.

# 3 Active implementation of Electroforming

The following chapter deals with the active implementaion of EF in $TiO_2$ microdevices on-chip. In Paper III, we demonstrate that the application of a bias voltage to junctions of $Ti/TiO_x$ nanowires may oxidize the Ti electrode acting as anode under ambient conditions. Partly oxidation of electrodes has been reported in resistive switches as well. For example, in $Pt/TiO_2/Al$ structures, oxidation of Al electrodes has been reported to be problematic for $O_2$ diffusion and is the reason why in these devices resistive switching is possible only when a positive bias is applied to the Pt, otherwise $O^{2-}$ ions are pulled from the $TiO_2$ into the Al electrode and oxidize it [52]. This means that under EF conditions not only the interior microscopic structure of the oxide can change but also its spatial extension. Since changes in the extension can modify the electronic properties of the oxide such effects should be taken into account, for example, when drift effects in these devices are discussed. In structures where the main part of the junction between metal and oxide is covered by the electrodes, as it is for example the case in our micron-scale sandwich structures, further growth of the oxide layer by oxidation of the electrodes may happen unnoticed. To demonstrate changes in the electrodes, one would have to cut through these structures to perform a structural analysis, e.g. by means of electron microscopy, which in turn would hinder further modification and the possibility to compare the results.

Our devices of planar design, however, have the advantage of an accessible oxide surface, allowing analysis by means of AFM and EDX. This way, we were able to study modifications in the geometrical, morphological and electronic properties of the $TiO_2$ that were induced by choice of the experimental parameters, like the applied voltage, exposure time, relative humidity and oxygen content in the atmosphere. Yang et al. [75] previously reported that even a one-time voltage application in the context of electroreduction can lead to destructive and difficult-to-control physical deformation in $TiO_2$ microdevices due to $O_2$ gas evolution at the anode. For this reason, they developed fabrication procedures to mitigate or even fully avoid the electroreduction step. Our results show that morphological and structural changes caused by high electric fields may also represent an experimental tool to tune the properties of an oxide device after lithographic processing.

In Paper IV, which is subject of the second part of this chapter, these results were utilized to define and modify Ti and Ti/Pt electrode geometries on-chip. We demonstrated that an assembled and fully operational $H_2$ sensor device can be fabricated this way. A deposited monolayer of Pt on top of Ti serves as catalyst in the sensing, but also significantly accelerates the anodization via catalytic splitting of water. Not only the number of lithographic steps can be reduced this way, but also can the $TiO_2$ be

easily produced and sensitized in one step, namely by application of a voltage on-chip. Furthermore, the special geometry allows to monitor the oxidation process by means of optical microscopy and in-situ resistance measurements.

In the following, Paper III is presented, together with additional considerations about the electric field distribution supporting our assumptions on how the effects of the experimental parameter variation can be explained. In addition, the functionality of an on-chip modified nanowire as gas sensor is demonstrated. In section 3.2, Paper IV together with supplemental results of the film characterization can be found.

# Paper III   Bias voltage - induced oxidation of titanium microelectrodes in planar Ti/TiO$_x$ heterojunctions

Bias voltage - Induced oxidation of titanium microelectrodes in planar Ti/TiO$_\text{x}$ heterojunctions

S. Herbertz, P. Aleksa, M. Zielinski, D. Welk, T. Heinzel[*]

*Condensed Matter Physics Laboratory, Heinrich-Heine-Universität, Universitätsstr. 1, 40225, Düsseldorf, Germany*

A B S T R A C T

It is shown that the application of bias voltages to planar Ti/TiO$_x$ microjunctions under ambient conditions can initiate growth of the oxide component by oxidation of the Ti electrodes on a Si chip. The geometrical, morphological and electronic properties of the titanium oxide can be modified by a suitable choice of the experimental parameters. In particular, the growth rate of the oxide, its roughness and its conductance depend on the applied voltage, on the exposure time as well as on the relative humidity and oxygen content of the atmosphere. The process is explained in terms of planar anodization, where the water film that forms under ambient conditions acts as electrolyte. Our results not only identify a possible source of drift effects in typical devices like memristors, gas sensors as well as microchip structures containing titanium electrodes, but also represent an experimental tool for electroforming, namely adjusting the properties of oxide films after the lithographic processing of the samples.

## Reference

S. Herbertz, P. Aleksa, M. Zielinski, D. Welk and T. Heinzel
Superlattices and Microstructures **124**, 231-239 (2018) ©2018 Elsevier
https://doi.org/10.1016/j.spmi.2018.09.006
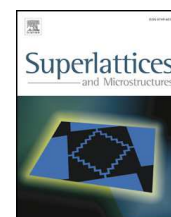
## Copyright statement

## Contributions

I planned the experimental set-up and prepared the samples. I contributed to the conduction of the experiments and analyzed the experimental data. I contributed to manuscript writing.

# Bias voltage - Induced oxidation of titanium microelectrodes in planar Ti/TiO$_x$ heterojunctions

S. Herbertz, P. Aleksa, M. Zielinski, D. Welk, T. Heinzel*

*Condensed Matter Physics Laboratory, Heinrich-Heine-Universität, Universitätsstr. 1, 40225, Düsseldorf, Germany*

## ABSTRACT

It is shown that the application of bias voltages to planar Ti/TiO$_x$ microjunctions under ambient conditions can initiate growth of the oxide component by oxidation of the Ti electrodes on a Si chip. The geometrical, morphological and electronic properties of the titanium oxide can be modified by a suitable choice of the experimental parameters. In particular, the growth rate of the oxide, its roughness and its conductance depend on the applied voltage, on the exposure time as well as on the relative humidity and oxygen content of the atmosphere. The process is explained in terms of planar anodization, where the water film that forms under ambient conditions acts as electrolyte. Our results not only identify a possible source of drift effects in typical devices like memristors, gas sensors as well as microchip structures containing titanium electrodes, but also represent an experimental tool for electroforming, namely adjusting the properties of oxide films after the lithographic processing of the samples.

## 1. Introduction

Titanium/titanium oxide junctions are present in a wide variety of devices. In some solid state gas sensors, for example, the conductivity of a porous TiO$_x$ layer can change by orders of magnitude as a consequences of gaseous adsorbates like hydrogen [1–3] or CO [4]. The relatively high mobility of oxygen vacancies [5,6] as well as the formation of Magnéli phases in TiO$_x$ [7] is used in Ti/TiO$_x$ memristors [8] to define the active element of the devices. In such structures, the Ti plays the role of an electrode that forms a weakly pronounced Schottky barrier or even an Ohmic contact to the TiO$_x$. Also, lateral Ti/TiO$_x$ structures have been used as gate electrodes on top of GaAs/Al$_x$Ga$_{1-x}$As high-electron mobility transistors where complex potential landscapes had to be defined in the two-dimensional electron gas residing at the heterointerface [9,10]. Furthermore, it has recently been reported that lateral Ti/TiO$_x$ nanojunctions in the adhesion layer of electrodes used for single molecule transport measurements, are responsible for the background conductance in such circuits [11]. In these applications, the TiO$_x$ plays the role of an insulator that separates the Ti electrodes which form the functional elements. The applications described in Ref. [8–11] have in common that a bias voltage is applied across the TiO$_x$, which is supposed either to have no effect at all on the oxide, or, in the case of the memristors, to induce some microscopic changes inside the oxide without changing its spatial extension, see also Ref. [12] for application examples. Here, we show that this assumption holds only for electric fields that are kept below a threshold value, which is about $5 \times 10^7$ V/m for the oxides used in the present study. At larger electric fields, the Ti electrode acting as anode may get oxidized under ambient conditions, thereby increasing the spatial extension of the oxide. This possibility should be taken into account, for example, when drift effects in such devices are discussed. On the other hand, it can be used also actively, for example to tune the properties of the TiO$_x$ during postprocessing of the

* Corresponding author.
  *E-mail address:* thomas.heinzel@hhu.de (T. Heinzel).
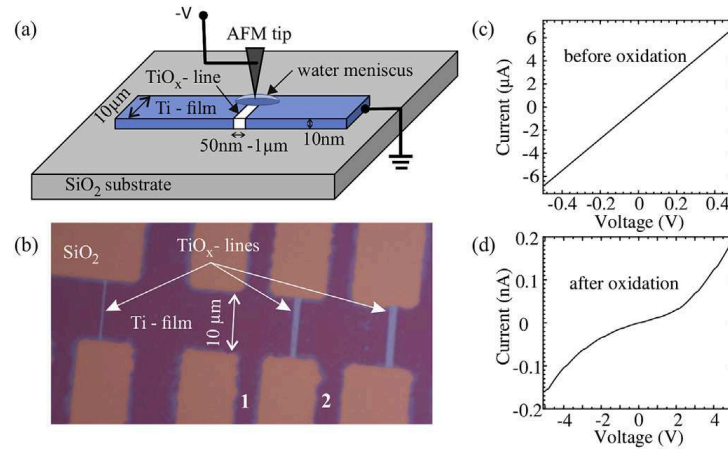
**Fig. 1.** (a) Sample preparation scheme. A local anodization of the Ti stripe is performed using an AFM tip as cathode. (b) Top view of a sample containing three oxide lines as seen in an optical microscope. The scan velocities of the AFM tip during writing were 1 μm/s (left), 0.1 μm/s (middle), and 1 μm/s (right), respectively. The IV characteristics measured between contacts 1 and 2 before and after the oxidation step are shown in (c) and (d), respectively. (For interpretation of the references to color in this figure legend, the reader is referred to the Web version of this article.)

original device.

The paper is organized as follows. In Section 2, the sample preparation and measurement setup are described. Section 3 contains the experimental results and their interpretation. The paper closes with a summary and an outlook in Section 4.

## 2. Sample preparation and experimental setup

Suitable samples are prepared by defining a Ti film (thickness 10 nm) on a Si/SiO$_2$ substrate by optical lithography, followed by deposition of the Ti in an electron beam evaporator and a lift-off step. The roughness of the Ti stripes is determined with an atomic force microscope (AFM) to $\approx 0.6$ nm, and their conductance is in rough agreement with that one expected for Ti with a conductivity of $\sigma_{Ti} = 2.38 \times 10^6 (\Omega m)^{-1}$. The samples are mounted in a chip carrier and wire-bonded for electrical access. The initial oxide line is prepared by scanning probe lithography, where a conductive AFM tip is negatively biased with respect to the grounded Ti stripe and scanned across the stripe with constant velocity, see Fig. 1 (a) for a scheme of our setup [13]. This implementation corresponds to a local anodization process with the AFM tip acting as cathode. The width $W_0$ of the resulting oxide lines depends on both the anodization voltage and the scan velocity [14]. In Fig. 1 (b), three oxide lines written at constant anodization voltage ($-18$ V) with different tip scan velocities are shown. The ambient relative humidity (rh) does not affect the resulting line width significantly as long as it remains in the range of 40 %— 60%. At lower humidities, the formation of the required water meniscus between film and AFM tip is inhibited, and oxidation is not observed. As shown in Fig. 1 (c,d), the initially Ohmic connection between source and drain (the contacts labeled 1 and 2, with a resistance of 77 kΩ) develops into non-linear behavior with a resistance around V = 0 of the order of 100 GΩ. This demonstrates that the TiO$_x$ line penetrates the Ti layer all the way down to the substrate. First of all, considering the conductivity of Ti given above and the geometry of the oxide line (width $W_0 = 200$nm and length $L = 10\mu$m), a resistance of R = 100 GΩ would correspond to a residual height of the Ti film of $H = \frac{W_0}{\sigma_{Ti} \times L \times R} \approx 10^{-19}$m, i.e., many orders of magnitude smaller than the height of one Ti monolayer. Second, a nonlinear current-voltage characteristics is a signature of electronic transport by hopping of charge carriers between randomly distributed, localized sites as present in disordered semiconductors or insulators [15].

To study the oxide growth during postprocessing, we used samples where the original Ti film was divided into two electrodes by an oxide line of width $W_0 = 200$ nm written with the AFM as described above. The sample was mounted in a measurement chamber where the temperature and the atmosphere could be controlled. Nitrogen and oxygen flows are each adjusted by a mass flow controller (*Bronkhorst*) and are carried via stainless steel tubes. Humidification is implemented via a bypass leading through a water bath, which saturates the gas mixture (100%) at flow rates around 1 l/min as used in the experiments. The relative humidity of the gas is adjusted with an accuracy of approximately 0.5% by setting the valves that control the flow through the bypass, in combination with a blocking valve to prevent backward flow. The gases are heated by passing them through a porous aluminum alloy block (*Exxentis*) with external heat supply, which is set to the required temperature. The measurement chamber itself has its own temperature control, in form of a Pt based heating element beneath the sample holder, and liquid nitrogen cooling controlled by an external pump (*Linkam*). The gas line between heating unit and measurement chamber is kept short to prevent temperature loss. The relative humidity and the gas temperature are monitored at multiple locations using reference sensors with both functionalities (*Sensirion*). The gases leave the set-up through an overpressure valve that prevents outer gases from diffusion into the measurement chamber (opening pressure 30 mbar).

All experiments were carried out in the dark and at room temperature (300 K). The samples were exposed to an air-like atmosphere (nitrogen with two concentrations of oxygen as well as several values of the rh). DC bias voltages between 10 V and 36 V were applied across such oxide lines via Ohmic contacts to the Ti electrodes, and in some cases, the conductance was monitored in-situ. For
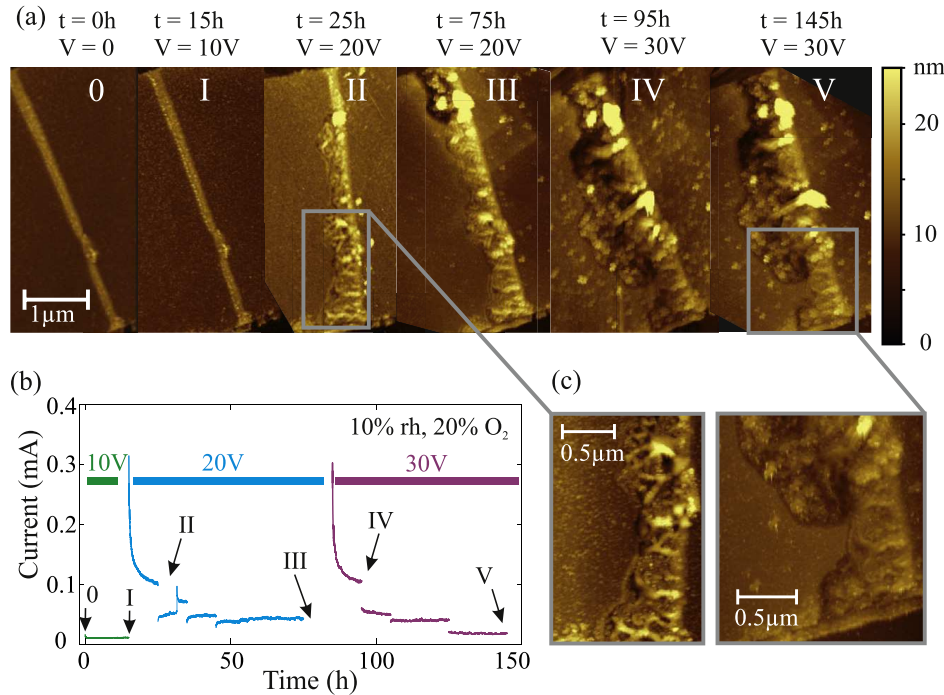
**Fig. 2.** Effect of a bias voltage to an AFM - written $TiO_x$ -line under ambient conditions (air with 10% rh). (a) Snapshots of the morphology as observed with an atomic force microscope at points in time as marked in (b), where the current measured in-situ is shown. The occasional discontinuities in the current originate from the interruptions of the growth process for the morphological characterizations. In (c), zoom-ins of the typical textures of the grown oxides are shown. (For interpretation of the references to color in this figure legend, the reader is referred to the Web version of this article.)

studies related to changes in the geometry and morphology, the growth process was interrupted for a sample transfer to an AFM operated at ambient conditions. Before the anodization experiment was resumed, the sample was heated in dry nitrogen to 180°C for 30 min, which ensures the removal of the water film. For electronic characterization, the atmosphere in the growth chamber was changed to dry nitrogen atmosphere, and the current-voltage characteristics were recorded.

## 3. Experimental results and interpretation

In Fig. 2, we show the morphological and electronic evolution of one oxide line under different applied bias voltages, exemplified in an atmosphere of air (80% nitrogen and 20% oxygen) with a low rh of 10%. At a bias voltage of $V = 10V$, corresponding to an average electric field of $5 \times 10^7 V/m$, no morphological changes are detected after an exposure time of 15 h (snapshot I in Fig. 2 (a)), and the current through the structure is constant, see Fig. 2 (b). As V is increased to 20 V, the current measured in-situ decreases strongly at the beginning and saturates after about 35 h exposure time, see Fig. 2 (b). An inspection of the oxide line after 10 h reveals that its average width W has increased, with the growth taking place towards the positively biased electrode (i.e. the anode in our setup), see snapshot II in Fig. 2 (a). This growth saturates in correlation with the current, see snapshot III, but can be re-initiated by increasing the voltage further, see snapshots IV and V. We observed a maximum average width of $W = 1200$ nm and a decrease of the conductance by a factor of about 20 under these conditions, after a total oxidation time of 150 h. During the process, the width develops strong spatial fluctuations, which amount to more than a factor of two at the end of the experiment, see Fig. 2 (c). Furthermore, the oxide line develops two characteristic patterns, namely a stripe-like texture in some regions and a structure with more localized mounds in other regions, see the zoom-ins shown in Fig. 2 (c). Interestingly, these textures also develop at the initial, AFM written part of the oxide line.

This phenomenology allows some conclusions concerning the underlying mechanisms [16]. The fact that only the anode gets oxidized suggests that the drift of ion-containing oxygen to the anode and the subsequent oxidation of Ti is the dominant process, while the opposite drift of $Ti^{4+}$ - ions towards the cathode followed by their oxidation, is of minor relevance, probably also because the reduction of $H^+$ - ions is the dominant process at the cathode. More specifically, recent experiments [17,18] have suggested that at the cathode, the excess electrons initiate the dissociation of water according to

$$4H_2 O + 4e^- \rightarrow 2H_2 + 4OH^-$$
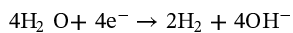
The $OH^-$ ions drift towards the anode where they oxidize the Ti - atoms via the reactions

$$Ti \rightarrow Ti^{4+};$$

$$Ti^{4+} + 4OH^- \rightarrow TiO_2 + 2H_2O$$
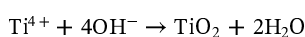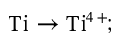
which can be accompanied by the competing reaction

$$4OH^- \rightarrow O_2 + 2H_2O + 2e^-$$
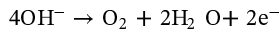
with the formation of oxygen gas. Thus, regarding the oxidation of Ti, the effective reaction reads

$$Ti + 2H_2O \rightarrow TiO_2 + 2H_2 \tag{1}$$

It is remarkable that this oxidation sets in at quite low relative humidities, where only chemi- and physisorbed layers of water molecules should be present which do not form hydrogen bonds between the water molecules, and proton conduction inside the water film is absent [19]. The measured in-situ conductance correlates with the width of the oxide, and its decrease over time can be predominantly attributed to the increasing separation between the two electrodes. Finally, the strong inhomogeneities that evolve under the bias voltage, plus the observation that also the initial oxide line changes its morphology, indicate that the oxidation is accompanied by some kind of electroforming, maybe in relation to electrostriction or local heating [16].

It should be noted that our anodization setup is unconventional in several respects. First of all, the electrolyte, in our case water, is one of two conductive media between the cathode and the anode, located in parallel to the already existing $TiO_x$. Second, the electrolyte can contain a considerable amount of oxygen gas, which depends on the oxygen partial pressure. To the best of our knowledge, the influence of oxygen gas in the electrolyte on the anodization process has not been studied hitherto. However, the anodization of metals with incorporated oxygen has shown that these oxygen atoms do participate in the anodization and accelerate the oxidation rate. Also, the films develop a larger roughness in the presence of oxygen [20]. We will get back to this issue below. Third, the studied morphology seen in Fig. 2 (a,c) is oriented predominantly along the direction of the anodizing electric field and not, as frequently reported, perpendicular to it [2,21,22]. Finally, the grown oxide film is very thin such that due to the proximity of the substrate, a significant fraction of it may be under strain, while in oxides of much larger thickness, the strain relaxes after a few lattice constants and the conventional bulk crystal structures like rutile or anatase are dominant. Thus, a straightforward application of models developed for other setups to our scenario may be inappropriate. It is beyond the scope of the present work to clarify the roles these differences may play. Rather, we focus on a phenomenological characterization of this anodization and its dependence on the ambient conditions, in view of its relevance for the performance of such microelectrodes in the devices mentioned above.

In order to study the effect of the humidity, a series of anodization experiments was performed, the results of which are summarized in Fig. 3. At zero rh (Fig. 3 (a)), application of bias voltages up to 20 V do not modify the morphology or the width of the
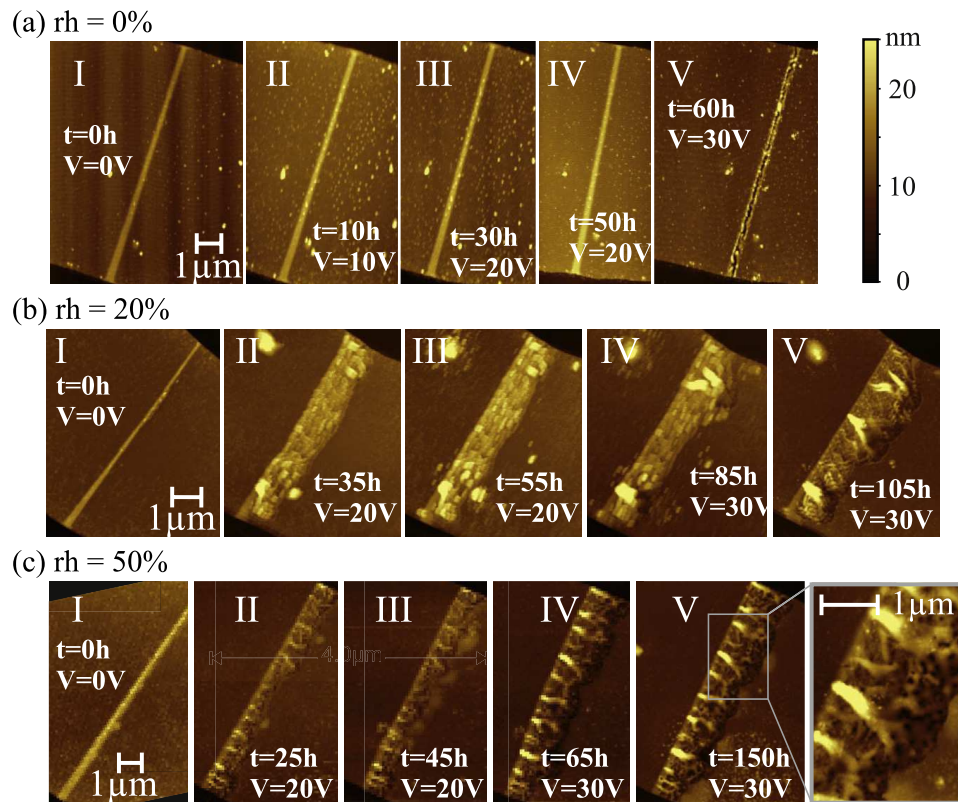


**Fig. 3.** Evolution of the $TiO_x$ stripe morphology under potentiostatic conditions in air with different relative humidities of 0 (a), 20% (b) and 50% (c), as observed with an atomic force microscope. (For interpretation of the references to color in this figure legend, the reader is referred to the Web version of this article.)

oxide line. As the bias voltage is increased to 30 V, the oxide line transforms into a trench. As expected, no oxide growth is possible in dry air. Rather, at large electric fields above $\approx 10^8$ V/m, this oxide line is destroyed. We tentatively attribute this to Joule heating which may decrease the adhesion of the $TiO_x$ to the substrate, or to electrostriction which may lead to cracks in the $TiO_x$ stripe and/or pulverization.

As the humidity is increased to 20%, the geometry of the oxide line gets modified by bias voltages of 20 V and larger, see Fig. 3 (b). An increase of W over time by a factor of about 8 is observed. Thus, as the rh is increased from 10% to 20%, the oxide growth gets faster and larger widths W are obtained. Also shown is the oxide growth at a rh of 50%, see Fig. 3 (c), where a liquid water film is present [19]. The growth rate of W is approximately the same as that one at 20% rh. The stripe-like texture in the morphology of the $TiO_x$ is more pronounced in comparison to that one observed under 10% rh. Its markedness increases over time, under increasing bias voltages and for larger relative humidity. Also, these stripes are arranged quasi-periodically. For example, at 30 V in rh 50%, ten such stripes are observed at a separation of about 1 $\mu m$. They start from the Ti electrode that acts as cathode and extend roughly to the center of the oxide line, after which a more homogeneous, pore-like morphology is observed, see also the enlargement in Fig. 3 (c). Such potentiostatic aging processes have been studied earlier. For example, post-growth crystallization under such conditions has been reported [23], while aging can also include dehydration and a subsequent crystal reordering [24]. This could lead to tensile stress in the initially stress-free, hydrated oxide [25,26]. We cannot exclude that the stripes are a consequence of electron avalanches that start from defects at the cathode/oxide interface and extend into the oxide [27], which is accompanied by local stress as well as by heating and may lead to structural changes. However, if this texture would originate solely from electron avalanches that emerge in the breakdown regime from defects where the electric field is particularly strong, such a regular pattern is not to be expected. Rather, it appears plausible that strain is involved which has to build over a certain transverse distance before it relaxes and leads to the observed quasi-periodic pattern.

In Fig. 4, the evolution of the average width (a) and height (b) of the oxide lines are reproduced. At relative humidities of 10% and 20%, we observe an increase of the oxide height during anodization which is just slightly above the experimental accuracy, see. Fig. 4 (b). The roughness of the film increases slightly both as the rh increases and as a function of anodization time, as indicated by the error bars. A marked increase of the oxide height by more than a factor of 2 is detected at a rh of 50% under a bias voltage of 30 V. Also here, the growth of the oxide is accompanied by an increase of its roughness.

It appears unlikely that this height increase is caused by mobile $O^{2-}$ - ions that react with Ti that has remained reduced inside the $TiO_x$. One explanation could be that $Ti^{4+}$ - ions dissolve in the water and migrate, in sufficiently strong electric fields, in antiparallel direction to the electric field lines into the $TiO_x$ where they react with $O^{2-}$ - ions and form additional $TiO_x$. A second possible contribution to this growth is the well-known evolution of oxygen gas during the oxidation both at the surface as well as in the bulk of the $TiO_x$ [28–30]. It has been argued that the oxygen gas forms from $O^{2-}$ ions at crystal imperfections with a decreased binding energy [31]. The dissociation of $OH^-$ ions at the anode according to the reaction stated above is a second possible way to generate oxygen gas. Also, evidence has been reported that the oxygen gas produced this way can form bubbles in the $TiO_x$ [18,32]. The high local pressure [32] may get released by rupturing the film locally. Actually, the current transients shown in Fig. 2 (b), which reveal intervals of weakly increasing currents with time, may also be taken as an indication for oxygen formation, since recently, an increasing current with time has been related to the electronic component of the current and to the formation of oxygen gas, even though it is not clear whether this model is applicable to our implementation [17]. With the water film formed, it may be more difficult for the oxygen to escape into the atmosphere and lead to the formation of voids inside the $TiO_x$ [20], as has been reported elsewhere for different anodization setups. In this case, the vertical growth is essentially due to a swelling and would go along with an increased porosity. Also, since it is well-known that $TiO_x$ can be hydrated to significant levels [33,34], water may get incorporated in the film via the forces the electric field inhomogeneities exert on the water molecules. Possibly, all these mechanisms contribute to some extent to the vertical growth. It should be noted that our results are in tune with the general observation that a faster growth process leads to oxide films with smaller mass density and more disorder [16].

Complementary information can be obtained from the current-voltage (IV) - characteristics as a function of the bias voltage and the period of time over which it is applied, see Fig. 5. In dry air, see Fig. 5 (a), we observe a relatively small increase of the
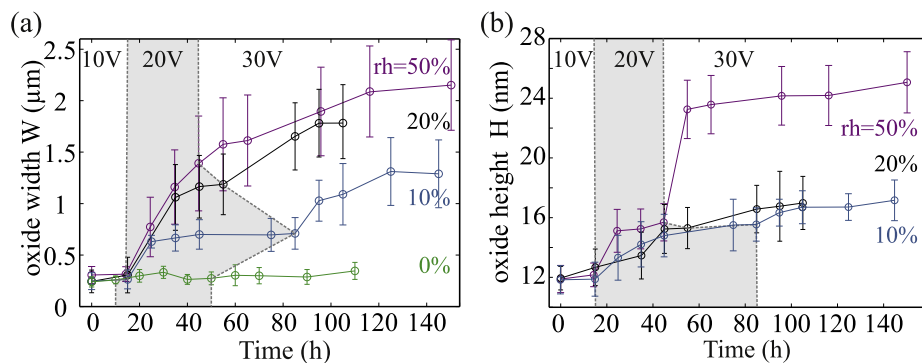


**Fig. 4.** Measurements of the width (a) and height (b) of the oxide lines during anodization at different relative humidities (rh) and bias voltages. The error bars denote the standard deviation, and the gray areas indicate the intervals where a constant bias voltage of 20 V was applied for all relative humidities. (For interpretation of the references to color in this figure legend, the reader is referred to the Web version of this article.)
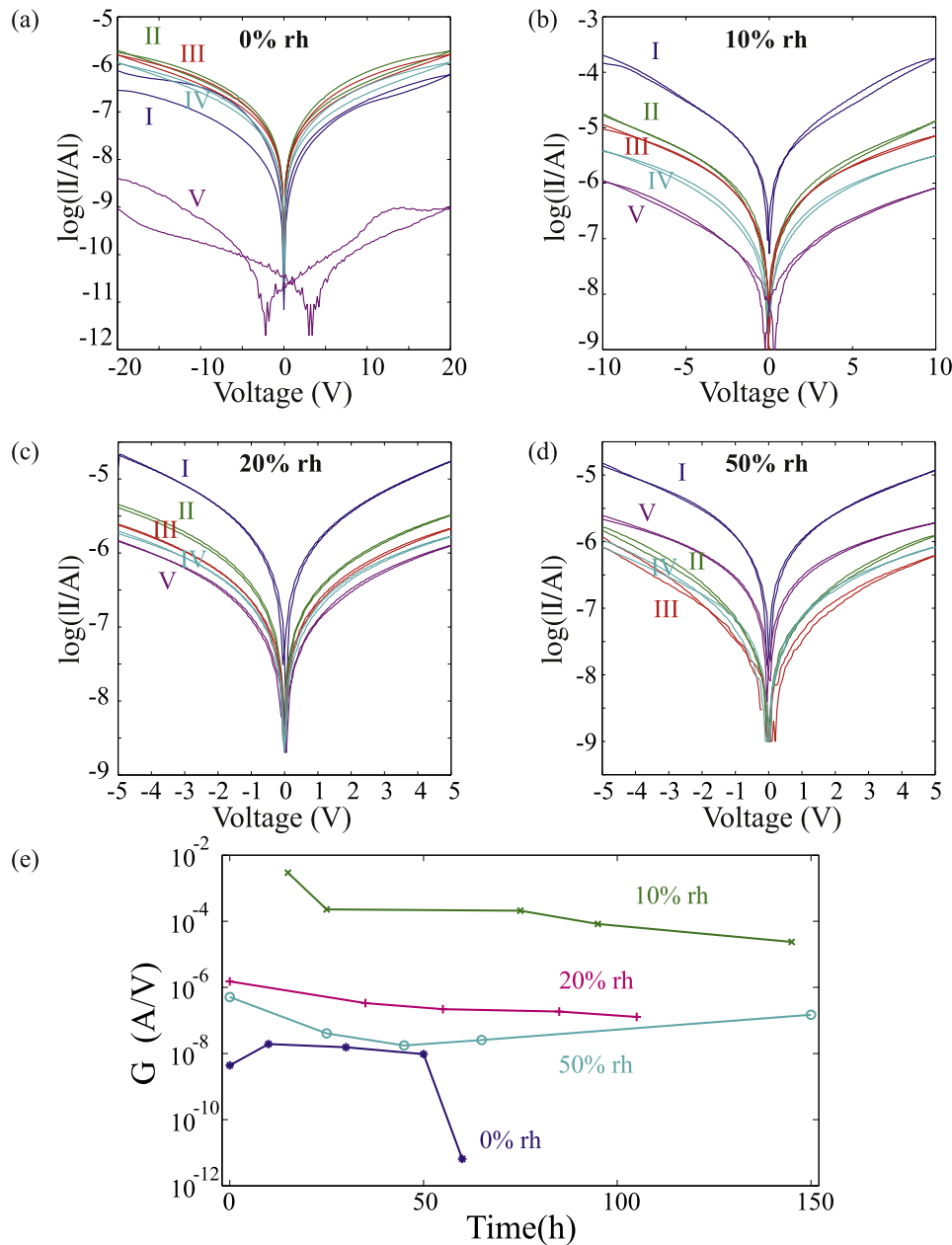
**Fig. 5.** Changes of the current-voltage characteristics during the oxide growth in air with relative humidities varying between 0 (a) and 50% (d). The corresponding conductances extracted from the slope of the current-voltage characteristics close to V = 0 are shown in (e). Roman numbers refer to the topographic pictures in Figs. 2 and 3. (For interpretation of the references to color in this figure legend, the reader is referred to the Web version of this article.)

conductance between I and II. This is attributed to memristive effects inside the TiO$_x$ [35]: a redistribution of oxygen vacancies as well as the formation of local Magnéli phases mentioned above may increase the conductance. This is typically accompanied by hysteretic behavior, which we observe here as well. In between points in time III to V, the conductance decreases by more than three orders of magnitude. This is in tune with the removal of the TiO$_x$ in large electric fields, such that the cross section of the conductive path shrinks until finally, the current starts to flow via the substrate. Since electrostriction may precede the removal of the oxide, it appears also plausible that a change of the IV - traces is observable even in stages during which the oxide is still present. At low humidities (rh of 10% and 20%, shown in Fig. 5(b) and (c)), a monotonous decrease of the conductance during all stages of the anodization process is detected. The conductances, i.e., the slopes of the current-voltage characteristics close to V = 0, are plotted separately in Fig. 5 (e). We take this as an indication that in this regime, the width of the oxide film dominates the conductance, while structural and morphological modifications are of minor relevance, although a weak hysteresis is visible in some traces. As the humidity is increased into the regime where a fluid water film is present (rh = 50%, Fig. 5 (d)), the evolution of the IV traces gets non-monotonous, i.e., the conductance decreases in stages I to III and increases afterwards, even though the width of the oxide film is still growing. In comparison to the morphology pictures shown in Fig. 3 and the evolution of the height in Fig. 4 (b), it immediately catches the eye that the increase of the conductance correlates with the onset of the growth in vertical direction, indicating that
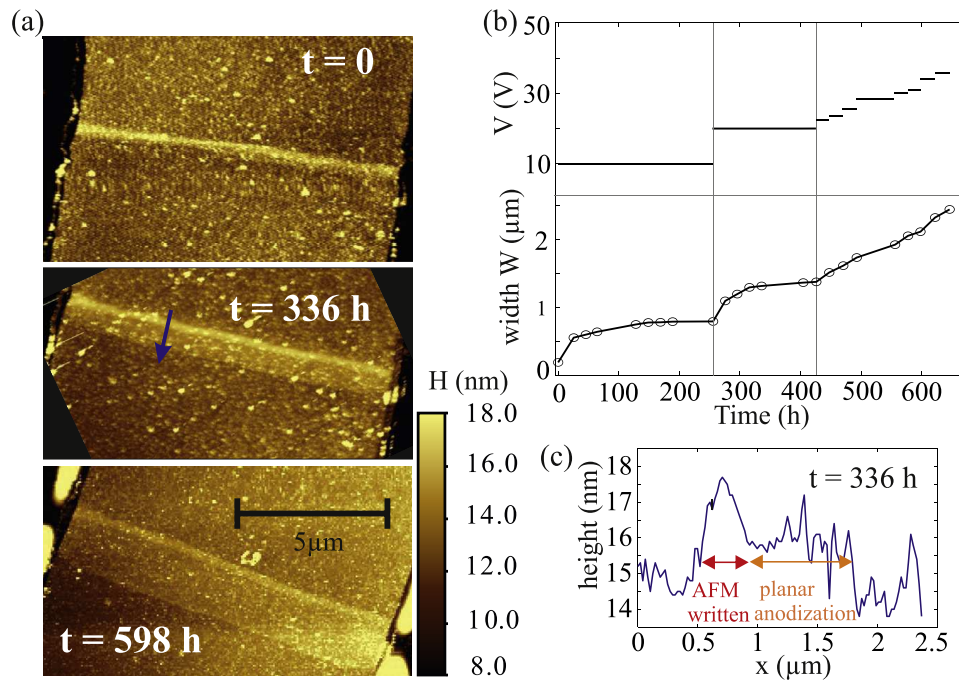
**Fig. 6.** Growth dynamics and morphology in the absence of atmospheric oxygen. (a) Snapshots of the oxide line before (top) during (center) and after (bottom) the anodization experiment. The points of time t refer to the duration of the experiment as shown in (b), where the applied voltages and the resulting average width W of the oxide line are given. In (c), the height profile along the blue arrow in (a) is reproduced, showing that the initial oxide line written by the AFM is higher than the oxide grown under the longitudinal bias voltage. (For interpretation of the references to color in this figure legend, the reader is referred to the Web version of this article.)

indeed additional $TiO_x$ is formed by the drift of $Ti^{4+}$ - ions into the oxide. Note that the stripes do form also under smaller voltages and humidities, such that their formation does not correlate with the evolution of the conductance.

It was already mentioned above that molecular oxygen may contribute to the anodization of Ti as well [36]. To shed some light on the role of the atmospheric oxygen in our experiment, we studied the growth of the oxide line in nitrogen atmosphere at a low rh of 10%, i.e., the same rh as in the experiment shown in Fig. 2 it will be compared to, see Fig. 6. Under these conditions, the threshold voltage for anodization is somewhat lower, since a clear increase in width already at $V = 10$ V is observed, corresponding to a threshold electric field of $\approx 2 \times 10^7$ V/m, see Fig. 6(a and b). This oxide film is thinner than the original oxide line and has a noticeable smaller roughness than the oxide that has been grown in the presence of atmospheric oxygen, see Fig. 6 (c). For example, a roughness of $\approx 0.72$ nm is measured after an anodization time of 336 h. Qualitatively, however, the increase in width has a similar time dependence and appears to be dominated by the longitudinal electric field. This is supported by the data shown in Fig. 6 (b) for times $t > 400$ h where potentiodynamic growth has been established, which show an approximately linear relation between the voltage and the width W. Thus, the presence of oxygen gas increases the threshold voltage for the growth and causes the roughening of the film, in agreement with earlier studies on samples where oxygen was incorporated in the metal [20]. A clarification of the underlying mechanisms is beyond the scope of the paper. Possibly, due to the smaller partial oxygen pressure gradient between the sample and the atmosphere, the oxygen gas that forms during the oxidation may have more difficulties to escape into the environment when atmospheric oxygen is present. Incorporation of atmospheric oxygen into the Ti may also play a role. Furthermore, the oxygen contents of $TiO_x$ grown in air may be higher than that one grown in nitrogen atmosphere. Since oxygen vacancies increase the conductivity of $TiO_x$, this would change the electric field distribution between the oxide and the $Ti/TiO_x$ Schottky barrier, which means that the effective bias voltage across the Schottky barrier is larger for the film grown in nitrogen atmosphere. Following this line of arguing, the smaller threshold voltage of the $TiO_x$ grown in nitrogen atmosphere suggests that the onset of the anodization is determined by the voltage drop across the $TiO_x/Ti$ interface at the anode.

## 4. Summary and conclusions

To summarize, we have shown that lateral $Ti/TiO_x$ heterojunctions, which are present in the implementations of various sample designs, like self-aligned gate electrodes, nanojunctions for single molecule measurements, memristors or on-chip gas sensors, can be substantially changed by the application of bias voltages across the $TiO_x$. The composition of the atmosphere, in particular the presence or absence of oxygen gas and the relative humidity, together with the applied bias voltage and the exposure time, form the parameters that control these modifications. Most importantly, the oxide line can be broadened, which changes the effective electrode separation as well as the resistance between them. The effects reported here should thus not only be taken into account when the behavior of the corresponding devices is discussed, but they may also be used actively to tailor the properties of the $Ti/TiO_x$ junctions according to the specific requirements. In dry atmosphere, a strong electric field can be used to adjust the conductance of

the oxide or to remove the oxide all together. For applications in the field of gas sensing, on the other hand, a rough surface and a porous morphology is advantageous, since it enables easier penetration of the gas into the oxide as well as deposition of metal clusters that activate the gas sensing. This can be achieved by exposing the sample to an electric field in an atmosphere that contains oxygen and has high relative humidity, such that a fluid water film is present on the sample. For obtaining a particular thin oxide of low roughness, anodization in the absence of atmospheric oxygen and a low relative humidity is preferable.

We have furthermore started to interpret the underlying physics and electrochemistry mainly with the help of analogies to established knowledge about comparable methods. Within this approach, the observed structural changes indicate that the phenomenology is caused by a combination of ionic motion inside the oxide, the incorporation of oxygen gas into the metal or the oxide, as well as by electromechanical mechanisms like electrostriction or field-induced dehydration of the oxide. This interpretation needs to be substantiated in further experiments which represent, however, a major effort and are beyond the scope of the present work, mainly for two reasons. First of all, an analysis using established tools like X-ray diffraction, photoelectron spectroscopy or Raman spectroscopy, for example, is hampered by the small oxide quantities involved in our experiments. Second, the specific experimental conditions for this anodization, namely the planar oxide growth in close vicinity to the substrate, the electrolyte which does not carry the full anodization current, as well as the fact that oxygen as well as chemi- and physisorbed water appears to be involved, may lead to unconventional contributions to the growth and ripening dynamics.

## Acknowledgements

## Appendix A. Supplementary data

Supplementary data related to this article can be found at https://doi.org/10.1016/j.spmi.2018.09.006.

## References

[1] O.K. Varghese, D. Gong, M. Paulose, K.G. Ong, C.A. Grimes, Hydrogen sensing using titania nanotubes, Sensor. Actuator. B 93 (2003) 338.
[2] M. Paulose, O.K. Varghese, G.K. Mor, C.A. Grimes, K.G. Ong, Unprecedented ultra-high hydrogen gas sensitivity in undoped titania nanotubes, Nanotechnology 17 (2006) 398.
[3] M. Cerchez, H. Langer, M.E. Achhab, T. Heinzel, H. Lüder, D. Ostermann, Dynamics of hydrogen sensing with Pt/$TiO_2$ Schottky diodes, Appl. Phys. Lett. 103 (2013) 033522.
[4] S.A. Akbar, L.B. Younkman, Sensing mechanism of a carbon monoxide sensor based on anatase titania, J. Electrochem. Soc. 144 (1997) 1750.
[5] J.J. Yang, F. Miao, M.D. Pickett, D.A.A. Ohlberg, D.R. Stewart, C.N. Lau, R.S. Williams, The mechanism of electroforming of metal oxide memristive switches, Nanotechnology 20 (2009) 215201.
[6] P. Knauth, H.L. Tuller, Electrical and defect thermodynamic properties of nanocrystalline titanium dioxide, J. Appl. Phys. 85 (1999) 897.
[7] D.-H. Kwon, K.M. Kim, J.H. Jang, M.M. Jeon, M.H. Lee, G.H. Kim, X.-S. Li, G.-S. Park, B. Lee, S. Han, M. Kim, C.S. Hwang, Atomic structure of conducting nanofilaments in $TiO_2$ resistive switching memory, Nat. Nanotechnol. 5 (2010) 148.
[8] D.B. Strukov, G.S. Snider, D.R. Stewart, R.S. Williams, The fourth circuit element, Nature 453 (2008) 80.
[9] R. Held, T. Heinzel, P. Studerus, K. Ensslin, M. Holland, Semiconductor quantum point contact fabricated by lithography with an atomic force microscope, Appl. Phys. Lett. 71 (1997) 2689.
[10] M. Sigrist, A. Fuhrer, T. Ihn, K. Ensslin, D.C. Driscoll, A.C. Gossard, Multiple layer local oxidation for fabricating semiconductor nanostructures, Appl. Phys. Lett. 85 (2004) 3558.
[11] M. Frimmer, G. Puebla-Hellmann, A. Wallraff, L. Novotny, The role of titanium in electromigrated tunnel junctions, Appl. Phys. Lett. 105 (2014) 221118.
[12] D. Ielmini, R. Waser (Eds.), Resistive Switching, Wiley-VCH, 978-3-527-33417-9, 2016.
[13] S. Herbertz, M. Cerchez, T. Heinzel, On-chip planar hydrogen sensor with sub-micrometer spatial resolution, Sensor. Actuator. B 221 (2015) 401.
[14] S. Lemeshko, S. Gavrilov, V. Shevyakov, V. Roschin, R. Solomatenko, Investigation of tip-induced ultrathin ti film oxidation kinetics, Nanotechnology 12 (2001) 273–276.
[15] W.F. Pasveer, J. Cottaar, C. Tanase, R. Coehoorn, P.A. Bobbert, P.W.M. Blom, D.M. de Leeuw, M.A.J. Michels, Unified description of charge-Carrier mobilities in disordered semiconducting polymers, Phys. Rev. Lett. 94 (2005) 206601.
[16] J.F. Vanhumbeeck, J. Proost, Current understanding of Ti anodisation: functional, morphological, chemical and mechanical aspects, Corrosion Rev. 27 (2009) 117.
[17] H. Lu, H. Fan, R. Jin, B. Chong, X. Shen, X. Zhu, Formation and morphology evolution of anodic $TiO_2$ nanotubes under negative pressure, Electrochim. Acta 215 (2016) 380.
[18] M. Yu, C. Li, Y. Yang, S. Xu, K. Zhang, H. Cui, X. Zhu, Cavities between the double walls of nanotubes: evidence of oxygen evolution beneath an anion-contaminated layer, Electrochem. Commun. 90 (2018) 34.
[19] Z. Chen, C. Lu, Humidity sensors: a review of materials and mechanisms, Sens. Lett. 3 (2005) 274.
[20] H. Habazaki, T. Ogasawara, H. Konno, K. Shimuzu, K. Asami, K. Saito, S. Nagata, P. Seldon, G.E. Thompson, Growth of anodic oxide films on oxygen-containing niobium, Electrochim. Acta 50 (2005) 5334.
[21] M.V. Diamanti, M.P. Pedeferri, Effect of anodic oxidation parameters on the titanium oxides formation, Corrosion Sci. 49 (2007) 939.
[22] M. El-Achhab, A. Erbe, G. Koschek, R. Hamouich, K. Schierbaum, A microstructural study of the structure of plasma electrolytically oxidized titanium foils, Appl. Phys. A 116 (2014) 2039.
[23] C. da Fonseca, A. Traverse, A. Tadjeddine, M. de Cunha Belo, A characterization of titanium anodic oxides by x-ray absorption spectroscopy and grazing x-ray diffraction, J. Electroanal. Chem. 388 (1995) 115.
[24] T. Ohtsuka, T. Otsuki, The aging of the anodic oxide of titanium during potentiostatic condition by ellipsometry, Corrosion Sci. 45 (2003) 1793.
[25] D.A. Vermilyea, Stresses in anodic films, J. Electrochem. Soc. 345 (1963) 110.
[26] S.N. Sahu, J. Scarminio, F. Decker, A laser-beam deflection system for measuring stress variations in thin-film electrodes, J. Electrochem. Soc. 137 (1990) 1150.
[27] J.M. Albella, I. Montero, J.M. Martinez-Duart, V. Parkhutik, Dielectric-breakdown processes in anodic $Ta_2O_5$ and related oxides - a review, J. Mater. Sci. 26 (1991) 3422.
[28] J.L. Delplancke, R. Winand, Galvanostatic anodization of titanium 2. reactions efficiencies and electrochemical-behavior model, Electrochim. Acta 33 (1988) 1551.

[29]  M.G. Verge, P. Mettraux, C.O. Olsen, D. Landolt, Rotating ring-disk electrochemical quartz crystal microbalance: a new tool for in situ studies of oxide film formation, J. Electroanal. Chem. 566 (2004) 361.

[30]  P.J. Boddy, Oxygen evolution on semiconducting $TiO_2$, J. Electrochem. Soc. 115 (1968) 199.

[31]  E. Zhuravlyova, L. Igesias-Rubianes, A. Pakes, P. Skeldon, G.E. Thompson, X. Zhou, T. QUance, M.J. Graham, H. Habazaki, K. SHimizu, Oxygen evolution within barrier oxide films, Corrosion Sci. 44 (2002) 2153.

[32]  E. Matykina, R. Arrabal, P. Skeldon, G.E. Thompson, H. Habazaki, Influence of grain orientation on oxygen generation in anodic titania, Thin Solid Films 516 (2008) 2296.

[33]  Y. Serruys, T. Sakout, D. Gorse, Anodic-oxidation of titanium in $1MH_2SO_4$, studied by rutherford backscattering, Surf. Sci. 282 (1993) 279.

[34]  T. Ohtsuka, M. Masuda, N. Sato, Cathodic reduction of anodic oxide-films formed on titanium, J. Electrochem. Soc. 134 (1987) 2406.

[35]  J.J. Yang, F. Miao, M.D. Pickett, D.A.A. Ohlberg, D.R. Stewart, C.N. Lau, R.S. Williams, J. Am. Chem. Soc. 131 (2009) 11308.

[36]  G.L. Lu, L. Bernasek, J. Schwartz, Oxidation of a polycrystalline titanium surface by oxygen and water, Surf. Sci. 458 (2000) 80.

# 3.1 On-chip modification

Estimations of the electric field distributions at the interfaces of oxide and planar Ti electrodes and across the oxide during on-chip oxidation were done using FEMM (*Finite Element Method Magnetics*). FEMM is an open source finite element analysis software package for solving electromagnetic problems in two dimensions. The program has an interactive shell with a CAD like interface where the geometry of the problem can be laid out and the material properties and boundary conditions are assigned. The area of interest is then divided into a large number of triangles, which is a crucial part of the finite element process and the relevant partial differential equations are solved for the desired field. For the problems considered here, which were approximated to be electrostatic, the program solves the second-order partial differential equation

$$-\epsilon \nabla^2 V(\boldsymbol{r}) = \rho(\boldsymbol{r}), \tag{3.1}$$

which is Poisson's equation for electrostatics. The field distribution was calculated for a cross section of two Ti electrodes of 10 nm height on top of a 300 nm layer of $SiO_2$, that are separated by 200 nm wide and 15 nm high oxide layer representing the AFM written nanowire. To model the different values for the ambient humidity that were used in the experiments in Paper III, water layers of varying thickness were added on top of Ti and $TiO_2$ in the design interface. The boundary conditions were chosen as the Ti electrode potentials (30 V and ground) and a value for the electrical permittivity $\epsilon$ was assigned to each of the other materials: $\epsilon_{TiO_2} = 86$, $\epsilon_{SiO_2} = 3.9$, $\epsilon_{H_2O} = 88$, and $\epsilon_{air} = 1$. Note that these considerations are based on differences in permittivity of the materials and consider electrostatic conditions only. Neither regions of different vacancy concentration, and with it, conductivity in the oxide are considered nor the distinct electronic properties of the metal/oxide Schottky interfaces. Also, no surface inhomogeneity or roughness variations are included. Nevertheless, some of the effects observed in Paper III may to some degree be attributed to the diversion of the electric field inside the $TiO_2$ nanowire, as will be discussed in the following.

In Fig. 3.1 the results of the calculation for the electric field distribution are shown for the $Ti/TiO_2/Ti$ structure. The picture is zoomed in on the interface of the oxide line and the electrode that serves as anode, i.e. the Ti electrode that gets oxidized. The magnitude of the electric field is color-coded as given in the scale and the field direction is depicted as arrows. The situation is shown for dry conditions, i.e. in air of 0 % r.h. [Fig. 3.1 a)], in moderate humidity of around 50 % r.h. leading to a water film in the nm range [184] [Fig. 3.1 b)] and in very humid conditions (80-100 %) with a 50 nm water film on top [Fig. 3.1 c)].

Obviously, the effect of a thick water layer on top of the oxide and the electrodes is that the electric field close to the interface is significantly increased inside the oxide. The potential and field distribution across the complete oxide are depicted in Fig. 3.2. The calculated values correspond to a profile from anode to cathode, crossing the oxide line at half height. With water, the potential drop [Fig. 3.2 a)] as a function of the distance deviates from the approximately linear shape it exhibits in dry conditions: Near the electrodes the potential drops on shorter scales compared to the region around the middle of the oxide line. In accordance to this, as can be seen in Fig. 3.2 b), the electric

field is much more homogeneous inside the oxide with no water in the vicinity, while with the water layer on top it drops by more than a factor of four inside a region of around 50 nm, which is one quarter of the whole oxide. In particular, the tangential component of the electric field $E_t$ that is parallel to the profile line and depicted in Fig. 3.2 d), is enlarged near the electrodes and decreased in the middle of the oxide. This means that drift of oxygen ions towards the anode, which we assumed to be dominating the growth, is driven by larger fields on a comparatively larger scale. Hence, apart from the function as oxygen source, water may also indirectly increase the growth rate of the oxide width in the beginning at higher relative humidity by deviating the electric field.
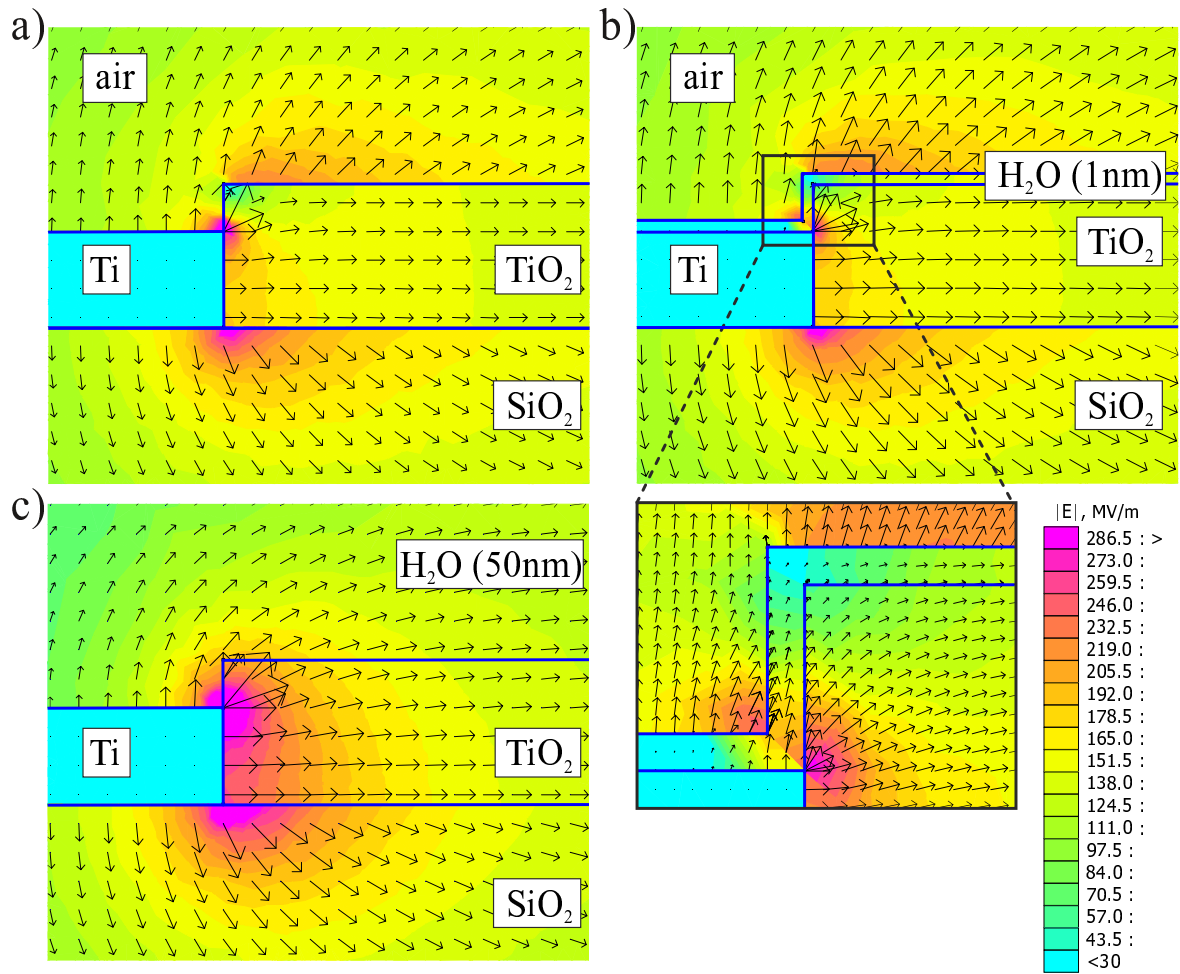


**Figure 3.1:** FEMM calculations of the electric field distribution in $TiO_2$ when a voltage of 30 V is applied to one electrode while the other is grounded. A 200 nm $TiO_2$ line separating two Ti electrodes is modeled for dry conditions (a), for medium r.h. with a 1 nm thick water layer on top (b) with a zoom-in on the threefold interface of Ti, $H_2O$ and $TiO_2$ (down right), and under saturated humidity with a 50 nm thick water layer on top (c).
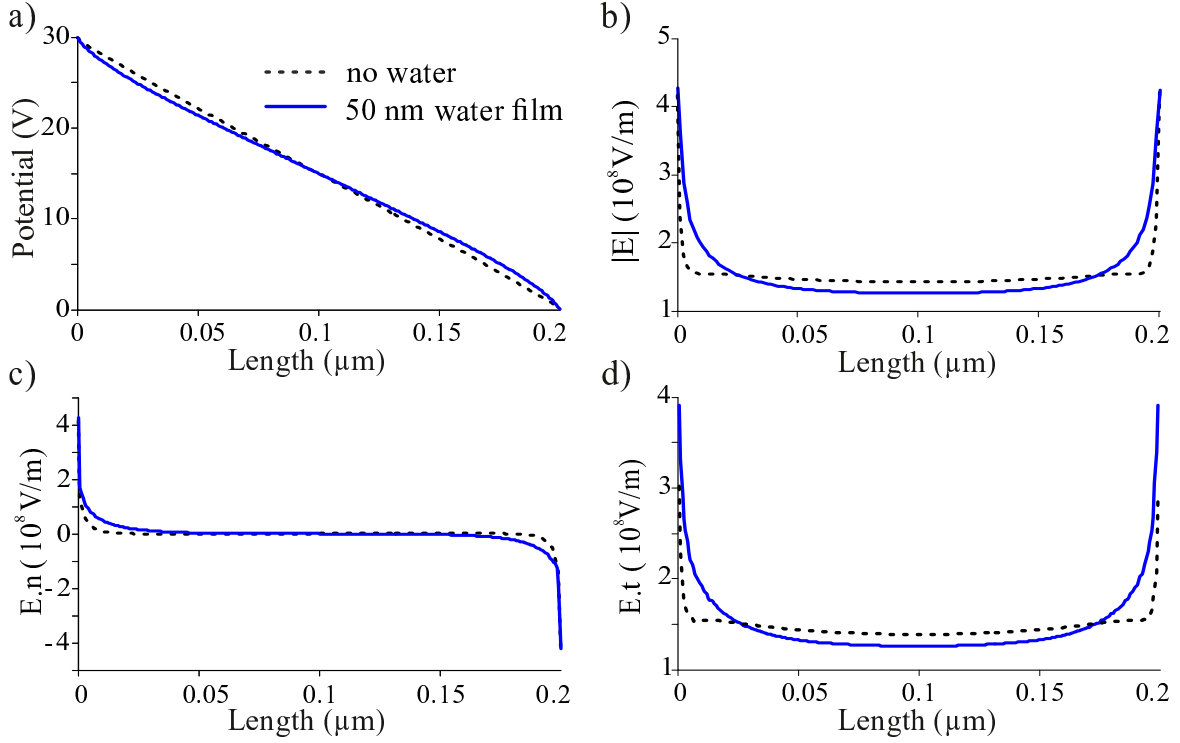
**Figure 3.2:** Profiles of a) potential and b) electric field across a 200 nm wide oxide line at half height. The plots in c) and d) show the electric field components normal and tangential to the profile, respectively.

Moreover, the normal component of the electric field, as shown in Fig. 3.2 c), is increased in the first 20-30 nm near the interfaces when water is present. This can also be seen comparing the vector arrows in Fig. 3.1 a) and c). Also, it is visible in the zoom-in on the threefold interface of Ti, $H_2O$ and $TiO_2$ that the electric field inside the water layer close to the oxide surface tends to orient itself parallel to the surface. This supports our assumption that Ti cations that dissolve in the water may, under sufficiently large electric fields, contribute to the vertical growth by migration through the water layer and subsequent reaction with oxygen anions to form additional oxide material. One reason for the assumption that vertical growth is caused by forming of additional oxide was the coincidence of the starting increase in the oxide height with the increase in the conductance. The quasi-periodic stripe pattern growing from the cathode side and porous like structure at the anode however emerged not to be correlated to changes in the conductivity. We tentatively attributed the latter to $O_2$ gas bubble evolution. According to some reports [51, 75, 244], $O_2$ gas forms and can leave the structure at the anode when a voltage is applied to reduce $TiO_2$ in order to create $V_O$. This is closely related to the forming of conducting channels discussed in section 2.2, which were found right adjacent to bubble areas [75]. Therefore it is imaginable that both, the 'external' oxygen species from air and humidity, and the 'internal' oxygen species that is left from a reduction from $TiO_2$ to $TiO_{2-x}$ contribute to the on-chip growth and complex morphology.

These small deformations and eruption-like features are interesting for potential applications as gas sensors, since the increased surface area may be better accessible for

gas molecules by offering more surface binding sites. Furthermore, a larger and more complex surface facilitates the deposition of catalysts like Pt without running the risk of short-circuiting the electrodes. To check the on-chip modified oxide structures from Paper III for their gas sensing functionality, two samples were sensitized with Pt after the experiments.
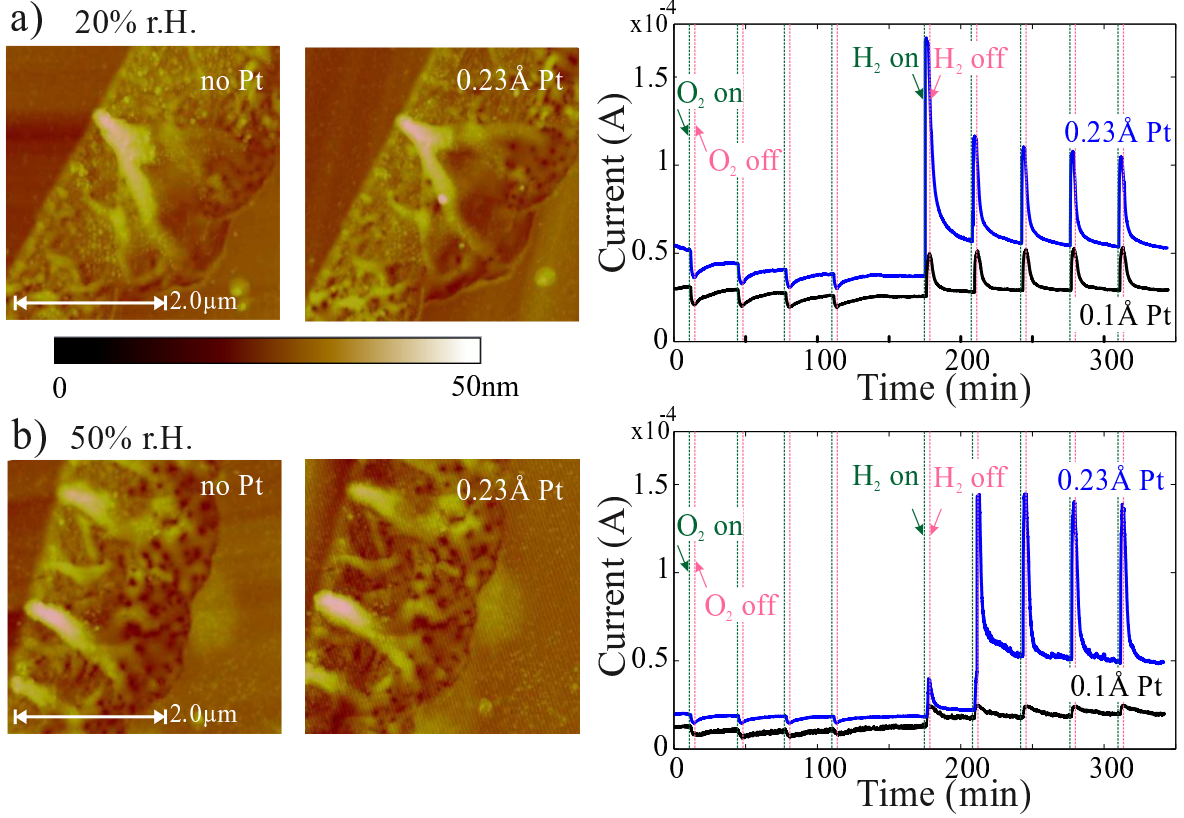


**Figure 3.3:** On-chip modified oxide lines produced in relative humidity of 20 % (a) and 50 % (b). On the left AFM scans are shown before and after Pt deposition. The plots on the right show a sequence of first 20 % $O_2$ pulses followed by 1000 ppm $H_2$ pulses in $N_2$ measured at 10 V bias and room temperature.

The pictures on the left in Fig 3.3 show detailed AFM scans of oxide lines modified on-chip under 20 % (a) and 50 % (b) relative humidity before and after sensitization with Pt. These two samples were chosen for a comparison of the sensing performance because of their similar conductance. The nominal Pt amount of 0.23 Å determined from sputtering parameters is far too little to form a full Pt layer [245], and on the other hand, cannot be observed as clusters or in any other way in the comparison of the surface scans. Nevertheless, this small amount allows a significant sensor response to $H_2$ gas as can be seen in Fig. 3.3 on the right.

The sensor response to hydrogen $S = (R_N - R_{H,3min})/R_N$ at the end of the series of three minute pulses for the structures decorated with 0.23 Å Pt is 0.48 for the structures grown at 20 % r.h. and 0.65 for the ones grown at 50 % r.h. This can be understood considering the larger roughness and swelling achieved during the oxidation in higher

humidity. The experiments were conducted at a bias voltage of $10\,V$, so the applied electric field is rather high and in the order of $10^7\,V/m$. Therefore, the observed drifts can be attributed to EF. Moreover, the necessity of leveling for both, reliable $H_2$ and $O_2$ detection, becomes clear in the impermanence of the response peaks observed during the first $H_2$ exposition. It can also be seen that an increase of the Pt amount from $0.1\,\text{Å}$ to $0.23\,\text{Å}$ enhances the response to $H_2$ significantly while the $O_2$ response does not change, which is an interesting point in terms of cross sensitivity.

Thus the on-chip produced oxide shows indeed similar interaction with gases compared to other $TiO_2$ devices discussed previously in this work. Not only in the field of gas sensors the results are very promising for potential applications of this procedure to create devices with tunable electrode separation, resistance and surface morphology.

# Paper IV    Lateral hydrogen microsensors prepared on-chip by local oxidation of platinum-decorated titanium films

## Lateral hydrogen microsensors prepared on-chip by local oxidation of platinum-decorated titanium films

S. Herbertz, D. Welk, and T. Heinzel[a]
*Solid State Physics Laboratory, Heinrich-Heine-Universität Düsseldorf, 40204 Düsseldorf, Germany*

Titanium microstripes on silicon dioxide substrates are oxidized locally by applying voltages on-chip to lateral electrodes under ambient conditions. This technique enables profound modifications of the electronic circuit. As an example, we transform Ti films decorated by a sub-monolayer of platinum into hydrogen gas microsensors in an otherwise completed device by a silicon-MOS compatible process. © *2018 Author(s). All article content, except where otherwise noted, is licensed under a Creative Commons Attribution (CC BY) license (http://creativecommons.org/licenses/by/4.0/).* https://doi.org/10.1063/1.5025764

## Reference

S. Herbertz, D. Welk and T. Heinzel
AIP Advances **8**, 055301 (2018) ©2018 AIP Publishing LLC
`https://doi.org/10.1063/1.5025764`

## Copyright statement

## Contributions

I established the experimental set-up and prepared the samples. I conducted the on-chip oxidation and gas sensing experiments. I analyzed the experimental data and wrote the main body of the manuscript.

# Lateral hydrogen microsensors prepared on-chip by local oxidation of platinum-decorated titanium films

S. Herbertz, D. Welk, and T. Heinzel[a]
*Solid State Physics Laboratory, Heinrich-Heine-Universität Düsseldorf, 40204 Düsseldorf, Germany*

Titanium microstripes on silicon dioxide substrates are oxidized locally by applying voltages on-chip to lateral electrodes under ambient conditions. This technique enables profound modifications of the electronic circuit. As an example, we transform Ti films decorated by a sub-monolayer of platinum into hydrogen gas microsensors in an otherwise completed device by a silicon-MOS compatible process. © *2018 Author(s). All article content, except where otherwise noted, is licensed under a Creative Commons Attribution (CC BY) license (http://creativecommons.org/licenses/by/4.0/).* https://doi.org/10.1063/1.5025764

Modifying electrode geometries on-chip is a promising concept for some applications such as electronics or sensing. It allows adaptation of lithographically prepared structures to the requirements, which may either be impossible to meet just by lithography, or may change over time, e.g. due to ageing or by failure of a device element. One example of such a concept is the application of electromigration for the fabrication of electrodes with separations in the range of one nanometer.[1] This technique is widely used in basic research to attach two electrical contacts to single molecules for transport measurements.[2,3] Also, nanosized $Fe_2O_3$-photodetectors have been prepared by on-chip thermal oxidation of iron films.[4] A particularly well suited material for on-chip modifications is titanium. The material can be deposited in form of thin films with thicknesses of a few nanometers, low roughness and a natural oxide of just a few nanometers thickness. Also, stable titanium oxides can be easily produced by thermal or electrochemical techniques. For example, thin Ti films have been oxidized locally by scanning lithography to form nanoelectrodes on the surface of semiconductor heterostructures.[5] Recently, it has been argued that oxidation of Ti layers used as adhesion layers provide the actual tunnel barrier in nanogapped electrodes for single molecule measurements.[6] Since titanium oxides are furthermore well-established components in applications as diverse as, e.g., reflective coatings, UV protection and catalysis,[7] solar cells,[8] gas sensors[9,10] or active elements in memristive circuits,[11,12] on-chip modifications of $Ti/TiO_x$ structures are of high potential interest.

Here, we show that Ti stripes can be oxidized on-chip by applying voltages to suitably designed lateral electrodes. This concept allows modifications of the electronic circuit by changing for example the resistance, the capacitance or the sensitivity to gas exposure. After a description of the sample preparation and the experimental setup, the lateral oxide growth is characterized and analyzed, followed by a demonstration of the preparation of a hydrogen microsensor by this technique. We conclude with a summary and an outlook.

Titanium films of 10 nm thickness are prepared in suitable geometries by optical lithography and subsequent RF sputtering of Ti (rate 0.1Å/s) on $Si/SiO_2$ wafer chips with a $SiO_2$ layer of 300 nm thickness, or on quartz substrates of 300 $\mu$m thickness. The sample layout is illustrated in Fig. 1(a).

For electrical contacting, pads of 20 nm Cr and 200 nm Au were prepared on top of the films at its ends by thermal deposition with an electron beam evaporator. Two types of samples were prepared for the oxidation step. The first type (labeled *Ti-stripes*) contains Ti stripes as just described. The two-dimensional sheet resistivity of these films, measured in a 4-probe geometry to avoid contact

---

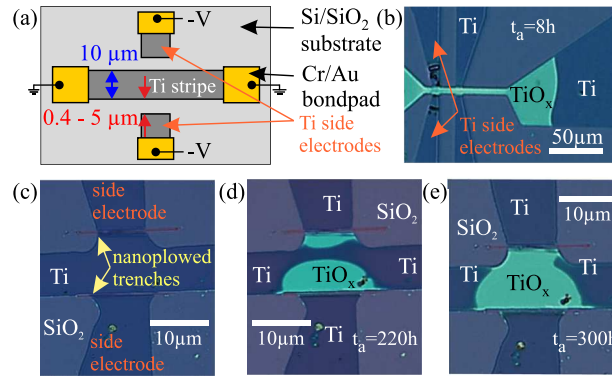[a]Electronic mail: thomas.heinzel@hhu.de

FIG. 1. (a) Scheme of the sample geometry. (b) Top view of a Ti/Pt stripe after an anodization time of $t_a = 8$ h. The TiO$_x$ appears as light cyan section of the stripe. A Ti stripe without Pt on top, sandwiched between the two side electrodes used as cathodes before (c), during (d, $t_a = 220$ h), and after (e, $t_a = 300$ h) the oxidation. In this sample, the gaps between the side electrodes and the stripe are formed by trenches that were prepared by AFM nanoplowing. All pictures have been taken in an optical microscope.

resistance contributions, is $\rho_{\text{Ti-stripes}} = 380$ $\Omega$, considerably larger than 42 $\Omega$ as expected from the literature value of the resistivity of Ti, i.e., $\rho_{\text{Ti}} = 420$ n$\Omega$m.[13] We attribute this difference to a combination of the effectively reduced film thickness due to the formation of the natural oxide of $2 - 6$ nm thickness,[14] plus the additional scattering by surface and interface roughness that is well-known for films with thicknesses in the range of the mean free path or below.[15,16] The second type of samples are Ti stripes where an additional sub-monolayer of Pt (nominal thickness 3 Å, deposition rate 0.05 Å/s) was sputtered directly on the Ti film, which resulted in a coverage with disconnected Pt islands. These samples are referred to as *Ti/Pt-stripes*. The sheet resistivity of these films is $\rho_{\text{Ti/Pt-stripes}} = 18.9$ k$\Omega$, much larger than $\rho_{\text{Ti-stripes}}$. We assume that due to the catalytic activity of Pt, an oxide layer of somewhat larger thickness may form on these Ti films when they are exposed to ambient conditions.

The key structural element of the samples is the pair of side electrodes that sandwich the Ti stripe to be oxidized, see Fig. 1(a, c). The lateral gaps were prepared either directly by optical lithography, or after the deposition of the Ti films by atomic force microscope (AFM) nanoplowing. Here, a diamond-coated AFM tip was used to disconnect the Ti film by mechanical scratching in the contact mode. Tip scan velocities of 1 to 4 $\mu$m/s were used, and the deflection set point controls the depth of the nanoplowed trenches. The widths of the lateral gaps in our samples vary between 400 nm and 5 $\mu$m.

All electronic sample modifications and measurements are carried out in a sealed sample chamber in which the temperature is actively stabilized to 20 °C. The composition of the atmosphere can be controlled via mass flow controllers for oxygen, nitrogen and hydrogen. The humidity is adjustable by guiding the dry nitrogen gas through a humidifier before it enters the sample chamber. Electrical feedthroughs allow the application and measurement of electrical signals.

The two side electrodes are used to oxidize the central Ti stripe by a lateral anodization process. The rate of the anodic oxidation depends on the applied voltage, the resistance of the forming oxide and the humidity.[17] The water film that forms naturally under ambient conditions acts as electrolyte. The relative humidity of the atmosphere is adjusted to 90 %. The oxidation process works also at lower humidities down to $\approx 40$ %, albeit with much slower oxidation rates. Negative voltages in the range $80$ V $\leq |V| \leq 90$ V are applied to both side electrodes with respect to the grounded Ti stripe. The on-chip oxidation process is illustrated in Figs. 1(c–e) on a Ti-stripe deposited on quartz glass, with two side electrodes with separations of $\approx 400$ nm, Fig. 1(c). For electrode voltages $V > -80$ V, no oxidation could be detected, while voltages $V < -90$ V were not used in order to avoid an electrical breakdown across the SiO$_2$. Fig. 1(d) shows the sample as seen in an optical microscope after applying $V = -80$ V for 220 h. The oxidized regions of the stripe are readily visible as bright areas. The microscopic picture of anodic oxidation of Ti has been described in detail elsewhere.[18] We attribute the different growth

rates at both sides to the slightly different widths of the lateral gaps between the stripe and the two electrodes. After an oxidation time of 300 h, the oxide extends across the whole stripe. The increase of the resistance to 10 GΩ indicates that the full cross section of the stripe has been oxidized. Under these conditions, the lateral oxide growth velocity is estimated to $v_g \approx 8.3$ pm/s. Atomic force microscopy is used to measure the increase of the film height by the oxidation. For this particular sample, the height increases by $\delta h = 6.1$ nm on average. The corresponding resistivity of the oxide is $\rho(TiO_x) \approx 10^{-2} \Omega m$, many orders of magnitude smaller than the literature values for $\rho(TiO_2)$ $\epsilon[10^{11}\ \Omega m, 10^{16}\ \Omega m]$, but comparable to the values reported for reduced $TiO_x$ with $x\epsilon[1.75, 1.9]$.[19] This indicates that the formed titanium oxide is strongly reduced, a conclusion which is supported by our observation that annealing the sample in dry air at $T = 180°C$ for $1h$, a process which oxidizes the material further, increases the resistivity by about two orders of magnitude.

We proceed by discussing the properties of the oxidized Ti/Pt-stripes on Si/SiO₂. The lateral gap between the stripe and the electrodes is $\approx 400$ nm. Fig. 1(b) shows an optical microscope picture of the sample after applying $-80$ V to the side electrodes for 10 h. The lateral oxide growth velocity is $v_g \approx 10.3$ nm/s, which is a factor of about 1300 larger than that one observed at the Ti-stripes. This suggests that Pt at the surface greatly accelerates the oxidation process via its catalytic activity. In order to shed some light on the role the Pt plays for the oxidation process, we performed atomic force microscopy (AFM) and laterally resolved energy dispersive X-ray spectroscopy (EDX) with a scanning electron microscope (SEM) on the films, see Fig. 2.

The AFM image of the oxidized surface shows an inhomogeneous topography with local elevations of heights up to 2 nm and with lateral extensions between 10 nm and 1 $\mu$m, see Fig. 2(a). The SEM-EDX analysis reveals that these elevations are not, as one might naively assume, Pt particles. Rather, they are either gold particles which stem from the wire bonding process and are of no further interest here, or they consist of nanoporous TiO₂ mounds with Pt at their centers, see Figs. 2(b, c). On the other hand, a difference of the oxygen or titanium signal between inside and outside these mounds could not be detected.

These observations suggest that Pt plays a major role in providing oxygen in a form usable for Ti oxidation in an electric field. Possibly, O₂ dissociation at the Ti surface[20] and fast catalytic splitting of adsorbed water at the Pt sites[21] provides large amounts of adsorbed OH groups according to

$$H_2O_{ad} + O_{ad} \rightarrow 2OH_{ad}. \qquad (1)$$
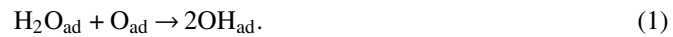
These OH groups may permeate the natural oxide layer, starting from the Pt islands. Formation of TiO₂ out of OH$_{ad}$ can take place according to

$$Ti + 2h^+ + 2OH^- \rightarrow TiO_2 + H_2. \qquad (2)$$
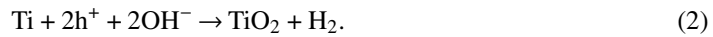
Thus, in Ti stripes covered with Pt islands exposed to an electric field, two oxidation processes occur simultaneously, namely a slow one, based on the consumption of adsorbed oxygen atoms
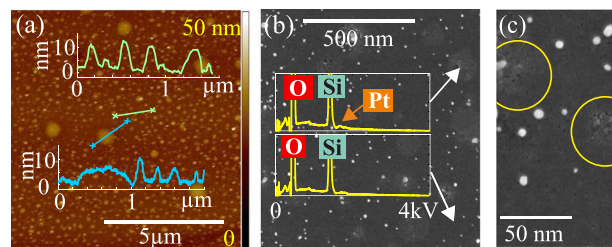


FIG. 2. (a) Topographical AFM scan across the on-chip oxidized surface of a Ti/Pt-stripe. The overlays show two line scans across typical surface structures. The yellow labels to the right indicate the range of the color height scale. (b) SEM image and EDX spectra taken at the points indicated by the arrows inside (lower trace) and outside (upper trace) a TiO$_x$ mound. Outside the mound, only the Si and O signals can be seen, which originate predominantly from the substrate due to the EDX penetration depth of $\approx 700$ nm. Inside the mounds, an additional, weak Pt signal can be detected. The acceleration voltage of the SEM was 5 kV. We note that observing an EDX signal of Ti requires larger acceleration voltages. The bright spots are Au nanoparticles. (c) SEM image at larger magnification which shows the nanostructure of the porous TiO$_x$ mounds.

according to the Mott model,[18] which takes place during oxidation of the Ti stripes, plus a faster one, which is catalytically driven by Pt and spreads radially from those Pt islands that are exposed to a sufficiently strong electric field and which results in more porous $TiO_x$.

A Pt submonolayer does not only accelerate the anodization process, it also forms a functional part in the operation of the oxidized stripes as hydrogen gas microsensors. Prior to the anodic oxidation step, the conductance of the Ti/Pt stripes is completely insensitive to even large atmospheric hydrogen volume fractions of $c(H_2) = 4\%$, see Fig. 3(a). After the on-chip oxidation step, however, a sensitivity of the conductance to hydrogen gas with volume fractions in the ppm regime at room temperature is observed, see Fig. 3(b, c). For comparison, we have also sputtered a Pt submonolayer on the anodically oxidized Ti-stripes, which results in a type of lateral sensor that has been discussed before, even though the oxidation technique was different.[22] Both sample types are sensitive to atmospheric hydrogen, showing that the differences in the oxidation process are not decisive for the sensing performance. However, differences in the sensing response do exist.

For a comparison, source-drain bias voltages between $V = 1$ V and $V = 18.7$ V were applied to the Ti- and the Ti/Pt stripes, respectively, such that the lateral oxides were exposed to the same electric field of $F = 62.5$ kV/m. In both types of sensors, we detect an onset of the response to hydrogen at a volume fraction of $\approx 20$ ppm and a sensing current that increases monotonically with $c(H_2)$.

The oxidized Ti/Pt-stripes have a significantly larger off-conductivity than the oxidized Ti stripes with subsequent Pt deposition, and the response $S = I_H/I_N$ is one order of magnitude larger in the Ti/Pt-sensors. This behavior may reflect the differences in the structure of the formed oxides, and the Pt particles in the Ti/Pt-films may be covered to some extent by the grown oxide, which would make them less accessible for the hydrogen gas. The response in air is comparable to that one in nitrogen for $c(H_2) \leq 1\%$ and gets larger than in nitrogen for higher hydrogen volume fractions, see Fig. 4(a, b). However, this is difficult to interpret within a physical picture considering the significant currents in the off-state which increase over time, most likely due to incomplete hydrogen removal. This effect is stronger in nitrogen atmosphere. This can be explained by the fact that dry air supports the desorption of hydrogen via the additional possibility of water formation at the surface.[23] Both the sensing and the recovery part on the transients can be fitted reasonably well by a sum of two
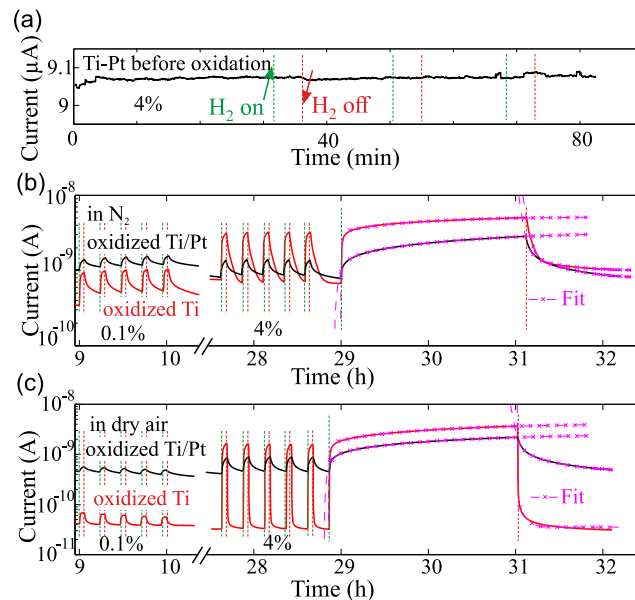


FIG. 3. Response to 4% hydrogen of Ti-Pt stripe (a), Sensing performance of on chip grown oxide films in dry nitrogen athmosphere (b), and in dry air (c) to 3 min $H_2$ pulses of volume fractions 100 ppm and 4%. In addition, the response to long exposure times is shown and fitted by a sum of two exponentials. Data were taken at a bias electric field of 62.5 kV/m at 25°C. The dashed green and red lines indicates the points in time when hydrogen gas was added to or removed from the atmosphere, respectively.
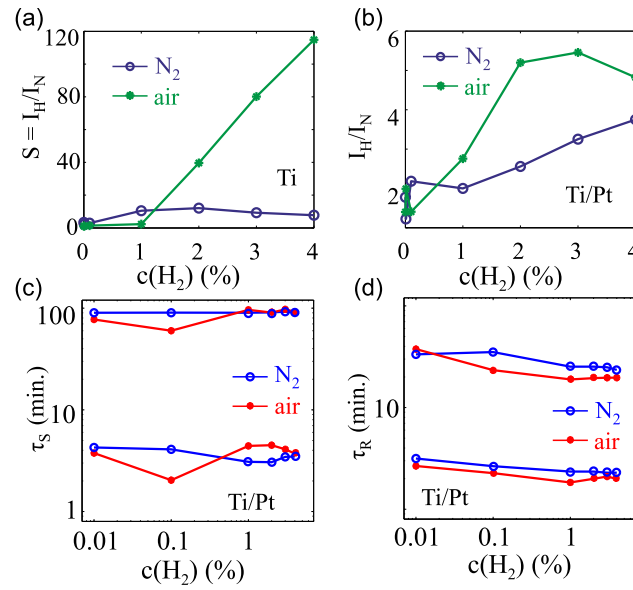
FIG. 4. Response S of the oxidized Ti- (a) and Ti/Pt- (b) stripes in nitrogen and air. In (c) and (d), the response ($\tau_S$) and recovery ($\tau_R$) time constants as obtained from the fits to the sum of two exponentials are shown, using an oxidized Ti/Pt film as an example.

exponentials, see Fig. 3(b). The time constants $\tau_S$ and $\tau_R$ for response and recovery are in the range of minutes and despite the extremely thin sensor films, they do not depend strongly on $c(H_2)$. There are no qualitative differences in the behavior of the time constants of the Ti-stripes as compared to the Ti/Pt-stripes, and we exemplify their properties using a Ti/Pt-stripe, see Fig. 4(c, d). Two distinct time constants can be observed in both atmospheres and in the response as well as in the recovery. They differ by roughly an order of magnitude. This suggests that the transformation of molecular atmospheric hydrogen into an electron donor inside $TiO_x$ and vice versa takes place in at least two steps. We first interpret the times in response to hydrogen exposure. The observed independence of $\tau_S$ on the hydrogen volume fraction suggests that even at our small degrees of Pt coverage, the chemical splitting of hydrogen molecules at Pt is not saturated. Rather, we assume that one limiting factor is the lateral, radial diffusion of atomic hydrogen from the Pt islands through the compact $TiO_2$. The chemical hydrogen diffusion coefficient in $TiO_2$ increases with its porosity. Assuming $D = 10^{-15}$cm$^2$/s for compact $TiO_2$,[24] an order-of magnitude estimation for the time needed to cross the average distance between Pt particles of 50 nm gives $\approx$ 3 h. The shorter observed time scale may reflect the porosity of the film, which would result in much larger effective diffusion constants. The fact that we observe two time scales may be due to different diffusion channels or to the dynamics of the electron transfer from the hydrogen atom into the $TiO_x$. A similar interpretation can be given for the recovery time constants. Measurements on samples with varying Pt coverage and film thicknesses would provide further insight into these mechanisms, which are beyond the scope of the present work.

To summarize, we have demonstrated that Ti stripes on top of Si/SiO$_2$ can be oxidized on-chip by local anodization using lateral microelectrodes. This process, which can be visualized easily *in-situ* in an optical microscope, enables profound modifications of the electronic and sensing properties of the circuit. A coverage of the pristine Ti film by a submonolayer of Pt greatly accelerates the anodization, most likely via catalytic splitting of water. As an application example, a Ti stripe covered with Pt was transformed on-chip into an efficient hydrogen sensor with this Si-MOS compatible technology. The samples can be designed in such a way that the oxidation sets in at much larger voltages than used in typical sensing experiments. This allows, for example, the definition of redundant sensor array layouts in which the elements can be selectively activated during post-assembly of the chip.

[1] H. Park, A. K. Lim, A. P. Alivisatos, J. Park, and P. L. McEuen, Appl. Phys. Lett. **75**, 301 (1999).

[2] H. Park, A. N. Pasupathy, J. I. Goldsmith, C. Chang, Y. Yaish, J. R. Petta, M. Rinkoski, J. P. Sethna, H. D. Abruna, P. L. McEuen, and D. C. Ralph, Nature **417**, 722 (2002).

[3] W. J. Liang, M. P. Shores, M. Bockrath, J. R. Long, and H. Park, Nature **417**, 725 (2002).

[4] L.-C. Hsu, Y.-P. Kuo, and Y.-Y. Li, Appl. Phys. Lett. **94**, 133108 (2009).

[5] R. Held, T. Heinzel, P. Studerus, K. Ensslin, and M. Holland, Appl. Phys. Lett. **71**, 2689 (1997).

[6] M. Frimmer, G. Puebla-Hellmann, A. Wallraff, and L. Novotny, Appl. Phys. Lett. **105**, 221118 (2014).

[7] R. E. Williams, *Titanium dioxide: production, properties and effective usage*, ISBN 978-3-86630-812-1 (Vincentz Network, 2013).

[8] J. Nowotny, *Oxide Semiconductors for Solar Energy Conversion: Titanium Dioxide*, ISBN 9781439848395 (CRC Press, 2011).

[9] N. Yamamoto, S. Tonomura, T. Matsuoka, and H. Tsubomura, Surf. Sci. **92**, 400 (1980).

[10] X. Chen and S. S. Mao, Chem. Rev. **107**, 2891 (2007).

[11] D. B. Strukov, G. S. Snider, D. R. Stewart, and R. S. Williams, Nature **453**, 80 (2008).

[12] K. Szot, M. Rogala, W. Speier, Z. Klusek, A. Beshehm, and R. Waser, Nanotechnology **22**, 254001 (2011).

[13] E. A. Belskaya and E. Y. Kulyamina, High Temp. **45**, 785 (2007).

[14] J. Lausmaa and B. Kasemo, Applied Surface Science **44**, 144 (1990).

[15] Y. Namba, Japanese Journal of Applied Physics **9**, 1326 (1970).

[16] U. Schmid and M. Grosser, Appl. Phys. A **96**, 921 (2009).

[17] S. Lemeshko, S. Gavrilov, V. Shevyakov, V. Roschin, and R. Solomatenko, Nanotechnology **12**, 273 (2001).

[18] N. Mott, Trans. Faraday Soc. **43**, 429 (1947).

[19] R. F. Bartholomew and D. R. Frankl, Phys. Rev. **187**, 828 (1969).

[20] G. Lu, S. L. Bernasek, and J. Schwartz, Surface Science **458**, 80 (2000).

[21] S. Völkening, K. Bedürftig, K. Jacobi, J. Wintterlin, and G. Ertl, Phys. Rev. Lett. **83**, 2672 (1999).

[22] S. Herbertz, M. Cerchez, and T. Heinzel, Sensors and Actuators B **221**, 401 (2015).

[23] A. Michaelides and P. Hu, J. Am. Chem. Soc. **123**, 4235 (2001).

[24] G. C. Yu, Phys. Stat. Sol. (a) **198**(2), 302 (2003).

## 3.2 Microdevice preparation for gas sensing

In contrast to the on-chip broadening discussed in the previous section, where a $TiO_2$ nanowire served as 'seed' for further oxidation, no such structure is present in the Ti and Ti/Pt thin films of Paper IV. Instead, we ascribe a relevant function during the process to the native oxide layer. As mentioned in the beginning, the formation of this layer on thin metal films was early described by Mott and Cabrera [60, 85]. One assumption in this model is that electron transport through the thin oxide can happen via thermal emission or via tunneling. Together with adsorbed $O_2$ from air they can form layers of adsorbed oxygen anions [246] and as a result a strong electric field will be set-up in the oxide. The other assumption is that although the solubility of metal cations is considered very low, so passage of metal ions through the oxide via diffusion is improbable, migration of metal ions between interstitial positions towards the surface may take place. This way the oxide grows by metal ions migrating layer by layer through the oxide followed by reaction with the surface $O^{2-}$. Depending on the film thickness and temperature, different approximations are made to find expressions for the growth kinetics. For thin films and low temperatures the growth law

$$\frac{\mathrm{d}x}{\mathrm{d}t} = n\nu \cdot \exp\left(-\frac{W+U}{k_B\,T}\right)\exp\left(\frac{a\,e\,V}{k_B\,T\,x}\right) \tag{3.2}$$

is obtained. Here $x$ denotes the oxide thickness, $n$ is the number of ions at the metal/oxide interface per unit area, $\nu$ is the frequency of atomic vibrations which together with the first exponential term gives the classical Boltzmann probability of ion migration from one interstitial site to the next (with $W$ the energy difference between the positions and $U$ the activation energy), $2a$ being the distance between interstitial positions and the built up electric field $E = V/x$. The growth driven by this built-up field between surface and metal continues until a limiting thickness is reached, which ranges for Ti from 0.5 nm to 7 nm depending on the metal composition, the temperature and the surrounding medium [59].

This natural oxide layer on top of the Ti and Pt films is shown in Fig. 3.4 a) and b), respectively, in a cross section of the stripes corresponding to the vertical profile depicted in the bottom left hand corner of Fig. 3.4. As mentioned in section 1.2, the oxide surface also provides binding sites for oxygen, water and OH groups. During anodic oxidation also $O^{2-}$ transfer through the oxide is possible. We assumed this to be the ion species dominant for the voltage driven growth of the nanowires in the previous section, since only the anode was oxidized. Oxidation via layer-by-layer Ti ion migration in the films here could principally occur according to the Mott and Cabrera theory, like it is schematically shown in the lowermost pictures in Fig. 3.4 a) and b). In some reports it is stated, that both Ti cation and O anion transfer contribute simultaneously to the oxide growth during anodization [59]. However, also here, $O^{2-}$ diffusion into the oxide might be more probable, as we stated in Paper IV, because the side electrodes do not exhibit any signs of oxidation.

We furthermore assumed, that the velocity of the oxide growth in the Pt decorated Ti films is increased due to catalytic splitting of adsorbed water. As can be seen in the figure, this may lead to a top down oxidation in the vicinity of the Pt islands, where

large amounts of OH groups become available [247]. Without this exploitable additional oxygen source, one would expect that the oxidation in the Ti films will begin on the sides where the electric field is at the maximum. The field strength for this set-up was also calculated using FEMM. Fig. 3.5 shows the edge of a $10\,\mathrm{nm}$ thick and $10\,\mathrm{\mu m}$ wide Ti stripe with a natural oxide layer of $2\,\mathrm{nm}$ thickness on top of the surface, that is separated from a side electrode by a $500\,\mathrm{nm}$ gap (not shown). The same color scale as in Fig 3.1 was used. It can be seen that despite the very large distance to the electrode compared to the film thickness, i.e. a factor of 50, still a considerable normal electric field is present in the oxide especially near the sides. This still holds, when the oxide growth has already started from the sides, as it is shown in Fig. 3.1 b). This vertical electric field component is required, when we assume top-down (bottom-up) diffusion of oxygen anions (titanium cations) through the oxide.
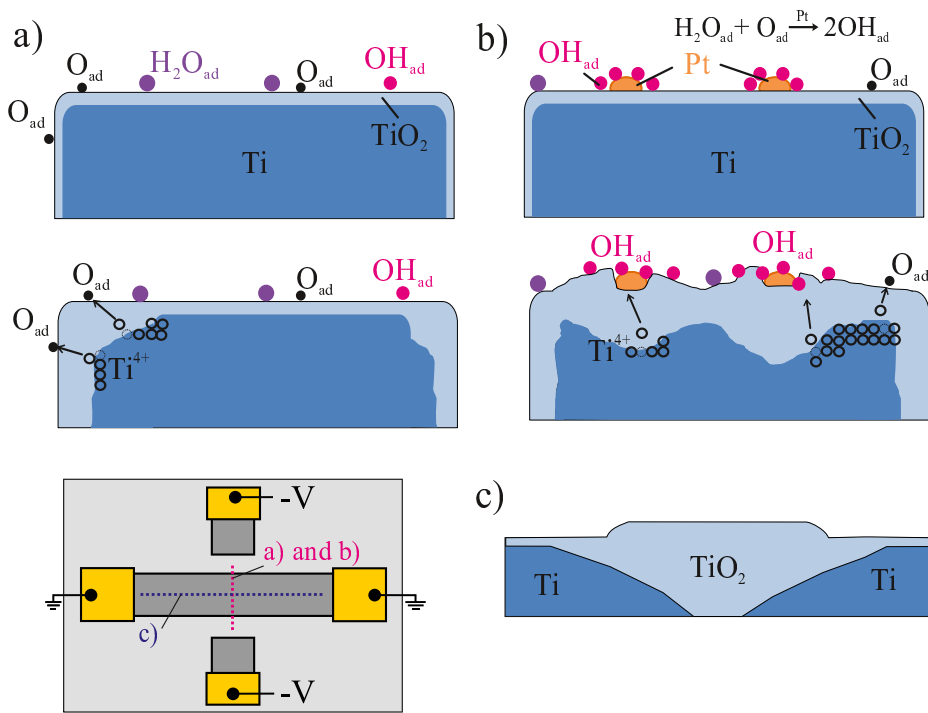


**Figure 3.4:** Suggested mechanisms of oxide growth in a) Ti thin films and b) Ti/Pt thin films before (top) and during (bottom) voltage application. The cross-sections in a) and b) belong to the vertical profile in the scheme at the bottom left handside. c) Proposed growth in the Ti/Pt thin films in a cross section longitudinal to the film, based on the information gained from EDX measurements.

Additional EDX measurements were carried out that supplement the data shown in Paper IV. For example, a larger acceleration voltage allows for detection of Ti components. In Fig. 3.6 on the left, EDX sum spectra are shown that were collected with an acceleration voltage of $20\,\mathrm{kV}$, during a line scan across a mound (yellow line) in the grown oxide of the Ti/Pt stripe. In the sum spectra, the Si (green), O (blue) and Ti (red) components are shown separately. Since no variations in the line scan can be observed, the mounds
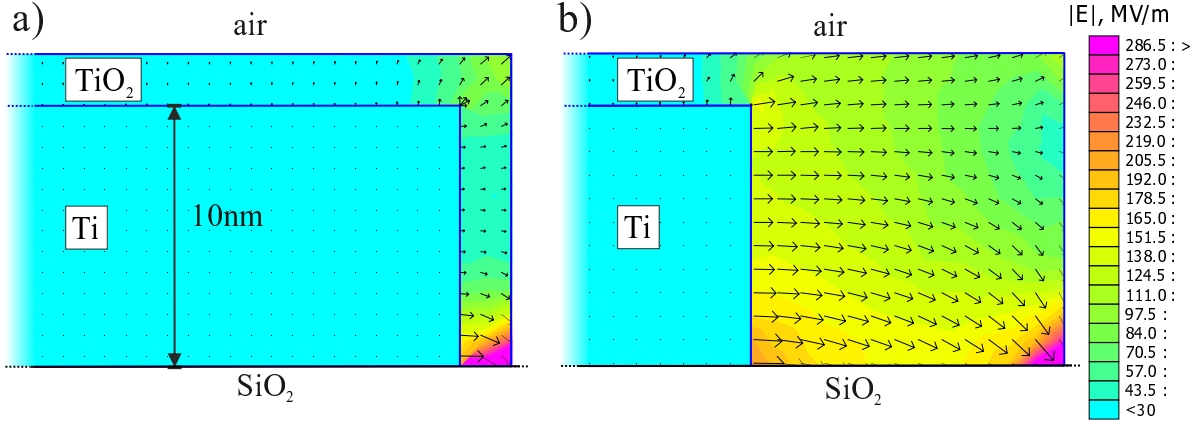
**Figure 3.5:** FEMM calculations of the electric field distribution in $TiO_2$ when a voltage of 80 V is applied to a side electrode with respect to the grounded stripe. The stripe and the electrode are separated by a 500 nm gap. The picture shows the zoom-in on the oxidizing Ti film with the field distribution inside the natural oxide layer (a) and the grown oxide (b).

on the rough surface and the surrounding presumably consist of the same material, namely $TiO_2$. The different structures visible as varied brightness in the SEM images can here be attributed to differences in height and roughness in accordance with the AFM data. As the data in Paper IV have shown, small traces of Pt were found at the center of these mounds confirming that definitely no complete and electrically connected layer of Pt is formed, but separated particles or islands. In fact, we assume that the mounts are formed as a result of the catalytic acceleration of the oxidation reaction when Pt and $H_2O$ come together. The EDX spectrum on the right was collected at one spot in the grown oxide. In both spectra, the low Ti component and strong $SiO_2$ signal components indicate that the main part of the signal comes from deeper layers and not from the surface. At larger acceleration voltages, in particular the surface signal becomes weaker compared to the signal stemming from deeper layers. The analytical area can be calculated using equation 1.17. For $SiO_2$ with a densitiy of $2.65\,\text{kg/m}^3$, $z_m$ is estimated to approximately $0.8\,\mu\text{m}$ at a penetration depth of $0.5\,\mu\text{m}$.

This should also be taken into account when looking at the data shown in Fig. 3.7. Here, line scans across the region of the $Ti/TiO_2$ transition in the oxidized Ti/Pt stripe with a 7000× (left) and 2000× (right) magnification are shown. The acceleration voltage was 5 kV. One would expect the oxygen amount to increase rather abruptly when going from the Ti to the $TiO_2$ as the transition on the surface is clearly visible in AFM scans and optical microscope as well as in electron microscope images. However, the oxygen amount (green in the left and red in the right picture) increases rather continuously over a wide distance of around $70\,\mu m$ before the visible transition is reached, i.e. where Ti should be, until saturation is reached shortly afterwards. On the one hand, this might be due to the low surface signal, but on the other hand this may also be related to the peculiar oxidation process that is catalytically driven by Pt. Oxidation might quickly spread over a large area and in the transition region might not be completed all the way down to the substrate. Presumably the Pt driven top-down oxidation might not be

completed near the visible transition, as is schematically shown in Fig. 3.4 c). Looking at a cross section in longitudinal direction along the Ti/Pt stripe, it is possible that full oxidation, that leads to an elevation measurable by means of AFM, only occurs in the region that is close to the side electrodes.
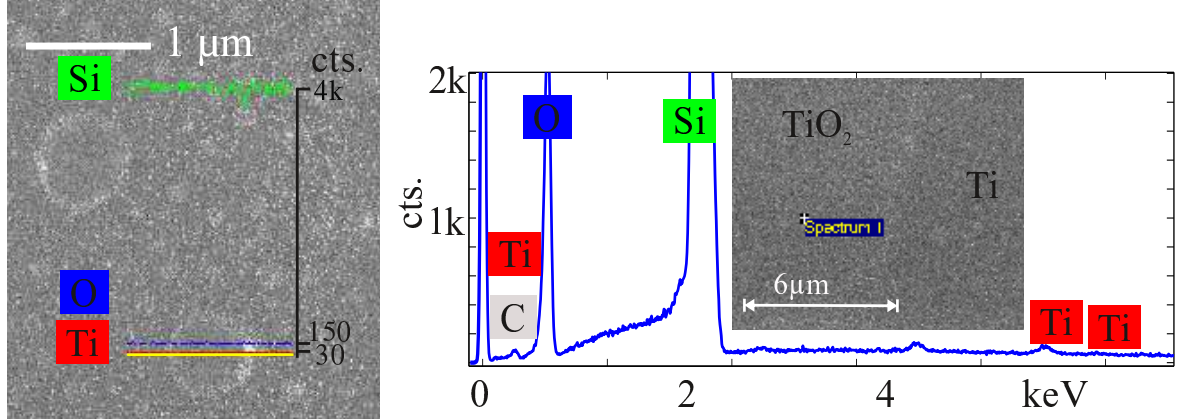


**Figure 3.6:** EDX sum spectra of a $TiO_2$ mound with Si, Ti, and O components (left) and spectrum of a spot in the oxidized region (right) taken with an acceleration voltage of 20 kV.
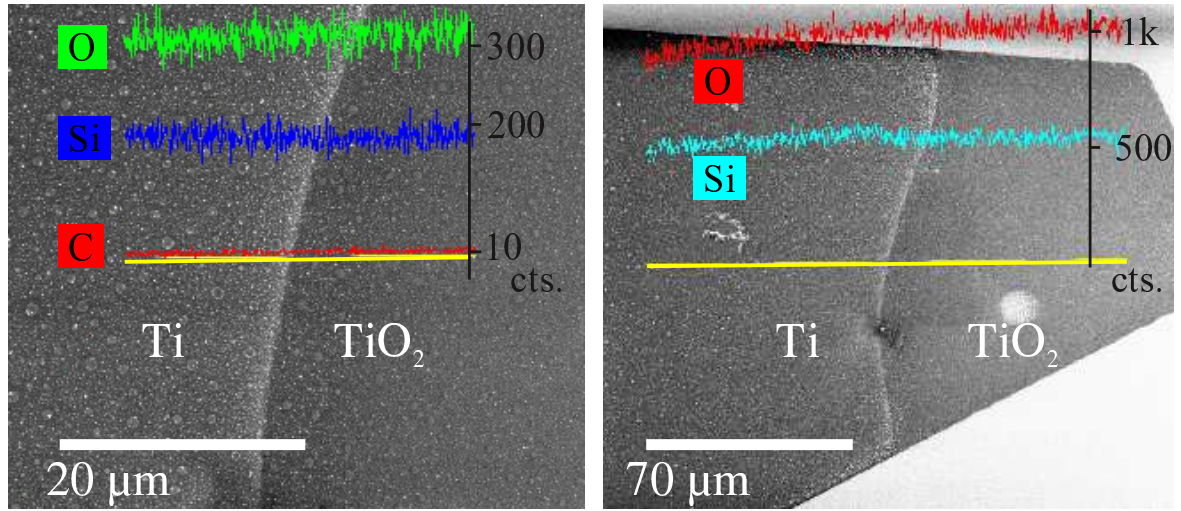


**Figure 3.7:** EDX line scans across the transition from Ti to $TiO_2$ in the oxidized Ti/Pt stripe, taken at 7000× (left) and 2000× (right) magnification. The acceleration voltage was 5 kV.

### Estimation of the denseness

From the AFM measurements of the absolute film height and roughness profiles, as well as measurements of the height difference between visibly oxidized and unoxidized regions, one can estimate the denseness of the on-chip formed oxide. For this, three different states of the film were distinguished as is sketched in Fig. 3.8. The left picture

corresponds to the naked Ti film directly after metalization. Its thickness $a$ should be in accordance with the nominal deposited amount of material, determined by the deposition rate and deposition time. The total height increases slightly to $b$ when the natural oxide layer is formed (2) when exposed to air. While $a$ is calculated from sputtering or evaporation parameters, $b$ can be extracted with good reliability from AFM height profiles over the $SiO_2$/Ti edge.
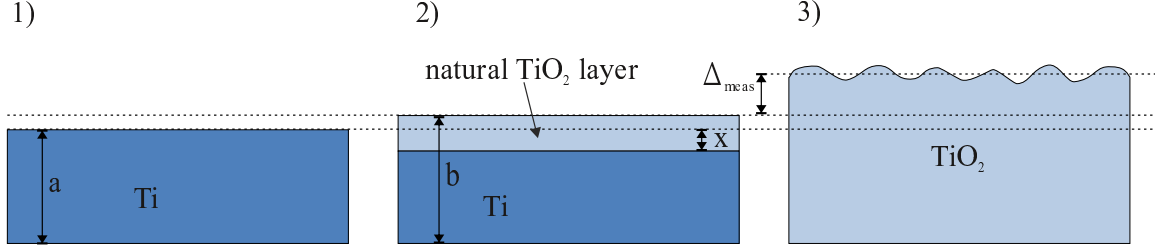


**Figure 3.8:** Parameters used in the estimation of the empty volume: the Ti film with nominal deposited thickness during the metalization step (1), the Ti film with the upper surface layers converted to natural oxide after exposition to air (2) and the film fully oxidized to $TiO_2$ after on-chip oxidation (3).

As described above, the formation of the native oxide happens through conversion of Ti so that the effective height of the Ti film is now decreased to $(a - x)$. After on-chip oxidation (3) the total height is increased once more by $\Delta_{meas}$ due to metal conversion and corresponding volume expansion. With the density $\rho$, volume $V$, molar mass $M$, Avogadro's number $N_A$ and number of Ti atoms $n_{Ti}$ the following expression for the first state is obtained

$$\rho_{Ti} \, V_{1,Ti} = \frac{M_{Ti}}{N_A} \, n_{Ti}. \tag{3.3}$$

Since no metal material is added or removed, the total number of Ti atoms $n_{Ti}$ is a conserved quantity during both, formation of the natural oxide layer and on-chip oxidation. The analog expressions for the Ti part and the $TiO_2$ part in the second state are therefore

$$\rho_{Ti} \, V_{2,Ti} = \frac{M_{Ti}}{N_A} \, G \, n_{Ti} \qquad \text{and} \qquad \rho_{TiO_2} V_{2,TiO_2} = \frac{M_{TiO_2}}{N_A}(1 - G) \, n_{Ti}, \tag{3.4}$$

where $G$ is the fraction of Ti that is not converted into $TiO_2$. If these two equations are combined and $G$ is eliminated, the resulting expression can be rearranged and inserted for $n_{Ti}$ in equation 3.3 to get

$$x = (a - b)\left(1 - \frac{\rho_{Ti}}{M_{Ti}} \frac{M_{TiO_2}}{\rho_{TiO_2}}\right)^{-1} \tag{3.5}$$

Here we used that $V_{1,Ti} \propto a$, $V_{2,Ti} \propto (a - x)$ and $V_{2,TiO_2} \propto (b - a + x)$. Assuming that the Ti film of thickness $(a - x)$ is completely converted into perfectly densely packed

$TiO_2$, the height difference $\Delta$ between the films in the second and third state is given by

$$\Delta = (a - x) \left( \frac{\rho_{Ti}}{M_{Ti}} \frac{M_{TiO_2}}{\rho_{TiO_2}} - 1 \right). \tag{3.6}$$

The height difference measured by AFM at the $Ti/TiO_2$ transition is referred to as $\Delta_{meas}$. This value should be larger than $\Delta$, when less densely packed or even porous $TiO_2$ is formed during on-chip oxidation. Finally, the fraction of filled space $R$ can be calculated using the derived expressions for the parameters

$$R = \frac{\Delta + b}{\Delta_{meas} + b}. \tag{3.7}$$

For the Ti stripe (Ti/Pt stripe) of a nominal thickness $a$=10 nm the values measured by AFM were $b$=12.3 nm (14.9 nm) and $\Delta_{meas}$=6.1 nm (4.3 nm). With $M_{Ti}$= 47.88 g/mol, $M_{TiO_2}$= 79.88 g/mol, $\rho_{Ti}$= 4.5 g/cm³ and $\rho_{TiO_2}$= 4.24 g/cm³ for rutile this yields $R \approx$ 96.2% for the Ti stripe and 92.2% for the Ti/Pt stripe. This suggests that both produced oxides are rather dense but the activity of Pt roughens the surface and yields a more open structure. The result furthermore indicates that the formed $TiO_2$ is indeed mostly rutile, since the density of anatase is lower (Tab. 1.2) which would demand a thickness increase of at least 7 nm if the growing oxide was completely densely packed.

# 4 Conclusion and Outlook

Several aspects of electroforming in $TiO_2$ have been discussed within this thesis. Here the main findings of the presented studies are briefly summarized and potential future research on the field is discussed.

Starting point of this work was the study of EF effects in microscale nanoporous $TiO_2$ devices that were operated as gas sensors. It has been shown that EF processes can coexist and interfere with the sensing response above a threshold bias voltage. Drifts in the sensor response can be easily avoided by keeping the electric field below the critical value for EF. More intriguing was the finding that hydrogen exposure and EF are interdependent in a non-trivial way. This involves not only acceleration of EF when $H_2$ is present but also two additional processes that increase the resistance in $TiO_2$ with $H_2$. Namely on the one hand, when $H_2$ is offered for the first time and on the other hand, a slower and more continuous resistance increase for longer exposures. This behavior was interpreted in terms of a phenomenological model, where oxygen deficient conductive current carrying channels form inside the $TiO_2$ with hydrogen-dependent conductivities. We noticed the universal character of these effects, when very similar signs of this interdependence arose in differently fabricated downscaled $TiO_2$ nanowires, while they were exposed to high electric fields and $H_2$ simultaneously. An important consequence of the found interdependence is that EF, in principle, can be modified and controlled not only electronically but also chemically. This might be interesting for applications where memristive operations are chemically triggered, for example in modeling of neuromorphic circuits and synaptic computing [72, 73]. The underlying microscopic origin, however, remains unclear. Experimental support is required in particular for our interpretation that hydrogen might trap electrons by substituting oxygen vacancies [55]. Also it is not clear, whether the samples undergo changes in the crystalline structure during initialization and $H_2$ exposure. We suggested that the phenomenology may be explained by Magnéli phase regions in the oxide that form during initialization, which may get further reduced by $H_2$ during EF to phases of lower conductivity like $Ti_2O_3$.

This actually raises the question for the interior processes occurring at the microscopic scale during initialization and EF. Better insight and information on the local conductivity and strucutral changes, like forming of filaments involving phase transitions, can be gathered on suitable samples by means of LC-AFM and STM in tunable pressure and atmosphere. This has been reported for $TiO_2$ structures with geometries comparable to the nanowires [51]. To perform these types of measurements on the $Ti/TiO_2/$sandwich structures, the top electrode would have to be removed, by etching for instance [52], while preserving the $TiO_2$ structure near the electrode. The main question that remains unanswered is: Do strongly reduced metallic type filaments form inside the nanowires and micron structures or are the changes in conductivity of a more homogeneous nature? The resistance measurements on the $TiO_2$ wires presented in Paper II and section 2.2

hint towards the latter, namely that the dominant mechanism for resistive changes when electric fields are applied is rather accumulation and depletion of oxygen vacancies and shifting of defect-rich regions inside the oxide. Nevertheless, forming of thin filaments of $Ti_4O_7$ of low density and diameter [52] is imaginable where the switching is attributed to the lower conductive area, which then constitutes the by far larger part of the volume. This is in contrast to the structures where resistive switching is attributed only to the $TiO_2$/electrode interface layer, where highly conductive $Ti_4O_7$ filaments of large diameters that intersperse the hole volume rupture and reconnect.

This assumption is based on the following observations: First, the signal margin, i.e. the ratio of $R_{on}$ and $R_{off}$ is much smaller in the nanowires, namely 5-10 compared to the maximum values that can be reached in $TiO_2$ of about 1000 as reported in various studies. Nevertheless, lower margins of the named range were also reported [52] in the context of a lower overall feature size ($<100\,\text{nm}$) and a low area densitiy of thin filaments (few tens per µm) where the resistive switching depends on the lower conducting area. A second hint for this is that the total resistance in the on-state is three orders of magnitude smaller than reported for most devices. Thirdly, the transition between the off- and on-state observed in the nanowires, as is depicted for example in Fig. 2.14 and the EF experiments of Paper I and II, is much smoother and steadier than would be expected from sudden rupture or joining of highly conducting channels. Such abrupt switching is usually triggered by applying a threshold voltage. An exception are the observed sudden decreases in the current during the on-chip modification in Paper III, which could be a sign of single thin channels of higher conductivity collapsing. It should be noted that varying current levels during operation were observed in all $TiO_2$ systems that were studied in this work, even in samples of the same type. Controlled fabrication and initialization processes are required to produce devices of satisfactory reproducibility and reliability [75], which is still a known problem and challenges the implementation of the complex $TiO_2$ system as resistive switches. Although the ability to confirm or negate these assumptions with a better insight into structural changes would be thrilling, one of the primary goals was the use-oriented query for easy fabrication techniques of gas sensitive $TiO_2$ devices.

Another main finding of this work is that EF conditions can initiate growth of the oxide component by oxidation of the Ti electrodes. Samples in planar design allowed for a study of the geometrical and morphological modifications that resulted from application of high voltages. These results identify another possible source of drift effects in typical devices like gas sensors or resistive switching devices and at the same time they represent an experimental tool, namely adjusting the properties of an oxide on-chip. Our approach to interpret the underlying physics and electrochemistry involves ionic motion inside the oxide, interaction with and forming of oxygen gas, as well as electromechanical effects. Further experiments are required to substantiate this interpretation.

Finally, the described technique was used to prepare a complete $H_2$ gas microsensor on-chip in a silicon-MOS compatible process. Not only redundant sensor array layouts with selective activation are possible applications, but many other modifications of electronic circuits are imaginable, e.g. fabrication of electrodes with separations in the range of one nanometer [248–254], tunnel junctions [255, 256] or tunable capacitors. In the sensing experiments, we attempted to evade effects of residual gases in the $TiO_2$ as

far as possible by heating and high gas flows during initialization. We rather excluded such effects when no characteristic signs for interactions with, for example, $O_2$ and $H_2O$ were observed in the current transients. Due to the small $TiO_2$ volumes, our set-up is unfortunately not fitted for an analysis of gases that may be formed during electrochemical processes. However, data from local temperature measurements indirectly hint towards water forming, which might occur in considerable amounts in the $TiO_2$ or at the surface at certain concentrations of $H_2$ and $O_2$ in the atmosphere.

# Bibliography

[1] U. Diebold, Surface Science Reports **48**, 53 (2003).

[2] X. Chen and S. S. Mao, Chemical Reviews **107**, 2891 (2007).

[3] L. De Nardo, G. Raffaini, E. Ebramzadeh, and F. Ganazzoli, The International journal of artificial organs **35**, 629 (2012).

[4] A. Kusior, J. Klich-Kafel, A. Trenczek-Zajac, K. Swierczek, M. Radecka, and K. Zakrzewska, Journal of the European Ceramic Society **33**, 2285 (2013).

[5] M. Radecka, M. Rekas, A. Trenczek-Zajac, and K. Zakrzewska, Journal of Power Sources **181**, 46 (2008).

[6] H. Sheng, H. Zhang, W. Song, H. Ji, W. Ma, C. Chen, and J. Zhao, Angewandte Chemie International Edition **54**, 5905 (2015).

[7] A. Fujishima and K. Honda, Nature **238**, 37 (1972).

[8] Ö. Cakabay, M. E. Achhab, and K. Schierbaum, Applied Physics A **118**, 1127 (2015).

[9] Ö. Cakabay, M. El Achhab, and K. Schierbaum, J. Phys. Chem. C **120**, 9061 (2016).

[10] D. H. Kim, Y.-S. Shim, H. G. Moon, H. J. Chang, D. Su, S. Y. Kim, J.-S. Kim, B. K. Ju, S.-J. Yoon, and H. W. Jang, The Journal of Physical Chemistry C **117**, 17824 (2013).

[11] R. Ramaneti, J. C. Lodder, and R. Jansen, Applied Physics Letters **91**, 012502 (2007).

[12] H. Saadaoui, X. Luo, Z. Salman, X. Y. Cui, N. N. Bao, P. Bao, R. K. Zheng, L. T. Tseng, Y. H. Du, T. Prokscha, A. Suter, T. Liu, Y. R. Wang, S. Li, J. Ding, S. P. Ringer, E. Morenzoni, and J. B. Yi, Phys. Rev. Lett. **117**, 227202 (2016).

[13] N. Yamamoto, S. Tonomura, T. Matsuoka, and H. Tsubomura, Surface Science **92**, 400 (1980).

[14] S. A. Akbar and L. B. Younkman, Journal of The Electrochemical Society **144**, 1750 (1997).

[15] H. Lu, H. Fan, R. Jin, B. Chong, X. Shen, S. Yan, and X. Zhu, Electrochimica Acta **215**, 380 (2016).

[16] O. K. Varghese, D. Gong, M. Paulose, K. G. Ong, and C. A. Grimes, Sensors and Actuators B: Chemical **93**, 338 (2003).

[17] C. Fàbrega, F. Hernández-Ramírez, J. D. Prades, R. Jiménez-Díaz, T. Andreu, and J. R. Morante, Nanotechnology **21**, 445703 (2010).

[18] M. Paulose, O. K. Varghese, G. K. Mor, C. A. Grimes, and K. G. Ong, Nanotechnology **17**, 398 (2006).

[19] T. Berger, T. Lana-Villarreal, D. Monllor-Satoca, and R. Gomez, Chemical Physics Letters **447**, 91 (2007).

[20] A. Kolmakov, D. O. Klenov, Y. Lilach, S. Stemmer, and M. Moskovits, Nano Letters **5**, 667 (2005).

[21] M. El Achhab, A. Erbe, G. Koschek, R. Hamouich, and K. Schierbaum, Applied Physics A **116**, 2039 (2014).

[22] M. El Achhab and K. Schierbaum, Journal of Sensors and Sensor Systems **5**, 273 (2016).

[23] M. E. Achhab, *Struktur reiner und platin-bedeckter elektrochemisch oxidierter Titanfolien und ihre Eigenschaften bei Wasserstoffoxidation*, Dissertation, Universität Düsseldorf, 2013.

[24] W. Lanford, Nuclear Instruments and Methods in Physics Research Section B: Beam Interactions with Materials and Atoms **66**, 65 (1992).

[25] C. Senöz, S. Evers, M. Stratmann, and M. Rohwerder, Electrochemistry Communications **13**, 1542 (2011).

[26] S. Evers and M. Rohwerder, Electrochemistry Communications **24**, 85 (2012).

[27] S. Evers, C. Senöz, and M. Rohwerder, Science and Technology of Advanced Materials **14**, 014201 (2013).

[28] S. Takagi, Y. Toji, M. Yoshino, and K. Hasegawa, ISIJ International **52**, 316 (2012).

[29] D. Araújo, E. Vilar, and J. P. Carrasco, International Journal of Hydrogen Energy **39**, 12194 (2014).

[30] V. G. Gavriljuk, B. D. Shanina, V. N. Shyvanyuk, and S. M. Teus, Corrosion Reviews **31**, 33 (2013).

[31] Q. Liu and A. Atrens, Corrosion Reviews **31**, 85 (2013).

[32] J. Capelle, I. Dmytrakh, and G. Pluvinage, Corrosion Science **52**, 1554 (2010).

[33] J. Ovejero-García, Journal of Materials Science **20**, 2623 (1985).

[34] G. Katano, K. Ueyama, and M. Mori, Journal of Materials Science **36**, 2277 (2001).

[35] M. S. Daw and M. I. Baskes, Phys. Rev. Lett. **50**, 1285 (1983).

[36] S. Fischer, K.-D. Schierbaum, and W. Göpel, Vacuum **48**, 601 (1997).

[37] W. Göpel, G. Rocker, and R. Feierabend, Phys. Rev. B **28**, 3427 (1983).

[38] T. Hübert, L. Boon-Brett, G. Black, and U. Banach, Sensors and Actuators B: Chemical **157**, 329 (2011).

[39] M. Cerchez, H. Langer, M. El Achhab, T. Heinzel, D. Ostermann, H. Lüder, and J. Degenhardt, Applied Physics Letters **103**, 033522 (2013).

[40] J. Bai and B. Zhou, Chemical Reviews **114**, 10131 (2014).

[41] A. S. Zuruzi, A. Kolmakov, N. C. MacDonald, and M. Moskovits, Applied Physics Letters **88**, 102904 (2006).

[42] Q. Wang, X. Guo, L. Cai, Y. Cao, L. Gan, S. Liu, Z. Wang, H. Zhang, and L. Li, Chem. Sci. **2**, 1860 (2011).

[43] K. Schierbaum, U. Kirner, J. Geiger, and W. Göpel, Sensors and Actuators B: Chemical **4**, 87 (1991).

[44] Z. Chen and C. Lu, Sensor Letters **3**, 274 (2005).

[45] H. Farahani, R. Wagiran, and M. N. Hamidon, Sensors **14**, 7881 (2014).

[46] G. Garcia-Belmonte, V. Kytin, T. Dittrich, and J. Bisquert, Journal of Applied Physics **94**, 5261 (2003).

[47] Y. Zhang, W. Fu, H. Yang, Q. Qi, Y. Zeng, T. Zhang, R. Ge, and G. Zou, Applied Surface Science **254**, 5545 (2008).

[48] D. B. Strukov, G. S. Snider, D. R. Stewart, and R. S. Williams, Nature **453**, 80 (2008).

[49] J. J. Yang, M. D. Pickett, X. Li, D. A. A. Ohlberg, D. R. Stewart, and R. S. Williams, Nature Nanotechnology **3**, 429 (2008).

[50] D.-H. Kwon, K. M. Kim, J. H. Jang, J. M. Jeon, M. H. Lee, G. H. Kim, X.-S. Li, G.-S. Park, B. Lee, S. Han, M. Kim, and C. S. Hwang, Nature Nanotechnology **5**, 148 (2010).

[51] K. Szot, M. Rogala, W. Speier, Z. Klusek, A. Besmehn, and R. Waser, Nanotechnology **22**, 254001 (2011).

[52] B. J. Choi, D. S. Jeong, S. K. Kim, C. Rohde, S. Choi, J. H. Oh, H. J. Kim, C. S. Hwang, K. Szot, R. Waser, B. Reichenberg, and S. Tiedke, Journal of Applied Physics **98**, 033715 (2005).

[53] A. Sawa, Materials Today **11**, 28 (2008).

[54] M. Strungaru, M. Cerchez, S. Herbertz, T. Heinzel, M. El Achhab, and K. Schierbaum, Applied Physics Letters **106**, 143109 (2015).

[55] F. Filippone, G. Mattioli, P. Alippi, and A. Amore Bonapasta, Phys. Rev. B **80**, 245203 (2009).

[56] S. Herbertz, M. Cerchez, and T. Heinzel, Sensors and Actuators B: Chemical **221**, 401 (2015).

[57] S. Herbertz, P. Aleksa, M. Zielinski, D. Welk, and T. Heinzel, Superlattices and Microstructures **124**, 231 (2018).

[58] T. Ohtsuka and T. Otsuki, Corrosion Science **45**, 1793 (2003).

[59] A. Aladjem, Journal of Materials Science **8**, 688 (1973).

[60] N. Cabrera and N. F. Mott, Reports on Progress in Physics **12**, 163 (1949).

[61] D. Husted, L. Gruss, and T. Mackus, Journal of The Electrochemical Society **118**, 1989 (1971).

[62] T. Ohtsuka, M. Masuda, and N. Sato, Journal of The Electrochemical Society **134**, 2406 (1987).

[63] S. Herbertz, D. Welk, and T. Heinzel, AIP Advances **8**, 055301 (2018).

[64] K. Zakrzewska and M. Radecka, Nanoscale research letters **12**, 89 (2017).

[65] T. W. Hickmott, Journal of Applied Physics **33**, 2669 (1962).

[66] D. Ielmini and R. Waser, *Resistive Switching: From Fundamentals of Nanoionic Redox Processes to Memristive Device Applications*, Wiley-VCH, 2016.

[67] L. Chua, IEEE Trans. Circuit Theory **18** (1971).

[68] S. Vongehr and X. Meng, Scientific Reports **5** (2015).

[69] J. Ouyang, *Emerging Resistive Switching Memories*, Springer, Cham, 2016.

[70] J. J. Yang, J. Borghetti, D. Murphy, D. R. Stewart, and R. S. Williams, Advanced Materials **21**, 3754 (2009).

[71] H. Jiang and Q. Xia, Nanoscale **5**, 3257 (2013).

[72] S. H. Jo, T. Chang, I. Ebong, B. B. Bhadviya, P. Mazumder, and W. Lu, Nano Letters **10**, 1297 (2010).

[73] M. D. Pickett, G. Medeiros-Ribeiro, and R. S. Williams, Nature Materials **12**, 114 (2013).

[74] R. Muenstermann, T. Menke, R. Dittmann, and R. Waser, Advanced Materials **22**, 4819 (2010).

[75] J. J. Yang, F. Miao, M. D. Pickett, D. A. A. Ohlberg, D. R. Stewart, C. N. Lau, and R. S. Williams, Nanotechnology **20**, 215201 (2009).

[76] R. Waser, D. Ielmini, H. Akinaga, H. Shima, H.-S. P. Wong, J. J. Yang, and S. Yu, *Introduction to Nanoionic Elements for Information Technology*, chapter 1, pp. 1–30, John Wiley & Sons, Ltd, 2016.

[77] S. G. Park, *Resistance Switching Mechanism in* $TiO_2$, Dissertation, Stanford University, 2011.

[78] S. Fullam, N. Ray, and E. Karpov, Superlattices and Microstructures **82**, 378 (2015).

[79] *List of chemical elements*, Wikipedia, the free encyclopedia, n.d. Web 4. Dec. 2018 `https://en.wikipedia.org/wiki/List_of_chemical_elements`.

[80] *Electron configurations of the elements (data page)*, Wikipedia, the free encyclopedia, n.d. Web 4. Dec. 2018 `https://en.wikipedia.org/wiki/Electron_configurations_of_the_elements_(data_page)`.

[81] *Periodic table (crystal structure)*, Wikipedia, the free encyclopedia, n.d. Web 4. Dec. 2018 `https://en.wikipedia.org/wiki/Periodic_table_(crystal_structure)`.

[82] *Electrical resistivities of the elements (data page)*, Wikipedia, the free encyclopedia, n.d. Web 4. Dec. 2018 `https://en.wikipedia.org/wiki/Electrical_resistivities_of_the_elements_(data_page)`.

[83] E. A. Bel'skaya and E. Y. Kulyamina, High Temperature **45**, 785 (2007).

[84] J. Lausmaa, Journal of Electron Spectroscopy and Related Phenomena **81**, 343 (1996).

[85] N. F. Mott, Trans. Faraday Soc. **43**, 429 (1947).

[86] A. Atkinson, Rev. Mod. Phys. **57**, 437 (1985).

[87] G. U. von Oertzen and A. R. Gerson, Journal of Physics and Chemistry of Solids **68**, 324 (2007).

[88] R. Restori, D. Schwarzenbach, and J. R. Schneider, Acta Crystallographica Section B **43**, 251 (1987).

[89] P. W. Atkins and J. de Paula, *Physikalische Chemie [Hauptbd.]*, Wiley-VCH, 2006.

[90] S.-D. Mo and W. Y. Ching, Phys. Rev. B **51**, 13023 (1995).

[91] *Rutile*, `Mindat.org` Database of minerals, n.d. Web 3. Dec. 2018 `https://www.mindat.org/min-3486.html`.

[92] *Anatase*, `Mindat.org` Database of minerals, n.d. Web 3. Dec. 2018 `https://www.mindat.org/min-213.html`.

[93] *Brookite*, `Mindat.org` Database of minerals, n.d. Web 3. Dec. 2018 `https://www.mindat.org/min-787.html`.

[94] K. Liu, A. I. Rykov, J. Wang, and T. Zhang, Advances in Catalysis **58**, 1 (2015).

[95] R. H. Austin and S.-f. Lim, Proceedings of the National Academy of Sciences **105**, 17217 (2008).

[96] T. Zacherle, P. C. Schmidt, and M. Martin, *Atomic and Electronic Structure of Oxides*, chapter 3, pp. 49–94, John Wiley & Sons, Ltd, 2016.

[97] A. Amtout and R. Leonelli, Phys. Rev. B **51**, 6842 (1995).

[98] L. A. Grunes, R. D. Leapman, C. N. Wilker, R. Hoffmann, and A. B. Kunz, Phys. Rev. B **25**, 7157 (1982).

[99] D. O. Scanlon, C. W. Dunnill, J. Buckeridge, S. A. Shevlin, A. J. Logsdail, S. M. Woodley, C. R. A. Catlow, M. J. Powell, R. G. Palgrave, I. P. Parkin, G. W. Watson, T. W. Keal, P. Sherwood, A. Walsh, and A. A. Sokol, Nature Materials **12**, 798 (2013).

[100] Y. Mi and Y. Weng, Scientific Reports **5** (2015).

[101] G. Xiong, R. Shao, T. Droubay, A. Joly, K. Beck, S. Chambers, and W. Hess, Advanced Functional Materials **17**, 2133 (2007).

[102] R. Su, R. Bechstein, L. Sø, R. T. Vang, M. Sillassen, B. Esbjörnsson, A. Palmqvist, and F. Besenbacher, The Journal of Physical Chemistry C **115**, 24287 (2011).

[103] A. Trenczek-Zajac, M. Radecka, M. Jasinski, K. Michalow, M. Rekas, E. Kusior, K. Zakrzewska, A. Heel, T. Graule, and K. Kowalski, Journal of Power Sources **194**, 104 (2009).

[104] K. A. Michalow, E. H. Otal, D. Burnat, G. Fortunato, H. Emerich, D. Ferri, A. Heel, and T. Graule, Catalysis Today **209**, 47 (2013).

[105] T. S. Bjørheim, A. Kuwabara, and T. Norby, The Journal of Physical Chemistry C **117**, 5919 (2013).

[106] S. Wendt, R. Schaub, J. Matthiesen, E. Vestergaard, E. Wahlström, M. Rasmussen, P. Thostrup, L. Molina, E. Lægsgaard, I. Stensgaard, B. Hammer, and F. Besenbacher, Surface Science **598**, 226 (2005).

[107] P. Knauth and H. L. Tuller, Journal of Applied Physics **85**, 897 (1999).

[108] I. Nakamura, N. Negishi, S. Kutsuna, T. Ihara, S. Sugihara, and K. Takeuchi, Journal of Molecular Catalysis A: Chemical **161**, 205 (2000).

[109] P. Roy, S. Berger, and P. Schmuki, Angewandte Chemie **123**, 2956.

[110] A. A. Bonapasta, F. Filippone, G. Mattioli, and P. Alippi, Catalysis Today **144**, 177 (2009).

[111] P. M. Kowalski, B. Meyer, and D. Marx, Phys. Rev. B **79**, 115410 (2009).

[112] G. A. Somorjai, Science **227**, 902 (1985).

[113] V. E. Henrich and R. L. Kurtz, Phys. Rev. B **23** (1981).

[114] X. Li, R. Ramasamy, and P. K. Dutta, Sensors and Actuators B: Chemical **143**, 308 (2009).

[115] M. K. Nowotny, L. R. Sheppard, T. Bak, and J. Nowotny, The Journal of Physical Chemistry C **112**, 5275 (2008).

[116] K. Takahashi and H. Yui, The Journal of Physical Chemistry C **113**, 20322 (2009).

[117] M. M. Islam, M. Calatayud, and G. Pacchioni, The Journal of Physical Chemistry C **115**, 6809 (2011).

[118] J. B. Bates, J. C. Wang, and R. A. Perkins, Phys. Rev. B **19**, 4130 (1979).

[119] G. C. Yu, physica status solidi (a) **198**, 302 (2003).

[120] A. Sclafani and J. M. Herrmann, The Journal of Physical Chemistry **100**, 13655 (1996).

[121] Q. Wu and R. van de Krol, Journal of the American Chemical Society **134**, 9369 (2012).

[122] S. Wendt, J. Matthiesen, R. Schaub, E. K. Vestergaard, E. Lægsgaard, F. Besenbacher, and B. Hammer, Phys. Rev. Lett. **96**, 066107 (2006).

[123] J. R. Smith, F. C. Walsh, and R. L. Clarke, Journal of Applied Electrochemistry **28**, 1021 (1998).

[124] D. Regonini, V. Adamaki, C. Bowen, S. Pennock, J. Taylor, and A. Dent, Solid State Ionics **229**, 38 (2012).

[125] R. F. Bartholomew and D. R. Frankl, Phys. Rev. **187**, 828 (1969).

[126] P. G. Wahlbeck and P. W. Gilles, Journal of the American Ceramic Society **49**, 180.

[127] S. Ratzsch, E.-B. Kley, A. Tünnermann, and A. Szeghalmi, Nanotechnology **26**, 024003 (2015).

[128] C. Bundesmann, T. Lautenschläger, D. Spemann, A. Finzel, E. Thelander, M. Mensing, and F. Frost, Applied Surface Science **421**, 331 (2017).

[129] R. L. Clarke and S. K. Harnsberger, Am. Lab. **20** (1988).

[130] G. B. Fisher and J. L. Gland, Surface Science **94**, 446 (1980).

[131] K. Ogle and J. White, Surface Science **139**, 43 (1984).

[132] J. N. Smith and R. L. Palmer, The Journal of Chemical Physics **56**, 13 (1972).

[133] S. Völkening, K. Bedürftig, K. Jacobi, J. Wintterlin, and G. Ertl, Phys. Rev. Lett. **83**, 2672 (1999).

[134] C. Sachs, M. Hildebrand, S. Völkening, J. Wintterlin, and G. Ertl, The Journal of Chemical Physics **116**, 5759 (2002).

[135] V. Gorodetskii, A. Sametova, A. Matveev, and V. Tapilin, Catalysis Today **144**, 219 (2009).

[136] A. Michaelides and P. Hu, Journal of the American Chemical Society **123**, 4235 (2001).

[137] J. L. Gland, Surface Science **93**, 487 (1980).

[138] H. Steininger, S. Lehwald, and H. Ibach, Surface Science **123**, 1 (1982).

[139] J. L. Gland, B. A. Sexton, and G. B. Fisher, Surface Science **95**, 587 (1980).

[140] L. M. Falicov and G. A. Somorjai, Proceedings of the National Academy of Sciences **82**, 2207 (1985).

[141] S. K. Kim, J. Shin, S. H. Moon, J. Kim, and S.-C. Lee, The Journal of Physical Chemistry C **117**, 18131 (2013).

[142] H. Herrera-Suárez, A. Rubio-Ponce, and D. Olguín, Computational Materials Science **56**, 141 (2012).

[143] K. Christmann, Surface Science Reports **9**, 1 (1988).

[144] B. Poelsema, K. Lenz, and G. Comsa, Journal of Physics: Condensed Matter **22**, 304006 (2010).

[145] B. Poelsema, K. Lenz, and G. Comsa, The Journal of Chemical Physics **134**, 074703 (2011).

[146] D. Wang, Z.-P. Liu, and W.-M. Yang, ACS Catalysis **8**, 7270 (2018).

[147] M. Alvisi, G. Galtieri, L. Giorgi, R. Giorgi, E. Serra, and M. Signore, Surface and Coatings Technology **200**, 1325 (2005).

[148] M. K. Kumar, L. K. Tan, N. N. Gosvami, and H. Gao, Journal of Applied Physics **106**, 044308 (2009).

[149] A. Ruiz, J. Arbiol, A. Cirera, A. Cornet, and J. Morante, Materials Science and Engineering: C **19**, 105 (2002).

[150] K. I. Lundström, M. S. Shivaraman, and C. M. Svensson, Journal of Applied Physics **46**, 3876 (1975).

[151] I. Lundström, S. Shivaraman, C. Svensson, and L. Lundkvist, Applied Physics Letters **26**, 55 (1975).

[152] U. Kirner, K. Schierbaum, W. Göpel, B. Leibold, N. Nicoloso, W. Weppner, D. Fischer, and W. Chu, Sensors and Actuators B: Chemical **1**, 103 (1990).

[153] K.-D. Schierbaum, Sensors and Actuators B: Chemical **24**, 239 (1995).

[154] R. Gross and A. Marx, *Festkörperphysik*, Oldenbourg Wissenschaftsverlag, 2012.

[155] M. Grundmann, *The Physics of Semiconductors*, Springer, 2010.

[156] T. Tamura, S. Ishibashi, K. Terakura, and H. Weng, Phys. Rev. B **80**, 195302 (2009).

[157] G. R. Bamwenda, S. Tsubota, T. Nakamura, and M. Haruta, Journal of Photochemistry and Photobiology A: Chemistry **89**, 177 (1995).

[158] V. Subramanian, E. Wolf, and P. V. Kamat, The Journal of Physical Chemistry B **105**, 11439 (2001).

[159] F. Li and X. Li, Chemosphere **48**, 1103 (2002).

[160] H. J. De Bruin, Nature **272**, 712 (1978).

[161] K. Schierbaum, S. Fischer, M. Torquemada, J. de Segovia, E. Román, and J. Martín-Gago, Surface Science **345**, 261 (1996).

[162] S. Fischer, J. Martín-Gago, E. Román, K. Schierbaum, and J. de Segovia, Journal of Electron Spectroscopy and Related Phenomena **83**, 217 (1997).

[163] J. H. Werner and H. H. Güttler, Journal of Applied Physics **69**, 1522 (1991).

[164] K. Hiehata, A. Sasahara, and H. Onishi, Nanotechnology **18**, 084007 (2007).

[165] K.-D. Schierbaum, S. Fischer, P. Wincott, P. Hardman, V. Dhanak, G. Jones, and G. Thornton, Surface Science **391**, 196 (1997).

[166] V. Chawla, R. Jayaganthan, A. Chawla, and R. Chandra, Journal of Materials Processing Technology **209**, 3444 (2009).

[167] A. Brudnik, A. Gorzkowska-Sobas, E. Pamula, M. Radecka, and K. Zakrzewska, Journal of Power Sources **173**, 774 (2007).

[168] B. Stefanov and L. Österlund, Coatings **4**, 587 (2014).

[169] P. Löbl, M. Huppertz, and D. Mergel, Thin Solid Films **251**, 72 (1994).

[170] A. Alberti, L. Renna, S. Sanzaro, E. Smecca, G. Mannino, C. Bongiorno, C. Galati, L. Gervasi, A. Santangelo, and A. L. Magna, Sensors and Actuators B: Chemical **259**, 658 (2018).

[171] S. Sanzaro, E. Smecca, G. Mannino, C. Bongiorno, G. Pellegrino, F. Neri, G. Malandrino, M. R. Catalano, G. G. Condorelli, R. Iacobellis, L. D. Marco, C. Spinella, A. L. Magna, and A. Alberti, Scientific Reports **6**, 39509 (2016).

[172] J. W. Lyding, T. Shen, J. S. Hubacek, J. R. Tucker, and G. C. Abeln, Applied Physics Letters **64**, 2010 (1994).

[173] J. A. Dagata, J. Schneir, H. H. Harary, C. J. Evans, M. T. Postek, and J. Bennett, Applied Physics Letters **56**, 2001 (1990).

[174] R. Held, T. Heinzel, P. Studerus, K. Ensslin, and M. Holland, Applied Physics Letters **71**, 2689 (1997).

[175] A. Dorn, M. Sigrist, A. Fuhrer, T. Ihn, T. Heinzel, K. Ensslin, W. Wegscheider, and M. Bichler, Applied Physics Letters **80**, 252 (2002).

[176] A. Fuhrer, A. Dorn, S. Lüscher, T. Heinzel, K. Ensslin, W. Wegscheider, and M. Bichler, Superlattices and Microstructures **31**, 19 (2002).

[177] B. Irmer, M. Kehrle, H. Lorenz, and J. P. Kotthaus, Applied Physics Letters **71**, 1733 (1997).

[178] B. S. Archanjo, P. F. Siles, C. K. B. Q. M. Oliveira, D. L. Baptista, and B. R. A. Neves, Advances in Materials Science and Engineering **2013** (2013).

[179] T.-H. Fang, T. H. Wang, and K.-T. Wu, Microelectronic Engineering **85**, 1616 (2008).

[180] Z. Su, L. Zhang, F. Jiang, and M. Hong, Progress in Natural Science: Materials International **23**, 294 (2013).

[181] H. Sugimura, T. Uchida, N. Kitamura, and H. Masuhara, Applied Physics Letters **63**, 1288 (1993).

[182] R. J. M. Vullers, M. Ahlskog, M. Cannaerts, and C. Van Haesendonck, Applied Physics Letters **76**, 1947 (2000).

[183] A. Opitz, M. Scherge, S. I.-U. Ahmed, and J. A. Schaefer, Journal of Applied Physics **101**, 064310 (2007).

[184] A. Verdaguer, C. Weis, G. Oncins, G. Ketteler, H. Bluhm, and M. Salmeron, Langmuir **23**, 9699 (2007).

[185] S. Lemeshko, S. Gavrilov, V. Shevyakov, V. Roschin, and R. Solomatenko, Nanotechnology **12**, 273 (2001).

[186] T.-H. Fang and K.-T. Wu, Electrochemistry Communications **8**, 173 (2006).

[187] P. Avouris, T. Hertel, and R. Martel, Applied Physics Letters **71**, 285 (1997).

[188] M. Calleja, J. Anguita, R. Garcia, K. Birkelund, F. Perez-Murano, and J. A. Dagata, Nanotechnology **10**, 34 (1999).

[189] J. A. Dagata, T. Inoue, J. Itoh, K. Matsumoto, and H. Yokoyama, Journal of Applied Physics **84**, 6891 (1998).

[190] D. Stiévenard, P. A. Fontaine, and E. Dubois, Applied Physics Letters **70**, 3272 (1997).

[191] B. Klehn and U. Kunze, Journal of Applied Physics **85**, 3897 (1999).

[192] X. Jin and W. N. Unertl, Applied Physics Letters **61**, 657 (1992).

[193] B. Irmer, R. H. Blick, F. Simmel, W. Gödel, H. Lorenz, and J. P. Kotthaus, Applied Physics Letters **73**, 2051 (1998).

[194] Z. J. Liu, X. Zhong, J. Walton, and G. E. Thompson, Journal of The Electrochemical Society **163**, E75 (2016).

[195] B. J. Hwang and J. R. Hwang, Journal of Applied Electrochemistry **23**, 1056 (1993).

[196] Q. Zhong, D. Inniss, K. Kjoller, and V. Elings, Surface Science Letters **290**, L688 (1993).

[197] *Energy Table for EDS Analysis*, www.jeol.com. UNAMUR, n.d. Web 7. Dec. 2017 https://www.unamur.be/services/microscopie/sme-documents/Energy-20table-20for-20EDS-20analysis-1.pdf.

[198] R. Castaing, Academic Press, 1960, volume 13 of *Advances in Electronics and Electron Physics*, pp. 317 – 386.

[199] C. Dette, M. A. Pérez-Osorio, C. S. Kley, P. Punke, C. E. Patrick, P. Jacobson, F. Giustino, S. J. Jung, and K. Kern, Nano Letters **14**, 6533 (2014).

[200] D. A. Panayotov and J. T. Yates, Chemical Physics Letters **436**, 204 (2007).

[201] A. J. Antończak, B. Stępak, P. E. Kozioł, and K. M. Abramski, Applied Physics A **115**, 1003 (2014).

[202] D. P. Puzzo, L. D. Bonifacio, J. Oreopoulos, C. M. Yip, I. Manners, and G. A. Ozin, J. Mater. Chem. **19**, 3500 (2009).

[203] M. Quinten, *A Practical Guide to Optical Metrology for Thin Films*, Wiley-VCH, 2012.

[204] H. A. Macleod, *Thin Film Optical Filters*, Hilger: Bristol, U.K., 1986.

[205] X. Zhang, A. Fujishima, M. Jin, A. V. Emeline, and T. Murakami, The Journal of Physical Chemistry B **110**, 25142 (2006).

[206] C. Schinke, P. Christian Peest, J. Schmidt, R. Brendel, K. Bothe, M. R. Vogt, I. Kröger, S. Winter, A. Schirmacher, S. Lim, H. T. Nguyen, and D. MacDonald, AIP Advances **5**, 067168 (2015).

[207] J. R. DeVore, J. Opt. Soc. Am. **41**, 416 (1951).

[208] I. H. Malitson, J. Opt. Soc. Am. **55**, 1205 (1965).

[209] G. Yang, P. Hu, Y. Cao, F. Yuan, and R. Xu, Nanoscale Res Lett. **5**, 1437 (2010).

[210] V. Galstyan, E. Comini, G. Faglia, and G. Sberveglieri, Sensors **13**, 14813 (2013).

[211] H. Gu, Z. Wang, and Y. Hu, Sensors **12**, 5517 (2012).

[212] M. Nakaoka, T. Hyodo, Y. Shimizu, and M. Egashira, ECS Transactions **16**, 293 (2008).

[213] J. M. Lee, J. Park, S. Kim, S. Kim, E. Lee, S.-J. Kim, and W. Lee, International Journal of Hydrogen Energy **35**, 12568 (2010).

[214] E. Della Gaspera, M. Bersani, G. Mattei, T.-L. Nguyen, P. Mulvaney, and A. Martucci, Nanoscale **4**, 5972 (2012).

[215] E. Della Gaspera, E. Menin, G. Maggioni, C. Sada, and A. Martucci, Materials **11** (2018).

[216] U. Aschauer and A. Selloni, Phys. Chem. Chem. Phys. **14**, 16595 (2012).

[217] C. Spreafico, W. Karim, Y. Ekinci, J. A. van Bokhoven, and J. VandeVondele, The Journal of Physical Chemistry C **121**, 17862 (2017).

[218] U. Roland, T. Braunschweig, and F. Roessner, Journal of Molecular Catalysis A: Chemical **127**, 61 (1997).

[219] T. S. Bjørheim, S. Stølen, and T. Norby, Phys. Chem. Chem. Phys. **12**, 6817 (2010).

[220] W. Göpel and K. Schierbaum, Sensors and Actuators B , 1 (1995).

[221] P. W. Peacock and J. Robertson, Applied Physics Letters **83**, 2025 (2003).

[222] F. Herklotz, E. V. Lavrov, and J. Weber, Phys. Rev. B **83**, 235202 (2011).

[223] E. Finazzi, C. Di Valentin, G. Pacchioni, and A. Selloni, The Journal of Chemical Physics **129**, 154113 (2008).

[224] B. Lyson-Sypien, M. Radecka, M. Rekas, K. Swierczek, K. Michalow-Mauke, T. Graule, and K. Zakrzewska, Sensors and Actuators B: Chemical **211**, 67 (2015).

[225] A. Kusior, M. Radecka, L. Zych, K. Zakrzewska, A. Reszka, and B. Kowalski, Sensors and Actuators B: Chemical **189**, 251 (2013).

[226] H. Tang, K. Prasad, R. Sanjines, and F. Levy, Sensors and Actuators B: Chemical **26**, 71 (1995).

[227] A. Janotti and C. G. Van de Walle, Nature Materials **6**, 44 (2007).

[228] R. Ramamoorthy, P. K. Dutta, and S. A. Akbar, Journal of Materials Science **38**, 4271 (2003).

[229] M. Atashbar, H. Sun, B. Gong, W. Wlodarski, and R. Lamb, Thin Solid Films **326**, 238 (1998).

[230] T. L. Thompson and J. T. Yates, The Journal of Physical Chemistry B **109**, 18230 (2005).

[231] M. Jakob, H. Levanon, and P. V. Kamat, Nano Letters **3**, 353 (2003).

[232] G. C. Bond and D. T. Thompson, Catalysis Reviews **41**, 319 (1999).

[233] F. Cosandey and T. E. Madey, Surface Review and Letters **08**, 73 (2001).

[234] M. Haruta, CATTECH **6**, 102 (2002).

[235] F. Cosandey, L. Zhang, and T. Madey, Surface Science **474**, 1 (2001).

[236] V. Subramanian, E. E. Wolf, and P. V. Kamat, Journal of the American Chemical Society **126**, 4943 (2004).

[237] D. A. Panayotov and J. T. Yates, The Journal of Physical Chemistry C **111**, 2959 (2007).

[238] B. Larsen, T. Janssens, B. Clausen, H. Falsig, C. Christensen, and J. Nørskov, Nano Today **2**, 14 (2007).

[239] W. Xiong, M. Wu, L. Zhou, and S. Liu, RSC Adv. **4**, 32092 (2014).

[240] D. Barreca, G. Carraro, E. Comini, A. Gasparotto, C. Maccato, C. Sada, G. Sberveglieri, and E. Tondello, The Journal of Physical Chemistry C **115**, 10510 (2011).

[241] J. Macak, F. Schmidt-Stein, and P. Schmuki, Electrochemistry Communications **9**, 1783 (2007).

[242] J. Blanc and D. L. Staebler, Phys. Rev. B **4**, 3548 (1971).

124

[243] S. Lee, J. S. Lee, J.-B. Park, Y. Koo Kyoung, M.-J. Lee, and T. Won Noh, APL Materials **2**, 066103 (2014).

[244] M. Yu, C. Li, Y. Yang, S. Xu, K. Zhang, H. Cui, and X. Zhu, Electrochemistry Communications **90**, 34 (2018).

[245] A. Mahata, P. Garg, K. S. Rawat, P. Bhauriyal, and B. Pathak, J. Mater. Chem. A **5**, 5303 (2017).

[246] A. Bielanski and J. Haber, Catalysis Reviews **19**, 1 (1979).

[247] M. Löfdahl, M. Eriksson, M. Johansson, and I. Lundström, Journal of Applied Physics **91**, 4275 (2002).

[248] K. Liu, P. Avouris, J. Bucchignano, R. Martel, S. Sun, and J. Michl, Applied Physics Letters **80**, 865 (2002).

[249] T. Li, W. Hu, and D. Zhu, Advanced Materials **22**, 286 (2010).

[250] G. Esen and M. S. Fuhrer, Applied Physics Letters **87**, 263101 (2005).

[251] S.-W. Chung, D. Ginger, M. Morales, Z. Zhang, V. Chandrasekhar, M. Ratner, and C. Mirkin, Small **1**, 64 (2005).

[252] H. Park, A. K. L. Lim, A. P. Alivisatos, J. Park, and P. L. McEuen, Applied Physics Letters **75**, 301 (1999).

[253] J. Park, A. N. Pasupathy, J. I. Goldsmith, C. Chang, Y. Yaish, J. R. Petta, M. Rinkoski, J. P. Sethna, H. D. Abruña, P. L. McEuen, and D. C. Ralph, Nature **417**, 722 (2002).

[254] W. Liang, M. P. Shores, M. Bockrath, J. R. Long, and H. Park, Nature **417**, 725 (2002).

[255] M. Frimmer, G. Puebla-Hellmann, A. Wallraff, and L. Novotny, Applied Physics Letters **105**, 221118 (2014).

[256] L. Qin, J.-W. Jang, L. Huang, and C. Mirkin, Small **3**, 86 (2007).

# Danksagung

An dieser Stelle möchte ich allen Personen danken, mit deren Unterstützung diese Arbeit entstanden ist.

Meinem Doktorvater Prof. Dr. Thomas Heinzel danke ich zuallererst dafür, dass er mir die Möglichkeit gegeben hat am IPkM zu promovieren und an interessanten Projekten zu arbeiten. Danke für die fachliche und menschliche Unterstützung in all der Zeit. Auch bin ich sehr dankbar dafür, dass er mich an seiner Stelle zum EMN-Meeting nach Hawaii geschickt hat, was eine unglaublich wertvolle und tolle Erfahrung war.

Prof. Dr. Klaus Dieter Schierbaum danke ich für viele konstruktive Gespräche während der verschiedenen Projekte. Danke auch dafür, dass er uns seine Sputteranlage hat nutzen lassen. Dr. Mhamed El Achhab danke ich für die freundliche Bereitstellung der elektrochemisch hergestellten Proben.

Auch danke ich Prof. Dr. Axel Görlitz für das Mentoring und Korreferieren.

Dank gebührt auch dem AiF ZIM vom BMWi (ZF 4185501Z5G) für die finanzielle Unterstützung und unseren Kooperationspartnern von neo hydrogen sensors GmbH: Dr. Dieter Ostermann, Helmut Lüder, Kai Bothe und Oliver Hissel.

Dr. Stefan Trellenkamp und Dr. Elmar Neumann vom HNF des Forschungszentrum Jülich danke ich für die Elektronenstrahllithographie, sowie SEM und EDX-Messungen an unseren Proben.

Für die technische Unterstützung bei den Experimenten und bei der Installation des neuen Messaufbaus danke ich Wilfried Gjungjek-Schützek, Uwe Zimmermann und Harald Götz.

Dank Bernd Schüler, Mihai Cerchez und Jakob Schluck habe ich mich schon zu Zeiten meiner Masterarbeit im Institut sehr gut aufgehoben gefühlt. Besonders danke ich Jakob dafür, dass er mir, vor allem in meiner Anfangszeit, sehr hilfsbereit und geduldig alle Geräte erklärt und Verfahren beigebracht hat. Bianka Lindenau danke ich dafür, dass sie sehr oft für mich unangenehme administrative Dinge erledigt hat und dafür, dass sie so ein freundlicher und einfühlsamer Mensch ist. Auch meinen (Ex-)Kollegen Stefan, Beate, Schlaurin, Schrack, Lisa, Karoline und Christian danke ich für die tolle Atmosphäre im Institut. Danke an Laurin, der stets bemüht war mir etwas Nihongo beizubringen und mit dem man ganz toll Musik machen kann. Auch danke ich Daniela, Paulus und Mara für die angenehme Zusammenarbeit. Besonders danke ich Matthias für seine Unterstützung. Danke natürlich auch dafür, dass er die Sputtermaschine(n) aufgebaut und mich darin eingewiesen hat und auch für das Korrekturlesen.

Zu guter Letzt sei auch Thorsten, Torben, Flori und natürlich Amanda gedankt, ohne die das alles nicht möglich gewesen wäre.